UNIVERSITAT ROVIRA I VIRGILI
DEVELOPMENT OF A THICK FILM GAS SENSOR FOR OXIGEN DETECTION AT TRACE LEVEL
Edgar Alexander Sotter Solano
DL: T-324-2010/ISBN: 978-84-691-2431-4

Development of a Thick Film Gas Sensor for Oxygen Detection at Trace Levels

Thesis submitted for the degree of doctor by
Edgar Sotter

Director:
Xavier Vilanova

Tarragona, May 2006

UNIVERSITAT ROVIRA I VIRGILI
DEVELOPMENT OF A THICK FILM GAS SENSOR FOR OXIGEN DETECTION AT TRACE LEVEL
Edgar Alexander Sotter Solano
DL: T-324-2010/ISBN: 978-84-691-2431-4

UNIVERSITAT ROVIRA I VIRGILI
DEVELOPMENT OF A THICK FILM GAS SENSOR FOR OXIGEN DETECTION AT TRACE LEVEL
Edgar Alexander Sotter Solano
DL: T-324-2010/ISBN: 978-84-691-2431-4

Dedicated to my family:
Edgar, Miryam,
Emely and Mónica

UNIVERSITAT ROVIRA I VIRGILI
DEVELOPMENT OF A THICK FILM GAS SENSOR FOR OXIGEN DETECTION AT TRACE LEVEL
Edgar Alexander Sotter Solano
DL: T-324-2010/ISBN: 978-84-691-2431-4

CONTENTS

ACKNOWLEDGMENTS / AGRADECIMIENTOS

Me gustaría agradecer a todas las personas que me han ayudado y han colaborado en la elaboración de esta tesis. En primer lugar, quiero dar las gracias a mi director Xavier Vilanova. Muchísimas gracias por haberme transmitido tus conocimientos, por los buenos consejos y sobretodo por tu paciencia y tu ayuda.

Estoy muy agradecido con todas las personas que de uno u otro modo han hecho un aporte durante el proceso de investigación. A Ana Ruiz por su colaboración con el proceso de síntesis del material. Muchas gracias a Alexey Vasiliev por su inestimable ayuda en la culminación de este trabajo. También quiero darle las gracias a Eduard Llobet, a Xavier Correig y a Viacheslav Khatko por todos sus buenos consejos.

Muchísimas gracias a Mariana Stankova y a Trifon Trifonov. Su ayuda fue muy importante en el desarrollo de este trabajo. Gracias también por la amistad que me han brindado, por los *Jack Daniels* y por las largas conversaciones. Също искам да ви благодаря за приятелството, което ми дадохте. За мен бяхте много голяма подкрепа. Много ви благодаря!

A Mariona Vinaixa y Viviana Duarte les quiero agradecer su apoyo en la preparación y desarrollo de los procesos químicos. Marioneta, gracias además por tu ayuda con la traducción del resumen al catalán…moltes gràcies maca! Gracias también a Raúl Calavia por toda la ayuda prestada, por las placas, por los programas, por los cambios de botellas… ya por fin te librarás de mí Raulet! A Edwin Espinosa le quiero agradecer no solo su ayuda en el trabajo, que fue inmensa, sino también su amistad y su compañía durante los interminables días de mediciones en el verano. A Stella Vallejos (Telucha) por ayudarme en parte del proceso de fabricación. También quisiera agradecerles a los técnicos del DEEEA, al Maré, al Badi, a Jaume, a Deosdad y al Carmelo. Gracias porque muchas veces hicieron más de lo que su trabajo les obligaba por ayudarme.

Quiero también dar las gracias a Jaromir Hubalek, Jan Prásek y a Zdenek Kral por su ayuda en la fabricación del substrato. Les quiero agradecer la gran amistad que me han dado, y por haberme mostrado que en la República Checa están buenas tanto las rubias como las morenas… me refiero a las cervezas. Esto también va por Radek! Dekuji moc!

Muchas gracias a aquellas personas que me colaboraron con la caracterización de los materiales. Mercè Moncusí y Arantxa Vilalta, por su colaboración con al análisis SEM. Muchas gracias a Francesc Guirado por haber efectuado los análisis XRD. Antonio de la Torre por haber realizado las medidas ICP. Gracias a Tariq Jawhari por su asistencia en las medidas Raman. Quiero agradecer a Vanesa Fierro y Vanesa Torné por su ayuda con las medidas de area BET. A Vanesa Torné quiero agradecerle además las veces que me echó una mano en los procesos químicos. A Francesc Medina y a Moisés Carreón les quiero

agradecer los consejos que me dieron en lo relacionado con la síntesis de los materiales mesoporosos.

También quiero dar las gracias a todos los compañeros de los laboratorios, no voy a nombrarlos a todos, porque la lista se haría muy larga. Gracias por haberme apoyado y aconsejado. Muchísimas gracias a Nuria, por haberme aguantado en estos años, por disfrutar conmigo los buenos momentos y por haberme apoyado en los malos; gracias por los 'relajantes' viajes, por las sidrinas, por los *Baileys* y por todo lo demás que no puedo enumerar porque no hay espacio…gracias por todo, tu amistad a sido un gran apoyo… ah, y gracias por tu ayuda en la escritura de algunos apartados de esta tesis ;-).

Gracias a Jesús y a Carmen por hacerme sentir como en casa las veces que necesité ir a casa. Quiero agradecerle también a Angie, quien estuvo siempre dándome fuerzas desde la distancia… te lo agradezco muchísimo. Gracias a Alex por su gran amistad. Gracias a Iván y a Joria por no dejarme deprimir con la tesis, gracias por la amistad que me han brindado.

Por último, pero no menos importante, quiero agradecer a mi familia, a mis padres y a mis hermanas, todo el apoyo y comprensión que me han dado. Aunque lejos, para mí siempre estuvieron a mi lado.

Gracias también a mi profesor de química del colegio, Fermín Zafra, quien lamentablemente ya no podrá leer este trabajo. Si tan solo supiese lo que me han servido sus clases.

Una vez más, gracias a todos. Han sido los mejores.

Agradezco también la beca predoctoral que me ha proporcionado la Universitat Rovira i Virgili y a la empresa Carburos Metálicos por haber financiado parcialmente este trabajo.

SUMMARY

Control of oxygen levels is a critical step in many industrial processes. In some of these processes, levels of oxygen must be detected and controlled even in ppm range. Although there are several probed methods for oxygen detection in these control systems, most of them are expensive and complex. More accessible methods as Lambda sensors or electrochemical cells present also problems: first ones need high concentration of oxygen, or an extremely accurate temperature control, to work without interference from other gases. Second ones may be affected by prolonged exposure to "acid" gases such as carbon dioxide and it is not recommended for continuous use in atmospheres which contain more than 25% of CO_2.

Due to many advantages as low cost, small size and robustness, semiconductor sensors appear as a good solution for oxygen detection. Some authors had reported detection of oxygen at ppm levels employing this kind of sensors. However, most of them were made through thin film technology. For industrial applications, the most usual technology is thick film, because it is easier to fabricate and to dope than thin film sensors. For thick film sensors, detection of traces of oxygen is still a very difficult goal to reach and usually high temperatures (>700 ºC) are needed.

The basic oxygen sensitivity mechanism of oxygen sensors based on semiconductor oxides is their strong dependencies of electrical conductivity on oxygen partial pressures. Titanium dioxide is the semiconductor material most widely used for oxygen detection. Titania (usually rutile crystalline phase) based sensors need to work at high temperatures (700 ºC – 1000 ºC), since oxygen detection in rutile state is mainly due to diffusion of oxygen ions in the bulk of the material. For bulk reaction it is necessary to work at these high temperatures, leading to high power consumption, which is not desirable for electronic applications.

On the other hand, anatase state Titania has more free electrons. So, oxygen detection can be associated to surface reactions, which take place at not so high temperatures (400 ºC – 500 ºC). Then, it can be derived that maintaining an anatase structure would allow the detection of oxygen at medium temperatures, which is desirable for sensor design.

It had been reported that when Titania is doped with pentavalent impurity ions, i.e. Nb^{5+}, such ions get into the anatase Titania crystalline structure, giving rise to a hindering in the phase transformation to rutile and an inhibition in grain growth. It has been also reported that Nb-doped Titania shows higher sensitivity towards oxygen than pure TiO_2. The doped material also shows lower impedance at low operating temperatures and hence, it is easier to design associated electronic circuitry.

In this work pure Titania and Niobium doped Titania nanopowders were synthesized by a simplified sol-gel route. Based on the literature, the doping concentration in doped materials was set to Nb/Ti = 3 at%. In order to set the crystalline structure of the active materials, they were calcined at four different temperatures: 600 ºC, 700 ºC, 800 ºC and 900 ºC.

The obtained materials were characterized by different techniques. The objective of these characterizations was to obtain information about the material structure that could be related to its detection properties. Inductively Coupled Plasma (ICP) spectroscopy was employed to determine the chemical composition of the samples and quantify the amount of each component. X-ray Diffraction (XRD) was used to establish the phases present in the crystalline structure of the material and to determine the size of the crystallites in each material. Area BET measurements were done to nanopowders to know the surface area and the porosity of each material. Scanning Electron Microscopy (SEM) was used to obtain details on the film structure and the grain size. To make quantitative and qualitative analysis, Energy-Dispersive X-ray Spectroscopy (EDS) was also applied.

For the measurements, an alumina substrate was developed to be used in the oxygen sensor. This substrate can support four active layers working at the same temperature forming a sensor array. However, due some problems related with the substrate package at working temperatures above 450 ºC, the use of this substrate for oxygen sensor application was delayed and the results obtained whit it were not complete enough to be presented in this work. In order to resolve the necessity of a substrate that can resist high working temperatures for oxygen sensing applications, it was introduced a new substrate acquired from the Kurchatov Institute (Moscow-Russia). The results exposed in this work were obtained by using this last substrate.

Using these substrates, the sensing capabilities of the materials were also tested. The sensitivity toward oxygen was measured under three different conditions: 20 ppm of O_2 in N_2 balance, 30 ppm and 15 pmm of O_2 in CO_2 balance. The sensors responses toward other pollutant gases (SO_2, CH_4, H_2S and C_2H_4) were also tested in order to see the influence of such gases in the oxygen detection process.

The best response toward oxygen was achieved in those sensors based on Nb-doped materials calcined at 700 ºC. This may be attributed to the niobium ions which hinder the grain growth and hence give rise to a high surface area that benefits the detection mechanism. The good response may be also attributed to the crystalline phase, mostly anatase, which allows the detection at desire temperatures (300 ºC – 600 ºC).

On the other hand, the doped materials calcined at 600 ºC had a poor response, in spite of they have better physical characteristics than doped materials calcined at 700 ºC. This problem was mainly related to some carbon deposits detected in these materials trough Raman analyses. Such carbon deposits may be residual of the synthesis process, which could not be eliminated during the calcination. Since these carbon structures cover a great part of the material surface, and they are also poorly catalytic, the result is a deactivation of the catalysis.

Concerning to the measurements carried out under CO_2 atmosphere, Nb-doped Titania calcined at 700 ºC also responded to oxygen. However, the response toward 15 ppm of oxygen presented an inversion from oxidative type to reductive type. At low oxygen concentrations, the CO^- ions from CO_2 disassociation are adsorbed on the active material

surface. The oxygen, instead deplexing, interacts with these ions forming CO_2, liberating electrons to the active layer giving rise to a reductive type response. On the other hand, the responses toward other pollutant gases such H_2S, SO_2, C_2H_4 and CH_4 were of reduction type, as they were expected, which support the idea that the change in the response type is not due to the change in the physics of the semiconductor oxide from n type to p type, but to a change in the reaction nature.

In order to improve the sensing capabilities of doped materials, it was attempted to increase their surface area and porosity by using a surfactant as a template during the synthesis process. The surfactant employed was dodecylamine, which forms a micellar structure that works as template in the nucleation process of the oxide, generating small grains with higher surface area and porosity. Among three different attempts, the best results were obtained when 8 ml of surfactant were added to the sol-gel solution just after the hydrolysis of the metal alkoxides. XRD analyses of this material showed that the addition of surfactant retards even more the phase transition from anatase to rutile and also hinder the crystallites growth. These results were supported by SEM micrographs and BET analysis, which show a hinder in grain growth and an increase of the surface area. Area BET also evidences an increment of the material porosity. However, the results of the oxygen measurement reveal a poor response of the considered material. The Raman spectroscopy of this oxide shows some peaks that correspond to carbon with different morphologies. As it was explained before, these deposits of carbon retard the response of this material toward oxygen.

RESUMEN

El control de los niveles de oxígeno es una etapa crítica en muchos procesos industriales. En algunos de estos procesos, los niveles de oxígeno deben ser detectados y controlados incluso en el rango de las ppm. Aunque existen varios métodos ya probados para la detección de oxígeno en estos sistemas de control, la mayoría de ellos son costosos y complejos. Otros métodos de detección más accesible como los sensores Lambda o las celdas electoquímicas también presentan problemas: los primeros requieren de altas concentraciones de oxígeno, o de controles de temperatura bastante precisos para poder trabajar sin interferencias de otros gases Los segundos pueden verse afectados por una prolongada exposición a gases "ácidos" como el dióxido de carbono y no se recomienda para uso continuo en atmósferas con un contenido de mas del 25 % de dicho gas.

Debido a muchas ventajas tales como su bajo costo, tamaño reducido y solidez, los sensores basados en semiconductores aparecen como una solución para la detección de oxígeno. Algunos autores han reportado la detección de oxígeno a niveles ppm empleando este tipo de sensores. Sin embargo, la mayoría de ellos han sido desarrollados mediante tecnología de capa fina. En aplicaciones industriales, la tecnología más usada es la de capa gruesa, ya que estos sensores son más fáciles de fabricar y de dopar que los sensores de capa fina. En los sensores de capa gruesa, la detección de trazas de oxígeno es aun una tarea difícil de alcanzar, siendo normalmente necesarias altas temperaturas (> 700 ºC) para lograrlo.

El mecanismo de detección de oxígeno en los sensores basados en óxidos semiconductores esta basado en la fuerte dependencia de la conductividad eléctrica de estos materiales a la presión parcial de oxígeno en el ambiente. El dióxido de titanio es el óxido semiconductor más ampliamente usado en la detección de oxígeno. Los sensores basados en TiO_2 (usualmente en la fase cristalina rutilo) necesitan trabajar a elevadas temperaturas (700 ºC – 1000 ºC), ya que la detección de oxígeno en la fase rutile se debe principalmente a la difusión de los iones de oxígeno en el volumen del material. Para que se produzca la reacción en el volumen hacen falta altas temperaturas, lo que conlleva un alto consumo de potencia que puede ser un handicap en determinadas aplicaciones industriales.

Por otro lado, el dióxido de titanio en fase anatase posee más electrones libres, así que la detección de oxígeno en este material puede asociarse a una reacción de superficie, la cual tiene lugar a no tan altas temperaturas (400 ºC – 500 ºC).Por lo tanto, puede concluirse que mantener la fase anatase permitiría la detección de oxígeno a temperaturas moderadas, lo cual es deseable para el diseño del sensor.

Se ha reportado que cuando el TiO_2 es dopado con iones pentavalentes, i.e. Nb^{5+}, tales iones se introducen en la estructura cristalina de dicho óxido en estado anatase, obstruyendo la transformación de dicha fase a rutile, inhibiendo el crecimiento del grano.

También se ha reportado que el dopado con niobio aumenta la sensibilidad del dióxido de titanio hacia el oxígeno. El óxido dopado también presenta una impedancia más baja a temperaturas de trabajo menores, por lo que se facilita el diseño de la electrónica asociada al sensor.

Basándonos en estos puntos, uno de los objetivos de esta tesis fue la síntesis, mediante un proceso de sol-gel, de diferentes tipos de dióxido de titanio para la fabricación de un sensor de oxígeno que opere en un margen de temperaturas moderado (300 ºC – 600 ºC). Para ello se desarrollaron óxidos dopados con un 3 % de niobio y óxidos sin dopar. Cada uno de ellos fue calcinado a diferentes temperaturas: 600 ºC, 700 ºC, 800 ºC y 900 ºC.

Con el objetivo de correlacionar la estructura y la sensibilidad y selectividad de los óxidos sintetizados, estos se sometieron a diferentes técnicas de caracterización. La espectroscopia de Plasma Acoplado Inductivamente (ICP) fue empleada para determinar la composición química de las muestras y cuantificar la porción de cada componente. La Difracción de Rayos-X (XRD) fue usada para establecer las fases presentes en la estructura cristalina del material y para determinar el tamaño el tamaño de los cristales en cada material. Se realizaron medidas de área BET con los nanopolvos para conocer el área superficial y la porosidad de cada material. La Microscopia de Escáner de Electrones (SEM) fue aplicado para obtener detalles de la estructura de la capa y del tamaño de las partículas. Para hacer un análisis cuantitativo y cualitativo de las capas se utilizó la Espectroscopia de Dispersión de Energía por Rayos –X (EDS).

Para realizar las medidas, se desarrolló un substrato de alúmina para ser usado en el sensor de oxígeno. Este substrato puede soportar cuatro capas activas trabajando a la misma temperatura formando una matriz de sensores. Sin embargo, debido a algunos problemas relacionados con el encapsulado del substrato cuando las temperaturas de trabajo sobrepasaban los 450 ºC, su empleo para el sensor de oxígeno se retrasó y los resultados obtenidos con el mismo no estaban lo suficientemente completos para ser presentados en este trabajo. Para solventar la necesidad de un substrato que pudiese resistir altas temperaturas para aplicaciones de detección de oxígeno, se introdujo un nuevo substrato adquirido en el Instituto Kurchatov (Moscú - Rusia). Los resultados expuestos en este trabajo se obtuvieron con este último substrato.

Una vez fabricados los sensores, las capacidades de sensado de los materiales fueron probadas. La sensibilidad hacia el oxígeno fue medida en tres situaciones diferentes: 20 ppm de O_2 en balance de N_2, 30 ppm y 15 ppm de O_2 en balance de CO_2. Las respuestas de los sensores hacia otros gases contaminantes (SO_2, CH_4, H_2S y C_2H_4) también fueron probadas para observar la influencia de dichos gases en el proceso de detección de oxígeno.

La mejor respuesta hacia el oxígeno se consiguió con los sensores basados en materiales dopados calcinados a 700 ºC. Esto puede atribuirse a los iones de niobio que inhiben el crecimiento del grano y por lo tanto producen un aumento del área superficial de dichos materiales, que beneficia al mecanismo de detección, y a su fase cristalina,

mayoritariamente anatase, la cual permite la detección a las temperaturas deseadas (300 ºC – 600 ºC). Las especies de niobio también contribuyen al proceso de catálisis.

Otro motivo puede ser la fase cristalina, mayoritariamente anatase, la cual permite la detección a las temperaturas deseadas (300 ºC – 600 ºC).

Por otro lado, los materiales dopados calcinados a 600 ºC tuvieron una pobre respuesta, a pesar de que estos tienen mejores características físicas que los calcinados a 700 ºC. Este hecho puede explicarse por la presencia de algunos depósitos de carbono, residuales del proceso de síntesis, que no pudieron ser eliminados durante la calcinación. La presencia de estos depósitos fue confirmada mediante los análisis Raman de estos materiales. Ya que estas estructuras de carbono cubren gran parte de la superficie del material, y que además son poco catalíticas, el resultado es una desactivación de la catálisis.

Concerniente a las medidas realizadas en atmósfera de CO_2, los óxidos dopados con niobio y calcinados a 700 ºC también respondieron al oxígeno. Sin embargo, la respuesta hacia 15 ppm de oxígeno presentó una inversión de tipo oxidante a tipo reductora. A bajas concentraciones de oxígeno, los iones de CO^-, provenientes de la disociación del CO_2, se adsorben en la superficie del material activo. El oxígeno, en lugar de deplexionarse, interactúa con estos iones para formar CO_2, liberando electrones a la capa activa, dando lugar así a una respuesta reductora. Por otra parte, las respuestas hacia otros gases contaminantes tales como H_2S, SO_2 y CH_4 fueron de tipo reductora, como era esperado, lo cual indica que el cambio de respuesta no puede atribuirse al cambio del óxido conductor de tipo n a tipo p, sino más bien a un cambio en la naturaleza de la reacción.

Para mejorar la sensibilidad de los óxidos dopados, se intentó incrementar su área superficial y porosidad usando un surfactante como plantilla o molde durante el proceso de síntesis. El surfactante empleado fue dodecylamina, la cual forma una estructura micelar que hace de molde durante el proceso de nucleación del óxido, generando así granos menores con mayor área superficial y mayor porosidad. Entre tres diferentes intentos, los mejores resultados se obtuvieron cuando 8ml de dodecylamina fueron agregados a la solución del sol-gel inmediatamente después de la hidrólisis de los alkóxidos. Los análisis de XRD de este material mostraron que la adición de surfactante retarda aun más la transición de fase de anatase a rutile y también evita el crecimiento de los cristalitos. Estos resultados son soportados por las microfotografías de SEM y los análisis BET, los cuales mostraron un retardo en el crecimiento del grano y un incremento del área superficial. El área BET también evidenció un incremento de la porosidad del óxido. Sin embargo, los resultados de las medidas de oxígeno revelaron una pobre respuesta de los sensores basados en el óxido en cuestión. Los espectros Raman de este material mostraron algunos picos correspondientes a carbono con diferentes morfologías. Como fue explicado previamente, estos depósitos de carbono retardan la respuesta de este óxido al oxígeno.

RESUM

El control dels nivells d'oxigen és una etapa crítica en molts processos industrials. En alguns d'aquests, els nivells d'oxigen han de ser detectats i controlats fins i tot en el rang de les ppm. Encara que ja es coneguin molts mètodes, ja provats per a la detecció d'oxigen, la majoria d'ells són costosos i complexes. Altres mètodes més accessibles com els sensors Lambda i les cel·les electroquímiques també presenten alguns problemes. Els primers requereixen d'elevades concentracions d'oxigen o bé de controls de temperatura força precisos amb la finalitat de treballar sense interferència d'altres gasos. Els segons es poden veure afectats per temps d'exposició massa perllongats a gasos "àcids" com el diòxid de carboni i no es recomana el seu ús en atmosferes amb un contingut de més del 25% d'aquests gas.

Són moltes les avantatges dels sensors de gasos: baix cost, mida reduïda i solidesa entre d'altres. Això fa que aquests dispositius despuntin com a solució per a la detecció d'oxigen. Molts autors han fet esment a la detecció d'oxigen a nivells de ppm emprant aquests tipus de sensors. De totes formes, la majoria s'han desenvolupat mitjançant tecnologia de capa fina. En aplicacions industrials, la tecnologia més usada és la de capa gruixuda, ja que aquests sensors són més fàcils de fabricar i de dopar que els de capa fina. En el cas dels sensors de capa gruixuda la detecció de traces d'oxigen és una tasca encara difícil i es necessita treballar a elevades temperatures (> 700 ºC).

El mecanisme de detecció d'oxigen en els sensors basats en òxids semiconductors es basa en la interdependència de la conductivitat elèctrica d'aquests òxids i la pressió parcial d'oxigen en l'ambient. El diòxid de titani és l'òxid semiconductor que més s'usa en la detecció d'oxigen. Els sensors basats en òxid de titani (en fase cristal·lina rutil) necessiten d'elevades temperatures per a un correcte funcionament (700 ºC-1000 ºC), ja que la detecció d'oxigen en la fase rutil es deu principalment a la difusió dels ion d'aquests gas en el volum del material. Per a que es produeixi la reacció en el volum o propi cos del material es necessiten elevades temperatures. Això comporta un consum també elevat de potència, que a la llarga serà un problema en determinades aplicacions industrials.

Al tenir l'òxid de titani en fase anatasa més electrons lliures, la reacció de l'oxigen amb aquests material es pot associar a una reacció superficial. Aquesta reacció es pot donar a temperatures més baixes, al voltant dels 400 ºC-500 ºC i per tant, mantenir la fase anatasa en l'òxid permet disminuir la temperatura de treball, la qual cosa és desitjable per al disseny del sensor.

Tal i com es reflecteix en algunes referències bibliogràfiques, en dopar l'òxid de titani amb ions pentavalents com el Nb^{5+}, aquests ions s'introdueixen en l'estructura cristallina de l'òxid de titani en fase anatasa, creant certa tensió interna que provoca una resistència al canvi de fase anatasa a rutil, inhibint el creixement del gra.

Per altra banda, també s'ha posat de manifest en moltes fonts que el dopatge d'òxid de titani amb niobi augmenta la sensibilitat d'aquests material vers l'oxigen. Aquests dopatge fa que l'òxid presenti una impedància menor, per la qual cosa es facilita el disseny de l'electrònica associada al sensor.

Tenint en compte aquestes dues premisses, un dels objectius d'aquesta tesi ha estat la síntesi, mitjançant la tècnica del sol-gel, de diferents tipus d'òxid de titani per a la fabricació d'un sensor d'oxigen que operi en una marge de temperatura relativament moderat (300 ºC-600 ºC). Es treballà amb òxids sense dopar i amb òxids dopats amb un 3 % de niobi. Cadascun es calcinà a diferents temperatures: 600 ºC, 700 ºC, 800 ºC i 900 ºC.

Amb l'objectiu de correlacionar l'estructura i la sensibilitat i selectivitat dels òxids sintetitzats, aquests es van sotmetre a diferents tècniques de caracterització. En primer lloc l'espectrometria de plasma acoblada inductivament (ICP) s'utilitzà amb el fi de determinar-ne la composició química i quantificar la proporció de cada component. En segon lloc també es va fer servir la difracció de raigs X (XRD) per a determinar les fases cristallines de l'òxid i la mida dels cristalls. També es va analitzar la porositat i es van fer mesures de l'àrea superficial (BET) dels nanopols . En darrer lloc, la microscopia d'escàner d'electrons (SEM) fou aplicada amb la finalitat d'obtenir detalls de l'estructura de la capa activa i de la grandària dels grans. Per a l'anàlisi quantitatiu i també qualitatiu de les capes s'utilitzà l'espectroscopia de dispersió d'energia per raig X (EDS).

Com a substrat, es va desenvolupar un substrat d'alúmina que pot albergar quatre capes actives treballant a una mateixa temperatura, conformant així una matriu de sensors. Treballant amb aquests substrat aparegueren certs inconvenients (relacionats amb l'encapsulat del sensor) operant a temperatures superiors als 450 ºC. Això comportà un retard en l'obtenció de resultats amb aquests substrat i es decidí introduir-ne un de nou, resistent a altes temperatures i adquirit en l'Institut Kurchatov (Moscou, Rússia). Tots els resultats presentats en aquesta tesi es van obtenir amb l'ús d'aquests últim substrat. En l'actualitat s'està treballant amb el primer d'ells.

Un cop fabricat els sensors, es provà la sensibilitat d'aquests en un sistema de flux continu. Es provaren tres diferents concentracions: 20 ppm d'O_2 amb balanç de N_2, 30 ppm d' O_2 amb balanç CO_2 i 15 ppm d'O_2 amb balanç CO_2. També es testaren les respostes dels sensors cap a altres gasos interferents (SO_2, CH_4, H_2S i C_2H_4) per a determinar la selectivitat d'aquests sensor vers l'O_2 en presència d'interferents.

La millor resposta vers l'oxigen s'aconseguí amb els sensors dopats i calcinats a 700 ºC. Aquesta millora es pot atribuir al dopatge amb niobi. Aquets metall inhibeix el creixement del gra i per tant s'aconsegueixen òxids amb major àrea superficial. Un altre motiu pot ser el retard del pas de la fase rutil a la fase anatasa induït també pel dopatge de Niobi.

La sensibilitat denotada pels òxids dopats amb niobi i calcinats a 600 ºC fou molt baixa tot i que en principi aquests òxids presentaven característiques físiques potencialment millors que els calcinats a 700 ºC. Aquests fet es pot explicar degut a la presència d' alguns depòsits de carboni que no es pogueren eliminar durant la calcinació. La presència d'aquests dipòsits fou confirmada per l'anàlisi Raman d'aquests materials. Les estructures de carboni presents en aquests residus cobreixen gran part de la superfície de l'òxid i contribueixen a la desactivació del procés catalític que té lloc en aquesta superfície.

Concernint a les mesures realitzades sota atmosfera de CO_2, els òxids dopats amb niobi i calcinats a 700 ºC també respongueren a l'oxigen. La resposta en el cas de 15 ppm d'O_2 s'invertí del tipus oxidant a tipus reductor. A baixes concentracions d'oxigen els ion

CO^- provinents de la dissociació del CO_2 s'adsorbeixen a la superfície del material actiu. L'oxígen, enlloc de deplexionar-se, interactua amb aquests ions per a formar CO_2, alliberant electrons a la capa activa i això fa que la natura de la resposta sigui reductora. Les respostes vers altres gasos contaminants com SO_2, CH_4, H_2S foren tipus reductor com era esperat, la qual cosa indicava que el canvi de resposta no era atribuïble al canvi de l'òxid conductor de tipus n a tipus p, si no més aviat en un canvi en la naturalesa de la reacció.

Amb l'objectiu de millorar la sensibilitat de l'òxid dopat es provà d'incrementar la seva àrea superficial i porositat utilitzant un surfactant com a motlle durant el procés de síntesi. El surfactant usat fou la dodecilamina, que forma una estructura miscel·lar que fa de motlle en el procés de nucleació de l'òxid, generant així grans menors amb major àrea superficial i major porositat. De tres diferents temptatives, els millors resultats es varen obtenir quan s'addicionaven 8 ml de dodecilamina a la solució del sol-gel immediatament després de la hidròlisi dels alcòxids. Les proves XRD mostraren que l'addició del surfactant retarda encara més la transició de les fases rutil a anatasa i també inhibeix el creixement dels cristalls. Aquests resultats es recolzen sobre les micrografies del SEM i l'anàlisi BET, que revelaren un creixement en la porositat del material i un gra menor. Malgrat aquests resultats prometedors en la determinació estructural, les mesures de l'oxigen amb aquests sensors revelaren una poca sensibilitat dels sensors modificats amb el surfactant. Els espectres RAMAN mostraren alguns pics corresponents a diferents morfologies de carboni. Els dipòsits d'aquests material en la superfície, tal i que com s'ha mencionat anteriorment, inhibeixen la resposta de la capa activa vers l'oxigen.

I. INTRODUCTION

In this chapter it is presented the purpose of the present project. In first place it is introduced the necessity of oxygen detection at low concentrations levels. Some industrial applications that highly need oxygen control, and therefore detection at such concentration, are revised. Then, it a brief explanation of the most usual technologies that have been employed so far for oxygen detection in the industrial field is presented. Then, a detailed review of solid state sensors for oxygen detection is introduced. In this subsection the three main sensor technologies involved in solid state oxygen sensors are revised: Electrochemical sensors, optical sensors and metal oxide semiconductor (MOX) sensors. Finally, the objectives of this work are presented.

I.1. Processes that require low oxygen concentration

Oxygen is one of the most important and abundant chemical species. It constitutes 20.9 % of the earth's atmosphere, and besides to be indispensable to sustain animal and plant life in the biosphere, it is widely employed for many industrial purposes. For some applications, e.g. combustion in steel-making furnaces and welding, high quantities of pure oxygen are needed [1, 2]. On the other hand, there are many instances where the presence of oxygen must be kept at low levels (ppm) or could even be harmful. Due the natural presence of oxygen in the atmosphere, the control, and therefore, the detection of oxygen in such process is critical. Some examples of these applications are described below.

I.1.1. Food and Beverage Packaging

The main cause of most food-spoilage is oxygen [3, 4], since its presence allows a myriad of aerobic food-spoiling microorganism to grow and thrive. Oxygen also spoils many foods through enzyme-catalysed reactions, as in the browning of fruit and vegetables, destruction of ascorbic acid and the oxidation of a wide range of flavours. Many oxidative food-spoiling reactions, including lipid oxidation, occur non-enzymically. Food-spoiling microorganisms are active above the freezing point of food and most prevalent in foods of high water activity. In addition, the rates of growth of many spoilage organisms increase exponentially with temperature up to the point where they can be thermally disrupted or destroyed. On the other hand, there are applications where it is necessary to maintain a content of oxygen inside the package in order to prevent the growth of anaerobic bacteria e.g. Mushroom storage [5]. Oxygen also is necessary in maintaining the bright red colour of fresh meat [6, 7]. Thus, keeping food chilled in an ambient atmosphere with low oxygen concentration is one of the most current and popular methods of food packaging and storage [7, 8].

A common example of the latter is modified atmosphere packaging [3, 4], a process in which the atmosphere within the food package is flushed with an inert gas, such as nitrogen or carbon dioxide, reducing the oxygen content to tipically 0.1 % - 2 %, depending on the food [9].

In the case of beverage packaging i.e. beer, the flavour of beer deteriorates from the moment it is packaged as a result of the oxidation of compounds such as unsaturated fatty acids, alcohols, and iso-alpha acids. Low oxygen content of packaged beer is a prerequisite for flavour stability. A level of 0.27 ppm or below has been proposed as an ideal oxygen level in the finished package [10-12].

I.1.2. Beverage Carbonation

To deliver the fizz, beverages require a high quantity of dissolved carbon dioxide. This carbonation is obtained naturally during the fermentation of sugar into alcohol (sparkling wine, beer, etc) or artificially by injecting carbon dioxide into a liquid [13].
For efficient carbonation, a low concentration of dissolved O_2 is recommended. This is why CO_2-deoxygenation is carried out prior to the actual carbonation, mainly for producing soft drinks, carbonated water and beer. However, the CO_2 must be analyzed before the carbonation to assure the low oxygen concentration and other gases. The International Society of Beverage Technologists (ISBT) specifications for the concentration limits of pollutant gases in CO_2 employed for carbonation is shown in Table I.1 [14-16].

Table I.1 *ISBT carbon dioxide guidelines [14-16]*

Pollutant gas	Beverage Grade Specification (maximum value permited)
O_2	30 ppm
CO	10 ppm
NH_3	2.5 ppm
NO_2	2.5 ppm
CH_4	20 ppm
SO_2	1 ppm
C_2H_4O	0.2 ppm
C_6H_6	0.02 ppm
C_2H_4	20 ppm
H_2S	0.1ppm

I.1.3. Gas Transportation

Oxygen from air can contaminate some gases (e.g. CH_4, CO_2, and H_2S) during their extraction. This oxygen reacts with the gas and humidity to form sulphuric acid producing corrosion in gathering lines. Depending on the gas to be transported, the oxygen contents in such gas must be in the range of 1-100 ppm to prevent corrosion [17, 18].

I.2. Usual Technologies Employed for Oxygen Detection

It is clear that oxygen detection at low concentrations is critical for many industrial applications. To carry out the detection process, two different technologies are usually employed in the industry: Near-Infrared Phodetectors and zirconia based sensors. These technologies are revised below.

I.2.1. Near-Infrared (NIR) Photodetectors

In this technology, the near-infrared luminescence of the oxygen is measured [19, 20]. A NIR light, laser, is passed through the gas and the light adsorption is measured with a photodetector. The photodetector convert the light signal into electrical signal that can be processed by an electronic system [21, 22]. A schema of this system is shown in Figure I.1.

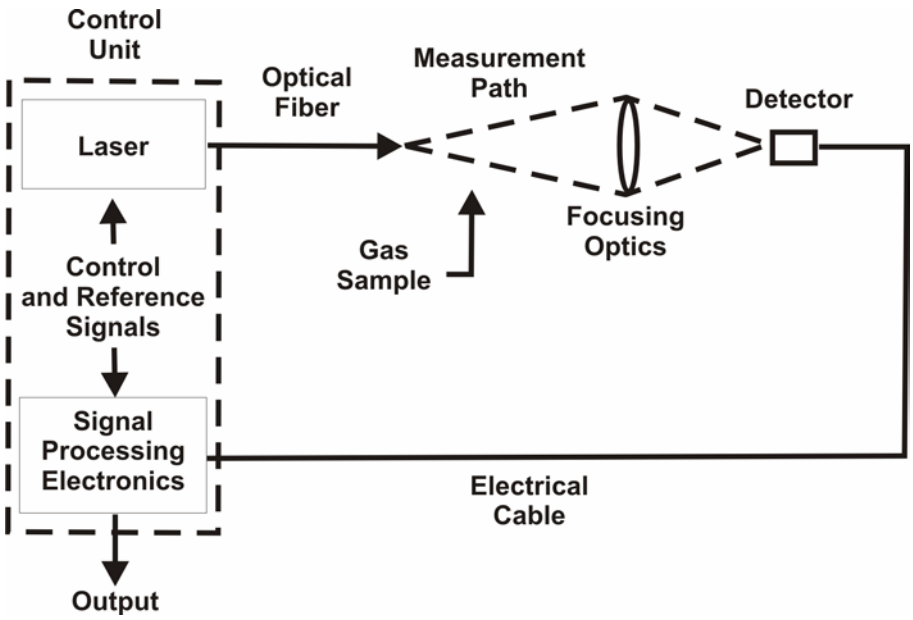

Figure I.1 *Schema of a NIR photodetector system [21]*

This technology is very accurate and has been widely tested, but the complexity of the system arise the production costs and makes necessary continuous technical supervision. However, by now it is the most used technology for static measurement equipments [20, 22]. For portable equipments, the usual technology is based on ceramics materials, i.e. Zirconia. This detection technology is exposed as follows.

I.2.2. Zirconia Based Sensors

This type of sensors is included in the electrochemical sensor technology that will be exposed in the next session. The detection process is based on the oxygen ion conductivity characteristic of an electrolyte i.e. zirconia. In this case, the ionic current through the electrolyte is proportional to the oxygen partial pressure in the sample gas and it is measured from the electrodes [23]. In Figure I.2 there are shown a typical commercial zirconia oxygen sensor and an analyzer system that use this kind of sensors [24, 25].

a. **b.**

Figure I.2 a. *Zirconia oxygen sensor (EMCO Packaging System)* ***b.*** *Oxygen analyzer System with electrochemical zirconia sensor (Cambridge Sensotech Ltda.) [24, 25]*

Electrochemical sensors technology is not as expensive as NIR Photodetectors and because is a more compact technology, it is widely employed for portable analyzers. In general, the use of solid state materials (e.g. solid electrolytes, semiconductors) in the gas sensing field has contributed to improvement in the gas sensitivity of the portable analyzers and to the cost reduction. Therefore, the research in gas sensing technologies is highly focused in solid state gas sensors. As follows, it is presented a summarized state of the art of solid state oxygen sensors.

I.3. Solid State Oxygen Sensors: State of the Art

This section contains a brief explanation of the main oxygen sensor technologies based on solid state materials that exist at this time: Electrochemical sensors, optical sensors and semiconductor oxide sensors. Other kind of solid state oxygen sensors were not commented because it was considered that they derive from these three types or that their use is not widely spread.

For each oxygen sensor type, it is made a short explanation of the detection mechanism, its application, and commentaries about the most recent trends in each technology, its main advantages and disadvantages.

I.3.1. Electrochemical Sensors

These sensors are electrochemical cells, which use solid state oxygen-ion-conductor materials, e.g. Zirconia, as electrolytes. An electrochemical cell is a device that converts chemical energy into electrical energy or viceversa, when a chemical reaction is occurring in the cell. Typically, it consists of two metal electrodes connected by an ionically conducting phase (Electrolyte). For oxygen sensing purposes, the most widely employed electrolytes are in solid state; however some electrochemical sensors (e.g. Panametric sensors) use aqueous solutions as electrolytes.

Depending on the working mode of the cell, electrochemical sensors can be divided in two main types: potentiometrics and amperometric.

I.3.1.1. Potentiometric

Potentiometric oxygen sensors are based on the physical behaviour of galvanic cells, in which electricity is produced as a result of the spontaneous reaction occurring inside them [26, 27]. In the sensor (Figure I.3), a reference partial pressure $P_{O_2}^{ref}$ is on one side of the electrolyte and an unknown one, P_{O_2}, to be determined is on the other side. An Electromotive Voltage (EMV) in volts, *E*, is generated between the electrodes by the tendency of oxygen ions within the electrolyte to drift from the high to low oxygen partial pressure side [28, 29].

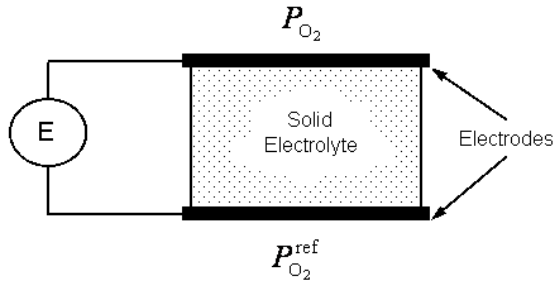

Figure I.3 *Basic structure of a potentiometric sensor*

The generated EMV between the two electrodes follows the Nerst's equation [23, 30, 31]:

$$E = \left(RT/nF\right)\ln\left(P_{O_2}/P_{O_2}^{ref}\right) \qquad \textbf{(I.1)}$$

where R is the universal gas constant, T is the operating temperature, F is the Faraday's constant, P_{O_2} is the sample gas and $P_{O_2}^{ref}$ is the reference gas. Hence, if $P_{O_2}^{ref}$ is known, then P_{O_2} may be determined from a measurement of E (at a given T).

Solid state potentiometric oxygen sensors typically use an oxygen ion conducting material as electrolyte. Many solid electrolytes with reasonable electrical conductivity have been studied and Table I.2 provides a partial list. Amongst these, yttria stabilized zirconia (YSZ) has been the material most used, due to its ionic nature and better stability in harsh environments[32-34]. The electrodes, in addition, are usually porous platinum layers, due the high catalytic properties of such material [35].

The reference partial pressure may be obtained from a gaseous source, e.g. ambient air or a gas cylinder. The most common application of potentiometric sensors with air as reference gas is the lambda sensor (Figure 1.2). The name of this sensor arises from the shape of the voltage characteristic of a Nernst cell, which looks similar to the Greek letter.

Since Bosch introduced a YSZ-based thimble type oxygen sensor in 1976, these potentiometric sensor has been widely used in the feedback control of air to fuel ratio of automobile engine exhaust gases [42]. The sensor output is fed back to the engine control so that the engine operates between the rich and lean fuel conditions, centred on the stoichiometric ratio. This unheated sensor relied on the exhaust gases to reach the operating temperature and therefore, an interval of time was required before optimum sensor functioning. During this interval, the feed back signal from the O_2 sensor is quite arbitrary.

This light-off time has been reduced from minutes to a few seconds by implementing design changes such as planar structures [43].

Table I.2 *Electrical conductivity values of solid oxide electrolytes at 600 ºC*

Oxygen ion conducting solid electrolytes*	Conductivity (S cm^{-1})	Ref.
Bi_2O_3	3 x 10^{-3}	[36]
Gd_2O_3 doped CeO_2	4 x 10^{-3}	[37]
$Bi_2Cu_{0.1}V_{0.9}O_{5.35}$	1 x 10^{-1}	[38-40]
$Ba_3In_2MO_8$	7 x 10^{-3}	[29]
YSZ (8 mol% Y_2O_3)	5 x 10^{-2}	[41]

*Other than YSZ, all the electrolytes posses certain level of electronic conductivity as well.

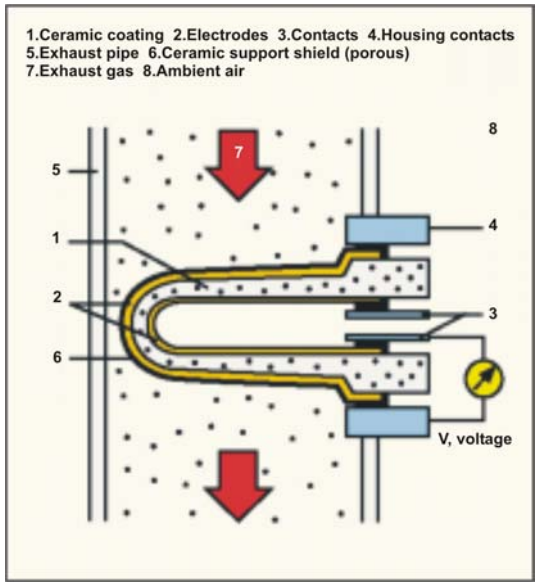

Figure I.4 *Structure of a lambda type potentiometric sensor working with air as gas reference [26]*

Planar oxygen sensor is based on the tape cast of thick film technology. Figure I.5 shows the cross sectional view of a planar O_2 sensor design. The active layer of such a

sensor, the base substrate, heater, reference air duct, electrodes, and the sensing element, are stacked together in a green state and laminated by high temperature treatments. This layer configuration enables integration of the heating element with the sensor body itself. The low thermal mass and reduced size of the sensing element (YSZ layer) and the integrated heater allows fast response and therefore, better control over the emissions during the engine start-up. An example of such sensors is the one developed and commercialized by Bosch (Figure I.6).

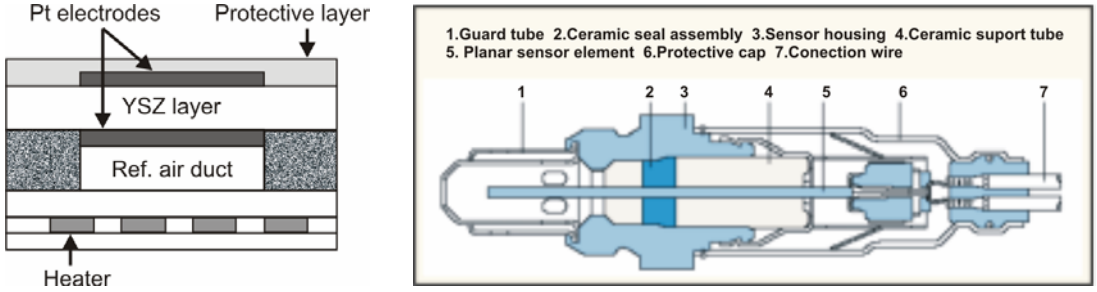

Figure I.5 *Cross sectional view of a planar potentiometric oxygen sensor [26, 42]*

Figure I.6 *Planar lambda sensor from Bosch*

A very important limitation of gas-referenced potentiometric sensors is that the range of operation must be around $P_{O_2}^{ref}$ to avoid errors induced by electronic conductivity produced due to the semipermeability of the electrolyte[44]. As the P_{O_2} value is decreased, the partial electronic conductivity increases as a result of electron generation. A similar

effect can also occur at high P_{O_2} values with the consequent generation of holes. Thus at high and low P_{O_2}, the EMF is modified by an overpotential due to the passage of current which also results in transport of oxygen from the high to the low pressure side [30]. The evolution of O_2 into the low pressure region causes substantial deviation in the P_{O_2} value measured at the electrode when P_{O_2} is small (e.g. p.p.m levels). The problems due to semipermeability are quite serious at high and low oxygen pressures and at high temperatures [45]. Then, it is necessary to introduce a modification to measure at low oxygen concentration.

The most common way to eliminate the problem of semipermeability is the use of a transition metal oxide as a reference. In this case, the metal oxide generates the reference oxygen pressure at a level predictable from thermodynamic calculation of the equilibrium constant for reactions of the type

$$\mathrm{M}_x\mathrm{O}_{2y} \rightleftharpoons x\mathrm{M} + y\mathrm{O}_2 \qquad \textbf{(I.2)}$$

where M is the metal and M_xO_{2y} is the metal oxide. For these reference systems, the oxygen pressure generated, $P_{O_2}^{ref}$, is a monotonic function of temperature and can be calculated from the van't Hoff isochore equation [46]:

$$\ln K' - \ln K = \frac{\Delta_r H}{R}\left(\frac{1}{T} - \frac{1}{T'}\right) \qquad \textbf{(I.3)}$$

where K, K' are the equilibrium constants at temperatures T and T' respectively and $\Delta_r H$ is the change in enthalpy during the reaction. A list of metal/metal oxides and the oxygen partial pressures generated by them is given in a review carried out by Maskell and Steele [47] and is shown in Figure I.7.

A typical schema of a potentiometric sensor with a transition metal oxide as source of oxygen reference is shown in Figure I.8. With this type of sensors it is possible to reach measurements of ppm levels of oxygen concentration [48-52]. Furthermore, this sensor presents advantages such as heat shock resistance, resistance to high pressures and the possibility of in situ measurements, without circulation of the analysed gas. However, the high dependence of redox reaction (I.2) on the temperature makes necessary the introduction of very accurate system for heating control [23].

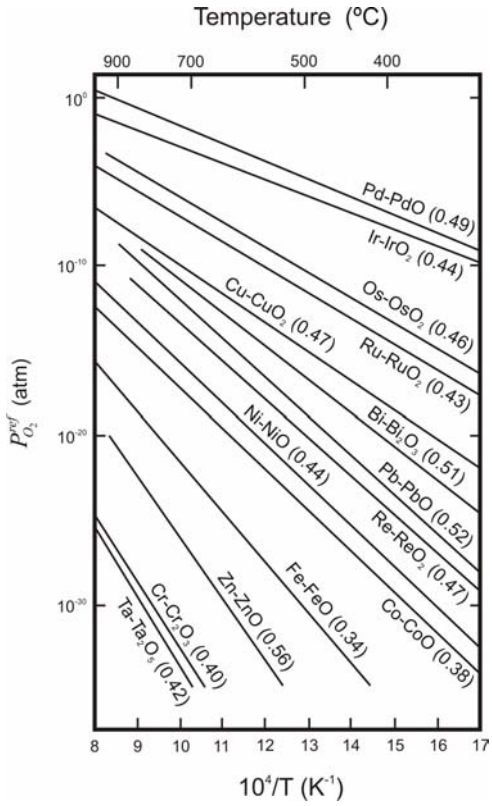

Figure I.7 *Oxygen pressure in equilibrium with a range of metal-metal oxide copules versus reciprocal temperatura. Temperature coefficients of EMF versus O_2 (1atm) are shown in parentheses (mVK^{-1}); estimated accuracy $\pm$ 0.03 [47]*

Other difficulty appears when ppm levels of O_2 have to be measured in inert gases. The exchange current density due to O_2 is low, and parasitic side reaction can become potential determining, e.g. [53]

$$H_2O + 2e \rightleftharpoons H_2 + O^{2-} \quad \textbf{(I.4)}$$

$$CO_2 + 2e \rightleftharpoons CO + O^{2-} \quad \textbf{(I.5)}$$

Small amounts of H_2O and CO_2 can produce large EMF deviations and the presence of metal-metal oxides couples on the electrodes perhaps deposited from dust, can perturb the measured EMF [30]. This problem is usually solved by the introduction of new materials as electrolytes and electrodes [54-58]. However, the implementation of non-common materials usually means high cost of fabrication. This added to the necessity of an accurate system for temperature control, highly increase the price of such devices [59].

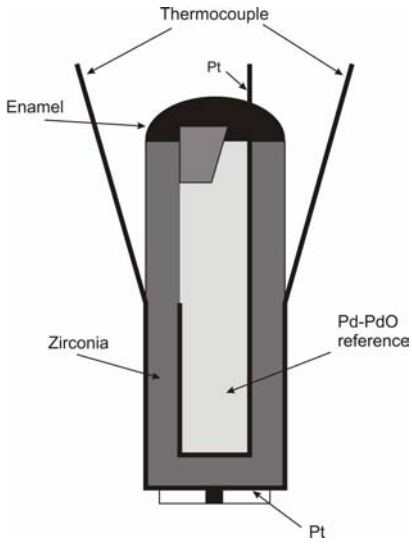

Figure I.8 *Mini-sensor with Pd-PdO reference system*

I.3.1.2. Amperometric

Amperometric oxygen sensors are based on the physical behaviour of electrolytic cells, in which a non-spontaneous reaction is driven by an external source of current [27]. In amperometric sensing mode, oxygen is pumped from one side of the electrolyte to the other by the application of an external potential to the cell. The resulting ionic current flowing through the electrolyte is a function of the oxygen concentration. The amperometric gas sensing mechanism is well known for measuring dissolved oxygen in liquids [60]. The diffusion coefficient of dissolved oxygen in aqueous solution is four or five orders of magnitude lower than the one for oxygen in gas phase (150 mm^2S^{-1} at 700 ºC). The high diffusion coefficient of gaseous oxygen results in an increase of the ionic current through the

electrolyte with the applied potential, until break down occurs and no limiting current is observed. In order to limit the current for a given concentration of oxygen, a diffusion barrier for oxygen is introduced ahead of the cathode. The diffusion barrier can either be a small aperture or a porous material on top of the cathode [35]. Figure I.9 shows a cross sectional view of an amperometric sensor based on YSZ electrolyte.

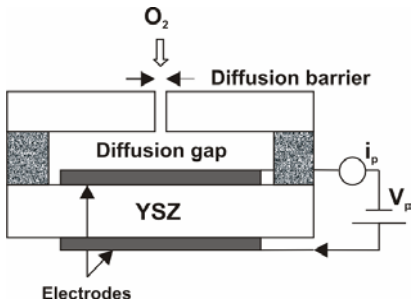

Figure I.9 *A current limiting difusión barrier amperometric oxygen sensor based on YSZ electrolyte [35]*

The gas sensing mechanism is controlled by the diffusion of oxygen and can be bulk or Knudsen diffusion process depending on the dimension of the aperture. If the diameter '*d*' of the diffusion hole is bigger than the mean free path '*l*' (i.e., the Knudsen number, Kn = l/d << 1), then the rate determining is gas-gas collisions rather than gas-wall collisions. This is the case of bulk diffusion. On the other hand, if $d<<l$, i.e., Kn >> 1, then the gas-wall collisions are dominant and the diffusion process is called Knudsen diffusion. The current-voltage characteristics and hence, the sensor properties are quite different between bulk and Knudsen diffusion, and thus, the limiting current is a function of the geometrical parameters of the diffusion barrier [61]. A detailed study by Usui et al. [62, 63] has shown that the limiting current varies with oxygen concentration (C_{O_2}) as $-\ln(1-C_{O_2})$ in bulk diffusion and linearly with C_{O_2} in Knudsen diffusion. It is also interesting to note that the apertures of diameter about 20-30 μm showed both bulk and Knudsen diffusion of oxygen for the total pressure above and below 40.5 x 10^3 Pa, respectively. For the total pressure of 130 Pa, the Knudsen diffusion dominates and the limiting current is directly proportional to the oxygen concentration. The current-voltage characteristics of a limiting current amperometric oxygen sensor in the Knudsen diffusion condition and the relationship between the limiting current and the oxygen concentration at low pressures are shown in Figure I.10a and b, respectively.

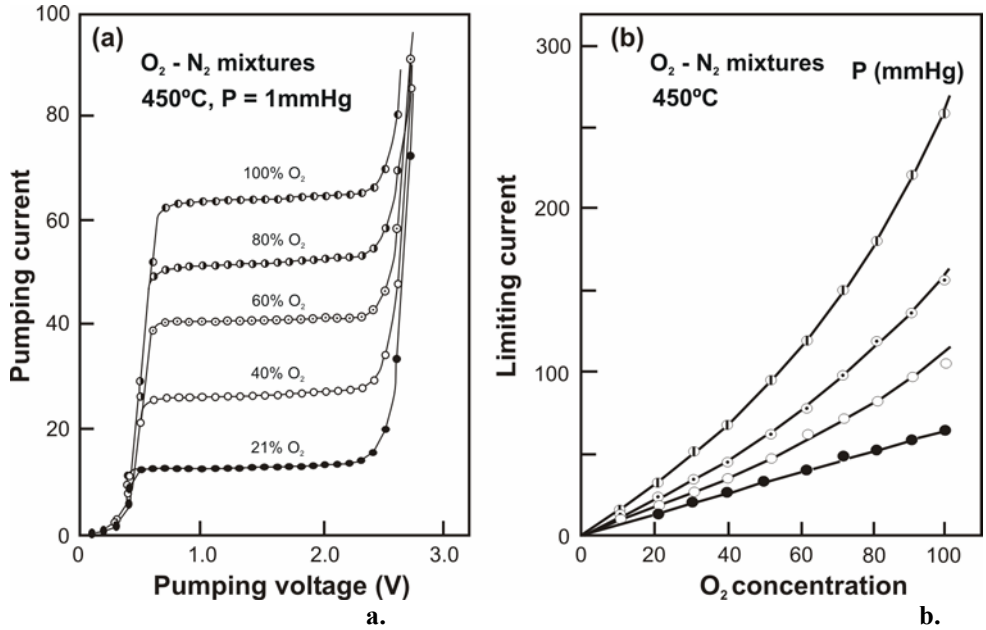

Figure I.10 *Limiting current-voltage characteristics o fan amperometric oxygen sensor for varying:* ***a.*** *pumping voltage and oxygen concentration and* ***b.*** *oxygen concentration and total pressure [63]*

For a linearly varying limiting current sensor, the diffusion aperture must obey the criterion Kn >> 1, for a given range of the total pressure. In such a case, the diffusion current of molecular oxygen (dN_{O_2}/dt) depends on the gradient of oxygen concentration (dC_{O_2}/dx), the effective diffusion cross section (Q) and the diffusion coefficient of oxygen D_{O_2} and is given by [42]

$$\frac{dN_{O_2}}{dt} = -D_{O_2} Q \frac{dC_{O_2}}{dx} \qquad \textbf{(I.6)}$$

And the pumping ionic current flowing through the electrolyte cell is given by the Faraday's law

$$i_p = 4F\frac{dN_{O_2}}{dt} \quad \textbf{(I.7)}$$

As the applied pumping voltage V_p is increased, the current also increases until the oxygen pressure near the cathode-electrolyte interface reaches a value near zero. Then, the current saturates at a value depending on the molecular current of the oxygen flow along the diffusion barrier. Now the limiting current i_p is directly proportional to the oxygen concentration in the test gas and linearly varying. As it can be seen in Figure I.10a, the lowest applied potential in the limiting current region is around 500-600 mV and that is the usual pumping voltage in most of this kind of sensors.

The amperometric oxygen sensors were devised for the operation under lean fuel ($\lambda > 1$) conditions in the combustion systems. But the disadvantage is that if the combustion region is switched from lean to rich ($\lambda \leq 1$), the anode which is exposed to fuel mixture experiences a potential change of about 500 mV. Then the applied voltage needs to be increased to more than 1 V for the limiting current to flow, and is enough to drive the reduction of CO_2 and H_2O at the cathode, causing erroneous i_p values. The limiting current increases again for a decrease of λ from the stoichiometric value of $\lambda = 1$ [28, 64] as shown in Figure I.11. So, for the observed value of the i_p, whether the combustion engine is operating under lean or rich region is unknown.

To overcome this problem, a two stage cell design has been developed: a pumping cell and a gauge cell or Nernst cell. In this sensor design, an internal diffusion gap volume is enclosed by the pumping and sensing (Nernst) YSZ elements and a porous material acts as the diffusion barrier. The sensing cell operates in the potentiometric mode and the output EMF given by equation 1.1 is used to control the pumping current by using a closed loop electronic circuit shown in Figure I.12 [42, 65]. This feedback circuit enables the Nernst cell to keep the oxygen partial pressure in the internal diffusion gap constant always around the stoichiometric mixture of the air and fuel ($\lambda = 1$). Thus, depending on the polarity of the pumping voltage, oxygen can either be pumped out or into the diffusion gap volume. In the steady stage, the oxygen flux pumped out of the diffusion gap is equal to the flux of oxygen leaking through the diffusion barrier into the gap and hence, create a constant P_{O_2} in that gap. In this condition [28, 66],

$$\frac{i_p}{4F} = \sigma_{O_2}(P_{O_2} - P_{O_{2,d}}) \quad \textbf{(I.8)}$$

where P_{O_2} and $P_{O_{2,d}}$ are the partial pressures of oxygen in the outer ambient and the internal diffusion gap, respectively. σ_{O_2} is the leak conductance of O_2 along the diffusion barrier. For a given geometrical parameters of the diffusion barrier,

$$\sigma_{O_2} = \frac{D_{O_2} A}{RTl} \qquad \textbf{(I.9)}$$

where D_{O_2} is the diffusion coefficient of oxygen, A and l are the effective of cross section and length of the diffusion barrier, respectively. By connecting the inner electrodes of the pumping and the Nernst cells in the diffusion gap volume to a short circuit, a uniform pressure of oxygen between those electrodes, $P_{O_{2,d}}$, can be expected and can be measured by the Nernst cell according to I.1

$$V_s = \frac{RT}{4F} \ln\left(\frac{P_{O_2}}{P_{O_{2,d}}}\right) \qquad \textbf{(I.10)}$$

$$i_p = 4F\sigma_{O_2} P_{O_2}\left[1 - \exp\left(-\frac{4FV_s}{RT}\right)\right] \qquad \textbf{(I.11)}$$

where V_s is the Nernst cell voltage (EMF). From this equation, it is clear that for a given temperature, if V_s is constant, the pumping currents is directly proportional to the product of σ_{O_2} and P_{O_2} for the full range of λ values from rich to lean region in the combustion system.

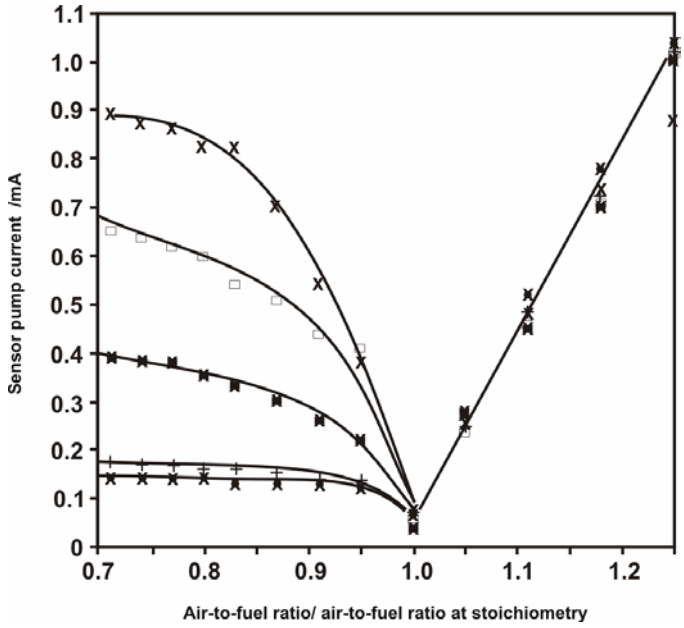

Figure I.11 *Characteristics of an amperometric sensor in the flue of a combustion system burning natural gas in air [64]*

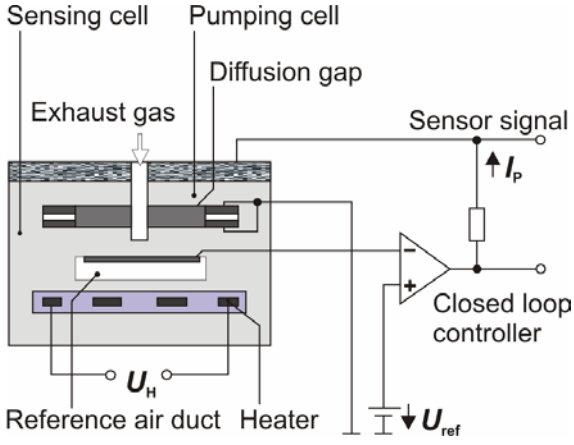

Figure I.12 *A dual cell, gauge and pumping, limiting current amperometric wide range oxygen sensor [65]*

The electronic feedback circuit, making use of an operational amplifier (op-amp) in the differential mode, control the pumping voltage polarity and hence, the direction of the current flow through the pumping cell which in turn provides a constant oxygen concentration in the internal diffusion gap and thus, a constant V_s is established throughout the sensing process. When the combustion engine runs in the lean fuel region, the oxygen rich exhaust gas diffuses into the diffusion gap and the output of the Nernst cell and drives the circuitry so that the oxygen is pumped out the diffusion gap and λ reaches the stoichiometric value (λ = 1). If the ambient is at the stoichiometric value of λ, no current flows through the pumping cell. When the ambient corresponds to the fuel rich condition, the Nernst EMF drives to the circuitry in the reverse direction causing the cell to pump oxygen into the diffusion gap adjusting the $P_{O_{2,d}}$ to a value near λ = 1. Thus there is a continuous change in the pumping current from positive to negative value as the combustion engine switches from rich to lean region as shown in Figure I.13. In consequence the dual chamber pump-gauge amperometric sensor with air reference measures directly the oxygen concentration in the exhaust gases and the control over the combustion process is made accurately for a wide range of λ values. The thick film technology with integrated heater makes these sensors very fast and provides and accurate measurement of oxygen in the lean region.

To determine the response time of these sensors, in addition to the rate of the electromechanical reactions, the diffusion properties of oxygen and the geometrical parameter of the diffusion barrier also play a role [67]. It is found to vary from fraction of a second to tens of seconds [61]. The oxygen diffusion is generally believed to be the determining rate step in these amperometric sensors. Regarding to the long-term stability, the thermal cycling of the sensors may change the microstructure and hence, the dimension of the porous diffusion barrier, causing drifts in the sensor response.

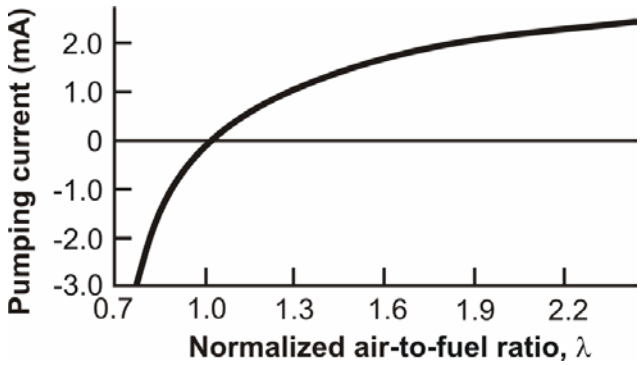

Figure I.13 *The pumping current characteristic curve of the duel cell amperometric sensor in the rich and lean fuel regions [65]*

Garzon et al. [68] have studied the suitability of mixed ionic-electronic conducting thin film membranes as dense diffusion barrier. The phenomenon of oxygen diffusion through the thin film surface to the zirconia interface is analogous to the oxygen diffusion through a porous diffusion layer or a diffusion hole. Lanthanum strontium manganate (LSM) is a well known mixed ionic-electronic conductor for oxygen membranes, and is found to exhibit better diffusion control for amperometric sensors. Peng et al. [69] have demonstrate that a composite of Pt and YSZ may also be used as a diffusion barrier for oxygen concentration below 6 % in the test gas. By employing sensors using thick or thin film technology, highly miniaturized versions of amperometric sensors with low power consumption can be realized [70].

Many of the present day fuel economy vehicles use dual cell amperometric sensors in spite of the higher complexity in packaging and design. The amperometric sensors in general are appropriate for measurements of high quantities of oxygen (>1 %) but not for measurements at ppm levels, due de proportionality of the response with the oxygen concentration. With aging, physical modification of the diffusion barrier of the sensor is possible and may cause problems. So, new materials and methods need to be devised regarding to long term durability of the diffusion barriers in the limiting current sensor [23, 35, 71].

I.3.2. Optical Sensors

Optical oxygen sensors are more attractive than conventional electrochemical devices because they have a fast response, do not consume oxygen and are immune to electromagnetic interference. This technology is based on the luminescence quenching of an indicator by oxygen. These indicators are usually luminescent and oxygen-quenchable organic dyes.

Typically, on absorption of light at their adsorption maxima, dye molecules exhibit long excited state lifetimes and emit radiation at longer wavelengths (fluorescence or phosphorescence). The excited state of the luminescence dye can be quenched by an energy transfer mechanism upon collision with oxygen molecules [72]

Fluorescence: $$L^* \rightarrow L + hv$$ **(I.12)**

Quenching: $$L^* + O_2 \rightarrow L + O_2^*$$ **(I.13)**

As a result, the intensity of luminescence is reduced along with the lifetime and the degree of quenching is proportional to the oxygen concentration.

Figure I.14 shows a schematic diagram of an optical oxygen sensor. The active components of the sensor are the luminescent dye encapsulated in a polymer medium, a light source (commonly a LED or laser) for exciting the dye at a particular wavelength (550-800 nm) [73], a photodiode to detect the fluorescent radiation and an optical fibre for the transmission of the light. The quenching of the luminescence can be characterized by the Stern-Volmer equation [74-77].

$$\frac{I_0}{I} = 1 + K_{\mathrm{SV}} \bullet P_{O_2} \qquad \textbf{(I.14)}$$

where I_0 and I are the luminescent intensities in the absence and presence of oxygen, P_{O_2} is the oxygen partial pressure in Torr and K_{SV} is the quenching constant, which determines the sensitivity of the optical oxygen sensor. K_{SV} is directly proportional to (i) the natural lifetime τ_0 (in the absence of oxygen) of the luminescent excited state, (ii) the oxygen solubility of the quenching medium given by the Henry's constant K_{H} and (iii) the quenching constant k_{Q} [74] and given by

$$K_{\mathrm{SV}} = \tau_0 K_{\mathrm{H}} k_Q \big/ 760 \qquad \textbf{(I.15)}$$

So, the sensitivity of a luminescence based oxygen sensor is influenced by the properties of both the luminescent material and the oxygen permeable encapsulating medium. The natural lifetime of the excited state τ_0, also depends on the encapsulating medium. However, the increased lifetime of the dye in a given medium may be not enough for good sensitivity if the oxygen solubility K_{H} in the medium is poor. In addition, the rate constant of the oxygen quenching, k_{Q} is dependent on the oxygen permeability, P, which is proportional to the diffusion coefficient of the oxygen D in the medium. The importance of oxygen diffusion is evident from the observations that the quenching response of fluoranthene dissolved in cyclohexane solution is slower than in polyethylene film [78]. Rapid response and high quenching efficiency have also been observed by using porous 'Vycor' glass as the matrix.

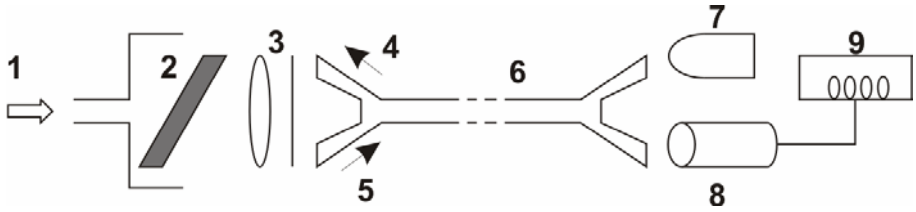

Figure I.14 *Schematics o fan optical oxygen sensor. (1) gas or liquid path, (2) lumophore dispersed on oxygen permeable membrane, (3) lens and filter, (4) exciting radiation, (5) fluorescence radiation, (6) optical fiber, (7) LED/Laser, (8) photodiode, and (9) display [35]*

Typical luminescent dyes and the polymer matrices used for optical oxygen sensor applications are shown in Table I.3. The polypyridyl compounds of Ru (II) and metalporphyrins (PtOEP & PdOEP) are the most extensively studied [79]. The luminescence character of the Ru (II) metal complexes is described by a charge transfer from ligand to metal. The long lifetimes of the excited states is a reflection of the triplet nature, due the spin-orbit coupling with the metal centre [80]. These excited states involve large changes in charge distribution and therefore, the spectral properties are strongly influenced by the surrounding medium. Figure I.15 shows the Stern-Volmer plots of oxygen sensitivity I_0/I vs. P_{O_2} for three molecules, $[Ru(bpy)_3]^{2+}$, $[Ru(phen)_3]^{2+}$ and $[Ru(Ph_2phen)_3]^{2+}$ encapsulated in a silicone rubber [74, 80]. Table I.4 shows that different lumophores embedded in different polymers exhibits varying sensing characteristics for oxygen [74, 78, 80-82]. Of the popular flourescent complexes of ruthenium, the lifetime and the sensitivity vary in order $[Ru(Ph_2phen)_3]^{2+} > [Ru(phen)_3]^{2+} > [Ru(bpy)_3]^{2+}$ as evidenced in Figure I.15, and the silicone rubber is found to be an efficient polymer medium [74, 80, 81, 83].

Table I.3 *Luminescent dyes and encapsulating polymers for optical oxygen sensors [74, 78-83]*

Lumophores	Encapsulating media
Fluoranthane, tris(2.2'-bipyridine) ruthenium II $[Ru(bpy)_3]^{2+}$, tris(1.10-phenanthroline) ruthenium II $[Ru(phen)_3]^{2+}$, tris(4.7-diphenyl-1.10-phenanthroline) ruthenium II $[Ru(Ph_2Phen)_3]^{2+}$, (1.10-phenanthroline) tris (thenoyltrifluoroacetonato) europium III $[Eu(tta)_3\ phen]^{3+}$, platinum-octaethylporphyrin (PtOEP), palladium-octaethylporphyrin (PdOEP)	Polyethylene Vycor porous glass Silicone rubber (PDMS) Silica gel Methanol Cellulose acetate butyrate (CAB) Poly(methylmethacrylate) (PMMA) Poly(vinylchloride) Polystyrene

One interesting point to note is the downward curvature in the Stern-Volmer (sensitivity) plots as seen in Figure I.15 [84]. This poses problems in calibrating these optical sensors. Though there are models based on theoretical fitting procedures e.g., power law model, two-site model, and Gaussian distribution of τ_0 and k_Q [74, 82, 83, 85], the physical understanding of the nonlinearity is still not adequate. The assumption is that the metal complex is in different environments with different quenching rate constants.

Table I.4 *Oxygen sensing characteristics of different lumophores embedded in different polymers*

Lumophore	Polymer	Natural lifetime τ_0 (μs)	Oxygen sensitivity, K_{SV}	Ref.
Fluoranthene	Vycor glass	-	0.003	[78]
$\left[Ru\left(bpy\right)_3^{2+}\left(ClO_4^-\right)_2\right]$	Silicon rubber-RTV 118	0.62	0.003	[74, 80]
$\left[Ru\left(phen\right)_3^{2+}\left(ClO_4^-\right)_2\right]$	-do-	0.92	0.009	[74, 80]
$\left[Ru\left(ph_2phen\right)_3^{2+}\left(ClO_4^-\right)_2\right]$	-do-	5.3	0.033	[74, 80]
-do-	Poly(acrylic acid)	-	0.0015	[81]
-do-	Poly(sodium 4-styrene sulfonate)	-	0.002	[81]
PtOEP	Ethyl cellulose	81	0.0196	[82]
PdOEP	-do-	1410	3.475	[82]

Another important set of dyes is the metal-porphyrin complexes, especially, platinum-octaethylporphyrin (PtOEP) and palladium- octaethylporphyrin (PdOEP)[82]. Due to the increased lifetime of the phosphorescent excited states in these complexes (100 μs – 1 ms), the sensitivity is normally larger than with the Ru (II) complexes. And also, the larger Stokes shift difference in the wavelength of the exciting and emitting radiations (>100 nm) makes the measurement easier [86]. The porphyrin based systems exhibit faster response times as compared to the Ru complexes. A typical dynamic response of a PtOEP in silica glass oxygen sensor is shown in Figure I.16. When changing form 100 % nitrogen to 100 % oxygen, the response time is 5 s and from O_2 to N_2, it is about 10 s. But, the t_{90} is still less than 5 s in both cases [87].

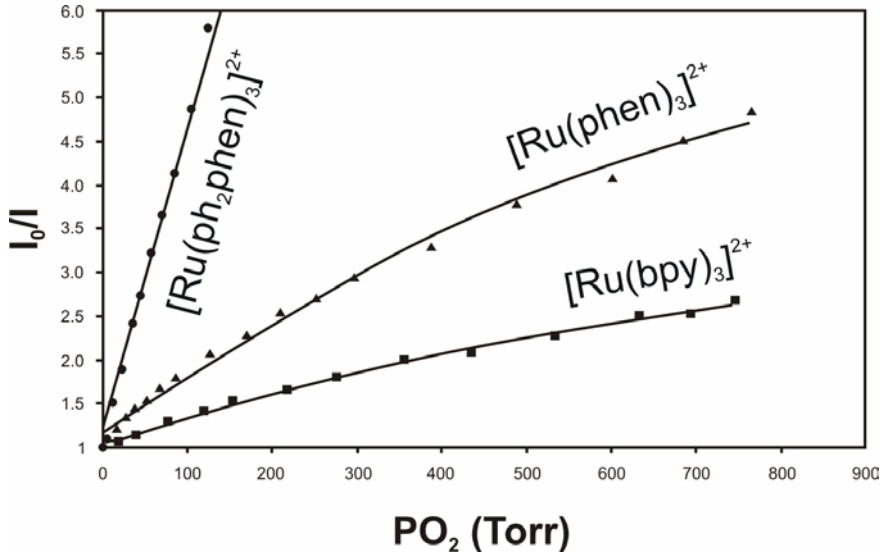

Figure I.15 *Stern-Volmer plots of I_0/I vs. P_{O_2} for three ruthenium complexes in silicone rubber [74, 80]*

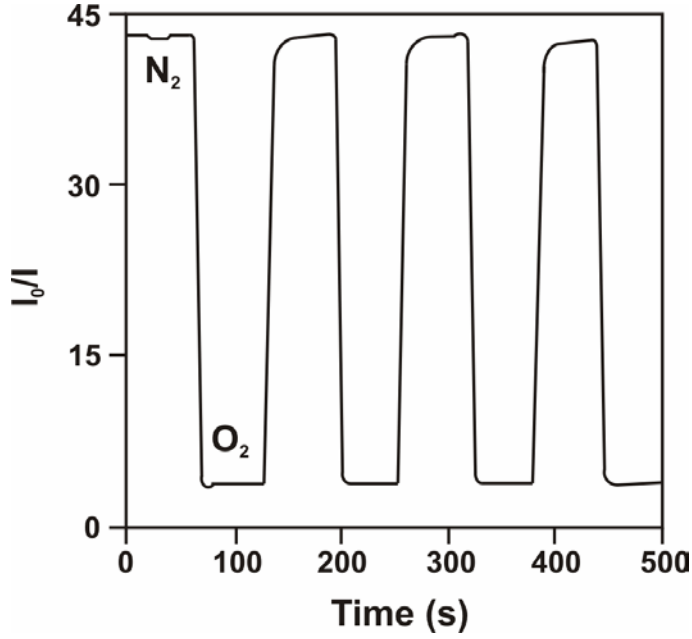

Figure I.16 *The response time and relative intensity change for PtOEP in silica glass when switching from 100 % N_2 to O_2 and back [87]*

As far the interferences effects from other gases are concerned, in both groups of sensors, when hydrophobic medium is used as a matrix, a variety of potential interferents including cyclopropane, halothane, N_2O, H_2S, CO_2 and humidity are well excluded [74, 88].

While research on optimizing the oxygen sensing characteristics of the luminescent materials is being carried out worldwide, the use of optical sensors already emerged. Optical sensors are more attractive than conventional electrochemical devices because they have a fast response, do not consume oxygen and are immune to electromagnetic interference [89]. By this moment, the construction of such sensors is still very expensive and bothersome [86, 90-92]. However, this technology is now employed for food packaging, nuclear magnetic resonance (NMR), and also many municipalities and waste water treatment plants in the USA have started using them [77, 93, 94]. Materials and performance optimization of these optical sensors are expected to increase their share of the package waste water market for dissolved oxygen sensors [35, 95-97].

I.3.3. Semiconductor Metal Oxide Sensors

Finally, the oxygen sensing based on semiconductor technology will be exposed. The oxygen sensitive mechanism of a semiconductor metal oxide (MOX) sensor is based on the resistance change of some semiconductors oxides, due to oxidation or reduction of the semiconductor oxide itself, according to the gases of the surrounding atmosphere. The gas with the major influence in these reactions is oxygen, which is the target gas in this work. For this process, high temperatures (>200 ºC) are usually needed. This technology offers advantages as small size that permits their use in portable equips and power consumption reduction, low cost consequence of the elevate semiconductor technology production, and capability for integration in complex systems, for example in sensor arrays. However, these sensors do have problems of reproducibility, stability and selectivity. New metal-oxide semiconductors and catalyst/promoter, operating temperature modulation and inclusion of filters and membranes are being investigated to improve selectivity [98-103].

A typical structure of a semiconductor gas sensor is shown in Figure I.17. The semiconductor oxide, known also as active material, is located over a substrate usually made of Si or Al_2O_3 [104]. Depending on the technology employed for the active material deposition, this layer may be a thin or a thick film. Thin film layers had shown, in general, better response at low temperatures than thick films. However, the lasts are more easy to make, dope and hence, to reproduce. This is the reason to be the most widely used for industrial applications [105, 106]. Since the response of this type of sensors is based on chemical reactions that take place in their surface, the necessary working temperature for these reactions is achieved by employing a heater. The changes in the active layer electrical conductivity are acquired with the help of a pair of electrodes [102].

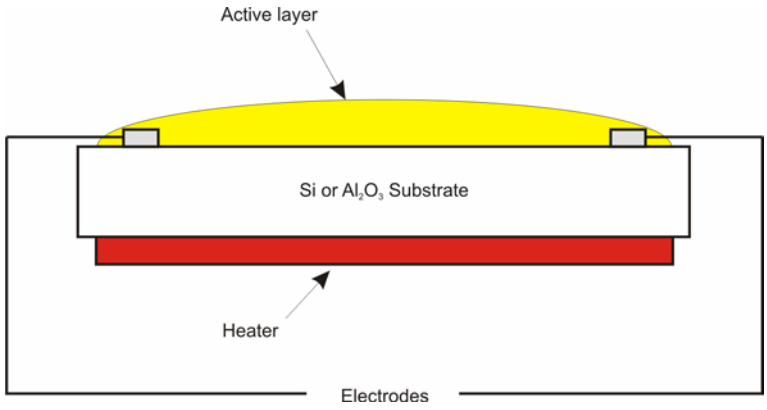

Figure I.17 *Typical structure of a semiconductor gas sensor*

The reaction between the gas and the material may be of two types. A first type of reaction takes place on the material surface and is related with the exchange of free electrons from the material with the adsorbed gas. The second type of reaction occurs inside the material bulk, and it is produce by the exchange of oxygen ions from the gas with the oxygen vacancies in the material. The surface reaction usually takes place at low temperatures (300 ºC – 500 ºC) while the bulk reaction takes place at higher temperatures (700 ºC - 900 ºC), however, sometimes, the two reactions may occur at the same time. These reactions are explained as follows.

At low and medium temperatures (about 300 ºC-500 ºC), oxygen is adsorbed on the oxide crystals surface as ions are formed by abstracting free electrons from the semiconductor solid, reducing the electrical conductivity. This reaction is described by equation I.16.

$$O_2 + 2e^- \rightarrow 2O_s^- \qquad \textbf{(I.16)}$$

Beside, this fact creates a monolayer of oxygen negative ions that produces a repulsion force over the free electrons inside the oxide crystal. Then, the electrons are confined in the centre of the crystals and a depletion layer is formed just below the crystal surface. So, a potential barrier appears between the oxide crystals, causing an additional reduction of the electrical conductivity.

In the presence of a reducing gas (R), this gas will react with the adsorbed oxygen, leaving free the previous trapped electrons and the new molecule keeps free. This reaction is described by equation I.17.

$$R + O_s^- \rightarrow RO + e^- \qquad \textbf{(I.17)}$$

As it can be seen, the free electrons in the oxide crystal increase, reducing the electrical resistance. This reaction affects also the shottky barrier. This barrier is obviously much less energetic when the reaction (I.17) occurs, due to the diminution of surface charge, as can be seen in Figure I.18 [104, 107].

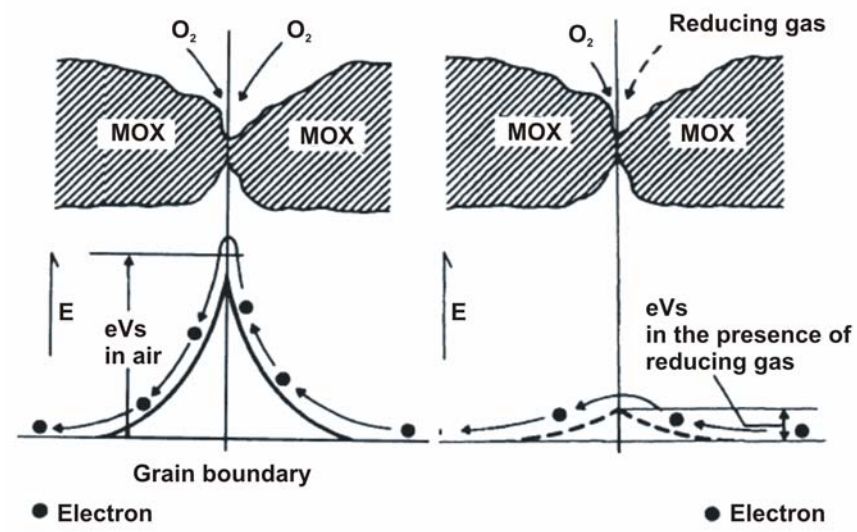

Figure I.18 *Schottky barrier between two nanocrystalls . Left, the presence of oxygen at surface increases the height of the barrier. Right, the number of such oxygen atoms diminished due to reducing gas oxidation reaction [102-104]*

In this way, after reducing gas exposure, there will be a smaller barrier on the polycrystalline surface and the electronic conduction between grains will be easier. Macroscopically, this implies an additional diminution of the electrical resistivity in the presence of a reducing gas.

In the case of oxidising gases, such as NO_2, an increase of Schottky barrier is expected due to the fixation of more molecules on the oxide surface. The ionic charge of

such molecules becomes higher than that of the oxygen and, therefore, the resistivity increases [104].

Likewise, reducing gases increase the resistance of p-type semiconductors, while oxidizing gases decrease it [107].

In general, a semiconductor oxide is a non-stoichiometric oxide, for example, an oxygen deficient oxide containing oxygen vacancies. At high temperatures (700 ºC – 1100 ºC), oxygen vacancies diffuse quickly from the interior of the grains to the surface or from the surface to the interior of the grains. The basic reaction between oxygen molecules in the gas phase, $O_2^{(g)}$, and the oxygen vacancies, $V_{\ddot{O}}$, in the bulk can be expressed as [107]:

$$O_{O^x} \leftrightarrow V_{\ddot{O}} + 2e^- + 1/2O_2^{(g)} \qquad \textbf{(I.18)}$$

On the other hand, the relationship between the oxygen partial pressure and the electrical conductivity of an oxide sensor can be represented by [108, 109]

$$\sigma = A\exp\left(-E_A/kT\right)P_{O_2}^m \qquad \textbf{(I.19)}$$

where σ is the electronic conductivity, A is a constant, E_A the activation energy for conduction and m is a parameter determined by both the type of the carrier (n or p) and the defects (e. g., oxygen vacancy) in the semiconductor. For an n-type semiconductor involving oxygen vacancies ($V_{\ddot{O}}$), the equilibrium constant for the mass action reaction (I.16) is given by

$$K = \left[V_{\ddot{O}}\right]n^2\left(P_{O_2}\right)^{\frac{1}{2}} \qquad \textbf{(I.20)}$$

where n is the concentration of electrons. For the charge balance, the concentration of oxygen vacancies is

$$[V_{\ddot{O}}] = n/2 \qquad \textbf{(I.21)}$$

then,

$$K = \frac{n^3}{2}\left(P_{O_2}\right)^{\frac{1}{2}} \qquad \textbf{(I.22)}$$

Thus, the electron concentration in the conduction band (n) can be related to the oxygen partial pressure by

$$n \,\alpha\, \left(P_{O_2}\right)^{-\frac{1}{6}} \qquad \textbf{(I.23)}$$

So, one can observe that m = -1/6. The value of $|m|$ is the sensitivity of the sensor, the higher the $|m|$ value, the higher the sensitivity and vice versa.

In recent years, a large effort has been devoted to develop oxygen sensors based on bulk conducting semiconductors. In which the reaction is due to the ionic exchange between the oxygen vacancies in the material bulk and the gas. Examples are summarized in Table I.5. Among these, TiO_2, in rutile crystalline phase, is the most widely used semiconductor for oxygen application [110-112]. It is an n-type semiconductor for a wide range of oxygen partial pressure (P_{O_2}: 1-10^{-30} atm). Since the valance band (filled O-2p states) is nonreceptive to holes and the conduction band (Ti-3d states) is receptive to electrons in undoped TiO_2, the crystal structure of TiO_2 (rutile) allows oxygen vacancies $V_{\ddot{O}}$, and titanium interstitials Ti^{4+} or Ti^{3+} to exist in the lattice [113]. So, in addition to reaction (I.18), other electron contributing reactions involving Ti^{3+} or Ti^{4+}, possible at high temperatures, are

$$TiO_2 \rightarrow Ti_{(int)}^{3+} + 3e^- + O_{2gas} \qquad \textbf{(I.24)}$$

$$TiO_2 \rightarrow Ti^{4+}_{(int)} + 4e^- + O_{2\,gas} \qquad \textbf{(I.25)}$$

also possible at high temperatures. Then the value of $|m|$ in (I.19) would be higher than 1/6, due to the mixed conduction mechanism [113, 114]. Figure I.19 shows the sensing characteristics of a TiO_2 thin film oxygen sensor [114]. It is clearly seen that the resistance of the sensor decreases with decreasing P_{O_2}, the usual characteristic of an *n*-type semiconductor.

Table I.5 *Bulk conduction materials used as oxygen sensors [109, 115-121]*

Materials	Typical values of *m*	Working temperature (ºC)
TiO_2	-4, -6	700 – 1000
$SrTiO_3$	-6, -4, +4, +3	700 – 1000
Ga_2O_3	-4, -2	900 – 1000
Nb_2O_5	-4, -8	700 – 1000
CeO_2	-6	700 – 1000
$BaFeNb_9O_{10}$	*	720
$BaTi_7Nb_4O_{25}$	*	720
$BaFe_{0.8}Hf_{0.2}O_3$	*	400 – 800

The use of TiO_2 based oxygen sensor is being extended, in particular for controlling the air-to-fuel ratio (λ sensor) in combustion systems [111]. However, the need of high working temperatures (above 700 ºC), and therefore the high power consumption difficult the adaptation of such sensors to some systems, e.g. portable electronic equipments. On the other hand, anatase state Titania has more free electrons that the rutile phase usually employed for oxygen sensors [122]. This characteristic help the surface reaction described in (I.16), which takes place at not so high temperatures (400 ºC – 500 ºC). Then, it can be derived that maintaining an anatase structure would allow the detection of oxygen at medium temperatures, which is desirable for sensor design [123, 124].

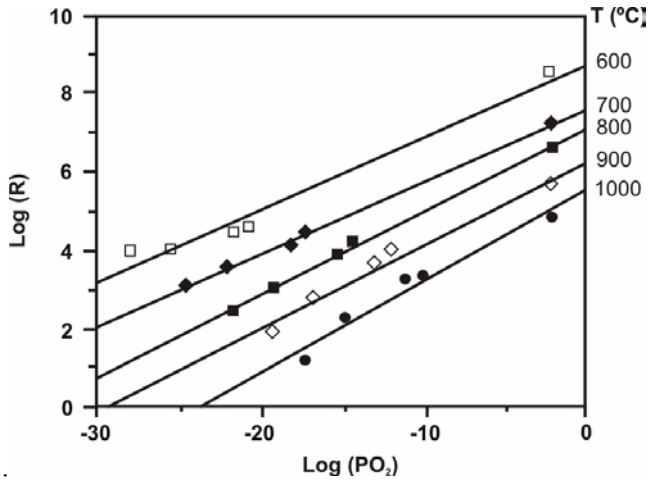

Figure I.19 *Resistance characteristics of a TiO_2 thin film oxygen sensor in different partial pressure of oxygen [114]*

When Titania is doped with pentavalent impurity ions, i.e. Nb^{5+}, such ions get into the anatase Titania crystalline structure, giving rise to a hindering in the phase transformation to rutile and an inhibition in grain growth. In undoped Titania, the change from anatase to rutile starts at about 600ºC. In doped Titania, the temperature to start this change is higher, around 750ºC. This effect is attributed to the extra valence of niobium ions, in comparison with titanium ones, which reduces oxygen vacancies in the anatase phase, retarding the transformation to rutile [125-127].

Furthermore, grain growth is inhibited due to the stress induced to the anatase structure by the Nb^{5+} substitutional ions, with slightly higher ionic radius value with respect to Ti^{4+}. Small grains mean more active area, which increases sensor sensitivity [107, 127]. It has been also reported that Nb-doped titania shows higher sensitivity towards oxygen and shorter response time than pure TiO_2 [128]. The doped material also shows lower impedance at low operating temperatures and hence, it is easier to design associated electronic circuitry [124]. J. Arbiol [125, 126] reported that there is an optimum range for the concentration of Nb dopant; this range is around unities of atomic percent of Nb^{5+} in Titania. The best doping concentration for Titania was found around 3 at% of Nb^{5+}.

I.4. Objectives

From the technologies previously described we can conclude that semiconductor oxide sensors are very promising to work in applications that involve low oxygen concentration contained in inert gases (i.e. Nitrogen) and acid gases (i.e. CO_2), due to their low cost, size and power consumption of the device. The thick film construction method of such sensors helps to simplify the fabrication process and also to crate a robust device. However, as it was commented, thick film sensors need to work at high temperatures (>700 ºC). The usual high temperatures needed for oxygen detection in this technology may be reduced by employing semiconductor oxides that works mainly with surface reaction, such as Titania in anatase crystalline phase.

Based on these arguments we intend, in this project, to develop a semiconductor oxide sensor to detect low oxygen concentrations in N_2 and CO_2. Due the easier fabrication and robustness, the construction technology that will be employed is thick film. We pretend to reduce the working temperature of the sensor, usually over 700 ºC, to temperatures between 400 ºC and 600 ºC, by employing anatase titania as active material. To reach this goal, three main sub-objectives have been outlined. First, it is necessary to found an appropriated substrate that can operate at the desired working temperatures; second, the active material must be synthesized and characterized and finally the sensor performance has to be determined. These sub-objectives are explained as follows.

I.4.1. Substrate Development

The substrate of the sensor must support temperatures up to 600 ºC, so the first step will be to find an appropriate material for the substrate. Then, the heater and electrodes must be designed and the materials for them and for the isolation layers must be defined. Finally, in this objective, the substrate must be constructed and the power consumption characterized.

I.4.2. Active Material

It has to be obtained a material which permit oxygen detection of oxygen traces at medium temperatures (below 600 ºC). That way Titanium dioxide will be synthesized to be used as active material. Besides, Niobium ions will be added to the Titania structure in order to hinder the crystalline phase transition and retain it in anatase state. Then, the two materials, pure Titania and Niobium-doped Titania will be physical characterized XRD, SEM, and BET techniques to compare and observe the effect of Niobium addition in the Titania lattice. The measured physical characteristics (crystalline phase, grain and crystallite

size, and finally, the surface and porosity) will be compared with the oxygen sensitivity properties of each material, in order to find the influence of such physical properties in the sensing capabilities of the materials. To carry out the oxygen sensing characterization, the materials must be deposited on the substrates and the resulted layers must be heat treated.

Based on the results obtained from material characterizations, it will be intended an improvement of the sensing capabilities of the materials, by optimizing their physical properties.

I.4.3. Sensor Characterization

Finally, the developed sensors must be tested for applications in oxygen detection in N_2 and CO_2, as it was commented in section 1.1. The sensing capabilities will be also characterized with different working temperatures (300 ºC, 400 ºC, 500 ºC and 600 ºC) to know the optimum one.

I.5. References

[1] J. Wei, "*Oxygen Purification with a Waferpure Gas Purification System - Aplications Notes*", Mykrolis (1995)

[2] L. Capogrosso, G. Zinno and H. Gasser-Coze, "*Optimized Steel Production with Oxygen for Blast Furnaces at ILVA, Taranto Works, Italy*", ILVA (2002)

[3] M.L. Rooney, "*Active Food Packaging*", Edited by Blackie, London, 1995

[4] A.L. Brody, B.R. Strupinsky and L.R. Kline, "*Active Packaging for Food Applications*", Edited by Technomic Publishing Co., Lancaster, USA, 2001

[5] A. Simón, E. González-Fandos and V. Tobar, "*The Sensory and Microbiological Quality of Fresh Sliced Mushroom (Agaricus bisporus L.) Packaged in Modified Atmospheres*", International Journal of Food Science and Technology, Vol. 40 (2005) 943–952

[6] A.R. Davies, Advances in Modified-Atmosphere Packaging, In: "*New Methods of Food Preservation*". New York, Blackie Academic & Professional, (1995), 304-320

[7] C. Nettles, "*Microbial Control by Packaging: A Review*", Critical Reviews in Food Science and Nutrition, Vol. 42 2 (2002) 151-161

[8] S.J. Eilert, "*New Packaging Technologies for the 21st Century: Review*", Meat Science, Vol. 71 (2005) 122–127

[9] A. Mills, "*Oxygen Indicators and Intelligent Inks for Packaging Food*", Chemical Society Reviews, Vol. 34 (2005) 1003-1011

[10] A.L. Brody, "*Micro-Oxygen Packaging Retains Quality in Beer*", Food Technology, Vol. 59 4 (2005) 69-71

[11] O. Corzo and N. Bracho, "*Prediction of the Sensory Quality of Canned Beer as Determined by Oxygen Concentration, Physical Chemistry Contents, and Storage Conditions*", Journal of Food Science, Vol. 69 7 (2004) S285-S289

[12] A.J. Irwin, R.L. Barker and P. Pipasts, "*The Role of Copper, Oxygen, and Polyphenols in Beer Flavor Instability*", Journal of the American Society of Brewing Chemists Vol. 49 (1991) 140-149

[13] A. Liquid, "*Food & Beverage: Carbonation*", Available from: http://www.airliquide.com/en/business/industry/food/applications/carbonation.asp

[14] S.M. Ringo, "*International Society of Beverage Technologists (ISBT) Carbon Dioxide Guidelines*", Master Brewers Association of the Americas - Technical Quarterly Vol. 39 1 (2002) 32-35

[15] J.R.G.d. Río, "*El CO_2 en el siglo XXI*", Cerveza y Malta, Vol. 153 (2002) 23-29

[16] J.M. Catalyst, "*Impurities in CO_2 – Sources and Specifications*", Available from: http://www.jmcatalysts.com/pct

[17] A.I. Inc., "*Application Guide*", Available from: http://www.aii2.com/applicationguide.html

[18] C. cost, "*Gas and Liquid Transmission Pipelines*", Available from: http://www.corrosioncost.com/pdf/gasliquid.pdf

[19] M. Niedre, M.S. Patterson and B.C. Wilson, "*Direct Near-Infrared Luminescence Detection of Singlet Oxygen Generated by Photodynamic Therapy in Cells In Vitro and Tissues In Vivo*", Photochemistry and Photobiology, Vol. 75 4 (2002) 382-391

[20] Hioki, "*Near-Infrared Photon Detector*", Available from: http://www.hioki.co.jp/eng/info/NIRE3-1ZM_web.pdf

[21] M.B. Frish, R.T. Wainner, B.D. Green, J. Stafford-Evans, M.C. Laderer and M.G. Allen, "*Progress in Reducing Size and Cost of Trace Gas Analyzer Based on* ", SPIE Optics East Advanced Enviromental, Chemical, and Biological Sensing Technologies II, Vol. 1199 (2004)

[22] P.J. Disimile, N. Toy and C.W. Fox, "*Low-Cost, Real-Time, Gas Detection System Using Infrared Laser Diodes*", Optical Diagnostic in Engineering, Vol. 6 1 (2003) 1-6

[23] W.C. Maskell, "*Inorganic Solid State Chemically Sensitive Devices: Electrochemical Oxygen Gas Sensors*", Journal of Physics E: Scientific Instrumentation, Vol. 20 (1987) 1156-1168

[24] EMCO, "*Gas Analysers*", Available from: http://www.emcouk.com/Gas_Analysers.shtml

[25] CambridgeSens, "*Superb Performance Oxygen Gas Analysers, Gas Monitors, Gas Detectors and Oxygen Gas Sensors for a Wide Range of Applications*", Available from: http://www.cambridge-sensotec.co.uk/

[26] Bosch, "*Oxygen Sensors*", Service Tech Magazine (2001) 13-15

[27] P.W. Atkings, "*Physical Chemistry*", Edited by Oxford University Press, Oxford, 1998

[28] M. Benammar, "*Techniques for Measurement of Oxygen and Air-to-Fuel Ratio Using Zirconia Sensors. A Review*", Measurement Science and Technology, Vol. 5 (1994) 757-767

[29] J.B. Goodenough, A. Manthiram, M. Paranthaman and Y.S. Zhen, "*Oxide ion electrolytes*", Materials Science and Engineering B, Vol. 12 (1992) 357-364

[30] J. Fouletier, "*Gas Analysis with Potentiometric Sensors. A Review*", Sensors and Actuators, Vol. 3 (1982/83) 295-314

[31] A.M. Anthony, J.F. Baumard and J. Corish, "*Results of a Collaborative Study on Zirconia-Based Oxygen Gauges*", Pure & Applied Chemistry, Vol. 56 (1984) 1070-1094

[32] T.A. Ramanarayanan, S.C. Singhal and E.D. Wachsman, "*High Temperature Ion Conducting Ceramics*", The Electrochemical Society Interface, Vol. 10 2 (2001) 22-27

[33] S.J. Skinner and J.A. Kilner, "*Oxygen Ion Conductors*", Materials Today, Vol. 6 3 (2003) 30-37

[34] R. Moos, "*A Brief Overview on Automotive Exhaust Gas Sensors Based on Electroceramics*", International Journal of Applied Ceramic Technology, Vol. 2 5 (2005) 401-413

[35] R. Ramamoorthy, P.K. Dutta and S.A. Akbar, "*Oxygen Sensors: Materials, Methods, Designs and Applications*", Journal of Materials Science, Vol. 38 (2003) 4271 – 4282

[36] N.M. Sammes, G.A. Tompsett, H. Näfe and F. Aldingera, "*Bismuth Based Oxide Electrolytes-Structure and Ionic Conductivity*", Journal of the European Ceramic Society, Vol. 19 (1999) 1801-1826

[37] M. Mogensen, N.M. Sammes and G.A. Tompsett, "*Physical, Chemical and Electrochemical Properties of Pure and Doped Ceria*", Solid State Ionics, Vol. 129 (2000) 63–94

[38] C. Xia and M. Liu, "*Novel Cathodes for Low-Temperature Solid Oxide Fuel Cells*", Advanced Materials, Vol. 14 7 (2002) 521-523

[39] F. Abraham, M.F. Debreuille-Gresse, G. Mairesse and G. Nowogrocki, "*Phase Transitions and Ionic Conductivity in $Bi_4V_2O_{11}$ an Oxide with a Layered Structure*", Solid State Ionics, Vol. 28-30 (1988) 529-535

[40] F. Abraham, J.C. Boivin, G. Mairesse and G. Nowogrocki, "*The Bimerox Series: A New Family of High Performances Oxide Ion Conductors*", Solid State Ionics, Vol. 40-41 (1990) 1934-1937

[41] N.M. Sammes and Z. Cai, "*Ionic Conductivity of Ceria/Yttria Stabilized Zirconia Electrolyte Materials*", Solid State Ionics, Vol. 100 (1997) 39-44

[42] E. Ivers-Tiffée, K.H. Härdtl, W. Menesklou and J. Riegel, "*Principles of Solid State Oxygen Sensors for Lean Combustion Gas Control*", Electrochimica Acta, Vol. 47 (2001) 807–814

[43] R. Radhakrishnan, A.V. Virkar, S.C. Singhal, G.C. Dunhamb and O.A. Marina, "*Design, Fabrication and Characterization of a Miniaturized Series-Connected Potentiometric Oxygen Sensor*", Sensors and Actuators B, Vol. 105 (2005) 312–321

[44] J. Fouletier, P. Fabry and M. Kleitz, "*Electrochemical Semipermeability and the Electrode Microsystem in Solid Oxide Electrolyte Cells*", Journal of the Electrochemical Society, Vol. 123 (1976) 204-213

[45] H. Dietz, W. Haecker and H. Jahnke, "*Advances in Electrochemistry and Electrochemical Engineering*", Edited by Wiley-Interscience, New York, 1977

[46] A.G. Mortimer and G.D. Reed, "*Development of a Robust Electrochemical Oxygen Sensor*", Sensors and Actuators B, Vol. 24-25 (1995) 328-335

[47] W.C. Maskell and B.C.H. Steele, "*Solid State Potentiometric Oxygen Gas Sensor*", Journal of Applied Electrochemistry, Vol. 16 (1986) 475-489

[48] C.S. Ltda, "*Rapidox 2100 Portable Oxygen Gas Analyser*", Available from: www.cambridge-sensotec.co.uk

[49] J. Ramírez-Salgado and P. Fabry, "*Feasibility of Potentiometric Oxygen Gas Sensor Based on Perovskite and Sodium Titanate Measuring Electrode*", Sensors and Actuators B, Vol. 82 (2002) 34–39

[50] J. Konys, H. Muscher, Z. Voß and O. Wedemeyer, "*Oxygen Measurements in Stagnant Lead–Bismuth Eutectic Using Electrochemical Sensors*", Journal of Nuclear Materials, Vol. 335 (2004) 249–253

[51] J.A. Fernández, J. Abellá, J. Barceló and L. Victori, "*Development of an Oxygen Sensor for Molten 44.5 % Lead–55.5 % Bismuth Alloy*", Journal of Nuclear Materials, Vol. 301 (2002) 47–52

[52] J.L. Courouau, "*Electrochemical Oxygen Sensors for On-Line Monitoring in Lead–Bismuth Alloys: Status of Development*", Journal of Nuclear Materials, Vol. 335 (2004) 254–259

[53] C.M. Mari, S. Pizzini, T.A. Giorgi, L. Rosai and M. Borghi, "*On the Accurate Calibration of an Electrochemical Oxygen Meter in the 10-7 Bar Range* ", Journal of Applied Electrochemistry, Vol. 7 3 (1977) 215-223

[54] S.J. Gentry and T.A. Jones, "*The Role of Cathalysis in Solid-State Gas Sensors*", Sensors and Actuators, Vol. 10 (1986) 141-163

[55] B.B. Owens, "*Solid State Electrolytes: Overview of Materials and Applications During the Last Third of the Twentieth Century*", Journal of Power Sources, Vol. 90 (2000) 2-8

[56] F.H. Garzon, R. Mukundan, R. Lujan and E.L. Brosha, "*Solid State Devices for Combustion Gas Sensing*", Solid State Ionics, Vol. 175 (2004) 487-490

[57] W. Göpel, G. Reinhardt and M. Rösch, "*Trends in the Development of Solid State Amperometric and Potentiometric High Temperature Sensors*", Solid State Ionics, Vol. 136–137 (2000) 519–531

[58] S. Colominas, J. Abellà and L. Victori, "*Characterisation of an Oxygen Sensor Based on In/In_2O_3 Reference Electrode*", Journal of Nuclear Materials, Vol. 335 (2004) 260–263

[59] Atlantis-Corp., "*ZIROX - Oxygen Measuring Modules for OEM (User Aspects in Comparison)*", Available from: http://www.atlantis.com.ua/pdf/sensors/zirox_module.PDF

[60] M.L. Hitchman, "*Measurement of Dissolved Oxygen*", Edited by John Wiley & Sons, New York, 1978

[61] G. Reinhardt, R. Mayer and M. Rösch, "*Sensing Small Molecules with Amperometric Sensors*", Solid State Ionics, Vol. 150 (2002) 79– 92

[62] T. Usui, A. Asada, M. Nakazawa and H. Osanai, "*Gas-Polarographic Sensor Using a Zirconia Electrolyte*", Journal of the Electrochemical Society, Vol. 136 (1989) 534-542

[63] T. Usui, A. Asada, M. Nakazawa and H. Osanai, "*Output Characteristics of a Gas-Polarographic Oxygen Sensor Using a Zirconia Electrolyte in the Knudsen Diffusion Region* ", Japanese Journal of Applied Physics, Vol. 26 (1987) L2061-2066

[64] W.C. Maskell, "*Progress in the Development of Zirconia Gas Sensors*", Solid State Ionics Vol. 134 (2000) 43–50

[65] J. Riegel, H. Neumann and H.-M. Wiedenmann, "*Exhaust Gas Sensors for Automotive Emission Control*", Solid State Ionics, Vol. 152– 153 (2002) 783– 800

[66] R.E. Hetrick, W.A. Fate and W.C. Vessell, "*Oxygen Sensing by Electrochemical Pumping*", Applied Physics Letters, Vol. 38 5 (1981) 390-392

[67] P.R. Warburton, M.P. Pagano, R. Hoover, M. Logman, K. Crytzer and Y.J. Warburton, "*Amperometric Gas Sensor Response Times*", Analytical Chemistry, Vol. 70 (1998) 998-1006

[68] F. Garzon, I. Raistrick, E. Brosha, R. Houlton and B.W. Chung, "*Dense Diffusion Barrier Limiting Current Oxygen Sensors*", Sensors and Actuators B, Vol. 50 (1998) 125–130

[69] Z. Penga, M. Liua and E. Balkob, "*A New Type of Amperometric Oxygen Sensor Based on a Mixed-Conducting Composite Membrane*", Sensors and Actuators B, Vol. 72 (2001) 35-40

[70] S. Yu, Q. Wu, M. Tabib-Azar and C.-C. Liu, "*Development of a Silicon-Based Yttria-Stabilized-Zirconia (YSZ), Amperometric Oxygen Sensor*", Sensors and Actuators B, Vol. 85 (2002) 212-218

[71] T. Takeuchi, "*Oxygen Sensors*", Sensors and Actuators, Vol. 14 (1988) 109-124

[72] B.R. Eggins, "*Chemical Sensors and Biosensors*", Edited by John Wiley & Sons, England, 2002

[73] D. García-Fresnadillo, M.D. Marazuela, M.C. Moreno-Bondi and G. Orellana, "*Luminescent Nafion Membranes Dyed with Ruthenium(II) Complexes as Sensing Materials for Dissolved Oxygen*", Langmuir, Vol. 15 (1999) 6451-6459

[74] A. Mills, "*Controlling the Sensitivity of Optical Oxygen Sensors*", Sensors and Actuators B, Vol. 51 (1998) 60–68

[75] W. Trettnak, C. Kolle, F. Reininger, C. Dolezal, P. O'Leary and R.A. Binot, "*Optocal Oxygen Sensor Instrumentation Based on the Detection of Luminescence Lifetime*", Advancs in Space Research, Vol. 22 10 (1998) 1465-1474

[76] J.M. Charlesworth, "*Optical Sensing of Oxygen Using Phosporescence Quenching*", Sensors and Actuators B, Vol. 22 (1994) 1-5

[77] R. Narayanaswamy and O.S. Wofbeis, "*Optical Sensors: Industrial, Enviromental and Diagnostic Applications*", Edited by O. S. Wolfbeis, Berlin, 2004

[78] I. Bergman, "*Rapid-Response Atmospheric Oxygen Monitor based on Fluorescence Quenching*", Nature, Vol. 218 (1968) 396

[79] X. Lu and M.A. Winnik, "*Luminescence Quenching in Polymer/Filler Nanocomposite Films Used in Oxygen Sensors*", Chemistry of Materials, Vol. 13 (2001) 3449-3463

[80] E.R. Carraway, J.N. Demas, B.A. DeGraff and J.R. Bacon, "*Photophysics and Photochemistry of Oxygen Sensors Based on Luminescent Transition-Metal Complexes*", Analytical Chemistry, Vol. 63 (1991) 337-342

[81] Y. Amao and I. Okurab, "*Optical Oxygen Sensing Materials: Chemisorption Film of Ruthenium(II) Polypyridyl Complexes Attached to Anionic Polymer*", Sensors and Actuators B, Vol. 88 (2003) 162–167

[82] P. Douglas and K. Eaton, "*Response Characteristics of Thin Film Oxygen Sensors, Pt and Pd Octaethylporphyrins in Polymer films*", Sensors and Actuators B, Vol. 82 (2002) 200-208

[83] J.R. Bacon and J.N. Demas, "*Determination of Oxygen Concentrations by Luminescence Quenching of a Polymer- Immobilized Transition-Metal Complex*", Analytical Chemistry, Vol. 59 (1987) 2780-2785

[84] H. Chuang and M.A. Arnold, "*Linear Calibration Function for Optical Oxygen Sensors Based on Quenching of Ruthenium Fluorescence*", Analytica Chimica Acta, Vol. 368 (1998) 83-89

[85] A. Mills, "*Response Characteristics of Optical Sensors for Oxygen: Models Based on a Distribution in t_0 or k_Q*", The Analyst, Vol. 124 (1999) 1301-1307

[86] D.B. Papkovsky, "*New Oxygen Sensors and their Applications to Biosesnsing*", Sensors and Actuators B, Vol. 29 (1995) 213-218

[87] S.-K. Lee and I. Okura, "*Optical Sensor for Oxygen Using a Porphyrin-doped Sol–Gel Glass*", The Analyst, Vol. 122 (1997) 81-84

[88] K. Eaton and P. Douglas, "*Effect of Humidity on the Response Characteristics of Luminescent PtOEP Thin Film Optical Oxygen Sensors*", Sensors and Actuators B, Vol. 82 (2002) 94-104

[89] M. Campbell, "*Sensor Systems for Enviromental Monitoring*", Edited by Chapman & Hall, Glasgow, 1997

[90] W. Trettnak, W. Gruber, F. Reininger and I. Klimant, "*Recent Progress in Optical Oxygen Sensor Instrumentation*", Sensors and Actuators B, Vol. 29 (1995) 219-225

[91] K. Tsukada, S. Sakai, K. Hase and H. Minamitani, "*Development of Catheter-Type Optical Oxygen Sensor and Applications to Bioinstrumentation*", Biosensors and Bioelectronics, Vol. 18 (2003) 1439-1445

[92] C.-H. Jeong, J.-S. Kim, W.-H. Kim, J.-H. Moon, B.-T. Lee and J.H. Kim, "*Application of the Channel Optical Waveguide Prepared by Ion Exchange Method to the Preparation and Characterization of an Optical Oxygen Gas Sensor*", Sensors and Actuators B, Vol. 105 (2005) 214–218

[93] T.C. O'Riordan, H. Voraberger, J.P. Kerry and D.B. Papkovskya, "*Study of Migration of Active Components of Phosphorescent Oxygen Sensors for Food Packaging Applications*", Analytica Chimica Acta, Vol. 530 (2005) 135–141

[94] F.C. O'Mahony, T.C. O'Riordan, N. Papkovskaia, J.P. Kerry and D.B. Papkovsky, "*Non-Destructive Assessment of Oxygen Levels in Industrial Modified Atmosphere Packaged Cheddar Cheese*", Food Control, Vol. 17 (2006) 286–292

[95] P.A.S. Jorge, P. Caldas, C.C. Rosa, A.G. Oliva and J.L. Santos, "*Optical Fiber Probes for Fluorescence Based Oxygen Sensing*", Sensors and Actuators B, Vol. 103 (2004) 290–299

[96] B.J. Basu, A. Thirumurugan, A.R. Dinesh, C. Anandan and K.S. Rajam, "*Optical Oxygen Sensor Coating Based on the Fluorescence Quenching of a New Pyrene Derivative*", Sensors and Actuators B, Vol. 104 (2005) 15–22

[97] Y. Fujiwara and Y. Amao, "*An Oxygen Sensor Based on the Fluorescence Quenching of Pyrene Chemisorbed Layer onto Alumina Plates*", Sensors and Actuators B, Vol. 89 (2003) 187-191

[98] G. Kiss, Z. Pintér, I.V. Perczel, Z. Sassi and F. Réti, "*Study of Oxide Semiconductor Sensor Materials by Selected Methods*", Thin Solid Films, Vol. 391 (2001) 216-223

[99] O.K. Tan, W. Cao, Y. Hu and W. Zhu, "*Nano-Structured Oxide Semiconductor Materials for Gas-Sensing Applications*", Ceramisc International, Vol. 30 (2004) 1127-1133

[100] M. Abaab, A.S. Bouazzi and B. Rezig, "*Competitive $CuAlS_2$ Oxygen Gas Sensor*", Microelectronic Engineering, Vol. 51-52 (2000) 343-348

[101] Y. Hu, O.K. Tan, W. Cao and W. Zhu, "*A Low Temperature Nano-Structured $SrTiO_3$ Thick Film Oxygen Sensor*", Ceramics International, Vol. 30 (2004) 1819-1822

[102] S.M. Sze, "*Semicondutor Sensors*", Wiley J, Edited by Simon M. Sze, New York, 1994

[103] M. Stankova, "*Gas Sensing Properties of RF Sputtered WO_3 Thin Films*", Doctoral thesis, Universitat Politècnica de Catalunya, Departament d'Electrónica, 2004

[104] A. Cirera, "*New Technologies and their Characterization for Nanostructured SnO_2 Gas Sensor Devices*", Doctoral thesis, Universitat de Barcelona, Departament d'Electrònica, 2000

[105] J. Atkinson, A. Cranny and C. Simonis, "*A Low-Cost Oxygen Sensor Fabricated as a Screen-Printed Semiconductor Device Suitable for Unheated Operation at Ambient Temperatures*", Sensors and Actuators B, Vol. 47 (1998) 171-180

[106] G.Martinelli and M.C. Carotta, "*Thick-Film Gas Sensors*", Sensors and Actuators B, Vol. 23 (1995) 157-161

[107] Y. Xu, X. Zhou and O.T. Sorensen, "*Oxygen Sensors Based on Semiconducting Metal Oxides: an Overview*", Sensors and Actuators B: Chemical, Vol. 65 (2000) 2-4

[108] P.T. Moseley and J. Crocker, "*Sensor Materials*", Edited by IOP Publishing, Bristol, 1996

[109] P.T. Moseley, "*Materials Selection for Semiconductor Gas Sensors*", Sensors and Actuators B, Vol. 6 (1992) 149-156

[110] J. Sheng, N. Yoshida, J. Karasawa and T. Fukami, "*Platinum Doped Titania Films Oxygen Sensor Integrated with Temperature Compensating Thermistor*", Sensors and Actuators B, Vol. 41 (1997) 131-136

[111] A. Takami, "*Development of Titania Heated Exhaust Gas Oxygen Sensor*", Ceramic Bulletin, Vol. 67 12 (1988) 1956-1960

[112] A.M. Azad, S.A. Akbar, S.G. Mhaisalkar, L.D. Birkefeld and K.S. Goto, "*Solid-State Gas Sensors: A Review*", Journal of the Electrochemical Society, Vol. 139 12 (1992) 3690-3695

[113] D.M. Smyth, "*The Defect Chemistry of Metal Oxides*", Edited by Oxford University Press, New York, 2000

[114] M. Li and Y. Chen, "*An Investigation of Response Time of TiO_2 Thin-Film Oxygen Sensors*", Sensors and Actuators B, Vol. 32 (1996) 83-85

[115] M. Ogita, K. Higo, Y. Nakanishi and Y. Hatanaka, "*Ga_2O_3 Thin Film for Oxygen Sensor at High Temperatuure*", Applied Surface Science, Vol. 175-176 (2001) 721-725

[116] A. Kohli, C.C. Wang and S.A. Akbar, "*Niobium Pentoxide as a Lean-Range Oxygen Sensor*", Sensors and Actuators B, Vol. 56 (1999) 121-128

[117] C. Beban, Y. Toyoda and M. Ogita, "*Oxygen Sensing at High Temperatures using Ga_2O_3*", Thin Solid Films, Vol. 484 (2005) 369-373

[118] P. Jasinski, T. Susuki and H.U. Anderson, "*Nanocrystalline Undoped Ceria Oxygen Sensor*", Sensors and Actuators B, Vol. 95 (2003) 73-77

[119] G. Sberveglieri, "*Recent Developments in Semiconducting Thin-Film Gas Sensors*", Sensors and Actuators B, Vol. 23 (1995) 103-109

[120] H. Meixner and U. Lampe, "*Metal Oxide Sensors*", Sensors and Actuators B, Vol. 33 (1996) 198-202

[121] X. Zhou, O.T. Sorensen and Y. Xu, "*Defect Structure and Oxygen Sensing Properties of Mg-Doped $SrTiO_3$ Thick Film Sensors*", Sensors and Actuators B, Vol. 41 (1997) 177-182

[122] H. Tang, K. Prasad, R. Sanjinés and F. Lévy, "*TiO_2 Anatase Thin Films as Gas Sensors*", Sensors and Actuators B: Chemical, Vol. 26 1-3 (1995) 71-75

[123] F. Hossein-Babaei, M. Keshmiri, M. Kakavand and T. Troczynski, "*A Resistive Gas Sensor Based on Undoped p-Type Anatase*", Sensors and Actuators B, Vol. 110 (2005) 28-35

[124] R.K. Sharma, M.C. Bhatnagar and G.L. Sharma, "*Mechanism in Nb Doped TiO_2 Oxygen Gas Sensor*", Sensors and Actuators B: Chemical, Vol. 46 (1998) 194-201

[125] J. Arbiol, "*Metal Additive Distribution in TiO_2 and SnO_2 Semiconductor Gas Sensor Nanostructured Materials*", Doctoral thesis, Universitat de Barcelona, Departament d'Electrónica, 2001

[126] J. Arbiol, J. Cerdà, G. Dezanneau, A. Cirera, F. Peiró, A. Cornet and J.R. Morante, "*Effects of Nb doping on the TiO2 anatase-to-rutile phase transition*", Journal of Applied Physics, Vol. 92 2 (2002) 853-861

[127] A. Ruiz, G. Dezanneau, J. Arbiol, A. Cornet and J.R. Morante, "*Study of the Influence of Nb Content and Sintering Temperature on TiO_2 Sensing Films*", Thin Solid Films Vol. 436 (2003) 90-94

[128] R.K. Sharma, "*Development and Characterization Solid State Materials for Oxygen Gas Sensors*", Doctoral thesis, Indian Institute of Technology, Department of Physics, 1996

II. FABRICATION PROCESSES

II.1. Introduction

In this chapter deals to the technological processes employed for the development of the gas sensor. First, the substrates used and their characterizations are described. Then, the synthesis process of the active material is detailed and finally, the technique followed for active layer deposition is presented.

II.2. Substrate

Most of the oxygen gas sensor, which had been used for industrial application are in the form of thick films [1-5], because it is easier to fabricate and to dope than thin film sensors [6]. Based on this fact, our work was focused on thick film technology. The films will be deposited on planar substrates, which contain measurement electrodes and a heating resistance. Since oxide sensors only work at high temperatures, a heating element must be built into the sensor. This heating resistance can be placed on the substrate opposite the active layer (Figure II.1a) or on the same side (Figure II.1b). In the first case, the temperature gradient on the substrate leads to greater power consumption, while the fabrication process of the second structure is more complicated.

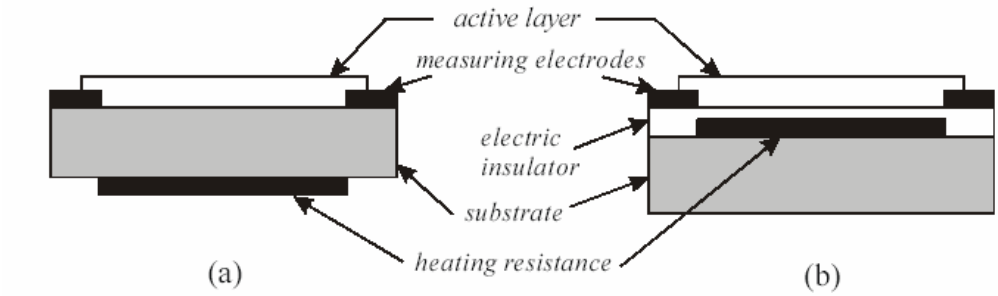

Figure II.1 *Cross section of two geometries for plane sensors [7]*

In the second case, the sensor can be considerably smaller and this makes possible to work with lower power consumption and allow sensor to be integrated in complex systems. These are the reasons for choosing this geometry in our investigation.

This heating element is often made of platinum (thin or thick layer) or other materials such as NiCr, polysilicon or Au. It is optimized to obtain a temperature distribution as homogeneous as possible. It is also important to obtain a stable and reproducibly temperature dependence on the electrical resistance, in order to set the sensor working temperature as precise and reproducibly as possible. The heater must ensure that the semiconductor oxide is uniformly heated with the minor energy loss. In some cases, the heater can also be used as a temperature sensor in order to establish a control loop.

In addition to the substrate, gas sensors require metal electrodes for electrical contacts. Due to the high temperatures during backing and tempering, low resistivity

materials as platinum or gold are most commonly used for electrodes. The selection of these materials is conditioned also by the fact that they do not react with the substance to be detected and do not oxidise [7]. Both materials are applied in thick or thin-layer technology. For the electrode shape, a simple interdigitated structure is usually used. Since many metal oxides have a low specific conductivity, the relationship of length to width should be adjusted so that the conditioning circuitry can easily measure the resistance of the sensor layer. As well as the interdigited structures mentioned, a variety of different electrical contact geometries have been investigated in the past.

Concerning substrate selection, it should be taken into account that high temperature is required (600 ºC – 700 ºC) and low power consumption is desired. Besides, substrate should be electrical insulator, good thermal conductor and noncatalytically active in front of neither gases nor sensing material. Silica microhotplates may be a solution for this application; however the maximum operating temperatures they can reach are around 400 ºC [8-10]. Other possible solution is ceramic substrates. The power consumption of such substrates is higher than Silica microhotplates; however, they can reach higher operating temperatures (~ 700 ºC). Although different kinds of ceramic can be used (steatite, cordierite, zirconia) the alumina is appreciated due to its stability. Moreover, the strength of the bound between aluminium and oxygen makes Al_2O_3 one of the most stable and inert materials for harsh environment applications. Besides, the commercial availability of alumina that can be supplied in different forms and shapes is appreciated [7, 11].

Two types of alumina based substrates are presented in this work. First Type I substrate was designed in University Rovira I Virgili (Tarragona-Spain) and fabricated in the Technical University of Brno (Brno-Czech Republic). Although Type I substrate have proved to work properly up to 500º C, when going up in temperature, soldered joints to the package showed serious problems. Since temperatures higher than 500º C where required, another substrate has been used to test the active layers to be developed. It was acquired from the Kurchatov Institute (Moscow-Russia). This second type of substrate can work up to 700 ºC, which is necessary for our application. The two types of substrates used in this thesis are described as follows.

II.2.1. Type I Substrate

The structure of this substrate corresponds to the schematic shown in Figure II.2 gold electrodes on the top, an insulating layer between electrodes and heater, causing the heater to be buried. This substrate permits the use of four different active layers in the same sensor working as sensor array. The sensor was fabricated using thick-film technology. The fabrication involved a number of steps including the sensor topology (heater, electrodes), paste selection, screen-printing, drying at low temperatures (125 ºC-150 °C), firing at high temperature (800 ºC-1000 °C), and packaging. The structure of this sensor is described in

Figure II.3. The paste selection and the procedure of sensor fabrication by screen-printing is described below [12, 13].

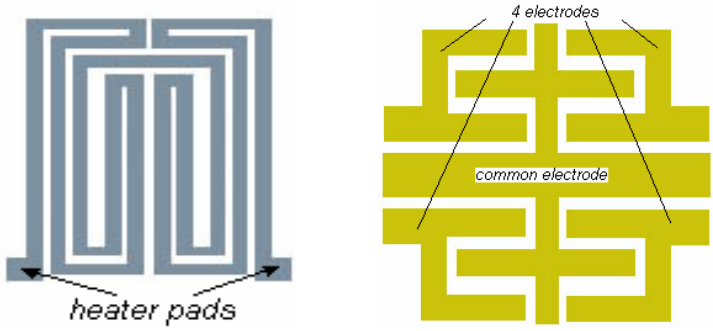

Figure II.2 *Screen printing of multi-layers*

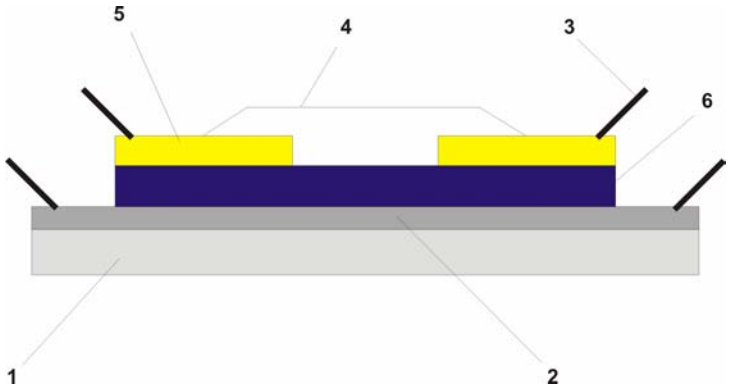

Figure II.3 *Structure of a type I sensor.* ***1.*** *Alumina substratum,* ***2.*** *heater,* ***3.*** *connecting wires,* ***4.*** *sensing layer,* ***5.*** *contact pads,* ***6.*** *isolation layer*

Screens and pastes with different properties were used at the various stages of the production. In the first stage, the heater was deposited onto a 250 µm thick alumina substrate. Pt-commercial conductor paste ESL 5545 was used. ESL 5545 was chosen because this paste is used on 96 % alumina substrates as resistance-thermometer and heater applications. The stainless steel screen (MESH 400/25 µm) was designed for this paste. For the electrodes, a newly developed gold ESL 8881-BA paste was used. The paste exhibits

high coverage and excellent wire bondability by Al and Au. A stainless steel screen (MESH 325/25 μm) was designed for the gold paste. Three insulating layers were applied between the heater and the electrodes to assure sufficient electric insulation between them. Two types of dielectric pastes were chosen. The first one, ESL 4913-G is a cadmium-free, lead-free, and nickel-free non-porous multilayer dielectric. This paste is particularly suitable for use on alumina substrates, however, in this case was not compatible with the selected gold paste for the electrodes. Only two layers with ESL 4913-G paste were printed. The second paste, ESL 4905-CH, which is compatible with gold paste, has an excellent TCE match to 96 % alumina, and was used for the third upper-insulating layer [14]. A stainless screen (MESH 325/30 μm) was used for all dielectric pastes. The angle of the fibbers was 45° for all screens.

The screen-printing process was carried out by a semiautomatic printing machine. The screen printing machine parameters were determined by the following method. The screen frame was mounted on the printing machine chase. The substrate was put in the substrate holder that fixes it by means of vacuum. This substrate holder is in horizontal position, just below the screen frame. A distance between the net and the substrate (snap-off) was set approximately within the range of 0.5-1.0 mm.

In order to achieve an appropriate value for the squeegee pressure, the squeegee rubber which is mounted upon the screen, was depressed to touch the screen causing the screen to touch the substrate. The right pressure value (between 30-60 psi) was taken when the optimal pressure of the squeegee rubber to the net was achieved. Then, the squeegee was lifted away from the screen, back to its starting position. The snap-off and the pressure were set for each type of the sensor's layer individually.

Once adjusted the screen printing machine parameters, the fabrication process started. The printing procedure was carried out at room temperature (20 ºC-23 ºC). Before printing, the screen and the support board were cleaned to eliminate any dust. The viscosity of the pastes was controlled and if necessary, modified by the addition of therpineol. Then, the substrate was put in the holder and printed. A key factor in this process was the substrate-mesh alignment. This was done adjusting the substrate holder by means of micro scroll bars to set the substrate marks under the mesh motive. It was necessary to repeat this exact process before each layer was printed. In order to ensure a repeatable printing process, a single printing direction was used throughout the printing of all the layers despite the possibility of printing with this machine in the both forward and return directions. The printing speed was constant throughout the fabrication of each of the layers because the printer has a default constant speed.

All the layers after printing were left at room temperature for levelling. This was done in order to eliminate any defects in the structure. Then, they were dried at 125 °C for 10-15 min and fired in a belt furnace with the four heating zones for 1 h before the printing of the next layer. The peak temperature of the firing process was set for all the layers to 850 ºC for 10 min. At this temperature, nano-particles of the powder were annealed in order to adhere together and to the substrate. A detailed view of the substrates is in Figure II.4.

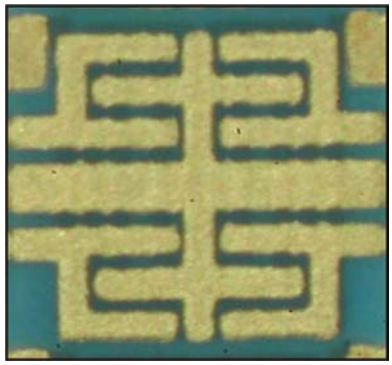

Figure II.4 *Auxiliary view on a comb structure of electrodes and pads for heater*

II.2.1.1. Characterization of Isolating Layers

As explained before, three insulating layers were applied between the heater and the electrodes to assure sufficient electric insulation of the heater. The examination of insulating resistance was done using multimeter Keithley 619, which is able to measure very high resistance (over 1 GΩ). The resistance was measured between the heater pads and the electrodes. One cable of the multimeter was connected with the heater pad and using the second cable I subsequently touched the electrodes surface in ten different places. The obtained resistance values in all cases were higher than 1 GΩ, which is much higher than the typical values of electrical resistances of metal oxide semiconductor layers.

II.2.1.2. Heater Characterization

The heater meander was designed to assure homogenous distribution of the sensor temperature, because these sensors have to work at higher temperatures than 300ºC. The position of the heater on the same side of the alumina substrate, with electrodes and active layers, allows simpler connection to TO-8 support.

In order to investigate the heaters characteristics, eight sensor chips were examined for their V/A characterization. The V/A characterization was carried out in the range of 3-10 V with a measuring step of 1 V. At voltages below 3 V, the temperature exhibits a non-linear behaviour. The corresponding current to the applied voltage was measured by means of the multimeter (HP 34401A). Then, the temperature influence on the increasing voltage was investigated using an infra-red thermometer (Quicktemp 850-1). For a correct measuring of the infra-red thermometer it was necessary to set, accurately, an emissivity of the material to be measured. In this case, the measured material was alumina, because a beam from the infra-red thermometer was pointed on the unprinted side of the alumina substrate. A

corresponding value of the emissivity was set to ε = 0.90. IR thermometer was used just up to 400 ºC, because it's the maximum value of its measuring range.

Figure II.5 shows the power consumed for the sensors at each working temperature. A linear regression was applied to these values. The resulted linear equation is expressed as follows:

$$P = 0.00648 \times T - 0.19926 \quad \textbf{(II.1)}$$

where P is the power consumption of the sensor and T is the working temperature. The maximum relative error of the power consumption is 6.6% if the temperature is set according to the linear regression.

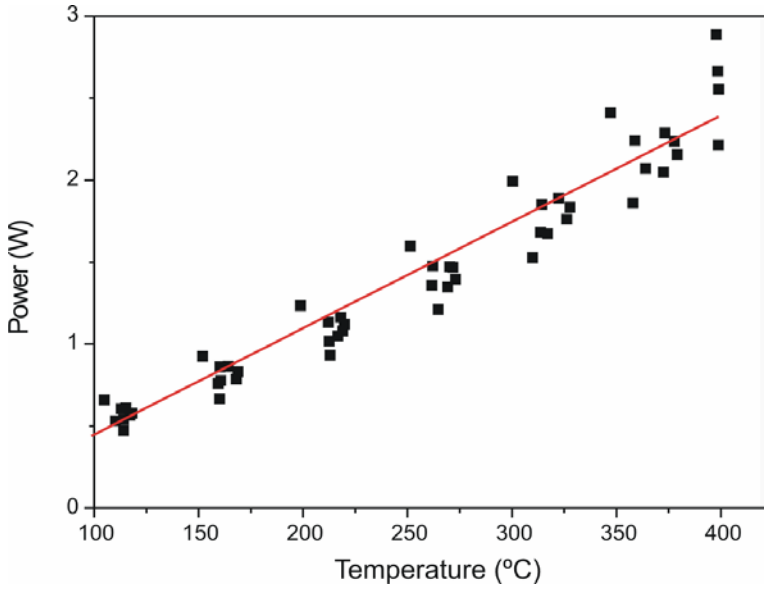

Figure II.5 *The power characteristic of the heater in Type I sensors*

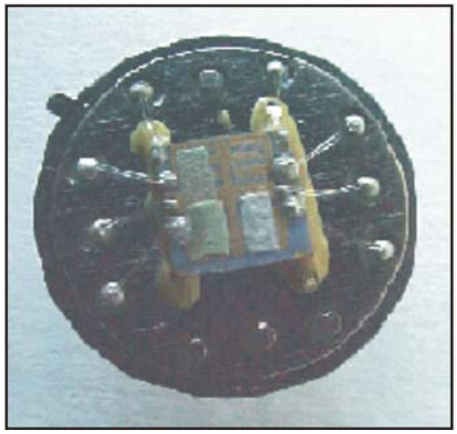

Figure II.6 *The sensor chip with four layers mounted and bonded onto TO-8 support*

II.2.1.3. Packaging

The substrate 2"x 2" and 250 µm thick with the printed sensors was cut on the reverse side by a laser beam and then broken up. The selected sensor chips from the same substrate were mounted onto a TO-8 package and wire bonded. Aluminium wires of 25 µm in diameter were used to perform a standard ultrasonic wire bonding. The bonded spots were fixed with Ag paste. The sensor is normally heated to relatively high temperatures; hence it cannot lie directly on the package because it could cause a power loss and the package to heat. Therefore, each sensor chip was distanced from the package by two lateral metal columns and glued with epoxy, commonly used for SMD. Figure II.6 shows the sensor chip mounted and bonded onto TO-8 support.

At working temperatures above approximately 450 ºC, a problem with the package appeared. The transfer of heat from the sensor to the solder joints of the package exceeds the melting point of the weld, causing this material to melt and the sensor is removed from the package. So, in order to test the developed materials, a new substrate was need, while finding a solution to this problem. Recently a new weld material based on Ruthenium, with higher melting point than the typical silver welds, was employed. The characterizations done to the substrate with Ruthenium solder joints showed that it can work up to temperatures near 800 ºC, without suffer joints melting. This substrate is being using for gas sensor application with good results. However, up to now, the measurements obtained with type I substrate are not complete and thus they could not be included in this thesis. Due the delay founding a solution for the joint melting in type I substrate, it was necessary the introduction of a new substrate (type II substrate) that will be detailed as follows.

II.2.2. Type II Substrate

This substrate was manufactured by multilayer thick film deposition of Pt based heater, insulation and contacts to the sensing layer. The use of two-side construction (Figure II.7) allows miniaturization of the sensor chip. The final dimensions of the sensor chip were as small as 1.5 mm x 0.3 mm x 0.15 mm. The thickness of the alumina substrate was decreased up to 0.1 μm. The sensor chip was bonded to TO-8 package (Figure II.8). The diameter of the package is equal to ~ 10 mm [15].

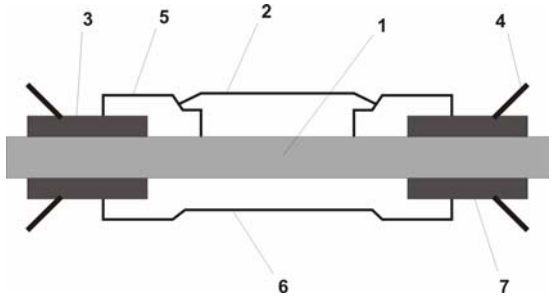

Figure II.7 *Structure of a type II sensor.* ***1.*** *Alumina substratum,* ***2.*** *sensing layer,* ***3.*** *contact pads,* ***4.*** *connecting wires,* ***5.*** *disjunction layer,* ***6.*** *heater,* ***7.*** *contact pads*

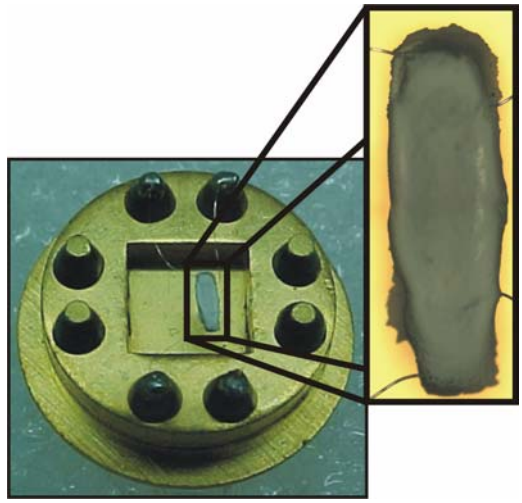

Figure II.8 *The sensor chip with the layer bonded onto TO-8 support*

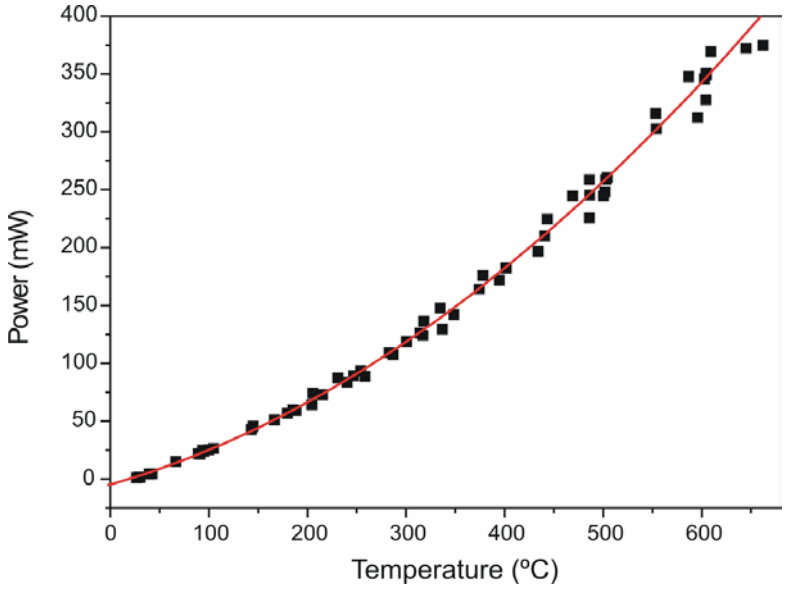

Figure II.9 *The power characteristic of the heater in Type II sensors*

As it was done for Type I substrate, the heater was also characterized to find its power consumption, depending on the working temperature. A voltage between 0 -3 V was applied to the heater with an increment of approximately 300 mV in each measurement. As it was not possible to use the IR thermometer, due to the small size of the sensor, the temperature of the sensor was calculated from the Temperature Coefficient of the Resistance (TCR) of the Pt-heater, following the next equation:

$$T = \frac{\left(\frac{R}{R_o} - 1\right)}{TCR} + T_o \qquad \textbf{(II.2)}$$

where T is the calculated temperature, R is the resistance of the heater, R_o is the resistance of the heater at room temperature and T_o is the room temperature. The TCR used for Pt was 2500 PPM/ºC. The resulted values of temperature vs. power consumed are represented in Figure II.9. It is possible to appreciate that for Type II substrate the curve of temperature vs. power consumption could be adjusted to a quadratic polynomial, unlike in Type I substrate,

where it was adjusted to a straight line. A polynomial regression using the calculated values leads to the following equation:

$$P = 5{,}60676\text{E-}4 \times T^2 + 0{,}24307 \times T - 4{,}82242 \quad \textbf{(II.3)}$$

where P is the power consumed and T is the working temperature. A relative error of 2 % is made when the power consumption is calculated from (II.3). From the characterization done to both type of sensor we find that the power consumption in Type I is 150 times higher than in Type II.

II.3. Active Material

The detection of oxygen in semiconductor sensors is done with semiconducting metal oxides. These materials, usually located on the sensor electrodes, react with the oxygen present in the atmosphere, changing their resistivity. This change of resistivity is used to measure the concentration of the oxygen in the environment. In next subsections, it is explained the synthesis of the semiconductor metal oxides employed in this work (pure TiO_2 and Nb-doped TiO_2) and the deposition of these materials on the sensors. As it will be appreciated in the chapter IV, some small variations will be applied to the synthesis process throughout this work; however the basic process is the same and it is described as follows.

II.3.1. Material Synthesis

Processes involving wet chemistry are preferably adopted for nanoscale materials synthesis. Among them, precipitation reactions, which basically follow simple precipitation processes, are often used. They are based on precipitation taking place in supersaturate solutions, which follow the rules of precipitation and growth. In these systems, the critical nucleation radius has to be exceeded as a prerequisite for further growth. The growth reaction will stop when the stock of precipitation ions is exhausted, i.e. when their concentration falls below the solubility. In these cases, if nucleation can be controlled, then the particle size of the precipitate can be tailored by adjusting concentration, solubility and temperature. However, in the case of extremely low solubility, this route leads to very diluted systems in which it is difficult to collect powders from the solution and it is difficult to handle the process for industrial technologies [16]. On the other hand, in concentrated systems agglomeration is unavoidable. The overall scene requires methods to control growth reactions stopping them at a desired level, and to avoid agglomeration in order to keep the particles isolated for suitable further processing. Therefore, precipitation reactions should be carried out in such a way that stable colloids are produced in the first step in a sufficient concentration.

Stabilization of colloids can be achieved by different methods. The most commonly used is to charge them electrically by selective adsorption of ions. In this case, the solid content of colloidal solution has to be in general low (less than 20 % in volume). This low solid content colloidal solution (sol) may be transformed into gel by destabilization, for instance by adjusting the pH to the point of zero charge of the surface. Consequently, the van der Waals forces are strong enough to agglomerate the systems to weekly stable solids (gels), which usually show a disordered structured with respect to the particle arrangement [17].

All in all, this scenario yields two basic requirements for nanoprocessing of small particles. First, it is necessary to control the nucleation and growth process in order to stop it at a selected particle size, and second, it is necessary to control the particle-particle interaction during gelation in such a way that high package densities can be obtained. For that purpose, we have followed a sol-gel route to obtain small TiO_2 nanoparticles. In the following subsection, the sol-gel route followed for obtained nanocrystalline pure and doped TiO_2 will be described.

II.3.1.1. Sol-Gel Process

Sol-gel technology is a method to synthesize nanophase metal oxide particles in a colloidal suspension. Primary concerns in this process are the control of the size, the chemical composition and the microstructure of the ultrafine particles. For application purposes, these particles are handled as powders, pallets and thin films, and they are subjected to a variety of heat treatments. The sol-gel process can be varied through changes in solution chemistry and stabilization technique to produce the desired particles morphologies [18]. In this regard, metal alkoxides are particularly useful precursors for the synthesis of the oxides. Metal oxides particles under 100 nm can be synthesized through room-temperature hydrolysis of metal alkoxides [18]. Structurally, a metal alkoxide consists of a M-O-R linkage, where M is the metal, O the oxygen, and R is an alkyl group. The opposite charges of M and O lead to a polarization in the M-O bond, which makes the alkoxide receptive to a nucleophilic reagent such as water. In the presence of water the alkoxide undergoes a nucleophilic addition-substitution reaction in which the alkoxy groups (OR) are replaced by hydroxyl groups ($^-$OH) provided by water. This process is known as hydrolysis. After hydrolysis, the metal hydroxide group link up by different mechanism generating a hydrated metal oxide network which eventually will form small nuclei (few nanometers). This process is called nucleation. For the case of a titanium alkoxide, the reaction can be schematically represented as follows [19]:

$$Ti(OR)_4 + xH_2O \rightarrow Ti(OH)_{4-x}OH_x + xROH \qquad \text{(Hydrolysis)}$$

$$Ti(OH)_{4-x}OH_x + Ti(OR)_4 \rightarrow (OR)_{4-x}TiO_xTi(OR)_{4-x} + xROH \qquad \text{(Condensation)}$$

Besides the alkoxide used in these reactions, many other factors influence the size and morphology of the TiO_2 particles, such as the concentration of reactants, the pH of solution, the temperature of hydrolysis, or the addition of the electrolytes.

In this work, non-doped TiO_2 samples were synthesized through a sol–gel route, starting from an alkoxide precursor. Following the experiment done by A. Ruiz [17, 20], 25 ml of Titanium (IV) isopropoxide, also called tetraisopropyl orthotitanate $Ti[OCH(CH_3)_2]_4$ 99 % purity, was mixed with isopropanol to get a 0.5 M solution to avoid early precipitations of oxides. The density of Titanium isopropoxide is 0.96 g/ml and its molecular weight is 284.22 g/mol, then the quantity of isopropanol needed to get the 0.5 M solution was calculated as follows:

$$\text{Volume of 0.5M solution} = 25\ ml \times \frac{0.96\ g}{1\ ml} \times \frac{1\ mol}{284.22\ g} \times \frac{10^3\ \text{m}l}{0.5\ mol} = 168.9\ ml \qquad \textbf{(II.4)}$$

$$\text{Volume of isopropanol solution} = 168.9\ ml_{\text{0.5M solution}} - 25\ ml_{\text{Ti isopropoxide}} = 143.9\ ml \qquad \textbf{(II.5)}$$

In the case of Nb-doped TiO_2, Niobium ethoxide, $Nb(OC_2H_5)_5$ 99.99 %, was also added to 0.5 M solution in the appropriate concentration to obtain an Nb/Ti atomic ratio of 3 %, which was the optimal doping concentration found by J. Arbiol in his doctoral thesis [21]. Since the molecule of titanium alkoxide precursor as well as the niobium one have only one atom of respective metal, the atomic ratio of these two compounds is proportional to their molar ratio. Then,

$$\text{Moles of Titanium isopropoxide}_{\text{25 ml}} = 25\ ml \times \frac{0.96\ g}{1\ ml} \times \frac{1\ mol}{284.22\ g} = 0.0845\ moles \qquad \textbf{(II.6)}$$

$$\text{Moles of niobium ethoxide} = 0.0845\ moles \times 0.03 = 0.002535\ moles \qquad \textbf{(II.7)}$$

The density of Niobium ethoxide is 1.268 g/ml and its molecular weight is 318.21 g/mol. Then,

$$\text{Volume of Niobium ethoxide} = 0.002535\ moles \times \frac{318.21\ g}{1\ mol} \times \frac{1\ ml}{1.268\ g} = 0.636 \times 10^{-3}\ ml \qquad \textbf{(II.8)}$$

Figure II.10 *Inflatable polyethylene chamber, Atmosbag, of Sigma-Aldrich*

Due to the high ability for oxidation of organic precursor, this process should be done inside an inert atmosphere. The inert atmosphere was created by using an inflatable polyethylene chamber (Figure II.10). The air inside the bag was taken out from it (vacuum was created) and nitrogen was introduced later. This procedure was repeated three times. After the precursors were diluted in isopropanol, the process could continue under natural atmosphere.

Another solution of water and acid nitric, HNO_3 70 %, was prepared in parallel. Then the mixture of organic precursors diluted in isopropanol was added, drop wise, to the acid solution under stirring (Figure II.11). The final composition of the constituent was set to satisfy $[Ti]:[HNO_3]:[H_2O] = 1:1:100$ in molar ratio. In the case of hydrolysis-condensation of titanium isopropoxide, the increasing in the initial water concentration produced higher nucleation rates, which resulted in a decrease in average particle size. Nagpal et al. [22] showed that the main factor on particle size is the effect of water concentration Based on this report and in A. Ruiz experiment [17], we selected a $[H_2O]/[Ti]$ ratio of 100. Because of the large amount of nitric acid, the hydrolysis proceeded without forming a precipitate, giving rise to a transparent sol with a pH = 1.

***Figure II.11 a**. 0.5 M solution of organic precursors in isopropanol **b.** Acid solution under stirring **c.** Stirring machine*

The density of HNO_3 is 1.383 g/ml and its weight is 63.0128 g/mol. Since the moles of HNO_3 are just the same as Ti, which is 0.0845 moles, then the litres of HNO_3 used in the process were calculated as follows:

$$\text{Litres of } HNO_3\ (70\ \%) = 0.0845\ moles \times \frac{63.0128\ g}{1\ mol} \times \frac{1\ ml}{1.383\ g} \times \frac{100\ \%}{70\ \%} = 5.5\ ml \qquad \textbf{(II.9)}$$

To calculate the water needed in the process, it had to be considered also the water contained in the 5.5 ml of HNO_3 70%, which is 1.65 ml. Then, because the ratio $[H_2O]/[Ti] = 100$, the moles of water should be 8.45 moles. The quantity of water added to HNO_3 was:

$$\text{Litres of } H_2O = \left(8.45\ moles \times \frac{18.0152\ g}{1\ moles} \times \frac{1\ ml}{0.995\ g} \right) - 1.65\ ml = 151.3\ ml \qquad \textbf{(II.10)}$$

Afterwards, the pH of the sol was increased carefully by adding, drop wise, approximately 30 ml of an aqueous solution (1M) of Ammonium Hydrogen Carbonate (pH = 9), up to achieve a consistent gel (Figure II.12).

Figure II.12 *Gel aspect*

II.3.1.2. Drying Process

The gel was dried in an oven UNE 300 of Memmert Co. First, the temperature was set to 120 ºC for 20 hours to evaporate water. Then, temperature was increased to 250 ºC for 10 hours to eliminate some compounds generated during synthesis. At the end, the gel was turned into big agglomeration of particles, in form of rocks (Figure II.13). These big particles were milled up to reach powder appearance.

II.3.1.3. Firing Process

The firing process was carried out in a programmable muffle Carbilite RWF 1200. The synthesised material was separated in four parts to be fired in air at 600 ºC, 700 ºC, 800 ºC and 900 ºC respectively. To avoid a fast growing of nanoparticles size, it was applied a ramp of temperature to reach each firing temperature. Two different rates for temperature ramp were employed: the first one, took from J. Arbiol et al. [23], was 10 ºC/min and the

second one, based on L. Gao et al. [24], was 2.5 ºC/min. The nanopowders remained under firing temperature for 2 hours, and then a free cooling ramp was applied to return to room temperature.

Figure II.13 *Particles obtained after gel drying*

II.3.2. Active Layer Deposition

For deposition of the TiO_2 nanopowders obtained following the procedure described above, they were suspended in an organic vehicle to form a paste. The viscosity of the paste should allow its deposition over the substrate. In a first approach a solution based on terpineol mixed with surfactants and other reology agents was employed as organic vehicle. Different assays of solvents solution were tried, but the boiling point of the resulted solution was always too low and the paste got dry quickly, increasing its viscosity. A paste with high viscosity is more difficult to spread over the substrate surface and has tendency to form cracks when it is dried [25, 26].

Finally, Glycerol was employed instead terpineol based solutions. The boiling point of glycerol is 290ºC, so it was expected that paste keep its physical properties even at temperatures 200ºC higher than room temperature. The milled nanopowders were dispersed in glycerol in a weight ratio of [Glycerol]/[TiO_2] = 3. The paste done with pure glycerol showed proper viscosity to be spread over the sensor.

After deposition of the paste on the sensor electrodes, a temperature treatment was carried out to the layers. This firing process was developed in-situ, using the heater element of the substrate. To control the temperature increase during the in-situ process, the heaters were connected to an automated power supply controlled by a computer using a LabView program. A schema of this treatment is shown in Figure II.14. First, the layer was dried at 300 ºC for 20 minutes (t_2 in Figure II.14) to eliminate the glycerol. Then, the structure of the layer was defined by heating the layer at 600 C (for those materials that were fired at 600 ºC) or 700 ºC (for those materials that were fired at 700 ºC and above) for 120 minutes (t_4 in Figure II.14).

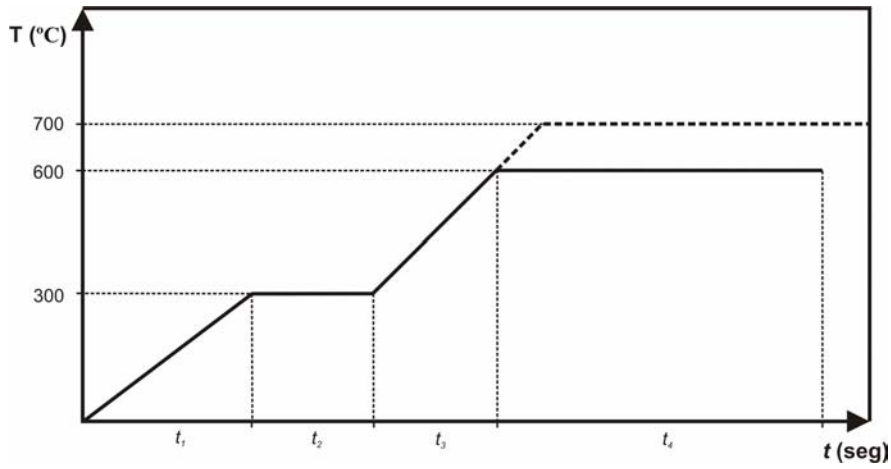

Figure II.14 *Schema of the heat treatment applied to the layers*

The time employed for reach each stage of temperature is defined as t_1 and t_3 in Figure II.14. The rate of temperature increase during the heating process previously commented is very important. A fast temperature increase may induce the formation of cracks in the layer. Some experiments were carried out to determine the best rates. In the first assays, the material was deposited over silicon substrates and alumina substrates. Then, temperature ramps of 100 ºC/min (t1) and 50 ºC/min (t3) were used for dry and fire the layers. In all the cases cracks appeared after temperature treatment. Examples of this are shown in Figure II.15 (**a.** and **b.**), where it is possible to appreciate two drops of pure Titania over silicon substrates. In Figure II.15 **a.** the temperature ramp used was 100 ºC/min; the fast change of temperature not only creates cracks, but also makes that the material in the centre of the drop leaps out. For the drop showed in Figure II.15 **b.**, it was used a slower

temperature ramp (50 ºC/min). In this case, the material in the centre of the drop remains there, but the cracks still appear in the drop.

The last temperature rate employed was 10 ºC/min. A drop heat treated by using this temperature rate is shown in Figure II.15 **c.** As it can be seen, there are not cracks in this drop. The slower change of temperature reduces the stress in the layer structure preventing the crack formation. Thus, the temperature rate employed for heat treatment of the layers (drying and firing processes) was set up to 10º C/min.

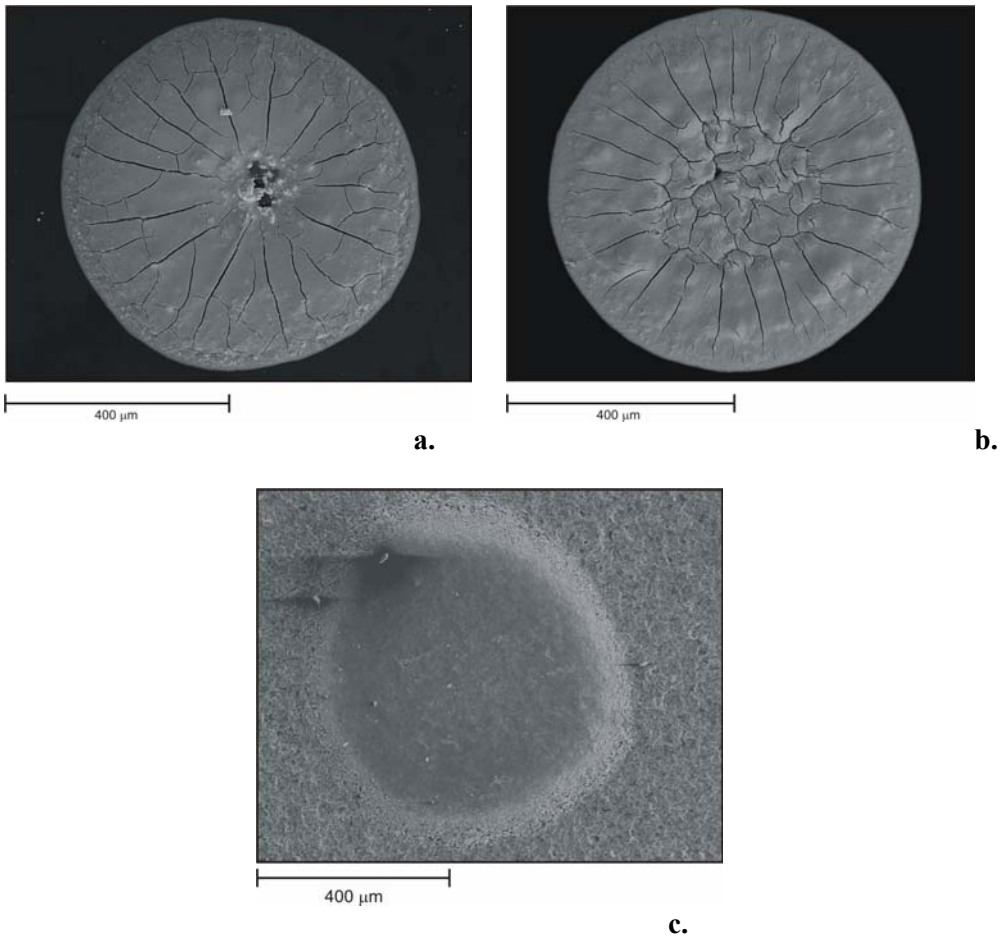

Figure II.15 *Drops of pure Titania:* ***a.*** *deposited over silicon substrate and heat treated with a temperature rate of 100 ºC,* ***b.*** *deposited over silicon substrate and heat treated using a temperature rate of 50 ºC/min,* ***c.*** *deposited over alumina substrate and heat treated with a temperature ramp of 10 ºC/min*

II.4. References

[1] R.K. Sharma and M.C. Bhatnagar, "*Improvement of the Oxygen Gas Sensitivity in Doped TiO_2 Thick Films*", Sensors and Actuators B: Chemical, Vol. 56 (1999) 215-219

[2] A. Takami, T. Matsuura, S. Miyata, K. Furusaki and Y. Watanabe, "*Effect of Precious Metal Catalyst in TiO_2 Thick Film HEGO Sensor with Multilayer Alumina Substrate*", Society of Automotive Engineers, Vol. 870290 (1988) 1.1183–1.1192.

[3] A. Takami, "*Development of Titania Heated Exhaust Gas Oxygen Sensor*", Ceramic Bulletin, Vol. 67 12 (1988) 1956-1960

[4] R.K. Sharma, M.C. Bhatnagar and G.L. Sharma, "*Mechanism in Nb Doped TiO_2 Oxygen Gas Sensor*", Sensors and Actuators B: Chemical, Vol. 46 (1998) 194-201

[5] R.K. Sharma, "*Development and Characterization Solid State Materials for Oxygen Gas Sensors*", Doctoral thesis, Indian Institute of Technology, Department of Physics, 1996

[6] V. Guidia, M.A. Butturi, M.C. Carotta, B. Cavicchi, M. Ferroni, C. Malagù, G. Martinelli, D. Vincenzi, M. Sacerdoti and M. Zen, "*Gas Sensing through Thick Film Technology*", Sensors and Actuators B: Chemical, Vol. 84 (2002) 72-77

[7] M. Stankova, "*Gas Sensing Properties of RF Sputtered WO_3 Thin Films*", Doctoral thesis, Universitat Politècnica de Catalunya, Departament d'Electrónica, 2004

[8] G. Sberveglieri, W. Hellmich and G. Müller, "*Silicon Hotplates for Metal Oxide Gas Sensor Elements*", Microsystem Technologies, Vol. 3 (1997) 183–190

[9] B.H. Weiller, P.D. Fuqua and J.V. Osborn, "*Fabrication, Characterization, and Thermal Failure Analysis of a Micro Hot Plate Chemical Sensor Substrate*", Journal of The Electrochemical Society, Vol. 151 3 (2004) H59-H65

[10] Y.S. Kim, S.-C. Ha, K. Kim, H. Yang, S.-Y. Choi, Y.T. Kim, J.T. Park, C.H. Lee, J. Choi, J. Paek and K. Lee, "*Room-Temperature Semiconductor Gas Sensor Based on Nonstoichiometric Tungsten Oxide Nanorod Film*", Applied Physics Letters, Vol. 86 (2005)

[11] A. Cirera, "*New Technologies and their Characterization for Nanostructured SnO_2 Gas Sensor Devices*", Doctoral thesis, Universitat de Barcelona, Departament d'Electrònica, 2000

[12] E. Llobet, P. Ivanov, X. Vilanova, J. Brezmes, J. Hubalek, K. Malysz, I. Gràcia, C. Canè and X. Correig, "*Screen-printed Nanoparticle Tin Oxide Films for High-Yield Sensor Microsystems*", Sensors and Actuators B, Vol. 96 1-2 (2003) 94-104

[13] P. Ivanov, J. Hubalek, K. Malysz, J. Pràsek, X. Vilanova, E. Llobet and X. Correig, "*A Route toward More Selective and Less Humidity Sensitive Screen-Printed SnO_2 and WO_3 Gas Sensitive Layers*", Sensors and Actuators B: Chemical, Vol. 100 1-2 (2004) 221-227

[14] Electro-Science, "*Thick-Film Materials & Ceramic Tapes Products*", Available from: http://www.electroscience.com/products.html

[15] J.H. Kim, J.S. Sung, Y.M. Son, A.A. Vasiliev, V.V. Malyshev, E.A. Koltypin, A.V. Eryshkin, D.Y. Godovski, A.V. Pisyakov and S.S. Yakimov, "*Propane/Butane Semiconductor Gas Sensor with Low Power Consumption*", Sensors and Actuators B: Chemical, Vol. 44 (1997) 452–457

[16] E. Matijevic, "*Ultrastucture Processing of Advanced Ceramics*", Wiley J, Edited by Wiley J, New York, 1988

[17] A. Ruiz, "*TiO_2 Nanoparticles for Gas Sensor Applications*", Doctoral thesis, Universitat de Barcelona, Departament d'Electrónica, 2003

[18] C.J. Brinker and G.W. Sherrer, "*Sol-Gel Science*", Edited by Academic Press, San Diego, 1990

[19] D.C. Hague and M.J. Ma, "*Controlling Crystallinity during Processing of Nanocrystalline Titania* ", Journal of the American Ceramic Society, Vol. 77 7 (1994) 1957-1960

[20] A. Ruiz, G. Dezanneau, J. Arbiol, A. Cornet and J.R. Morante, "*Study of the Influence of Nb Content and Sintering Temperature on TiO_2 Sensing Films*", Thin Solid Films Vol. 436 (2003) 90-94

[21] J. Arbiol, "*Metal Additive Distribution in TiO_2 and SnO_2 Semiconductor Gas Sensor Nanostructured Materials*", Doctoral thesis, Universitat de Barcelona, Departament d'Electrónica, 2001

[22] V.J. Nagpal, R.M. Davis and J.S. Riffle, "*In Situ Steric Stabilization of Titanium Dioxide Particles Synthesized by a Sol-Gel Process*", Colloids and Surfaces A: Physicochemical and Engineering Aspects, Vol. 87 1 (1994) 25-31

[23] J. Arbiol, J. Cerdà, G. Dezanneau, A. Cirera, F. Peiró, A. Cornet and J.R. Morante, "*Effects of Nb doping on the TiO2 anatase-to-rutile phase transition*", Journal of Applied Physics, Vol. 92 2 (2002) 853-861

[24] L. Gao, Q. Li, Z. Song and J. Wang, "*Preparation of nano-scale titania thick film and its oxygen sensitivity*", Sensors and Actuators B: Chemical, Vol. 71 (2000) 179-183

[25] J. Puigcorbé, A. Vilà, J. Cerdà, A. Cirera, I. Gràcia, C. Cané and J.R. Morante, "*Thermo-Mechanical Analysis of Micro-Drop Coated Gas Sensors*", Sensors and Actuators A: Physical, Vol. 97-98 (2002) 379-385

[26] J. Puigcorbé, A. Cirera, J. Cerdà, J. Folch, A. Cornet and J.R. Morante, "*Microdeposition of Microwave Obtained Nanoscaled SnO_2 Powders for Gas Sensing Microsystem*", Sensors and Actuators B: Chemical, Vol. 84 1 (2002) 60-65

III. TiO_2 AND Nb-DOPED TiO_2 CHARACTERIZATION

III.1. Introduction

In this chapter, it is presented the results of the physical characterization of the Titania based materials, which synthesis was explained in the last chapter. These materials are summarized in Table III.1. The materials, once deposited over the alumina substrate were also characterized. The objective of these characterizations was to obtain information about the material structure that could be related with its detection properties. For this purpose, we applied various techniques. Inductively Coupled Plasma (ICP) spectroscopy was employed to determine the chemical composition of the samples and quantify the amount of each component. X-ray Diffraction (XRD) was used to establish the phases present in the crystalline structure of the material and determine the size of the crystallites in each material. Area BET measurements were done to nanopowders to know the surface area and the porosity of each material. Scanning Electron Microscopy (SEM) was used to obtain details on the film structure and the grain size. To make quantitative and qualitative analysis, Energy-Dispersive X-ray Spectroscopy (EDS) was also applied.

Table III.1 *Codification of materials depending on the doping and the type of ramp applied for to reach the calcinations temperature*

Material	Composition	Ramp of temperature for calcination (ºC/min)
M5	TiO_2	10
M6	TiO_2 + 3at% Nb	10
M7	TiO_2	2.5
M8	TiO_2 + 3at% Nb	2.5

The sensing capabilities of the materials were also tested. The sensitivity toward oxygen was measured under two different configurations: 20 ppm of O_2 in N_2 balance and 30 ppm of O_2 in CO_2 balance. The sensors responses toward other pollutant gases (SO_2, CH_4, H_2S and C_2H_4) were also tested in order to see the influence of such gases in the oxygen detection process.

To understand some behaviour of the sensors, RAMAN spectroscopy was employed. This technique gives information at molecular level allowing the vibrational and rotational analysis of chemical species.

Each of these measurements is presented in separated subchapter, including a little description of the applied method, the results obtained and their discussion.

III.2. Powders Characterization

Three types of analyses have been carried out to the synthesized materials. The first one is Inductively Coupled Plasma (ICP) that has been used to determine the concentrations of doping atoms (niobium atoms) in the doped Titania. The results of this analysis can show us if the doping process achieved the desired concentration of niobium.

The second one, X-rays Diffraction (XRD) gives us an insight into the crystalline composition of the materials. The oxygen detection mechanism in Titania has a big dependence on its crystalline structure. In rutile phase, this mechanism is based on the diffusion of oxygen ions in the bulk of the material, in which it is necessary to work at high temperatures (700-1000ºC). On the other hand, anatase phase titania has more free electrons [1], so oxygen detection can be associate to surface reaction, that takes place at not so high temperatures (400 – 500ºC) [2, 3]. Therefore, it is important to establish the crystalline phases present in an active material to understand its behaviour during detection process. This technique allows us to determine also the crystallite size, which has also influence on the detection process. As it is known, in general, the lower the crystallite size, the higher the sensitivity achieved.

The porosity and the surface area of the material also play an important role in the detection process, since the interaction between the active material and the gas takes place on the surface. Thus, the knowledge of this parameter may help in the selection of the best material to be used for the oxygen sensor. This characteristic is also analyzed in this subsection with area BET measurements.

III.2.1. Inductively Coupled Plasma (ICP)

Inductively Coupled Plasma (ICP) spectroscopy is a multi-element technique that provides fast, reliable and accurate analysis of the elementary components concentration with high sensitivity. It is based on an inductively coupled plasma source that dissociates the sample into its constituent atoms or ions, exciting them to a level in which each atom emits light of a characteristic wavelength. Depending on the intensity of the light emitted and measured by a detector, the concentration of the particular element in the sample is calculated. During the analysis, the sample suffers temperatures of about 10000 ºC, where even the most refractory elements are atomized with high efficiency. As a result, the detection limit can reach levels as low as 1-10 ppb.

With this technique it is possible to determine the chemical composition of the samples. Moreover, it can give information about the amount of any noble metal placed in the surface or inside the bulk of a metal oxide sample [4]. Further details describing this technique, principles and sample handing can be found elsewhere [5].

III.2.1.1. Experimental Set-Up

The concentration of the additives in Titania has been analyzed in an ICP-OES analyzer (Induced Coupled Plasma – Optical Emission Spectroscopy) from Perkin-Elmer model *OPTIMA 3200RL*. The radiofrequency source was 40 MHz working at a power between 750 and 1500 W. The ICP analysis was realized in the Scientific Resources Service at the University Rovira i Virgili, Tarragona, Spain.

For the measurements, the samples need to be introduced in a solution into the analyzer. The material employed in this analysis was M6. Thus, the powders (50 mg), before any calcination treatment, were melted with HCL (1 ml), HF (1 ml) and H_2O (1 ml) in a Pressurized Microwave Decomposition System (from PAAR Inc).

III.2.1.2. Results and Discussion

The result of ICP analysis is summarized in Table III.2. It is possible to appreciate that the content of Niobium measured is close to the nominal. Then we can conclude that the doping process was successful.

Table III.2 *Result from ICP analysis*

Nominal Nb content (at.%)	Nb content measured from ICP (at.%)
3	2.75 ±0.2

III.2.2. X-Rays Diffraction (XRD)

The analysis of phase transition has been studied by using X-Rays Diffraction (XRD). With this technique is not only possible to distinguish phase states of the sample, but also to quantify the percentage of each phase in every one of the samples annealing stages.

This technique is based on the principle that a monochromatic X-ray, with an incident angle θ respect to a family of crystallographic planes (kkl), is diffracted with an angle 2θ. When this occurs, it is said that there is a reflection and is only produced when Bragg condition is verified (one family of reflections per each family of planes):

$$n \cdot \lambda = 2 \cdot d_{hkl} \cdot \sin(\theta) \qquad \textbf{(III.1)}$$

where λ is the wavelength of the incident radiation (1.5406 Å for CuK_α), d_{hkl} is the distance between the planes (hkl) and *n* is the refraction order in the family.

It can be seen that a correct determination of refraction angle θ conduces to a fast measure of the distance between planes.

In a powder diffractometer, which uses Bragg-Brentano geometry, the polycrystalline sample has a face or a surface plane where the diffraction takes place. The detector and the emission source are oriented in all moments in symmetric position respect to the normal of the sample plane, so that $\theta = \varpi$ (ϖ is the angle that forms the emitted ray with the surface of the sample). In fact, emission source, sample and detector occupy three consecutive positions on a circumference: the emission source and detector are oriented toward the centre of the sample and the normal of the plane surface of it is in the direction to the circumference centre. That assures that Bragg's conditions (III.1) for a set of points situated in a certain zone of the sample surface and, therefore the detector collects in a consecutive way the emergent rays from the different points. Position and orientation of the detector and the emission source are varying in a synchronized way, keeping the symmetric positions. In that way, a discrete spectrum of the reflections of families of planes parallel to sample surface is obtained, as the emission source and the detector check the different values of the angle 2θ.

If the grains of the sample are perfectly co-aligned, e.g. a perfect texture, only the reflections corresponding to families of planes parallel to the sample surface will appear. On the other hand, if the grains of the sample are perfectly disordered, e.g. a polycrystalline sample or a powder sample, the reflection corresponding to all families of planes will appear (while they do not satisfy additional conditions). So, the information obtained from this technique gives an approximated idea about the degree of the preferential orientation of certain crystalline specie.

In the case of a sample in powder form, we get a spectrum with all possible reflection when moving the angle 2θ. The resulting spectrum can be compared with other spectrums catalogued in the databases of The Joint Committee for Powder Diffraction Studies (JCPDS), which allow the identification of the crystalline species present in the sample [6].

Quantitive analysis is done by employing the Rietveld XRD Quantification Method. With this method, the weight fraction w_p for phase "p" is calculated as follows:

$$w_p = \frac{\left(S_p M_p V_p / B_p\right)}{\sum_{p=1}^{N_p}\left(S_p M_p V_p / B_p\right)} \qquad \textbf{(III.2)}$$

where N_p is the number of phases, S_p is the Rietveld scale factor for phase, M_p is the unit cell mass for phase, V_p is the unit cell volume for phase and B_p is the Brindley correction factor for phase [7].

The mean dimension, *d*, of crystallites was obtained by elaborating the most intense X-ray peak of each phase by Scherer's equation:

$$d = \frac{K\lambda}{FWHM \times \cos\theta} \qquad \textbf{(III.3)}$$

where *K* is a constant related to the crystallite shape, FWHM (Full Width Half Maximum) is the width of the main peak of the phase measured at the half of the height of the peak, as it is shown in Figure III.1. The accuracy of this method is limited by the uncertainties in *K* and the errors measuring the FWHM. This equation is quite satisfactory for studies comparing the crystallite sizes of a number of samples belonging to a related series [8].

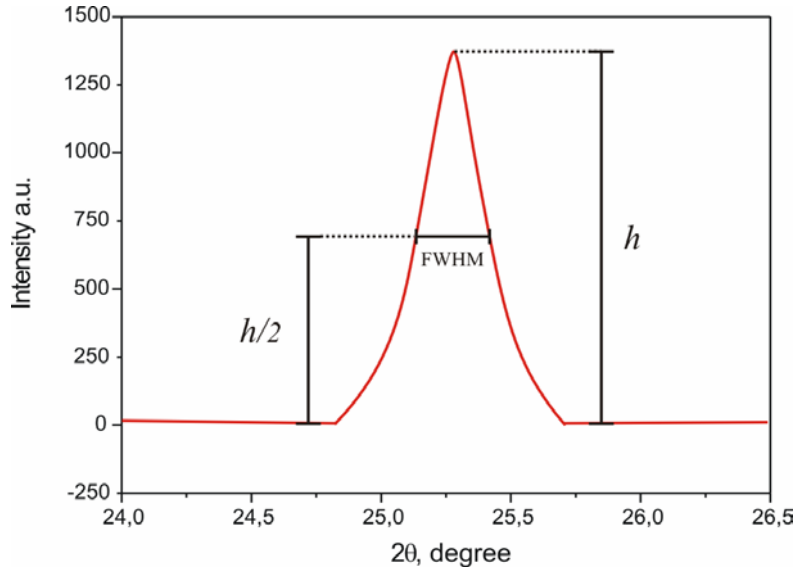

Figure III.1 *Full Width Half Maximum (FWHM) measured in a typical peak of phase in a material XRD pattern*

III.2.2.1. Experimental Set-Up

XRD measurements were made using a Siemens D5000 diffractometer (Bragg-Bretano parafocusing geometry and vertical θ-θ goniometer) fitted with a curve graphite diffracted-beam monochromator, incident and diffracted-beam Soller slits, a 0.06º receiving slit and scintillation counter as a detector. The angular 2θ diffraction range was between 20º and 45º. The data were collected with an angular step of 0.05º at 3 s per step and sample rotation. $Cu_{k\alpha}$ radiation was obtained from copper X-ray tube operated at 40 kV and 30 mA.

For quantitive analysis, it was used the software TOPAS from Bruker Advanced X-Ray Solutions.

In the Scherer's equation, used for calculation of the crystallites size, the following constant values: K=1.0 and λ = 15.4 nm were used.

III.2.2.2. Results and Discussion

The XRD pattern of material M5 is shown in Figure III.2. In this figure it is possible to appreciate the fast evolution of phase in this material. The change of phase from anatase to rutile is almost complete at 700 ºC. The results of the quantitative analysis are represented in Figure III.3.

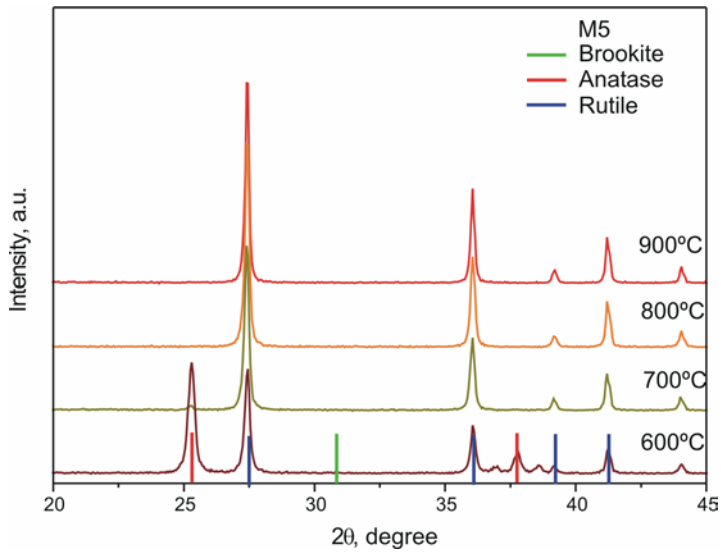

Figure III.2 *XRD patterns of material M5 calcined at different temperatures*

From the results of quantitative analysis it is observed that at 600 ºC the material is divided in a similar proportion of anatase and rutile phase. Any sign of brookite phase was found at this temperature. At 700 ºC, the anatase phase is almost disappeared and we can consider that the whole material is in rutile phase. At 800 ºC the sample is 100 % in rutile phase and there is not any change in the crystallinity state of the material when increasing the temperature to 900 ºC. This is because rutile phase is completely stable and the change of phase is irreversible.

If we make an extrapolation with the results of quantitative analysis, we can assure that the phase transition in material M5 started at temperatures about 500 ºC or even lower. This early change of phase means a fast stabilization of crystalline structure.

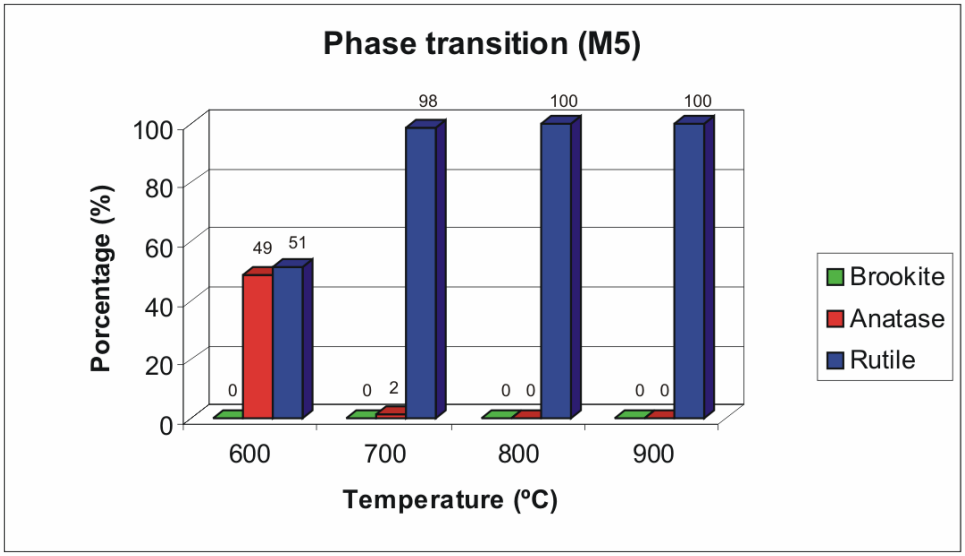

Figure III.3 *Percentage of each crystalline phase contained in the materials. These values were obtained from the quantitative analysis of XRD patterns of sample M5*

The crystallite size was extracted from the FWHM of the main peak for each phase (Figure III.4). The change of size in anatase crystallites with the increment of the calcination temperature is summarized in Table III.3. The crystallite sizes of rutile phase are in Table III.4.

It is appreciable the difference in size in the crystallites of anatase and rutile phases. Anatase crystallites are smaller than rutile ones. This result is in accordance with other authors [9, 10]. Nevertheless, it is also observed that the growth of the crystallite size in

anatase phase with temperatures faster than those in rutile phase. The size of anatase crystallites increases in almost 100 % when the calcination temperature is increased from 600 ºC to 700 ºC. On the other hand, the size of rutile crystallites experiment an increment of only 25 % when calcination temperature pass from 600 ºC to 900 ºC.

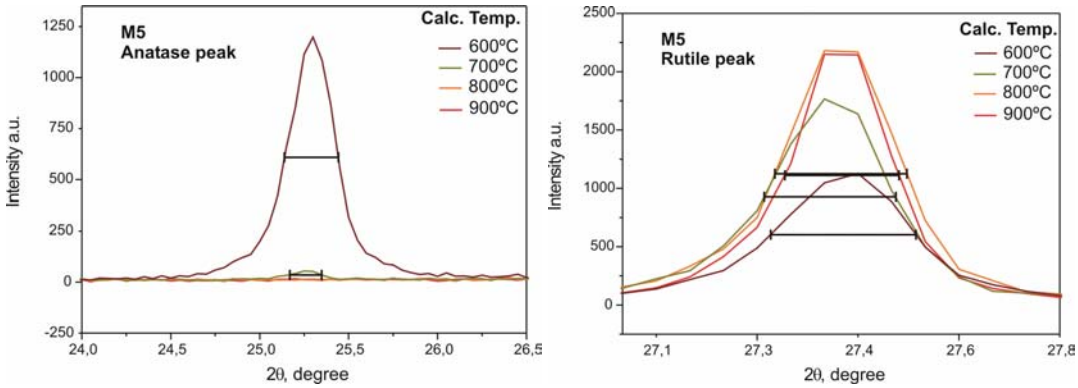

Figure III.4 *Measurement of the FWHM in* ***a.*** *main anatase peak and* ***b.*** *main rutile peak, in M5*

Table III.3 *Size of anatase crystallites in M5 and the values employed for its calculation*

Temperature (ºC)	FWHM (rad)	θ (rad)	Crystallite size (nm)
600	5.33E-03	4.42E-01	31.97
700	3.14E-03	4.41E-01	54.24

Table III.4 *Size of rutile crystallites in M5 and the values employed for its calculation*

Temperature (ºC)	FWHM (rad)	θ (rad)	Crystallite size (nm)
600	2.49E-03	4.79E-01	69.65
700	2.26E-03	4.78E-01	76.73
800	2.27E-03	4.79E-01	76.52
900	1.96E-03	4.79E-01	88.59

The growth of rutile crystallites is slower at the first three calcination temperatures. Between 700 ºC and 800 ºC, it appears to be an inhibition of growth in rutile crystallites. This inhibition disappears at 900 ºC where the highest growth in these phase crystallites is presented.

Using the values of crystallite sizes of the phases from Table III.3 and Table III.4 and the quantity of each phase present in the materials, it was made a weighting average of the crystallite size of each material. The result of this average is shown in Table III.5.

The quantity of anatase phase in M5-600, which is 50 %, reduces the crystallite average. When anatase phase is extinct, at 700 ºC, the mean crystallite size depends only on the rutile phase and then there is a big increment in this value.

Table III.5 *Weighting average crystallite size of M5 in function of the calcination temperature*

Temperature (ºC)	Average crystallite size (nm)
600	50.87
700	76.06
800	76.52
900	88.59

The XRD pattern of material M6 is shown in Figure III.5. Here we can see the effects of the addition of niobium ions to Titania lattice. Unlike M5, in M6 calcined at temperatures below 700 ºC, the anatase phase is the main crystalline structure (see Figure III.6). At 800 ºC there is still some quantity of anatase phase in the material (12 %). The complete change to rutile does not occur up to 900 ºC.

In his doctoral thesis, J. Arbiol gives the physical explanation of the effects of Nb ion additions to TiO_2 lattice on phase transition process anatase-rutile. According to J. Arbiol [11], during doping process, Nb^{5+} ions enter substitutionally in the lattice, occuping Ti^{4+} vacancies [12] without affecting the basic TiO_2 structure (anatase or rutile) [13] since the ionic radii of Nb^{5+} (0.70 Å) is comparable to that of Ti^{4+} (0.68 Å) [10, 14-16]. But, in order to assure the material charge neutrality, these Nb^{5+} ions should be compensated by an oxygen vacancies decreasing. In anatase-rutile transformation, the anatase pseudo-close-packed planes of oxygen {112} are retained as the rutile close-packed planes {110} and a cooperative rearrangement of the titanium and oxygen ions occur within this configuration [17]. The oxygen vacancies placed in anatase planes act as nucleation sites for the anatase to rutile phase transformation [18], therefore a minimum ratio of oxygen vacancies in anatase {112} planes is needed in order to assure the phase transition process. Then, the phase inhibition is attributed to the extra valance in niobium ions, which reduces oxygen vacancies in anatase phase, thus regarding the transformation to rutile [15, 19].

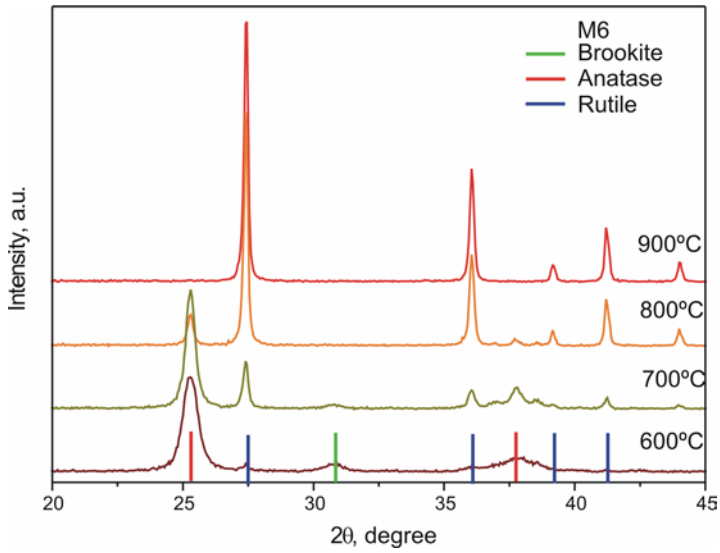

Figure III.5 *XRD patterns of material M6 calcined at different temperatures*

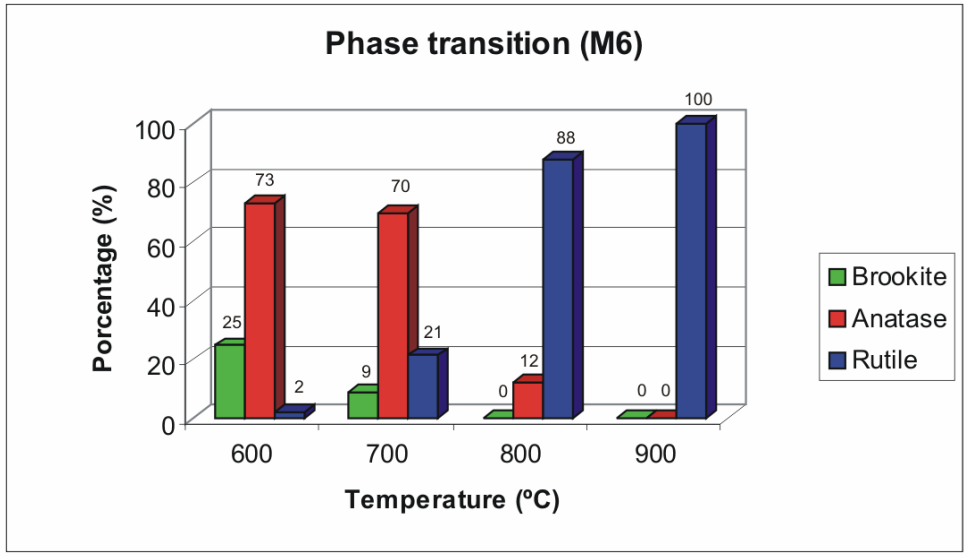

Figure III.6 *Percentage of each crystalline phase contained in the materials. These values were obtained from the quantitative analysis of XRD patterns of sample M6*

It was found considerable quantities of brookite phase in material M6 calcined at 600 ºC (25 %) and 700 ºC (9 %). This phase of Titania is usually found before the formation of anatase and rutile crystalline states. Nevertheless, the brookite phase could change directly to rutile phase without passing through anatase phase [20]. The changes of the percentages of the crystallines phases at 700 ºC suggest that there is a transformation of a part of brookite phase directly to rutile phase. At 800 ºC there is not evidence of brookite phase in the material.

The Brookite phase has less free carriers than anatase and its electrochemical behaviour is very alike to rutile's [21]. Its presence could hinder the response of a material towards oxygen at working temperatures around 500 ºC.

The presence of anatase phase is higher in M6 materials than in M5 materials. Then it is concluded that M6 materials appears to be more suitable for the purpose of this project, which is the oxygen detection at lower temperatures (400 ºC-600 ºC).

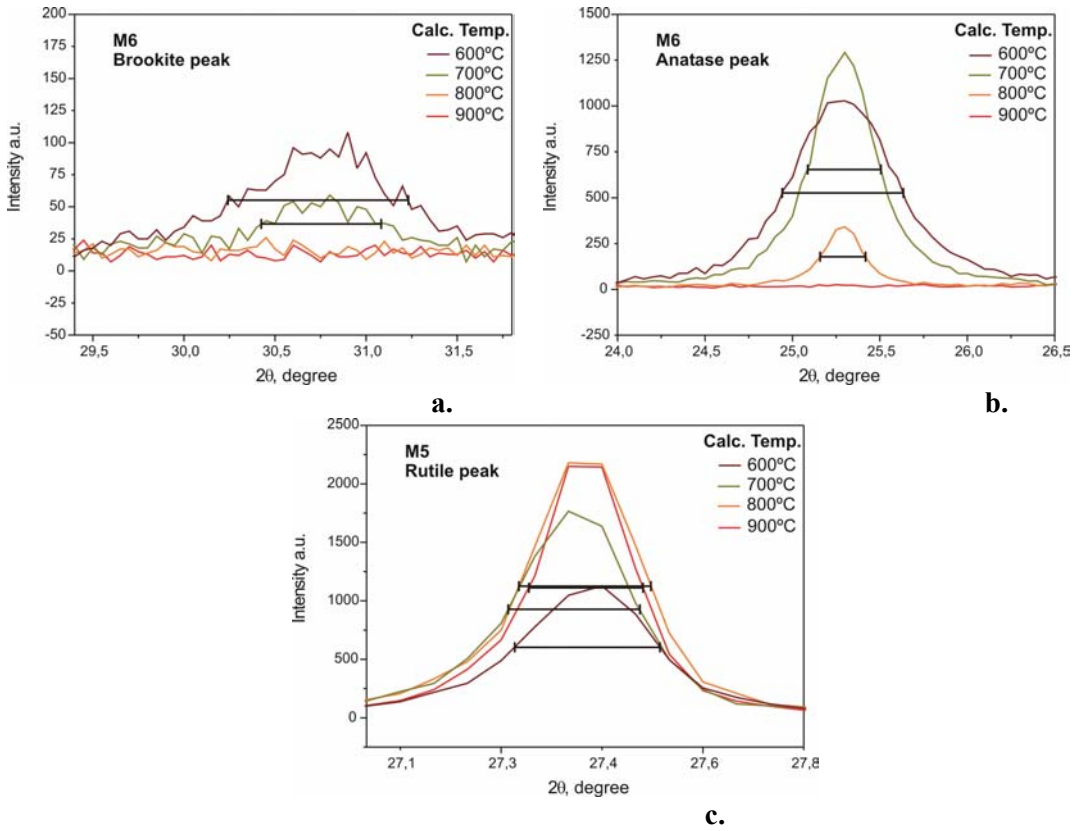

Figure III.7 *Measurement of the FWHM in* ***a.*** *main brookite peak,* ***b.*** *main anatase peak and* ***c.*** *main rutile peak, in M6*

In Figure III.7 it is shown the FWHM of all the main peaks in XRD patterns for M6. The changes of crystallites size with the increment of the calcination temperature of brookite, anatase and rutile phase are summarized in Table III.6, Table III.7 and Table III.8 respectively.

The size of the crystallites in material M6 is lower than in material M5. This happens in all phases. This is also due to the incorporation of Nb in Titania lattice. The niobium ions occupy substitutionally titanium sites due to the similarity of their ionic radii. Nevertheless, Nb^{5+} radius (0.70 Å) is a bit larger than Ti^{4+} radius (0.68 Å). The result of this is that Nb atoms induce stress in Titania lattice, which may hinder the growth of anatase and rutile phase crystallites in the material, as found by Sharma et al. [10].

As it happened in M5, the size of the crystallites in M6 depends on the crystalline phase. The size of the crystallites in brookite phase is the smallest. This size is increased as the change of phase is produced in the crystalline structure of the material.

Table III.6 *Size of brookite crystallites in M6 and the values employed for its calculation*

Temperature (ºC)	FWHM (rad)	θ (rad)	Crystallite size (nm)
600	1.73E-02	5.38E-01	10.37
700	1.15E-02	5.38E-01	15.60

Table III.7 *Size of anatase crystallites in M6 and the values employed for its calculation*

Temperature (ºC)	FWHM (rad)	θ (rad)	Crystallite size (nm)
600	1.22E-02	4.41E-01	14.00
700	7.35E-03	4.41E-01	23.17
800	4.56E-03	4.41E-01	37.35

Table III.8 *Size of rutile crystallites in M6 and the values employed for its calculation*

Temperature (ºC)	FWHM (rad)	θ (rad)	Crystallite size (nm)
700	3.68E-03	4.78E-01	47.14
800	3.19E-03	4.78E-01	54.41
900	3.28E-03	4.78E-01	52.88

It appears that the crystallite growth is related with its size and hence, with the phase. The earlier is the phase transition (the lower is the temperature for the transition), the faster is the growth of the crystallites. This is the case of crystallite growth in rutile phase, which is the slowest one, compared with the other phases. The crystallites sizes in rutile phase increase only a 12% when the firing temperature increases from 600 ºC to 900 ºC. Nevertheless, the faster growth does not occur in brookite phase, which has the smallest crystallites, but in anatase. In brookite phase, the crystallites grow a 50% when the calcination temperature is increased from 600 ºC to 700 ºC. On the other hand, the anatase crystallites grow a 64% with the same temperature increment and a 164% when the calcination temperature is increased to 800 ºC.

As in the previous material M5, a weighting average of the crystallite size was made. The result of this average is shown in Table III.9.

At lower temperatures (600 ºC and 700 ºC) the higher content of anatase and the portion of brookite keep the crystallite size in low dimensions. A steep increment in this size takes place when only the rutile phase remains in the material.

As it can be observed, crystallites in M6 are smaller than in M5. The small crystallites drive to small grains and therefore to a higher surface area. Then it is expected that M6 based materials have more surface area than M5 based materials, which means a better interaction between the gas and the active material.

Table III.9 *Weighting average crystallite size of M6 in function of the calcination temperature*

Temperature (ºC)	Average crystallite size (nm)
600	12.99
700	27.52
800	52.36
900	52.88

The XRD pattern of material M7 (doped material calcined using a slower ramp of 2.5 ºC/min) is shown in Figure III.8. The results of the quantitative analysis are represented in Figure III.9. The change of phase is similar to that presented in M5. At 700 ºC the crystalline structure has changed almost completely to rutile. Nevertheless, at 600 ºC the quantity of anatase in M7 is lower than in M5. There was also found a small quantity of brookite phase in M7. This phase was not found in M5. Due to the only difference between these two materials is the ramp of temperature employed to reach the calcination temperature (10 ºC/min for M5 and 2.5 ºC/min for M7), the lower quantity of anatase phase and the presence of brookite phase could be attributed to a slight retard in phase transition produced when the temperature ramp employed is slower. This retard is only appreciable when material is calcined at 600 ºC.

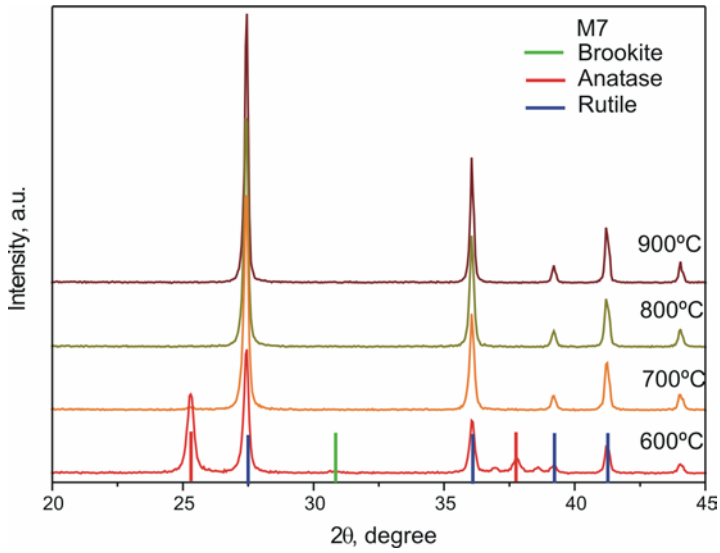

Figure III.8 *XRD patterns of material M7 calcined at different temperatures*

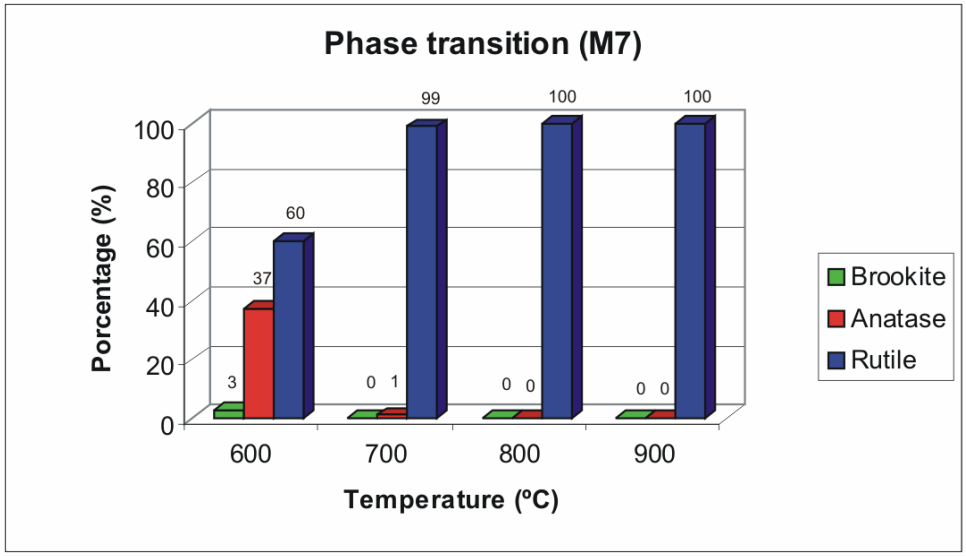

Figure III.9 *Percentage of each crystalline phase contained in the materials. These values were obtained from the quantitative analysis of XRD patterns of sample M7*

As in M5, we can assure that the phase transition in material M7 started at temperatures about 500 ºC or even lower. At 800 ºC the stabilization of the crystalline structure is complete.

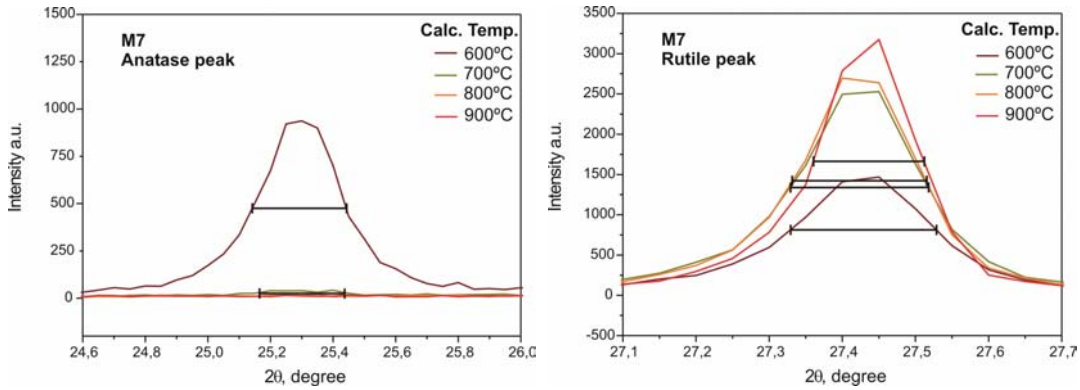

Figure III.10 *Measurement of the FWHM in* ***a.*** *main anatase peak and* ***b.*** *main rutile peak, in M7*

Table III.10 *Size of anatase crystallites in M7 and the values employed for its calculation*

Temperature (ºC)	FWHM (rad)	θ (rad)	Crystallite size (nm)
600	5.24E-03	4.42E-01	32.52
700	4.73E-03	4.42E-01	36.05

Table III.11 *Size of rutile crystallites in M7 and the values employed for its calculation*

Temperature (ºC)	FWHM (rad)	θ (rad)	Crystallite size (nm)
600	3.50E-03	4.79E-01	49.58
700	3.32E-03	4.79E-01	52.36
800	3.23E-03	4.79E-01	53.72
900	2.66E-03	4.79E-01	65.20

In Figure III.1 it is shown the FWHM of anatase and rutile main peaks in XRD patterns of M7. The FWHM of the brookite main peak in M7-600 was not possible to measure due to the low height of this peak. The changes of crystallites size with the increment of the calcination temperature of anatase and rutile phase are summarized in Table III.10 and Table III.11 respectively.

Comparing Table III.3-4 and Table III.10-11, is possible to see that the size of the crystallites in M7 is smaller than in M5, in both anatase and rutile. At 600 ºC only the size of the anatase crystallites is the same in M5 and M7.

The growth ratio in rutile is low, as in all the other cases. Nevertheless, for anatase, which had a high growth ratio in the last two materials, in M7 is comparable to rutile. While the anatase crystallites grows a 70 % in M5 when the calcination temperature passes from 600 ºC to 700 ºC, this increment is only a 10 % for M7.

The weighting average of the crystallite sizes, performed as in the previous cases is shown in Table III.12. The value of the crystallites does not increase with the temperature as much as in other materials. So, we can conclude that the slower calcination ramp contributes to hinder the crystallite growth. This can also explain the lower dimensions of the crystallites in this case compared to material M5. Nevertheless, since the crystallite sizes in this material are higher than in M6, the ramp influence on this parameter is not so important than the effect of niobium inclusion.

Table III.12 *Weighting average crystallite size of M7 in function of the calcination temperature*

Temperature (ºC)	Average crystallite size (nm)
600	42.76
700	52.36
800	53.72
900	65.20

The XRD patterns of material M8 calcined at different temperatures are shown in Figure III.11. The results of the quantitative analysis of these patterns are represented in the Figure III.12. The phase evolution of material M8 when calcination temperature is increased is comparable to that of M6. The addition of Niobium ions to Titania lattice induces a retard in the phase transition. Nevertheless, the retard of phase transition is higher than in M6. This effect is more evident in M8-800, where anatase content is 26 %, while in M6-800 was only the half, 12%. Brookite phase is also more abundant in M8 than in M6 at the temperatures where this phase is presented. As it happened with material M7, the slower temperature ramp used in the calcination process also contributes to the inhibition of phase transition, causing and additional retard.

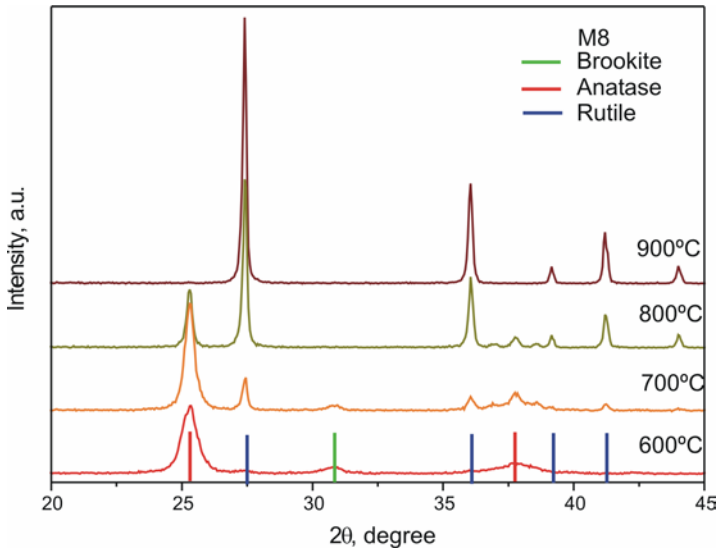

Figure III.11 *XRD patterns of material M8 calcined at different temperatures*

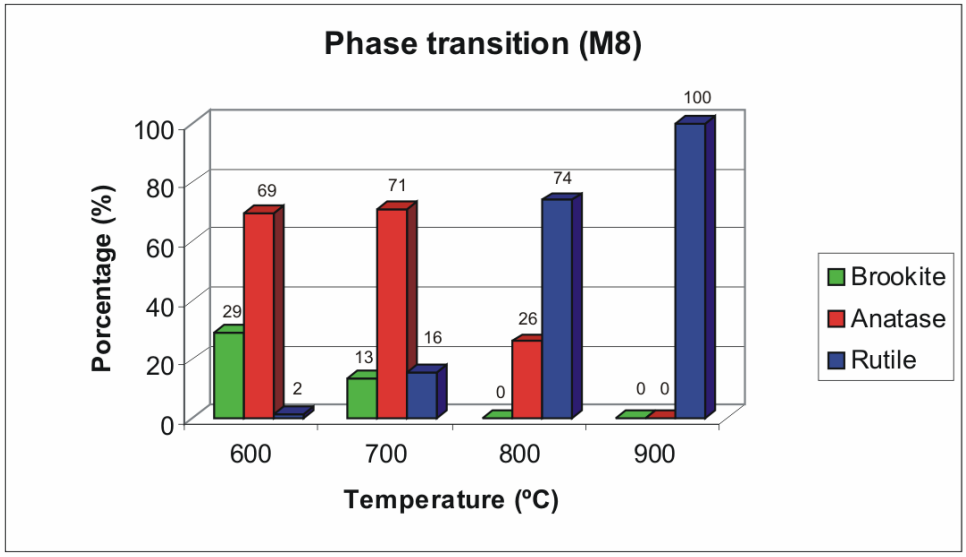

Figure III.12 *Representation of the quantitative analysis of XRD pattern of material M8*

In Figure III.13 it is shown the FWHM of all the main peaks in XRD patterns for M8. The changes of crystallite size with the increment of the calcination temperature of brookite, anatase and rutile phase are summarized in Table III.13, Table III.14 and Table III.15 respectively.

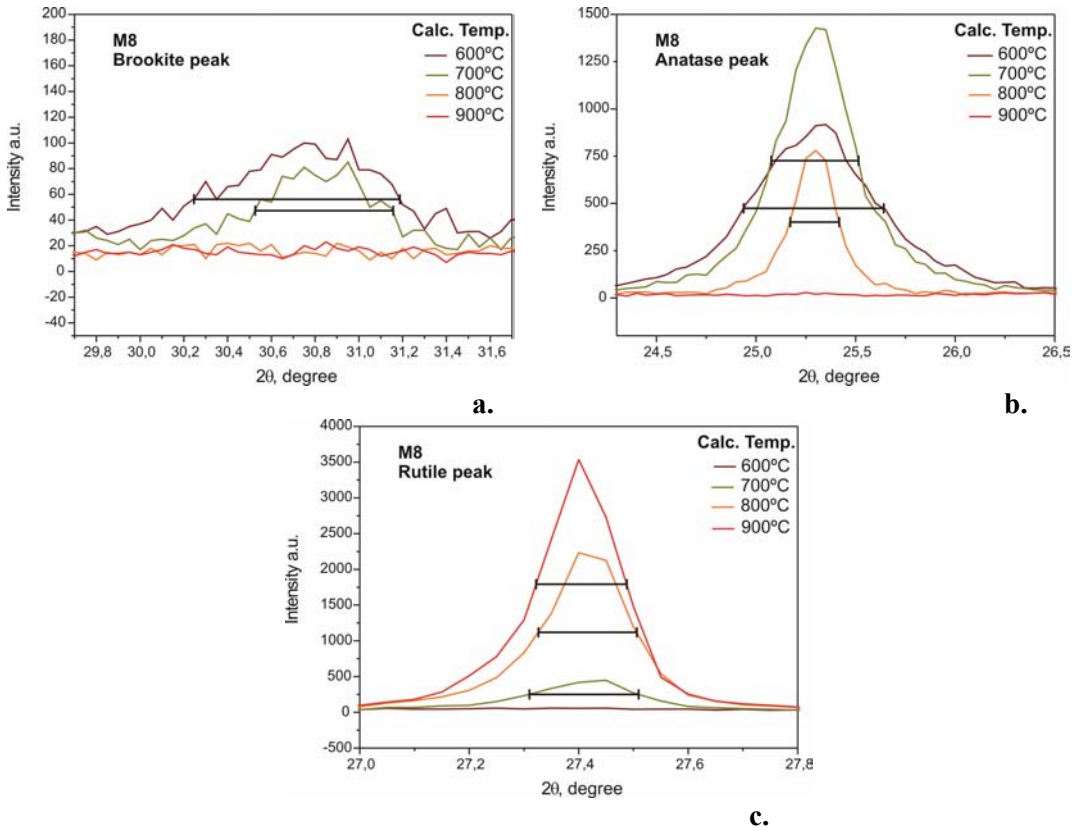

Figure III.13 *Measurement of the FWHM in* ***a.*** *main brookite peak,* ***b.*** *main anatase peak and* ***c.*** *main rutile peak, in M8*

Table III.13 *Size of brookite crystallites in M8 and the values employed for its calculation*

Temperature (ºC)	FWHM (rad)	θ (rad)	Crystallite size (nm)
600	1.63E-02	5.38E-01	10.97
700	1.10E-02	5.38E-01	16.36

Table III.14 *Size of anatase crystallites in M8 and the values employed for its calculation*

Temperature (ºC)	FWHM (rad)	θ (rad)	Crystallite size (nm)
600	1.23E-02	4.42E-01	13.88
700	7.65E-03	4.42E-01	22.26
800	4.29E-03	4.42E-01	39.72

Table III.15 *Size of rutile crystallites in M8 and the values employed for its calculation*

Temperature (ºC)	FWHM (rad)	θ (rad)	Crystallite size (nm)
700	3.48E-03	4.79E-01	49.88
800	3.14E-03	4.78E-01	55.27
900	2.89E-03	4.78E-01	59.94

The crystallite sizes growth in material M8 has the same behavior with the firing temperature than in material M6. Brookite has the smallest crystalline size, followed by anatase and rutile. On the other hand, anatase phase has the fastest growth ratio, followed by brookite and rutile. All this means that the temperature ramp does not have any effect in the crystallite growth in doped materials. In these two materials, M6 and M8, the growth mechanism depends more on the Niobium ions present in the lattice that on the calcination temperature ramp.

It was made a weighting average of the crystallite size of each material using the values of crystallite sizes of the phases, shown in Table III.13, Table III.14 and Table III.15, and the quantity of each phase present in the materials. The result of this average is shown in Table III.16.

Table III.16 *Weighting average crystallite size of M8 in function of the calcination temperature*

Calcination Temp. (ºC)	Average crystallite size (nm)
600	13.01
700	25.91
800	51.23
900	59.94

At lower temperatures (600 ºC and 700 ºC), the higher content of anatase and the portion of brookite keep the crystallite size smaller. The most visible increment in this size occurs only when the rutile phase remains in the material.

III.2.3. Area BET

Gas adsorption on solid surfaces and in pore spaces is a complex phenomenon involving mass and energy interaction and phase changes. The analysis is based on BET theory. The fundamental assumption is that the forces active in the condensation of gases also are responsible for the binding energy in multi-molecular adsorption. By equating the rate of condensation of gas molecules onto an already adsorbed layer to the rate of evaporation from that layer and summing for an infinite number of layers, a plot of $P/[V_a(P_o-P)]$ vs. P/P_o should yield a straight line with intercept $1/V_mC$ and slope $(C-1)/V_mC$, where C is a constant, P_o the gas saturation pressure, V_a is the volume of gas adsorbate at pressure P and V_m and C may be obtained from a regression line through the points. The volume of the monolayer having been determined allows the surface area of the sample to be determined using the area occupied by a single adsorbed molecule [22].

From surface BET it can be obtained an equivalent value of crystallite size. This value could be calculated from the following equation[8]:

$$d = \frac{6 \times 10^3}{S_{BET} \times \rho} \qquad \textbf{(III.4)}$$

ρ = average titanium oxide density (4.9 g/cm^3)
d = crystallite diameter (nm)

When a gas comes into contact with a solid surface, molecules of the gas will adsorb (stick) on the surface in quantities that are a function of their partial pressure in the bulk. The measurement of the amount of gas adsorbed over a range of partial pressures at a single temperature result in a graph, known as an adsorption isotherm. Many different types of isotherms have been observed in the literature [23, 24]; these isotherms can have very different shapes, depending on the type of adsorbent, the type of adsorbate, and intermolecular interactions between the gas and the surface.

The first systematic attempt to interpret adsorption isotherms for gas-solid equilibrium was introduced by Brunauer, Deming, Deming and Teller [25] (BDDT) in 1940. These authors classified isotherms into five types. The BDDT classification has become the

core of the modern International Union of Pure and Applied Chemistry (IUPAC) classification of adsorption isotherms [26, 27]; these BDDT isotherms and an additional one introduced much later by Somasundaran [28], which completes the IUPAC classification, are illustrated in Figure III.14. Type I isotherms characterize microporous adsorbents. Types II and III describe adsorption on non-porous and macroporous solids with strong and weak adsorbate-adsorbent interactions, respectively. Type IV isotherm is typical of mesoporous materials. Type V isotherm, as type III is typical in weak adsorbate-adsorbent interactions, but with the difference that in the final section it is not asymptotic. Finally, the isotherm type VI, is not so much common. This type of adsorption occurs in steps only for materials with a non-porous and uniform surface.

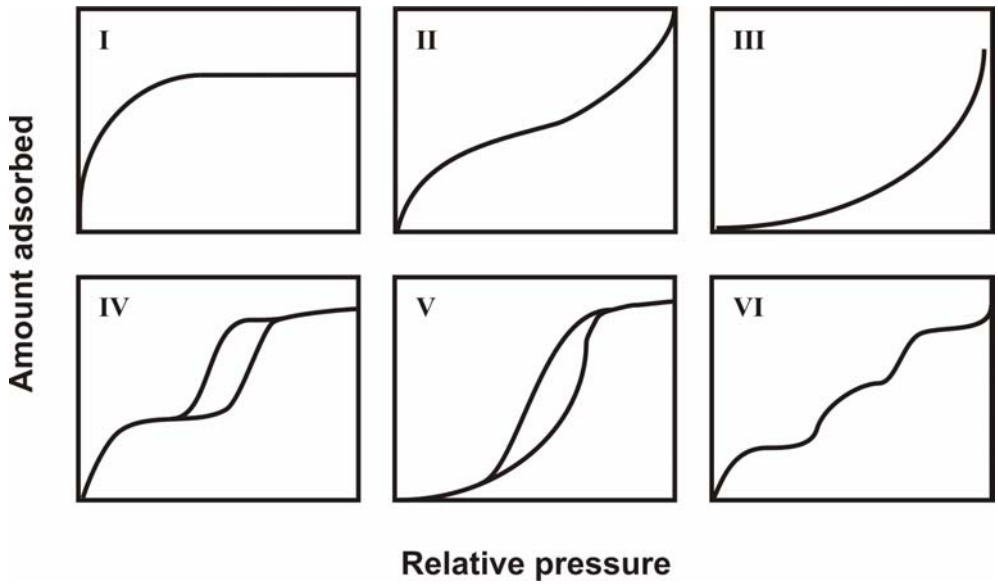

Figure III.14 *The IUPAC classification for adsorption isotherms*

In the case of adsorption where capillary condensation occurs, hysteresis loops appear. The different forms of hysteresis cycles may give an idea about the form of the pores. The IUPAC classify these cycles in four types, associated with the porous structure of the material [27]. This classification is shown in Figure III.15. The type H1 is associated with compact agglomerations of spheres, approximately uniforms, directed in regular way, with narrow distribution of pore sizes. The H2 type is attributed to the effect of the interconnection in the pores net. The H3 type is associated with aggregates of particles with

sheet shape that give rise to pores with form of crack. The same happens with the type H4, but in this case, the type I character of the isotherm indicates the existence of microporosity. In all cases, it may appear a hysteresis at lower pressure that is attributed to the retention of molecules in very narrow pores or to chemisorptions.

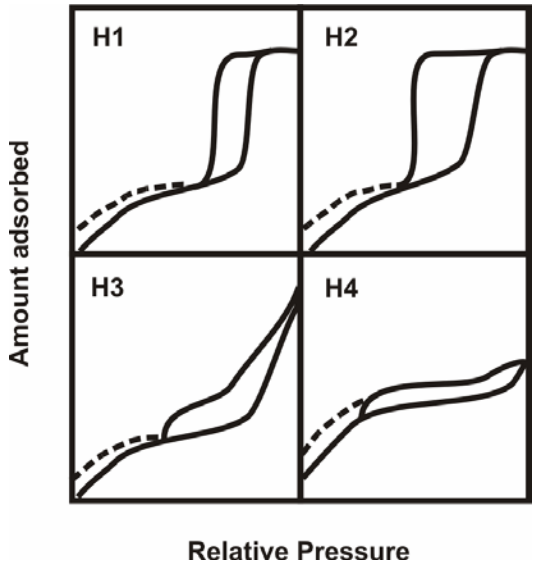

Figure III.15 *The four classifications of adsorption isotherms with hysteresis loops*

III.2.3.1. Experimental Set-up

A Micromeritics ASAP2020 gas sorption analyzer was employed for determining surface area, porosity, pore size and pore distributions of the Titania nanomaterials. These measurements were done in the laboratories of the research group in plant polymers of Universitat Rovira i Virgili. 1 g of each material was used for the analyses. These samples were degasified during 2 hours at 90 ºC and during 6 hours more at 150 ºC. Finally, the adsorption of N_2 at 77K was measured.

III.2.3.2. Results and Discussion

The results from BET analyses are summarized in Table III.17. It can be appreciated that the surface area decreases when calcination temperature increases. This is attributed to both, the growth of the material crystals and the reduction of the porosity. However, there maybe a third reason of this increase in the surface area. Making a comparison between the calculated values of crystallites from XRD measurements (Table III.5, Table III.9, Table III.12 and Table III.16) and the calculated values of crystallites from BET analyses (Table III.18) it is observed that the BET sizes are bigger that XRD sizes. The higher size of crystallites calculated from BET analyses may be an indication of the coalescence of the crystallites, because only the surface of crystallites in contact with the air is measured in this analysis and then a conglomerate of crystallites is measured as one unique crystallite.

The BET area in doped materials is higher than in sheer Titania. This supports the idea that the addition of Nb ions to the Titania lattice hinders the growth of the material crystallites. Also is possible to appreciate that the calcination with the slower ramp helps to avoid the reduction of the surface area which could be due to an inhibition of the crystallite growth or of crystallites coalescence.

Table III.17 *BET surface of the materials*

Calcination Temperature (ºC)	**S_{BET} (m^2/g)**			
	M5	***M6***	***M7***	***M8***
600	6	54	6	56
700	1	18	2	24
800	0.5	8	1	10
900	0.5	1	0.6	3

Table III.18 *Crystallite sizes calculated from BET surfaces*

Calcination Temperature (ºC)	**Crystallite size (nm)**			
	M5	***M6***	***M7***	***M8***
600	204	23	204	22
700	1224	68	612	51
800	2449	153	1224	122
900	2449	1224	2041	408

From the results exposed in Table III.17 and Table III.18, it is concluded that doped materials will have a higher sensitivity toward oxygen than the un-doped ones. This is because doped materials have higher surface area. Moreover, it appears that the lower the calcination temperature, the higher the surface area of the material and else the higher the expected sensitivity. The doped materials calcined at temperatures over 800 ºC, the surface area is even lower than for un-doped materials calcined at low temperatures.

In Figure III.16 it is shown the adsorption and desorption isotherms of N_2 at 77K of all materials. It is observed that the isotherms of pure Titania materials calcined at 600 ºC and in general all Nb-doped Titania are of type IV in the IUPAC classification (Figure III.14). This type of isotherm is typical in mesoporous materials. Isotherms of pure materials calcined at temperatures above 700 ºC and doped material (M6) calcined at 900 ºC, have an isotherm type II which is attributed to non-porous materials. Thus the porosity of materials diminishes when the calcination temperature increases. The addition of Niobium also retards this effect.

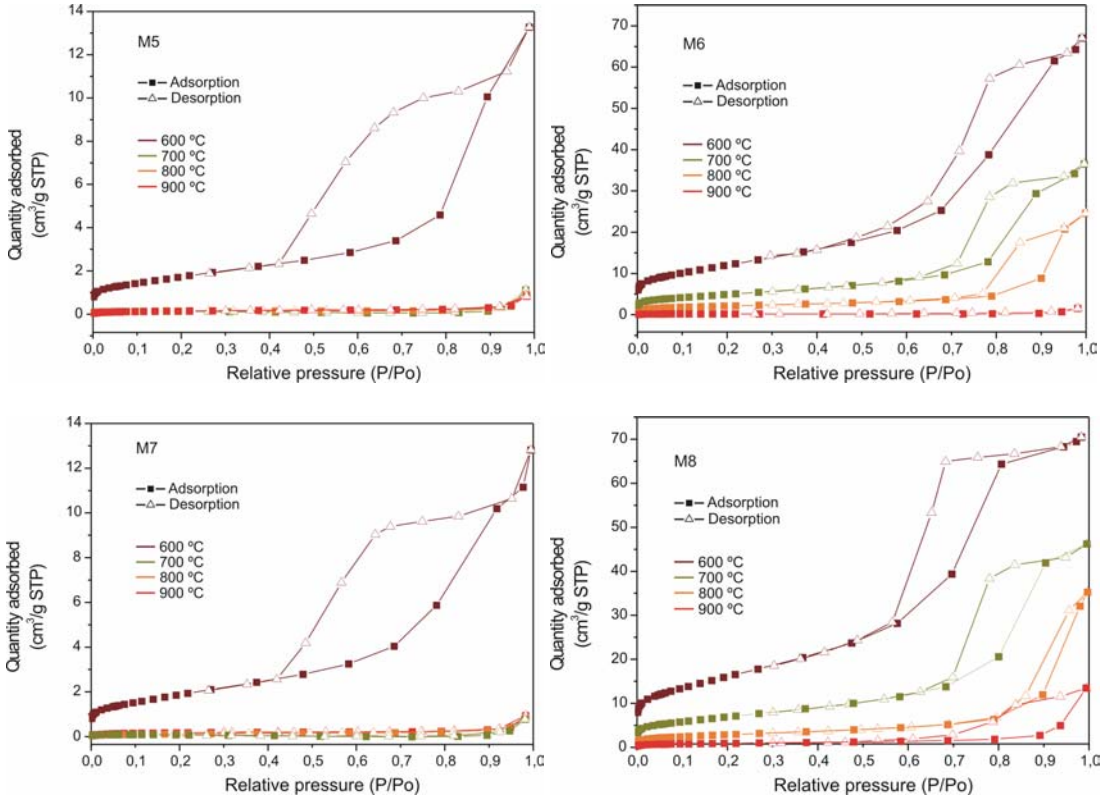

Figure III.16 *Adsorption and desorption isotherms of N_2 at 77K of all materials.*

Taking into account the IUPAC classification of isotherms with hysteresis (Figure III.15), the materials that present this behavior may be classified as type H1. This is associated to materials with narrow distribution of pore sizes.

III.3. Active Layer Analysis

The active material is located on the sensor in the form of layer. Thus, besides the powder characterization, it is also important to characterize the active material layer. SEM microphotographies were taken to know the porosity of the layer and the size of the final grains. Van der Waals forces make that after the drying and calcination of the layers, the grains join forming conglomerations that reduce the active area. It is expected that the active area with smaller grains and higher porosity will have better interaction with the gas and thus, better sensitivity.

EDS analysis was also performed to the layers to support the results obtained from the ICP analysis. In this way, it has been confirmed that the doping concentration of Niobium in Titania is near 3 at%.

III.3.1. Scanning Electron Microscopy (SEM)

Scanning Electron Microscopy (SEM) is the most common technique for layer characterization and is designed to provide image of high spatial resolution, usually using the secondary electron signal. The image displayed on a cathode ray tube (CRT) is created by scanning the focused electron beam in a raster pattern across some area of the sample, while synchronously scanning an analogous pattern on the CRT.

The CRT brightness is modulated on the basis of the intensity of the signal of interest. SEMs typically use accelerating voltages between 5 and 30 kV. The major advantage of this technique is that it does not destroy the sample. However, when the sample is not conductive, it is necessary to cover it with a thin layer of carbon or gold to avoid charging effects [29].

III.3.1.1. Experimental Set-up

The SEM analysis was realized in the Scientific Resources Service at the University Rovira i Virgili, Tarragona, Spain. The technical characteristics of the applied equipment are summarized in Table III.19.

For the analysis, the materials nanopowder were dispersed in glycerol in the same way used to fabricate the sensors (section II.3.2) and deposited over alumina substrates. Then, the layers were dried at 300 ºC for 20 minutes and fired at the corresponding temperature, depending on the material. Those materials whose powder calcination was done at 600 ºC were fired at 600 ºC; while the others were fired at 700 ºC. The samples were then coated with a thin gold layer, which was sputtered to avoid charging effects. Micro-images

were taken using a focal distance of 8 mm, a voltage of 25 kV and a magnification of 50000 x.

Table III.19 *Technical characteristics of the SEM equipment employed*

SEM model	Joel JSM 6400
Resolution	0.3 nm
Magnification	15-300 000 x
Voltage	from 0.5 to 40 kV
Sample rotation	360°
Sample inclination	90°
Back disperse electron detector	Yes

In this study, the change in the grain size could not be observed clearly from the SEM images, because this technique limits the photograph resolution. Because of this, a statistical study of the grain diameters was undertaken. Different computer programs such as Digital Micrograph or ImageJ have the function Analyze particles, which allows to make different types of analysis. One of them is to obtain a grain size histogram. This function is very useful, but not always applicable. We tried to apply it for our images, but there was a problem. Some of the particles were not outlined well. Then, when the program was searching for the grain boundaries, it took several particles as just one. By this means, the program gave us a mean grain size bigger than the real one. To avoid this problem, another method was applied. It consisted in the manual measuring of 100 grains from each image. For these measurements, the corresponding program tool was used. After that, the results were input in another program (Origin) and a statistic analysis was performed. In the tables where the results of this analysis are summarized, *d* is the mean diameter of the grains, SD is the standard deviation ($SD = \sqrt{Var}$, where $Var = \frac{1}{n-1}\sum_{i=1}^{n}(X_i - \bar{X})^2$) and SE is the standard error of the mean ($SE = \frac{SD}{\sqrt{n}}$)

III.3.1.2. Results and Discussion

The SEM pictures of the material M5 (pure Titania calcined employing the temperature ramp of 10 ºC/min) calcined at 600 ºC, 700 ºC, 800 ºC and 900 ºC are shown in

Figure III.17. The evolution of the grain diameter of this material is summarized in Table III.20.

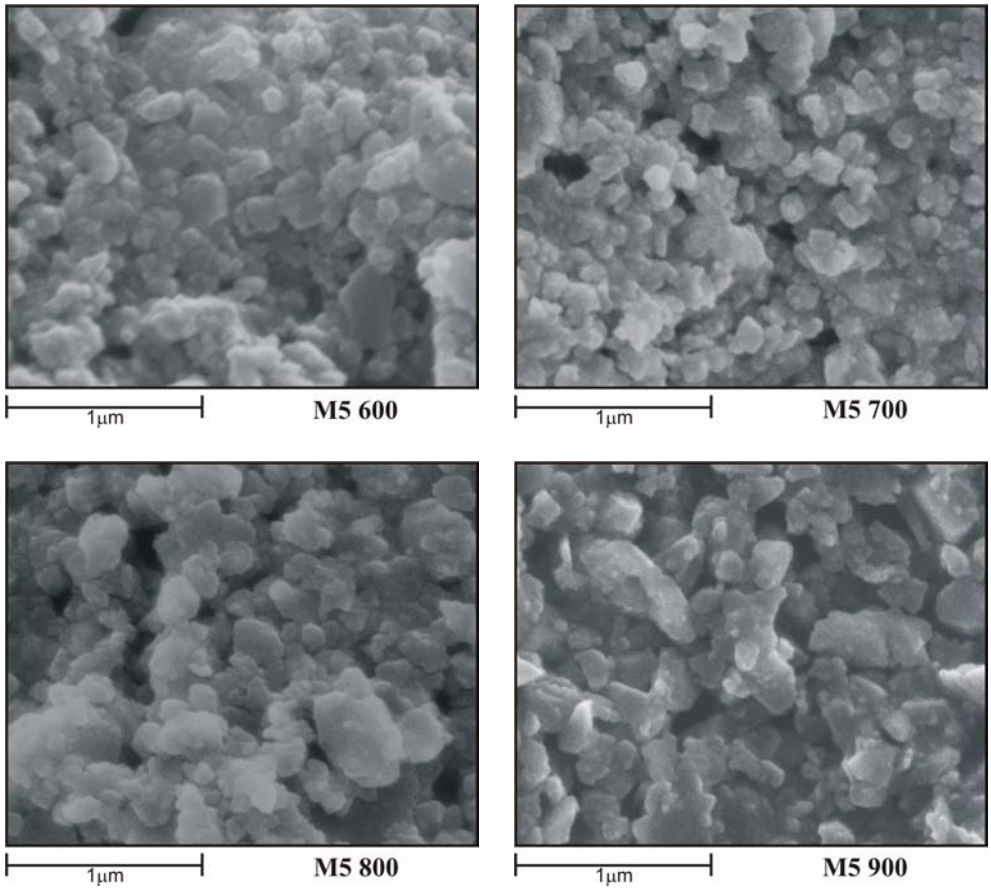

Figure III.17 *SEM images of M5 calcined at different temperatures*

The results obtained are comparable to the obtained for XRD analysis of the powder. According to the histogram of the material M5-600 (Figure III.18), the grains have a mean diameter of approximately 60 nm (Table III.20). This size is high in comparison with other materials calcined at the same temperature, which will be shown later. When calcination temperature is increased, the grain size increases fast until reaching a diameter about 83 nm at 900 ºC.

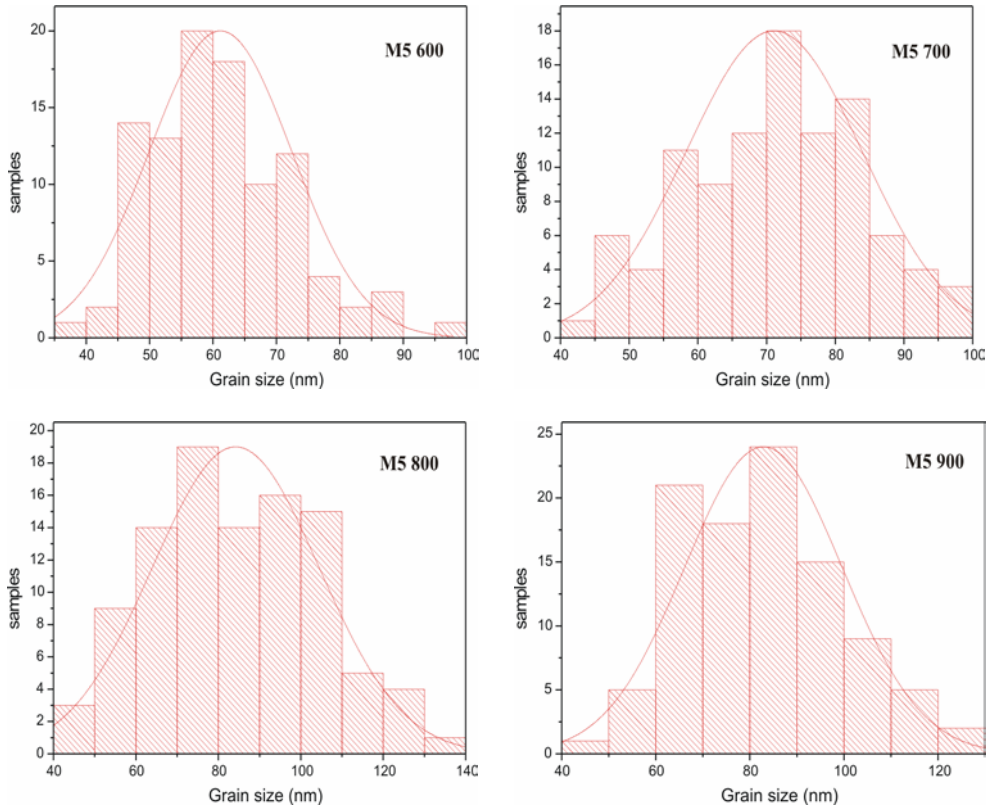

Figure III.18 *Grain size histograms of M5 calcined at different temperature*

Table III.20 *Grain size evolution of the grains belong to material M5*

Material	*d* (nm)	SD	SE
M5-600	61.2	11.2	1.1
M5-700	71.1	12.8	1.3
M5-800	84.2	20.2	2.0
M5-900	82.9	16.7	1.6

The increment in the mean grain size is closely related with the quantity of rutile phase present in the material. The grains formed by anatase crystals are smaller than those formed by rutile crystals. This is because the rutile crystals, on the contrary that anatase crystals, tend to coalesce when crystallinity is improved until reaching a complete

stabilization [11]. The small quantity of anatase phase in material M5-600, observed in XRD results, contribute to retard the grain growth. Nevertheless, when this phase disappear at 700 ºC, the rutile crystals, which are the only presents in the material, start to coalesce faster forming bigger grains.

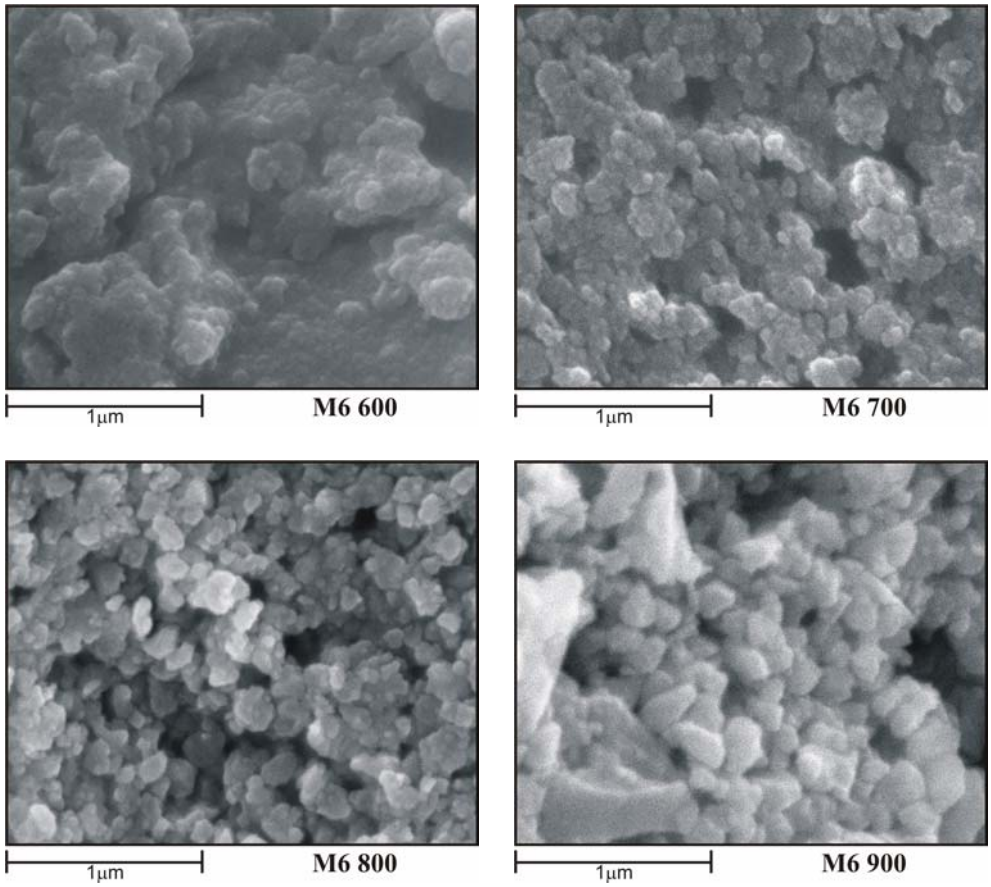

Figure III.19 *SEM images of M6 calcined at different temperatures*

At 900 ºC, the size of the grains is almost the same that at 800 ºC. It appears that the fast grain growth at lower calcination temperatures stops at 800 ºC. The size of M5-900 is even the smallest one among all the materials calcined at the same temperature. This may be attributed to the early stabilization of the material crystallinity. The material M5 does not have any additive that retards the phase transition. Besides, the temperature ramp employed in the calcination process was also the faster one. Thus, the material reaches the crystalline

stabilization quickly. When this state is reached, the crystals stop fusing with others. This fact can explain that over certain calcination temperature, the grains remain at almost the same size, in spite of the increasing calcination temperature.

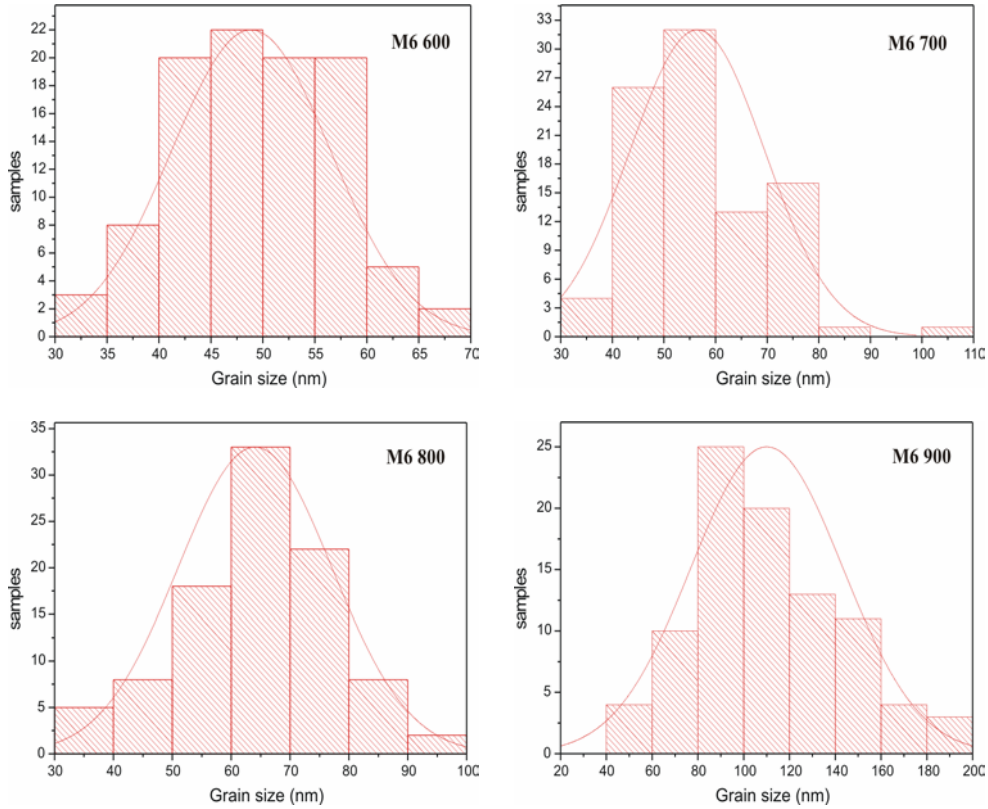

Figure III.20 *Grain size histograms of M6 calcined at different temperatures*

Table III.21 *Grain size evolution of the grains belong to material M6*

Material	*d* (nm)	SD	SE
M6-600	48.9	7.65	0.7
M6-700	56.5	13.00	1.3
M6-800	64.0	13.00	1.3
M6-900	110.1	33.17	3.5

Although the particles in M5-900 are small compared with the other materials calcined at the same temperature, as it was commented, the highly stable crystallinity and content of rutile phase in it, observed in XRD results, make necessary working temperatures over the 700 ºC for gas detection. Since the objective of this thesis is to obtain a oxygen sensor working at low temperatures, this material seems to be not convenient for the development of our sensor.

As it can be appreciated in Figure III.19 and Figure III.20, the grain sizes of material M6 calcined at 600 ºC, 700 ºC and 800 ºC are smaller than those of material M5 calcined at the same temperatures. The material M6-800 is almost the same size than material M5-600. The small grain size supports the fact that the addition of Nb ions to the Titania lattice retards the change of phase and inhibits the grain growth. In this way, the results obtained by others authors are also in good agreement with ours [9, 10].

The inhibition of the phase transition in Titania by the addition of Nb ions was already explained in the XRD section. Making a comparison of SEM results with those obtained with XRD analysis, it is possible to see a relation between the increments of the grain diameter and the content of rutile phase in the material. The higher the quantity of rutile phase, the bigger the grains are. As it was explained before, the reason of this relation is the tendency of rutile crystals to coalesce between them, tendency that does not exist in anatase crystals[11]. Therefore, the grains formed by anatase crystals are usually smaller that those formed by rutile crystals. It is important to remark that there are cases, very common, where anatase crystals and rutile crystals coexist in a same grain. In this cases, the presence of anatase phase retard the growth of the entire grain.

The additional Nb ions in the crystalline structure of Titania play themselves also an important role in the inhibition of grain growth. As it was explained in for XRD results, in the incorporation of Nb in Titania lattice, the niobium ions occupy substitutionally titanium sites, due to the similarity of their ionic radii. Nevertheless, Nb^{5+} radius (0.70 Å) is a bit bigger than Ti^{4+} radius (0.68 Å). The result is that Nb ions induce stress in Titania lattice, which may hinder the growth of anatase and rutile phase crystallites in the material.

In Table III.21 it is also observed that the grain size grows in a linear way from 600 ºC (48.9 nm) to 800 ºC (64 nm) with a rate of approximately 7.5 nm each 100 ºC of increment in the calcination temperature. This linear growth is kept until the calcination temperature reaches 900 ºC. At this temperature, the grain size suffers a dramatic increment becoming the largest one among all the analyses materials calcined at the same temperature. The explanation of this phenomenon is that the Nb^{5+} ions remain inside anatase bulk until the temperature is high enough to give the necessary mobility to the niobium ions to sinter. Thus the Nb aggregates created would be expulsed out from anatase structure and would be finally placed on TiO_2 surface in an oxidized Nb phase. At the same time, once the main part of the Niobium has left the anatase structure, a fast transformation to rutile would happen, since at those high temperatures (800 ºC-900 ºC), the phase transition would be highly favoured [11, 30].

The crystals now free of the stress that comes from the Niobium ions can grow more easily. They also start to coalesce between them when they change to rutile phase. This caused the sudden increase of the grain size at 900 ºC.

Nevertheless, it could be noticed that the increase of the grain size in the material M6-900 is very important compared with M5-900. This could be attributed to sudden coalescence between crystals produced when Titania lattice got free of Niobium. When the Niobium ions were finally expelled out, the crystals start to coalescence faster until they reach a stable crystallinization.

The next material to be analyzed is M7. The SEM images and histograms of this materials calcined at different temperatures are shown in Figure III.21 and Figure III.22 respectively. The evolution of the grain size is summarized in Table III.22.

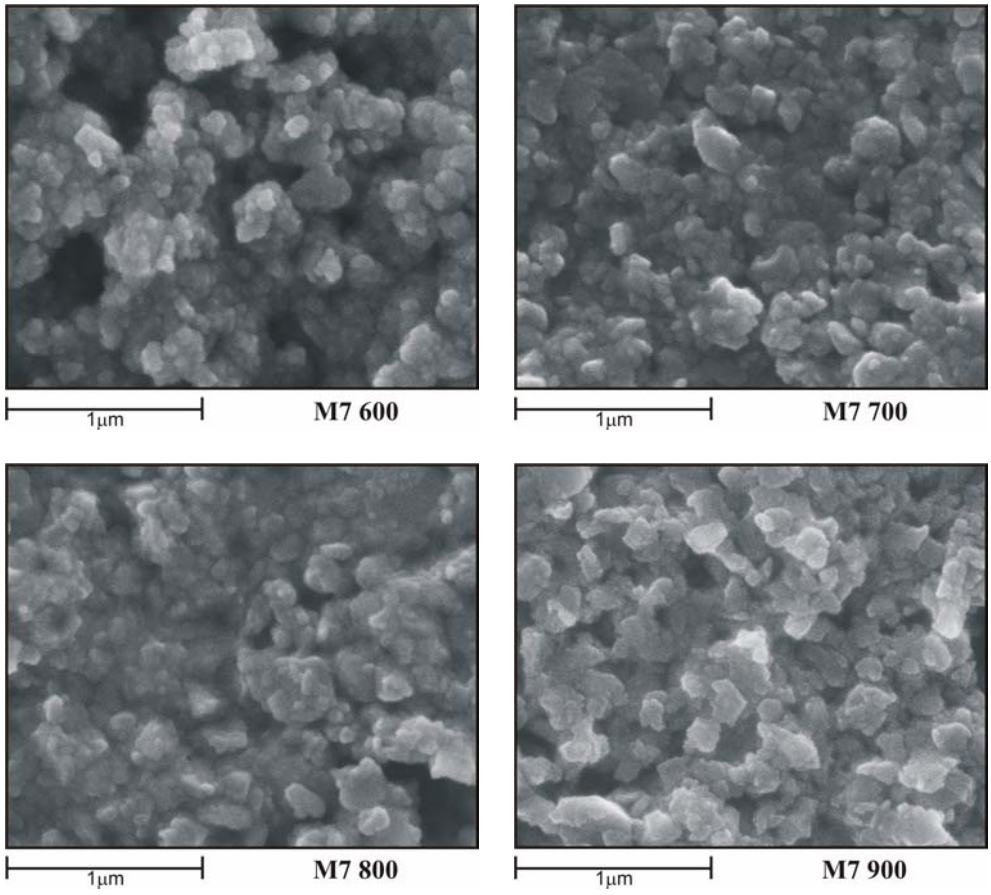

Figure III.21 *SEM images of M7 calcined at different temperatures*

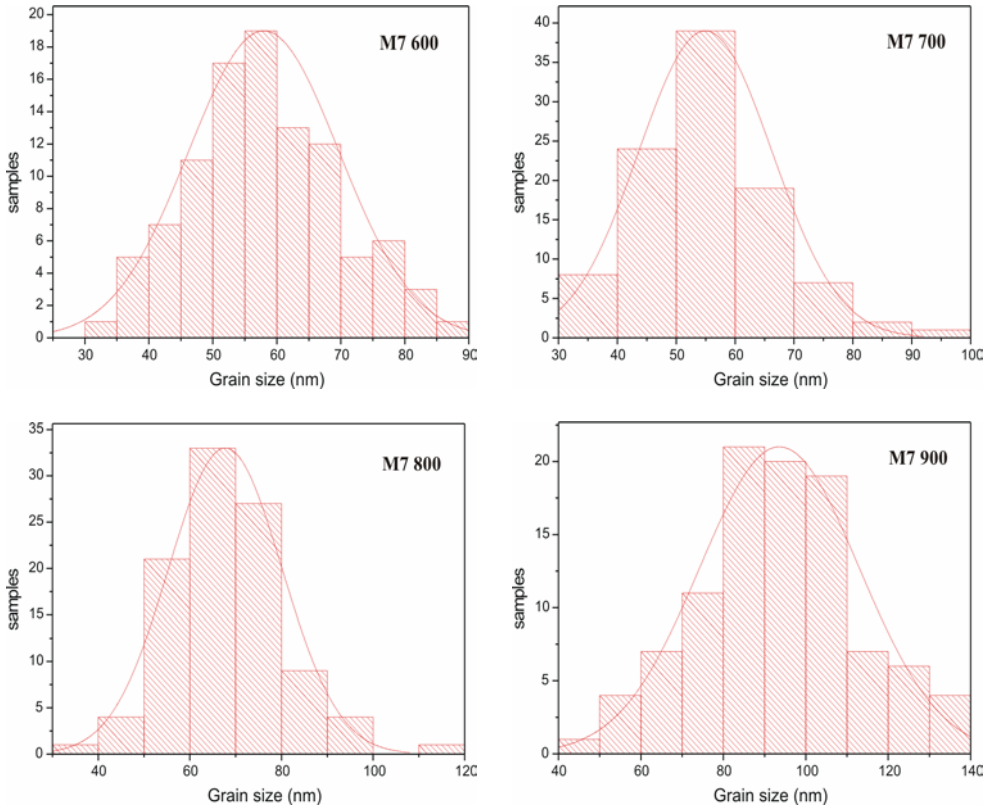

Figure III.22 *Grain size histograms of M7 calcined at different temperatures*

Table III.22 *Grain size evolution of the grains belong to material M7*

Material	*d* (nm)	SD	SE
M7-600	57.9	11.7	1.2
M7-700	54.9	11.3	1.1
M7-800	67.7	12.4	1.2
M7-900	93.6	19.3	1.9

Although this material is not doped with Niobium, it was not observed the fast grain growth that was observed in M5 when it was calcined at low temperatures (600 ºC and 700 ºC). The grain size appears to be almost constant when the material M7 is calcined at those temperatures. Then, when calcination temperature is increased to 800 ºC, the grains grow at the same rate than in M5, 10 nm per 100 ºC. Finally, at 900 ºC there is a high

increase in the grain size, similar to the one observed in material M6 at the same temperature.

XRD results showed that the quantity of rutile phase highly increases from material M7-600 (60.4 %) to material M7-700 (98.8 %). Then, it is supposed that the crystals in rutile phase would grow and coalesce increasing the size of the grains in material M7-700. Nevertheless it does not happen. Instead of this, the grain size appears to remain constant. The grain size evolution in material M7 showed that the coalescence mechanism of rutile crystals might be influenced by the velocity of temperature increment. In this material, the ramp employed to reach the calcination temperature (2.5 ºC/min) is slower than that employed in M5 and M6 (10 ºC/min). Below 700 ºC, the slow temperature ramp prevents the fast crystallinization of the material. Therefore, the change of phase occurs, but the growth and coalesce of the rutile crystals are not produced.

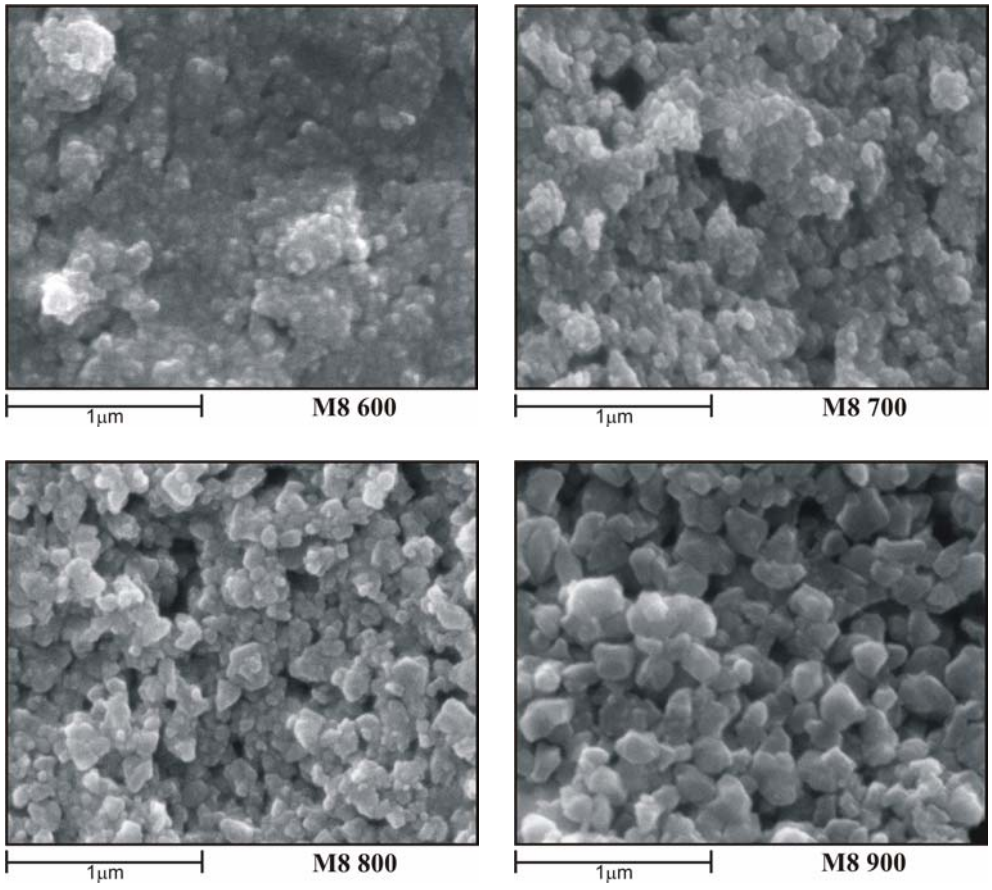

Figure III.23 *SEM images of M8 calcined at different temperatures*

Over 700 ºC, it appears to be an inflection point in the behaviour of the grains in M7. In spite of the slow temperature ramp, the reached temperature provides enough energy to the system to force the fast crystallinization. When this occurs, the crystals grow and coalesce forming bigger grains. This process is observed until the higher calcination temperature is reached, at 900 ºC.

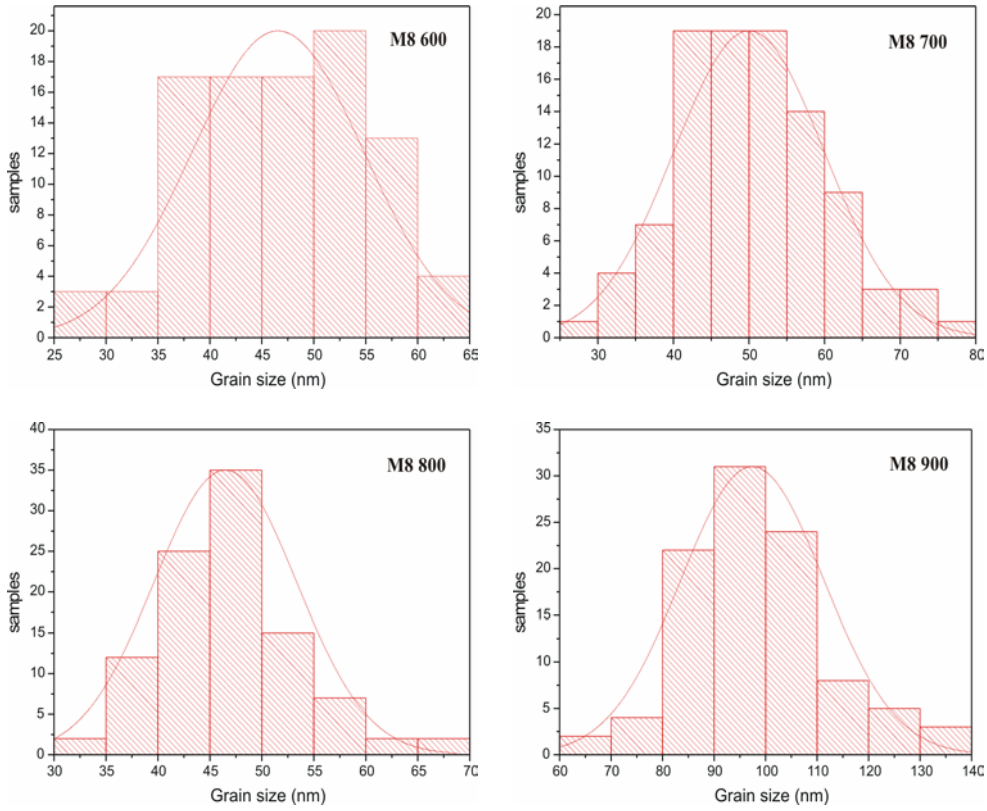

Figure III.24 *Grain size histograms of M8 calcined at different temperatures*

Table III.23 *Grain size evolution of the grains belong to material M8*

Material	*d* (nm)	SD	SE
M8-600	46.5	8.2	0.8
M8-700	50.0	10.0	1.0
M8-800	46.5	6.8	0.7
M8-900	97.4	13.9	1.4

Another material calcined employing the slower temperature ramp is M8. SEM images and histograms of this material are shown in Figure III.23 and Figure III.24 respectively. The grain size evolution is summarized in Table III.23.

The mean diameter of the grains in M8 calcined at 600 ºC is the smallest among all the materials calcined at the same temperature. This size remains almost constant until 800 ºC. When the material M8 is calcined at 900 ºC, the size of the grains experiment a tremendous growth similar to that experimented by the material M6 when it was calcined at the same temperature.

The behaviour of the material M8 at temperatures below 800 ºC could be explained in the same way that of M7. At these temperatures, the slow temperature ramp prevents the fast coalescence between the crystals of the material. Moreover, the niobium ions in the crystalline lattice also contribute to retard the growth of the crystals as it was explained for M6. The contribution of these two phenomenons is the reason of the smallest grain size of the material M8 when it is calcined at temperatures below 800 ºC.

When material M8 is calcined at 900 ºC, all the niobium ions are expelled out from the Titania crystals. At this moment the material experiments the same behaviour of M6 at the same temperature. A fast crystallization of the material is produced. This contributes to the growth and coalescence of the crystals, giving rise to an enlargement of the diameter of the grains.

III.3.2. Energy-Dispersive X-ray Spectroscopy (EDS)

To make a quantitative composition analysis, Energy-Dispersive X-ray Spectroscopy technique (EDS) was applied. This technique allows a rapid evaluation of a specimen, i.e. identification of the elements that are present in a sample. In its simplest form, quantitative analysis proceeds by determining the energies of x-ray emission. At low x-ray energy (less than 3 keV), peak separation and the limited resolution of the EDS spectrometer will likely restrict element identification to only one peak. But at low-energy L or M lines will be accompanied by high-energy K or L lines in the 4-20 keV range, which can aid identification [31]. Below 1 keV, quantitative EDS analysis is difficult.

This technique is not as accurate as ICP for quantitative analysis of elements in a material. However it helped to confirm the results from ICP measurements and also to make a fast evaluation of the elements concentrations in M6 and M8 type materials that were synthesized later and that were not analyzed by ICP.

The equipment employed for the EDS analysis is the same employed for SEM. Therefore, samples were prepared in almost the same way as for SEM analysis. The doped material nanopowder (M6 and M8) calcined at 600 ºC, were dispersed in glycerol and deposited over alumina substrates. Then, the layers were dried at 300 ºC for 20 minutes and fired 600 ºC. For EDS, the samples were then coated with a thin carbon layer, which was sputtered to avoid charging effects.

Taking the spectrum in different points of the sample, we made a quantitative analysis. The results are shown in Table III.24. The spectrum of Co was used as reference. The error is defined as the rate between the Standard Deviation ($SD = \sqrt{Var}$, where $Var = \frac{1}{n-1}\sum_{i=1}^{n}(X_i - \bar{X})^2$) and the mean value $\bar{X}$ of the measurements.

Table III.24 *Results of the quantitative analysis (All results are normalized)*

Sample	At% O	At% Ti	At% Nb	%Total
M6-600[1]	61.05	35.80	3.15	100
M8-600[1]	49.88	47.02	3.10	100

The results from EDS analysis confirm that the atomic ratio Nb/Ti is about 0.03. This means that doping process was successful.

III.4. Sensor Characterization

The sensor capabilities for gas detection were tested. First, all the sensors were tested toward 20 ppm of oxygen in a flux of N_2. With this first measurement, it is intended to establish a relation between the materials and layers characteristics and their sensing properties. This gives an idea about which material is the most proper for oxygen detection.

One important application of an oxygen sensor is the control of the levels of that gas in the carbon dioxide employed for food and beverage processing. In accordance with ISBT (International Society of Beverage Technologists, USA) specifications, the quantity of oxygen in the CO_2 used in such processes must not exceed 30 ppm [32]. Bearing this in mind, the sensor with the best response toward traces of oxygen in nitrogen was also tested toward oxygen and other polluting gases (SO_2, CH_4, H_2S and C_2H_4) using CO_2 as a carrier gas.

III.4.1. Oxygen Sensing Characterization in N_2

III.4.1.1. Experimental Set-up

For the characterization of the sensing properties, the sensor was connected into a test chamber (with a volume of 16 cm^3). In the first stage, pure nitrogen (C-50) was input into the test chamber and the sensor base line was established. A constant flow of 140 ml/min was fixed to avoid interference of pressure in the measurements. Then, a flow with nitrogen and oxygen was mixed with the pure nitrogen flux using mass-flow controllers. The accuracy of each mass-flow meter was +1 % of its full scale. A schema of the measurement system is shown in Figure III.25. The sensors were tested at four different temperatures: 300 ºC, 400 ºC, 500 ºC and 600 ºC. Three repetitions of each measure for each sensor were done. The change in the active layer resistivity was measured employing a Keithley 6517A Electrometer. The sensor response (SR) is defined as follows:

$$SR = \frac{\Delta R}{R_{N_2}} \qquad \textbf{(III.5)}$$

where ΔR is the value of the change in sensor resistance when the oxygen is passed and R_{N_2} is the resistance of the sensor under pure nitrogen. The error among the whole

measurements of the sensors of a same material is also shown and is defined as the rate between the Standard Deviation ($SD = \sqrt{Var}$, where $Var = \frac{1}{n-1}\sum_{i=1}^{n}(X_i - \bar{X})^2$) and the mean value $\bar{X}$ of the measurements.

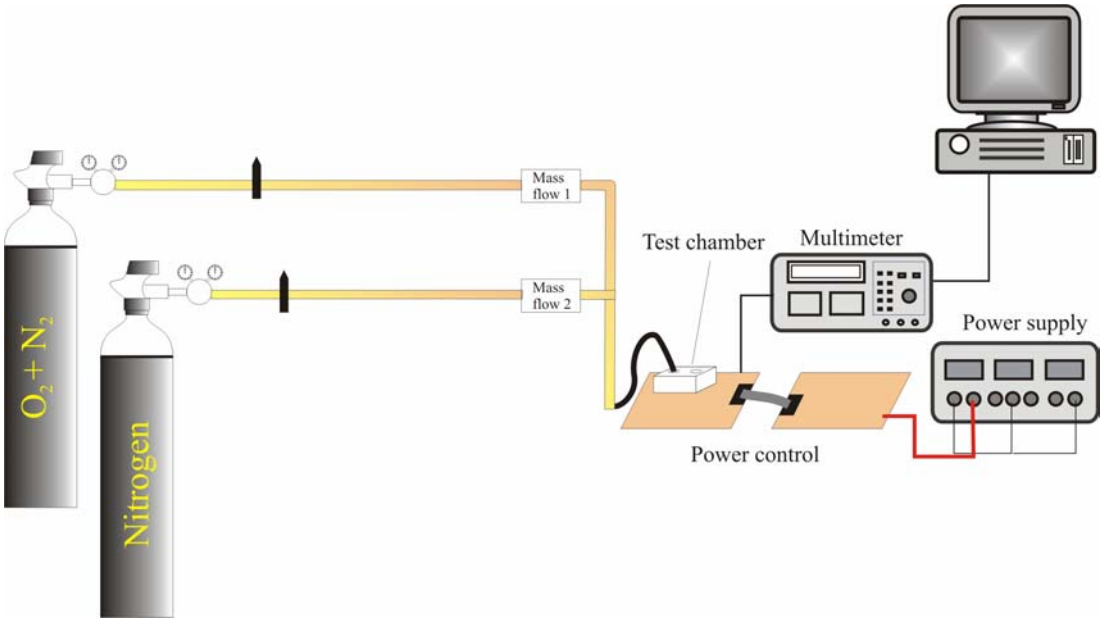

Figure III.25 *Schema of the gas measurement system employed to test the Titania based sensors developed in this work [29]*

In a first step the sensitivity to 20 ppm of oxygen was evaluated. Then, the materials with the highest response were also tested at 15 and10 ppm of oxygen to check their sensitivity at lower oxygen concentration. In those materials it was also checked the response time and the recovery time. As it is possible to see in Figure III.26, when the target gas is introduced, the response time is defined as the time elapsed from the 10 % to the 90 % of the response, measured from the baseline resistance. At the same time, when the target gas is purged, with a flux of pure nitrogen, the recovery time is defined as the time passed from the 90 % to the 10 % of the response value, also measured from the baseline resistance.

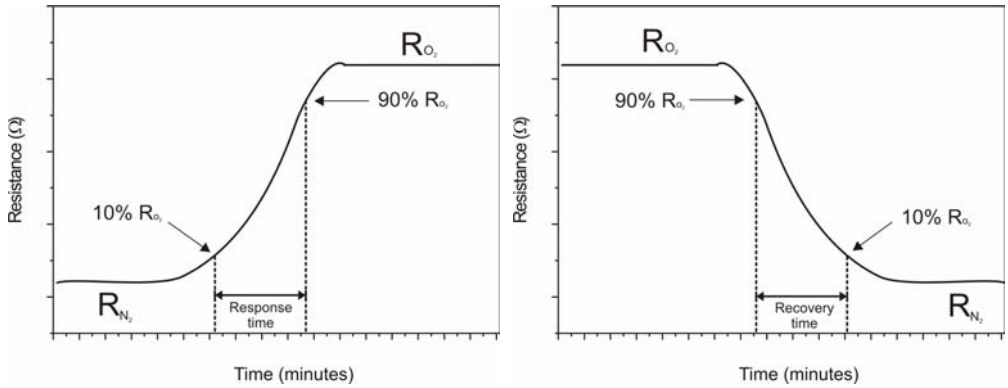

Figure III.26 *Definition of response time and recovery time of a gas sensor response*

III.4.1.2. Results and Discussion

The first tested material was M5. The results are summarized in Table III.25 and represented in Figure III.27. All the responses are quite low, as expected from the previous analysis. M5-700 shows the worse responses, decreasing when the operation temperature is increased. On the other hand, the response seems to improve when increasing the operation temperature for the other cases. This tendency is only broken for M5-800 working at the maximum temperature (600 ºC).

Table III.25 *Responses of sensors made from M5 based materials toward 20 ppm of oxygen working at different temperatures. The carrier gas was pure nitrogen*

	Sensor response ($\Delta R / R_{N_2}$)							
Working temperature (ºC)	**M5 - 600**		**M5 - 700**		**M5 – 800**		**M5 - 900**	
	Resp.	**Error**	**Resp.**	**Error**	**Resp.**	**Error**	**Resp.**	**Error**
300	0.22	3.0%	0.20	4.0%	0.20	2.8%	0.12	5.3%
400	0.23	7.7%	0.18	1.0%	0.24	5.8%	0.19	3.3%
500	0.27	5.0%	0.17	10.0%	0.26	8.2%	0.24	5.6%
600	-	-	0.16	10.0%	0.21	2.1%	0.25	9.2%

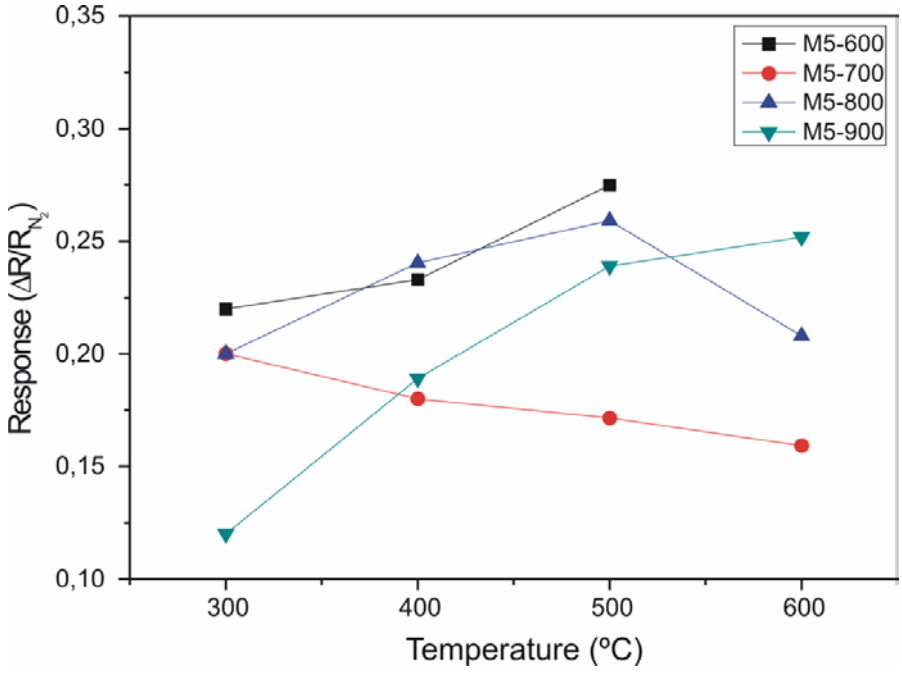

Figure III.27 *Comparison of the responses of sensors made from M5 based materials toward 20 ppm of oxygen, working at different temperatures. The carrier gas employed was pure nitrogen*

Based in the previous characterizations (XRD and SEM), it may be conclude that the low responses in M5 based materials could be attributed to the predominant rutile phase in their crystalline structure and to the grain size, that in M5 was the highest one.

The rutile phase, as it was previously commented, is poorly active at temperatures below 700 ºC. The detection mechanism in rutile Titania based sensors is principally related to the ion vacancies in the material bulk, which needs high temperatures to be formed. The M5 based materials are mostly constituted by rutile phase, in particular those calcined at 700 ºC and over. Then the working temperatures employed in this work are not enough to activate the working mechanism of these sensors.

The high grain size, which is related with the crystalline phase, also hinders the sensitivity of these materials toward oxygen. The active surface is inversely proportional to the grain size, and then when the grains grow there is less surface to interact with the gas. The grains in M5 based materials are, in general, the biggest among all the other materials, therefore, from the point of view of the active area, it is not strange the low sensitivity of the sensors based on this material

According with XRD results, material M5 calcined at 600 ºC (M5-600) has a high quantity of anatase (48.83 %). This anatase phase present in the material should help to the reaction with the oxygen. Nevertheless, the results show that this is not happening. The

crystalline phases (brookite, anatase or rutile) present in the Titania play a very important role in its capabilities to detect oxygen at the temperatures we are using in this project. However, there are others features, as grain size and porosity, which may also influence the detection. In the case of the material M5-600, these other features are not favorable.

The responses of sensors fabricated with M6 based materials toward 20 ppm of oxygen and working at different temperatures are summarized in Table III.26. A comparison of these responses is shown in Figure III.28. It can be seen an improvement of the sensors responses for all materials (with different firing temperatures), compared to M5 based sensors. As it was shown in the XRD and SEM results, the addition of Niobium ions to the Titania lattice modify the physical characteristics of the materials allowing a better interaction with the gas in the detection process. Moreover, these Nb foreign ions also create defects in the material that help the oxygen ions from the gas to be adsorbed [10, 11, 33].

Table III.26 *Responses of sensors made from M6 based materials toward 20 ppm of oxygen working at different temperatures. The carrier gas was pure nitrogen*

	Sensor response ($\Delta R / R_{N_2}$)							
Working temperature (ºC)	**M6 - 600**		**M6 - 700**		**M6 - 800**		**M6 - 900**	
	Resp.	**Error**	**Resp.**	**Error**	**Resp.**	**Error**	**Resp.**	**Error**
300	0.114	7.0%	1.447	2.5%	0.262	8.8%	0.172	9.4%
400	0.185	7.9%	1.817	0.2%	0.826	5.0%	0.704	3.2%
500	0.226	9.5%	1.999	5.2%	0.443	2.6%	0.510	4.2%
600	-	-	1.225	2.7%	0.633	8%	0.633	7.0%

Figure III.28 shows that the best results for M6 material were obtained for a calcination temperature of 700 ºC. The response of material M6 calcined at 700 ºC stands out from the rest.

The response of this sensor increases proportional to the working temperature up to 500 ºC, where the maximum response is obtained. Then, there is an inflection point in the temperature-response curve, obtaining at 600 ºC a value even lower than the value obtained at 300 ºC. This inflection point could be attributed to an improvement in the crystallinization of the anatase crystallites, which diminish the surface defects, affecting the adsorption of oxygen species on the surface. However, the change of phase to rutile does not take place so this crystallinization is reversible. Moreover, 600 ºC is still a low temperature for the detection with rutile phase.

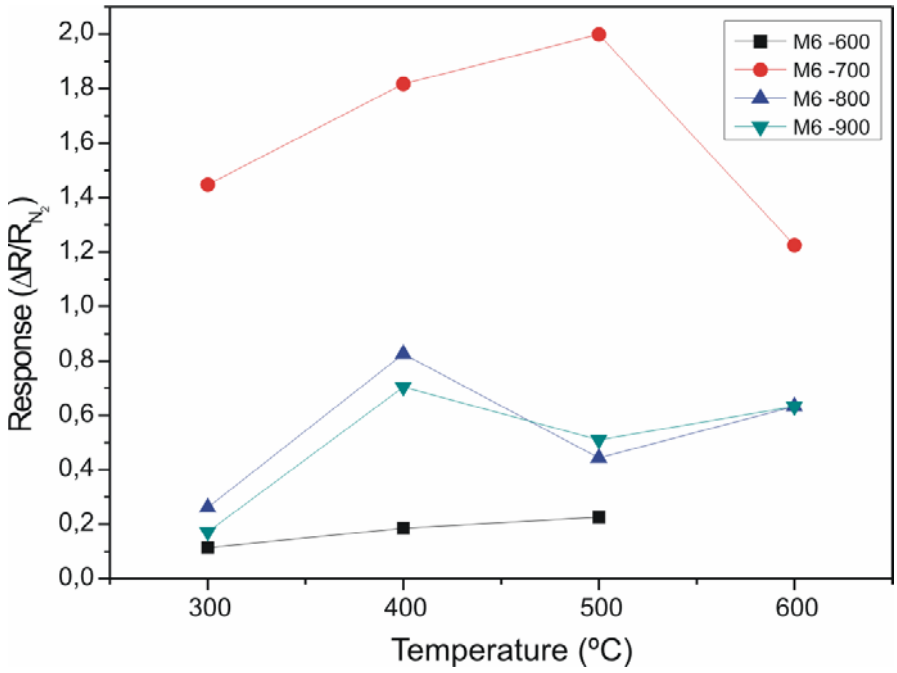

Figure III.28 *Comparison of the responses of sensors made from M6 based materials toward 20 ppm of oxygen, working at different temperatures. The carrier gas employed was pure nitrogen*

The responses obtained for M6-800 and M6-900 are quite similar. Since these two materials are mainly in anatase phase like M5 and the grain size is comparable or even higher than in the case of M5, one could expect response comparables to those obtained for M5 or even worse. But, as can be derived comparing Figure III.27 and Figure III.28, the responses of M6-800 and M6-900 are better than those obtained for M5. So, the Niobium introduced in the case of M6 clearly improves the sensitivity of thisTiO_2 to oxygen.

On the other hand, M6-600 shows the worse results. According to the XRD results, the quantity of anatase phase in M6-600 is even higher than in M6-700. This material has also more surface area than M6-700. Then, it should be expected a higher response of M6-600 based sensor in comparison with that of M6-700. A possible explanation of this low response may be the brookite phase contained in M6-600 (24.74 %). At this temperature, the crystallinity of the brookite particles is improved, with the consequent diminishing of the surface defects, which can affect the adsorption of oxygen species on the surface.

The responses of sensors fabricated for M7 based materials toward 20 ppm of oxygen and working at different temperatures are summarized in Table III.27. A comparison of these responses is shown in Figure III.30. The responses of M7 based material toward 20 ppm of oxygen were low in general and comparable to those obtained for M5, although

slightly better. These results confirm that the lower crystallite size obtained with the slower temperature ramp influences slightly the sensor sensitivity.

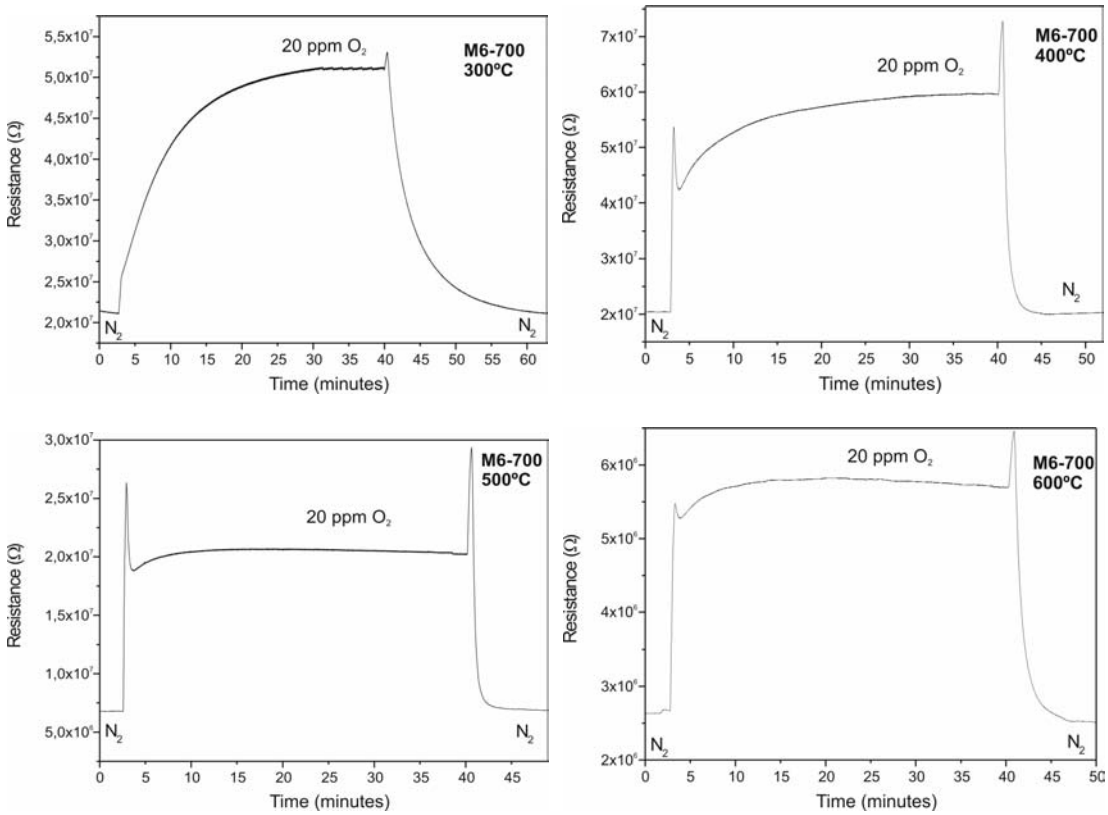

Figure III.29 *Typical responses of the sensor made from M6-700 toward 20 ppm of oxygen, working at different temperatures. The carrier gas employed was pure nitrogen*

In Figure III.30 is it possible to see that the responses of M7 based materials are very similar to the response M5 based materials. As for M5, only the material calcined at 700 ºC decreases the sensitivity when increasing the operation temperature. For the other cases, the sensitivity increases with temperature except for M7-800 working at the maximum temperature. This behavior was also observed for M5.The increase in sensitivity due to the increment of operating temperature is higher in this case. So, the lower dimension of the crystallite size of M7 makes this material more sensitive to changes in the operation temperature.

Table III.27 *Responses of sensors made from M7 based materials toward 20 ppm of oxygen working at different temperatures. The carrier gas was pure nitrogen*

	Sensor response ($\Delta R / R_{N_2}$)							
Working temperature (ºC)	**M7 - 600**		**M7 - 700**		**M7 - 800**		**M7 - 900**	
	Resp.	**Error**	**Resp.**	**Error**	**Resp.**	**Error**	**Resp.**	**Error**
300	0.15	9.6%	0.29	7.7%	0.11	5.3%	0.06	7.1%
400	0.16	8.3%	0.27	9.1%	0.16	6.5%	0.12	4.2%
500	0.26	9.0%	0.23	8.1%	0.24	4.9%	0.29	3.1%
600	-	-	0.22	7.4%	0.11	1.7%	0.30	1.0%

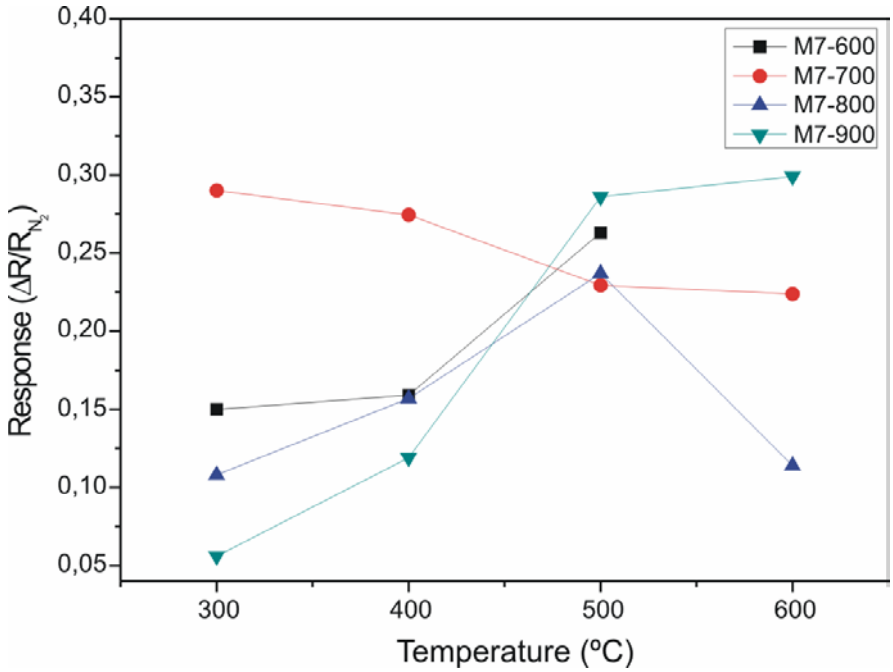

Figure III.30 *Comparison of the responses of sensors made from M7 based materials toward 20 ppm of oxygen, working at different temperatures. The carrier gas employed was pure nitrogen*

The responses of sensors fabricated for M8 based materials toward 20 ppm of oxygen and working at different temperatures are summarized in Table III.28. A comparison of these responses is shown in Figure III.31.

Table III.28 *Responses of sensors made from M8 based materials toward 20 ppm of oxygen working at different temperatures. The carrier gas was pure nitrogen*

	Sensor response ($\Delta R / R_{N_2}$)							
Working temperature (ºC)	**M8 - 600**		**M8 - 700**		**M8 - 800**		**M8 - 900**	
	Resp.	**Error**	**Resp.**	**Error**	**Resp.**	**Error**	**Resp.**	**Error**
300	0.29	10.0%	1.50	0.7%	0.21	6.2%	0.31	9.0%
400	0.25	5.6%	1.51	2.9%	0.22	1.4%	0.28	4.0%
500	0.11	5.0%	1.53	3.9%	0.22	5.1%	0.22	6.7%
600	-	-	0.94	2.2%	0.21	7.3%	0.22	0.5%

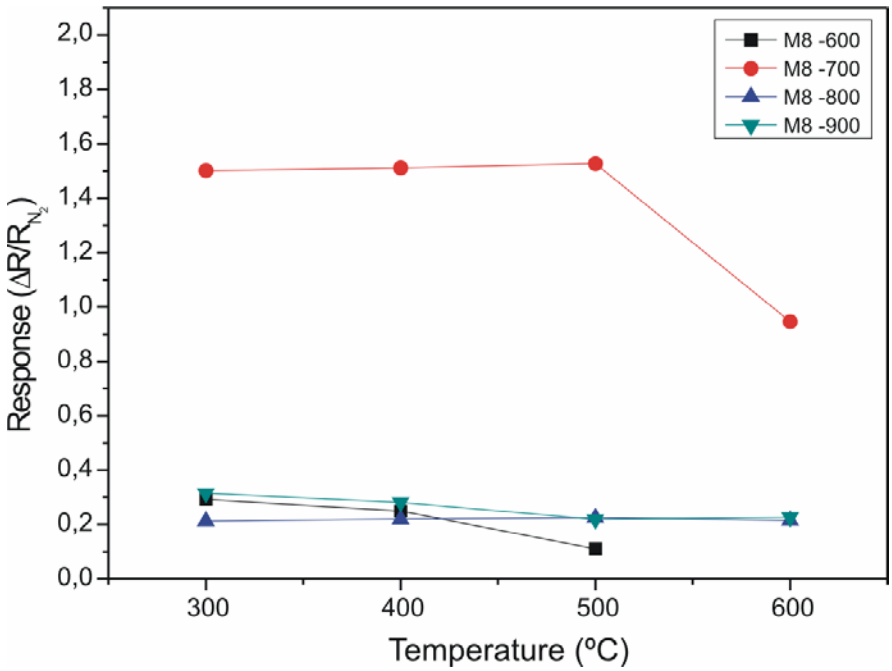

Figure III.31 *Comparison of the responses of sensors made from M8 based materials toward 20 ppm of oxygen, working at different temperatures. The carrier gas employed was pure nitrogen*

Similarities in the response of both materials (M6 and M8) were expected, because of the similarities in their physical characteristics. This is only partially true, because for both materials the best response has been achieved for the material calcined at 700 ºC (although for M8, the response is ~20 % less than in M6) and besides, for the lower operation temperature, responses are similar for materials calcined at the same temperature. Nevertheless, when increasing the operation temperature the responses of M6 has a lager improvement than M8, that shows almost not influence with this parameter- Only the response of M8-700 (the best material) decreases for the highest temperature (600ºC).

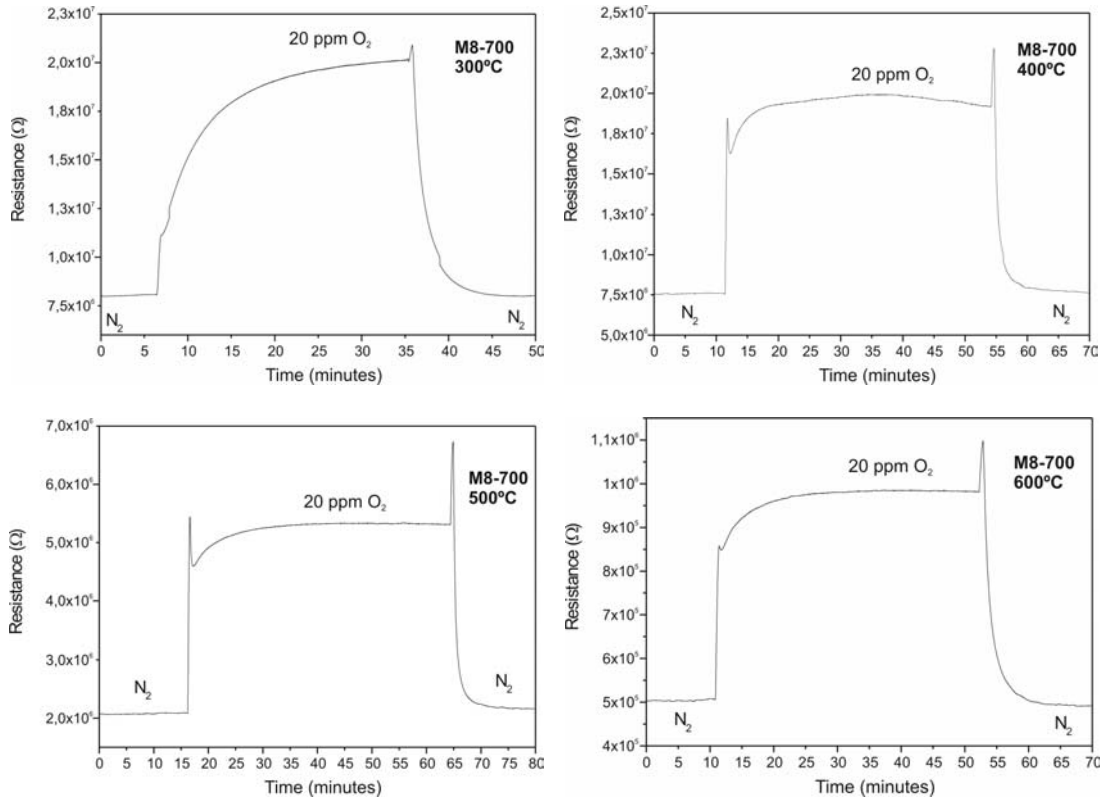

Figure III.32 *Typical responses of the sensor made from M8-700 toward 20 ppm of oxygen, working at different temperatures. The carrier gas employed was pure nitrogen*

The sensors fabricated with materials M6-700 and M8-700, which had the best responses, were also tested to lower concentrations of oxygen. Measurements show that they can differentiate among 10 ppm, 15 ppm and 20 ppm (Figure III.33).

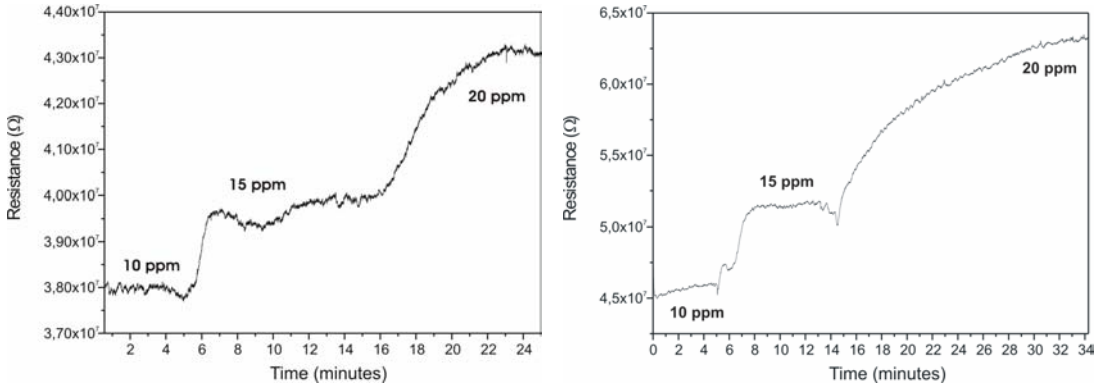

Figure III.33 *Typical response of the sensor made from* ***a.*** *M6-700 and* ***b.*** *M8-700 toward 20 ppm, 15 ppm and 10 ppm of oxygen, working at 500 ºC. The carrier gas employed was pure nitrogen*

The response time and the recovery time of sensors are other important parameters to be analyzed. They are related with the velocity of the reaction between the material and the gas, and also with the diffusion of the gas in the porous layer. These values were measured, averaged and summarized in Table III.29.

Table III.29 *Time response and time recovery of all sensors working at different working temperatures*

	Time response and time recovery (seconds)							
Working temperature (ºC)	**M5 - 600**		**M5 - 700**		**M5 – 800**		**M5 - 900**	
	Resp.	**Rec.**	**Resp.**	**Rec.**	**Resp.**	**Rec,**	**Resp.**	**Rec.**
300	679	1500	760	897	730	986	440	700
400	711	1790	500	600	1060	2100	373	1050
500	789	2568	72	48	810	470	787	2200
600	-	-	150	50	780	1600	975	1940

Table III.29 (Cont.) *Time response and time recovery of all sensors working at different working temperatures*

Working temperature (ºC)	Time response and time recovery (seconds)							
	M6 - 600		M6 - 700		M6 – 800		M6 - 900	
	Resp.	Rec.	Resp.	Rec.	Resp.	Rec,	Resp.	Error
300	520	1000	914	616	1000	2200	970	2340
400	600	490	681	75	750	2507	1018	500
500	690	1100	90	58	632	3050	550	480
600	-	-	111	93	457	2830	913	2490

Working temperature (ºC)	Time response and time recovery (seconds)							
	M7 - 600		M7 - 700		M7 – 800		M7 - 900	
	Resp.	Rec.	Resp.	Rec.	Resp.	Rec,	Resp.	Error
300	750	1100	1017	788	860	500	580	550
400	690	1470	860	750	1300	1400	700	1305
500	870	2510	200	120	900	900	720	1800
600	-	-	447	180	933	825	1000	2320

Working temperature (ºC)	Time response and time recovery (seconds)							
	M8 - 600		M8 - 700		M8 – 800		M8 - 900	
	Resp.	Rec.	Resp.	Rec.	Resp.	Rec,	Resp.	Error
300	510	800	809	210	700	1500	732	2870
400	630	450	400	120	690	2902	790	917
500	674	900	300	117	587	3200	440	1300
600	-	-	225	170	521	2712	690	2230

Since the best responses were obtained with a working temperature of 500 ºC. This temperature was also taken as reference for a comparison of the responses and recovery times among the different sensor. The response and recovery times are represented in Figure III.34 and Figure III.35 respectively.

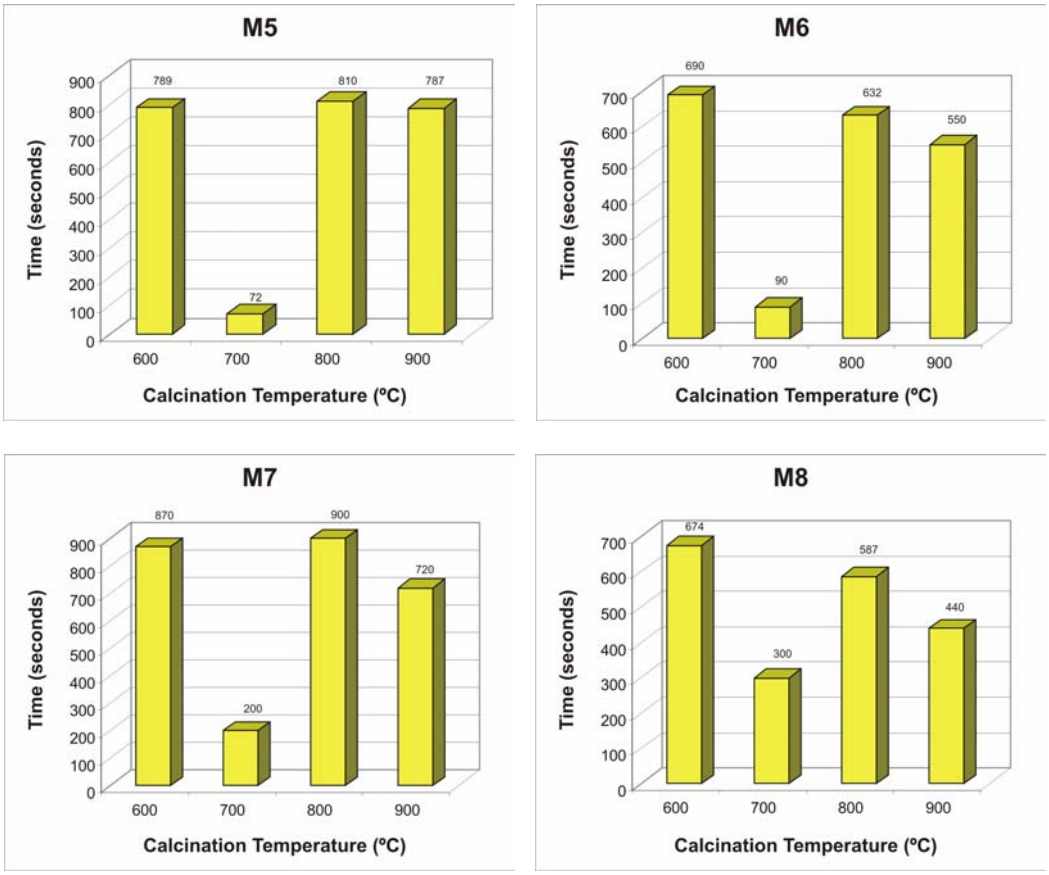

Figure III.34 *Comparison of the response times of all materials working at 500 ºC*

According to Sharma et al [34], the addition of Niobium ions to the Titania lattice reduces the time response of the sensor. However, as it can be appreciated in Figure III.34, in the results obtained in this project there is not a big difference between the pure and doped materials regarding the response time. Then, the addition of Niobium does not have any notorious relevance in the velocity of the diffusion, adsorption and catalytic reaction of the oxygen species on the Titania surface. On the other hand, the calcination temperature has a considerable influence in the response time. For all the materials, those calcined at 700 ºC have the faster response time. It is important to notice that, even though the calcination temperature is strongly related with the crystalline phase of the materials, the differences among the response times of the sensors do not appear to depend on the crystalline phase.

Concerning the recovery time (Figure III.35), the addition of Niobium affects this parameter. As can be seen in Figure III.35, for not doped materials (M5 and M7), the recovery time increases with the calcination temperature, except for those materials calcined

at 600 ºC, which show the slowest response. For doped materials, the recovery time shows a maximum value for materials calcined at 800 ºC. Regarding if the materials are doped or not, the fastest recovery times are for those materials calcined at 700 ºC. All these facts support the idea that the velocity of reactions (catalysis, adsorption and desorption) appears not depend on the crystalline phase and with any other physical property characterized in this work.

A second comparison of the response and recovery time was done between materials with the best responses (M6-700 and M8-700) working at 300 ºC, 400 ºC, 500 ºC and 600ºC.

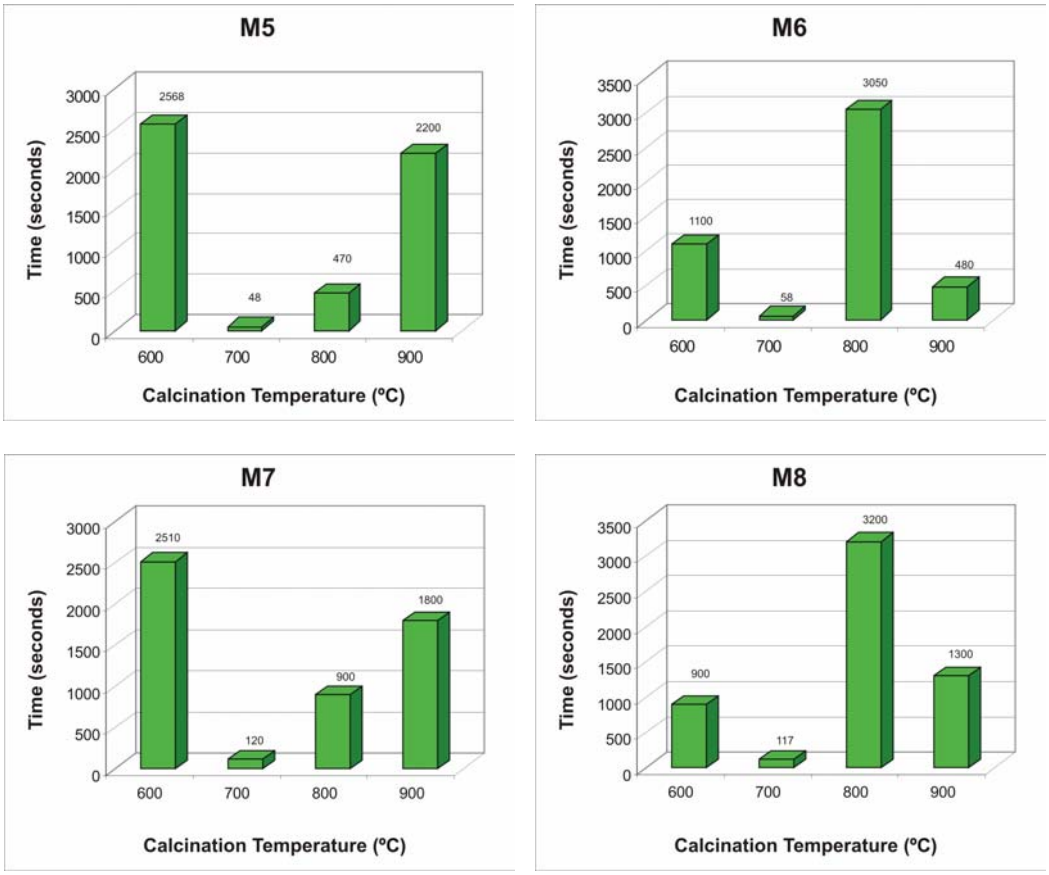

Figure III.35 *Comparison of the recovery times of all materials working at 500 ºC*

The response and recovery curves of M6-700 based sensor had been normalized and putted together in a same graph (Figure III.36). The time values are compared in Figure III.37. It can be observed that at 300 ºC, the response of the sensor is the slowest one. Then, it decreases slightly up to 500 ºC where a sharply decrease occurs.

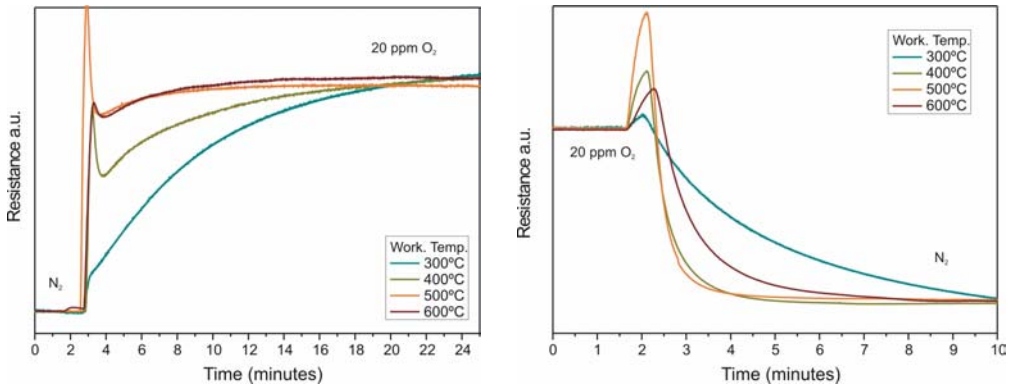

a. **b.**

Figure III.36 *Normalized curves of* ***a.*** *response time and* ***b.*** *recovery time, of M6-700 working at different temperatures. The measured gas was oxygen (20 ppm) and the carrier gas employed was pure nitrogen*

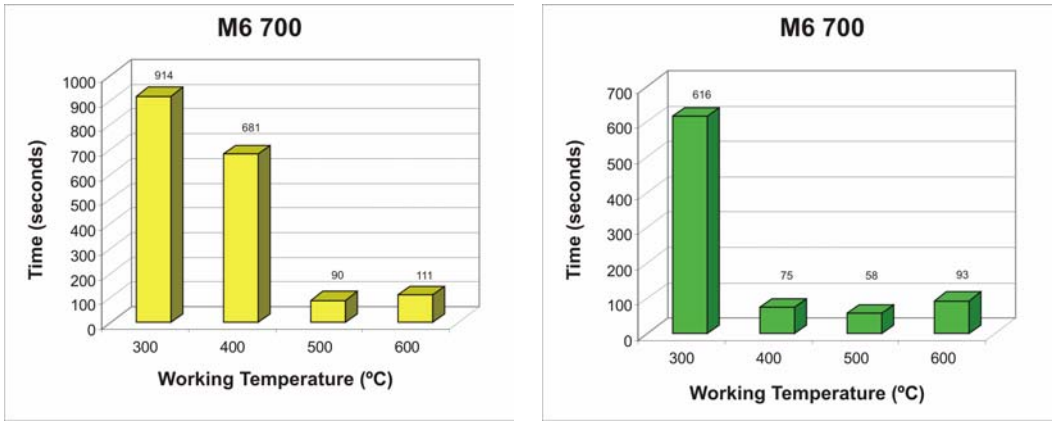

a. **b.**

Figure III.37 *Comparison of* ***a.*** *response time and* ***b.*** *recovery time, of M6-700 working at different temperatures. The measured gas was oxygen (20 ppm) and the carrier gas employed was pure nitrogen*

Concerning to the recovery time, it can be appreciated that the values are smaller than those of the response time. That is, the gas is adsorbed slower than it is desorbed. The slowest recovery time was found at 300 ºC, where the sensor takes 616 seconds to come back to the baseline. Then, there is a drastic reduction in the recovery time of the sensor. At 400 ºC and 500 ºC, the sensor takes 75 and 58 seconds respectively to reach the baseline. So, the recovery time decreases when the operating temperature is increased.

The previous results probably indicate an improvement or an acceleration in the processes involved in the detection mechanism (catalysis, gas diffusion and adsorption-desorption of oxygen species), when the working temperature is increased.

As it was done for M6-700, the response and recovery curves of M8-700 based sensor were normalized and putted together in the same graph (Figure III.38). The time values are compared in Figure III.39. The behaviour is similar to M6-700. At 300 ºC the 90 % of the response is reached up to 809 seconds, which is the lowest response time of this material. The lowest time response of this material was found at 600 ºC, which is 300 seconds.

In the recovery time, it can be appreciated that the values are smaller than those of the response time. It is also appreciable that the values of the time recovery do not vary so much. The lowest recovery time was found at 300 ºC, where the sensor takes 210 seconds to come back to the baseline. At 400 ºC and 500 ºC, the sensor takes 120 and 117 seconds respectively to reach the baseline. At this point (500 ºC) there is an inflection in the values of the recovery time. At 600 ºC the recovery time increases to 170 seconds.

The change in response and recovery times for one temperature to other in M8-700 is more uniform than for M6-700. The time values at temperatures from 500 ºC and above are faster in M6-700. Then, it appears that the detection mechanism at high temperatures is better in material M6-700.

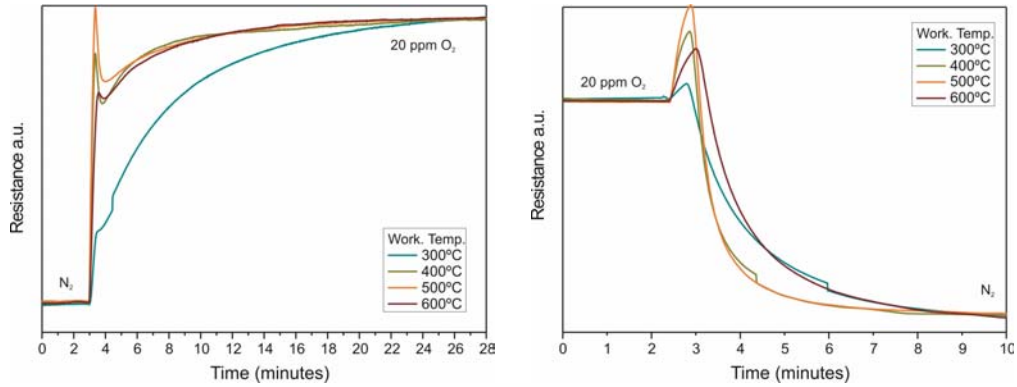

Figure III.38 *Normalized curves of* ***a.*** *time response and* ***b.*** *time of recovery, of M8-700 working at different temperatures. The measured gas was oxygen (20 ppm) and the carrier gas employed was pure nitrogen*

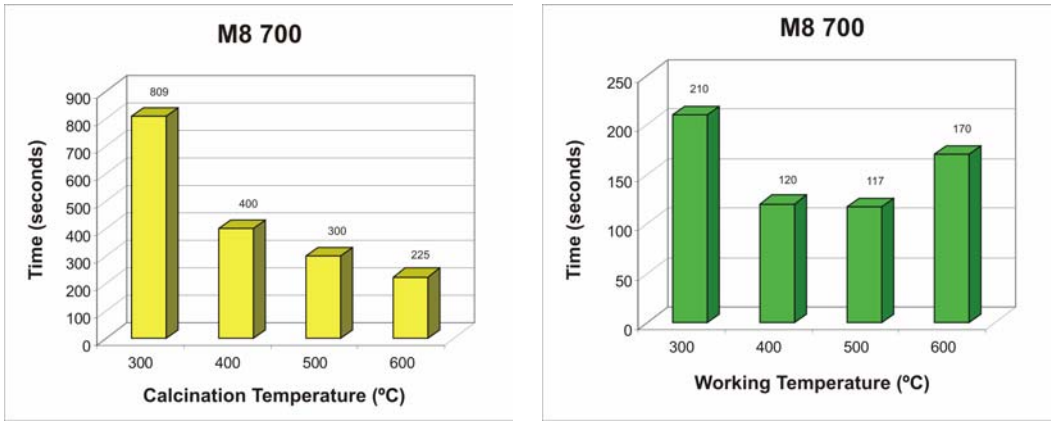

a. **b.**

*Figure III.39 Comparison of **a.** response time and **b.** recovery time, of M8-700 working at different temperatures. The measured gas was oxygen (20 ppm) and the carrier gas employed was pure nitrogen*

III.4.2. Sensing Characterization in CO_2

As it was commented in the Introduction Chapter of this thesis, in some industrial processes in which it is necessary to maintain a low oxygen concentration, the atmosphere is CO_2. In food industry, for example, CO_2 is used to replace air in the package, when the food content is sensitive to N_2. In this application the concentration of O_2 presents in the CO_2 must be between 0.1 % - 2 %, depending on the food. Other application is beverage carbonation, where the limits of O_2 must not exceed 30 ppm. Therefore, it is necessary to characterize the behaviour of the developed sensor under CO_2 atmosphere. This will allow the implementation of such sensors in the applications previously commented. However, oxygen is not the only pollutant gas usually present in CO_2. Other gases as SO_2, CH_4, H_2S and C_2H_4 may also be present. Due the possibility of cross sensitivity between oxygen and those gases, it will be tested the sensor response to typical concentration of SO_2, CH_4, H_2S and C_2H_4, employed in food and beverage industry.

III.4.2.1. Experimental Set-up

Since sensors based on material M6-700 (doped TiO_2 calcined at 700 ºC) working at 500 ºC have shown the best performance in detecting traces of oxygen, they have been tested as possible candidates to detect oxygen in this type of application. As it was commented, the influence of others pollutant gases was also tested. In this case a flow with CO_2 and the

target gas (O_2, SO_2, CH_4, H_2S or C_2H_4) was mixed with the pure CO_2 flux using mass-flow controllers. The measurements were carried out as it is described in III.4.1.1.

III.4.2.2. Results and Discussion

The summary of the results is represented in Figure III.40. It can be appreciated that the response of the sensor toward 30 ppm of oxygen in CO_2 (1.4) is lower than those obtained for 20 ppm of oxygen in nitrogen (2.0). Besides, a change in the behaviour of the sensor occurs for 15 ppm of oxygen in CO_2, where the response of the sensor is in a reducing way, which is unusual in Titania sensors, even when they are doped [14, 35]. The behaviour of the sensor toward other pollutant gases was those expected (negative value that means a reducing response) [36-38]. The response to 100 ppb of H_2S is remarkably high. Besides, high response of the sensors toward SO_2 and CH_4 are observed too. Morris et al. [37] reported a response of -0.39 toward 1000 ppm of SO_2 in air working with a Nb-doped Titania sensor at 550 ºC. In our case, the response toward 1 ppm of SO_2 in CO_2 was almost the same value (-0.37). With the same parameters Morris at al. [37] also reported a response of -0.14 toward 1000 ppm of CH_4 in air, while in our work it was obtained a response of -0.16 to 30 ppm of CH_4 in CO_2. No response was obtained for C_2H_4.

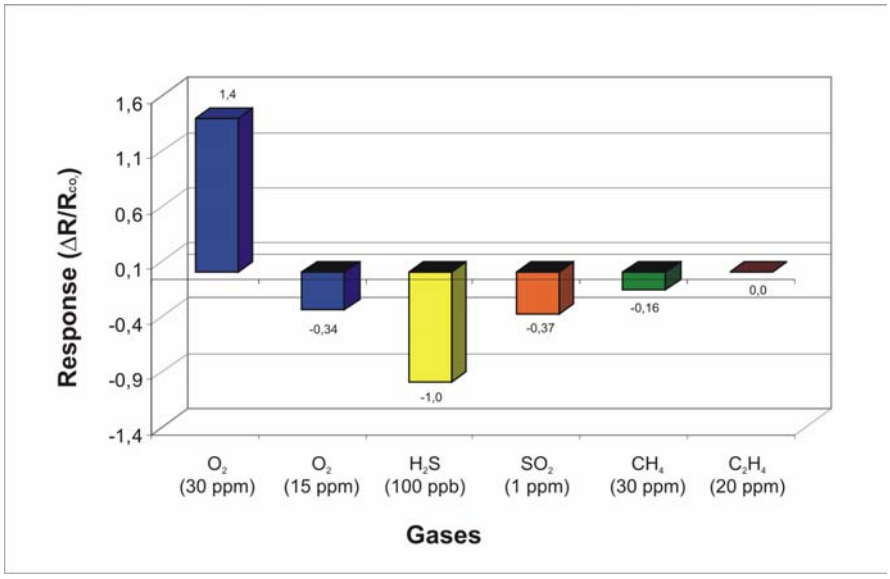

Figure III.40 *Response of the sensor toward different gases at a working temperature of 500 ºC. Positive and negative values means oxidizing and reducing responses respectively.*

The change of sensor response type, from oxidizing to reducing, only occurs when the concentration of oxygen is reduced. Any change in the response behaviour was observed with the others gases. Thus the change of response could not be attributed to a change of physical characteristic of the material from n-type to p-type. A possible explanation of this change in the response when the oxygen concentration is reduced is described as follows. In a first state, most of the oxygen adsorbed on active layer surface is expelled. The evacuating oxygen free electrons back to the bulk, giving rise to a decrease of the active material resistivity. This explanation is consistent with the behaviour of the sensors resistence baseline in air, (~50 MΩ), that is higher than in CO_2 (units of MΩ)

At the same time, it may be supposed that the high temperature and the strongly catalytic property of TiO_2, produces a desegregation of CO_2 molecules on the active layer surface (Figure III.41), producing CO^- and O^- which are adsorbed on the surface. Reaction equation is described as follows:

$$2e^- + CO_2 \rightarrow CO^-_* + O^-_* \qquad \textbf{(III.6)}$$

* means that species are adsorbed on the surface.

In the desegregation reaction electrons are taken from the bulk, which produces an increase in the potential barrier between grains, and hence an increase in the resistivity of the active layer. However this increase in the layer resistance is not perceptible compared with decrease produced by the evacuation of the oxygen.

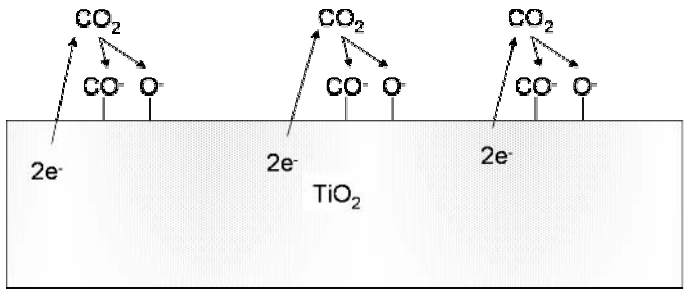

Figure III.41 *Desegregation of CO_2 in CO and O species. Those species are adsorbed on Titania surface*

When the system explained before gets equilibrium and traces of O_2 are introduced, those molecules that reach surface also desegregate, taking electrons from the bulk. But instead remain adsorbed on the surface, these free species join with already CO^- adsorbed and form CO_2, liberating electrons toward the bulk (Figure III.42). The reaction is described in equations (III.7) and (III.8):

$$2e^- + O_2 \rightarrow 2O^- \quad \textbf{(III.7)}$$

$$O^- + CO_*^- \rightarrow CO_2 + 2e^- \quad \textbf{(III.8)}$$

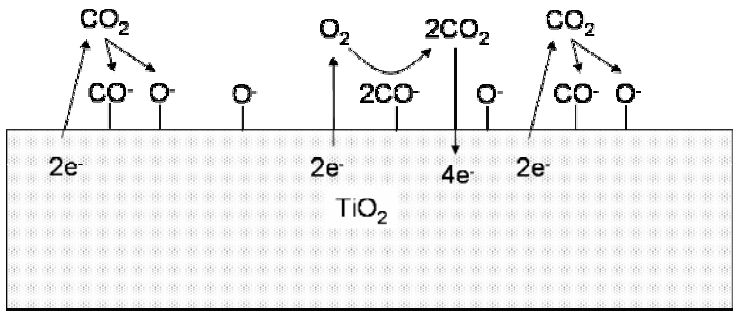

Figure III.42 *Effect of the oxygen traces in the adsorption of CO and O species on Titania surface*

From equation (III.7) and (III.8), it is also possible to see that electrons given back to the bulk are more than those taken from the bulk. So the potential barrier will be reduced and hence the resistivity of the material.

If the concentration of oxygen increase, the equilibrium of process described for equations (III.7) and (III.8) is broke and will tend to equation (III.7). The excess of O^- species that do not join with adsorbed CO^- is adsorbed on the surface. This means that the quantity of electrons taken from bulk will be higher that those given back to there, and then resistivity of active material will increase. This behaviour is the common reaction of a n-type material toward an oxidizing environment.

III.5. Raman Spectroscopy

In a first stage, Raman technique was thought to be used in order to verify the hypothesis exposed in the last subsection, about the change in response behaviour for oxygen detection in CO_2. However, the resolution of the equipment employed in the measurements was not enough to detect CO species adsorbed on the Titania surface. Therefore the hypothesis could not be confirmed. On the other hand, Raman results spread light on the problem of low response toward oxygen of doped materials calcined at 600 ºC.

As it was observed, there was a hinder in the response toward oxygen of materials M6 600 and M8 600, in spite of their crystalline phase and surface area properties make them proper for oxygen detection. This hinder in the response could not be attributed to any of the physical property characterized in this work up to this point. However, the Raman results reveal the presence of some carbonic elements in the material that were not detected with XRD analysis, because they were not crystalline materials. This technique is explained as follows.

Raman spectroscopy is based in the diffusion processes given by the electronic polarization caused by ultraviolet or visible light. Raman gives information at molecular level allowing the vibrational and rotational analysis of chemical species. Briefly, the radiation interacts with the molecular vibrational energy levels due to the light scattering phenomena, in which the electromagnetic radiation interacts with a pulsating polarizable electron cloud.

As a consequence of the diffusion effect, this technique presents several advantages. On one hand, there is no needing of any sample preparation making easier its implementation. Moreover, it provides a non-destructive microanalysis of structures and electronic properties.

As well as XRD, this technique has been widely used for the identification of material structure phase, and moreover for the analysis of phase transition. The principles of this technique are widely reported elsewhere [39, 40].

III.5.1. Experimental Set-up

The measurements were done in the Scientific Resources Service at the University of Barcelona, Spain. For the Raman analyses we used a spectrometer Raman Jobin Yvon T64000. The excitation source was a visible laser Ar^+ coherent INNOVA 300. The microscopy was Olympus BH2 with high spatial resolution. We used a triple monochromator (1800 g/mm) and a bidimensional CCD detector refreshed with liquid nitrogen. The power of the Raman laser was set at 200 W.

To acquire the Raman spectrum of the nanopowders, they were deposited over a glass surface without any kind of sample preparation; the spectrum was obtained by only focusing on the samples. For the in-situ measurements of the material, the layers of sensors were analyzed. Such analyses were carried out under different conditions. First, the layer was analyzed at room temperature. Then, the temperature of the layer was increased to 200 ºC and 500 ºC, and the same measurements were done. All the measurements were carried out in air atmosphere. With this last measurement it is intended to find out any difference between the material in nanopowders and in the layers induced during deposition, drying and firing process; and to find any shift in the peaks of the Titania, which is related with the formation of oxygen vacancies in the material when temperature is increased. This is a very important feature for oxygen detection and its absence means that the material is useless for oxygen sensing.

In this section, the Raman spectres obtained for materials M6-600 and M6-700 will be shown. That way it is intended to find differences between the elements present in both materials: M6-600, which does not have good response toward oxygen, and M6-700, which has the best response toward oxygen. M8-600 and M8-700 will not be presented due the physical and sensing characterizations carried out up to now demonstrate that they have a very similar composition and behaviour to M6-600 and M6-700 respectively.

III.5.2. Results and Discussion

III.5.2.1. M6 600

The Raman spectrum between 18 and 650 cm^{-1} of M6-600 nanopowder is shown in Figure III.43. As it can be seen, a well-defined Raman peak is located at 142 cm^{-1} and three broader features are found at 396, 516 and 639 cm^{-1}. This spectrum clearly corresponds to anatase phase [8, 41]. The small peaks situated at 243, 320 and 363 cm^{-1} indicates the presence of brookite phase, but in lower proportion to anatase. This supports the result obtained by XRD. The results from M6-600 layer are similar to those obtained from the nanopowders, which suggest that there is not any alteration of the material during the process of deposition, drying and firing of the layer.

As it commented for XRD results, the presence of a considerable amount of brookite phase in the material M6-600 could be one of the reasons of the low response of such material toward traces of oxygen. This phase has less free carriers than anatase and its electrochemical behaviour is very alike to rutile's [21]. With the employed calcination temperature (600 ºC), the crystallinity of the brookite particles is improved with the consequent diminishing of the surface defects, which can affect the adsorption of oxygen species on the surface [42]. On the other hand, this calcination temperature is too low to

create enough surface defects in anatase crystals, with the same result in the oxygen adsorption.

Raman spectrums at higher frequencies shed more light on the reasons of the lower response of M6-600. In Figure III.44 it can be appreciated some peaks that correspond to carbon with different morphologies. The peaks and their correspondences are summarized in Table III.30. These deposits of carbon are the residual of the synthesis process that could not be eliminated during the calcination. An example is the peak located at 1039 cm^{-1} in Figure III.44a, which clearly matches with one of the main peaks in the spectrum of ammonium carbonate used for the sol gellification (Figure III.45). The other carbonic compounds could be formed by the cristallinization of the organic part of the precursors.

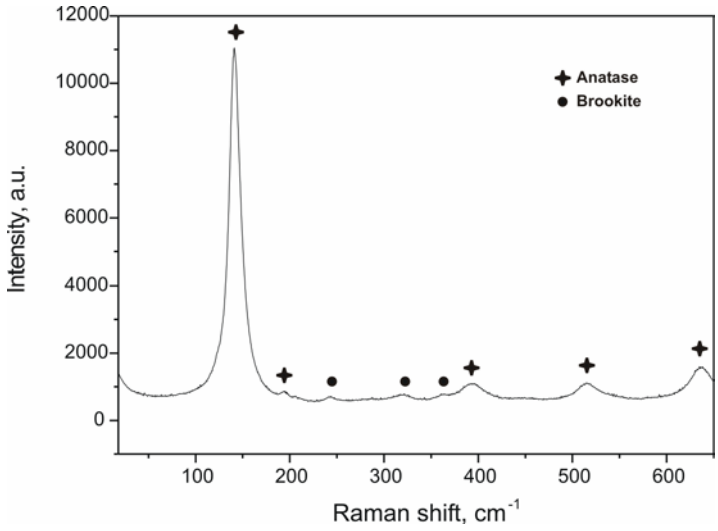

Figure III.43 *Raman spectrum of M6-600 nanopowder at room temperature*

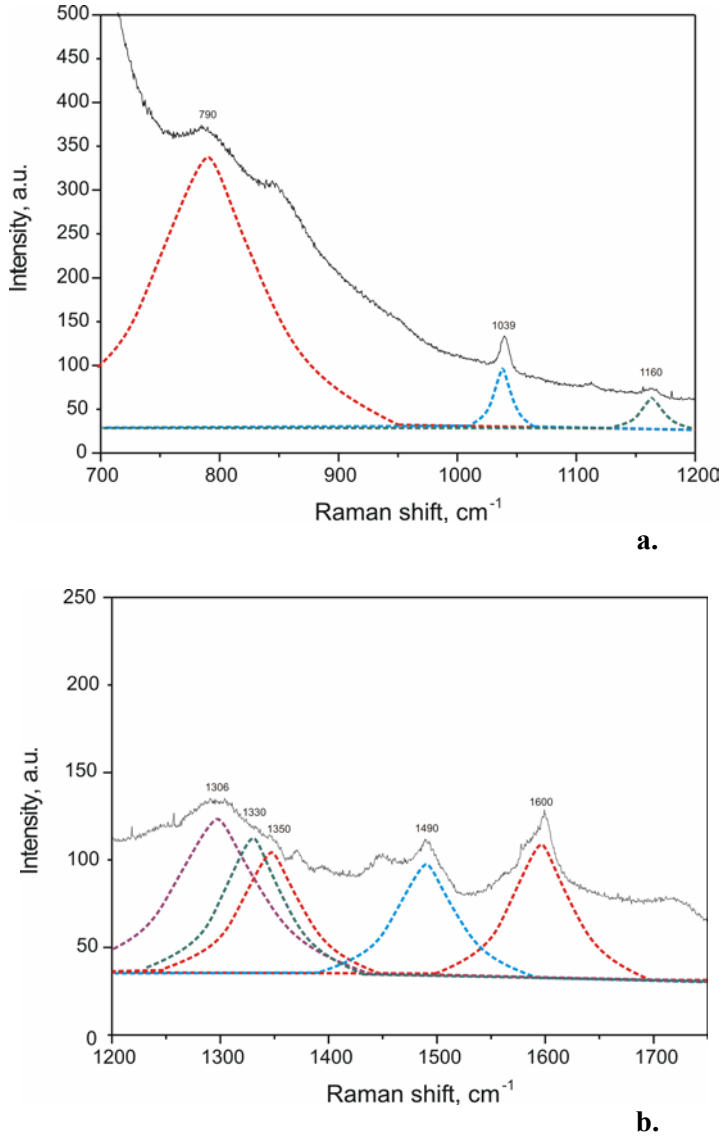

Figure III.44 *Raman spectrum at high frequencies of M6-600 nanopowder at room temperature*

The problem with these deposits of carbon is that they cover the surface of the active material and hinder its interaction with the oxygen. And, because these carbon structures are also poorly catalytic, the result is a deactivation of the catalysis [43-45].

As it was appreciated in previous characterizations, the material M6-600 has the highest area and quantity of anatase phase among all synthesized materials. Nevertheless the considerable quantity of brookite phase and carbonic deposits in it, retard the catalysis and the interchange of electrons and oxygen species with the gas. This is reflected in the low response of this material toward oxygen.

Table III.30 *Some Raman features in the range between 700 and 1750 cm^{-1}, present in the spectrum of M6-600*

Raman peak (cm^{-1})	Possible correspondence
790	Hydrogen free carbon structure [46, 47]
1039	Ammonium Carbonate
1160	Nanosized diamond crystals [48, 49]
1306	Hexagonal diamond [50, 51]
1330	Cubic diamond [46]
1350	*D* peak of microcrystalline graphite [47, 52]
1490	Contributions from the photon density of states in finite-size crystals of graphite [46, 53]
1580	*G* peak of graphite [47, 52]

As follows, the material M6-600 was analyzed when temperature increase. When temperature was increased, first up to 200 ºC and then up to 500 ºC, the phase was kept, but it was observed a shift in the main peak (E_g) of Raman spectrum (Figure III.46). This peak shifts from 141 cm^{-1} at room temperature to 146 cm^{-1} at 200 ºC and to 150 cm^{-1} at 500 ºC. Parker and Siegel [54] suggested that the shift of the anatase peaks is related to the oxygen stoichiometry of the material. They observed, through a series of heat treatment experiments, that the grain growth of the crystallites after be annealed at 600ºC does not affect the Raman spectrum. However, an oxygen reduction of fully oxidized samples induced a shift in it. Then, this shift could be attributed to the appearance of defects caused by oxygen vacancies. The fact that the shift is reversible when temperature is decreased supports this idea.

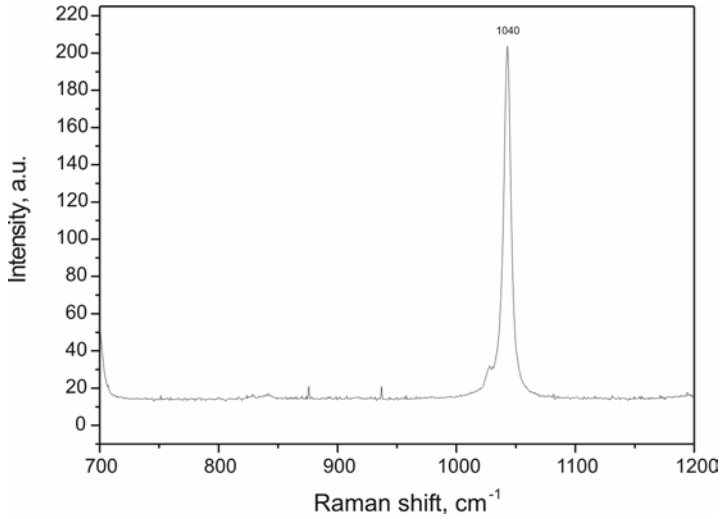

Figure III.45 *Raman spectrum of Ammonium Carbonate employed for Sol gellification during the synthesis process*

Based in these results it is possible to affirm that the poor response of the material is not a consequence of the crystalline phase but of the carbon deposits remains in the material surface.

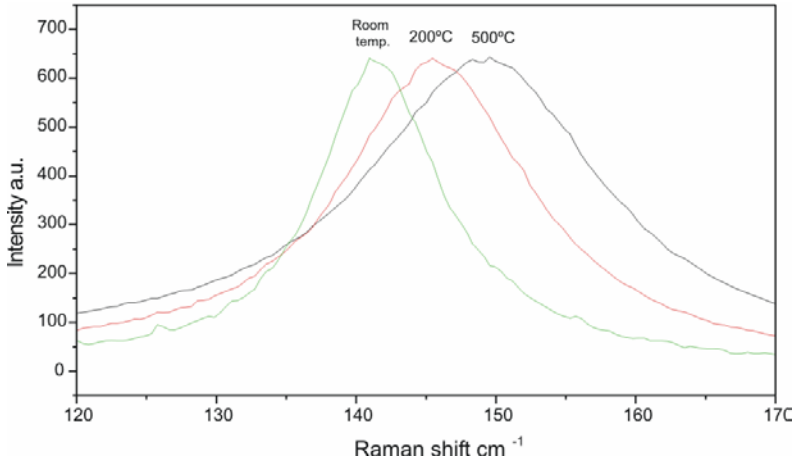

Figure III.46 *Shift in Raman spectrum of M6-600 at different temperatures (room temperature, 200 ºC and 500 ºC)*

III.5.2.2. M6 700

The material with the best response to oxygen was M6-700. The spectrum of this material is shown in Figure III.47. It can be seen that its structure is mostly anatase, like M6-600. Small peaks corresponding to brookite phase are also observed, but unlike M6-600, these brookite peaks are almost inappreciable. These results support the ones of XRD analyses.

The spectrums at higher frequencies show more differences between the two materials (Figure III.48). After calcination at 700ºC, only the peaks corresponded to hydrogen free carbon structures (790 cm^{-1}), hexagonal diamond (1306 cm^{-1}) and graphite (1350 and 1600 cm^{-1}) remain, but at lower quantities than in M6-600. Less deposits of carbon mean a wider surface area for catalysis and for the interaction between the active material and the oxygen species.

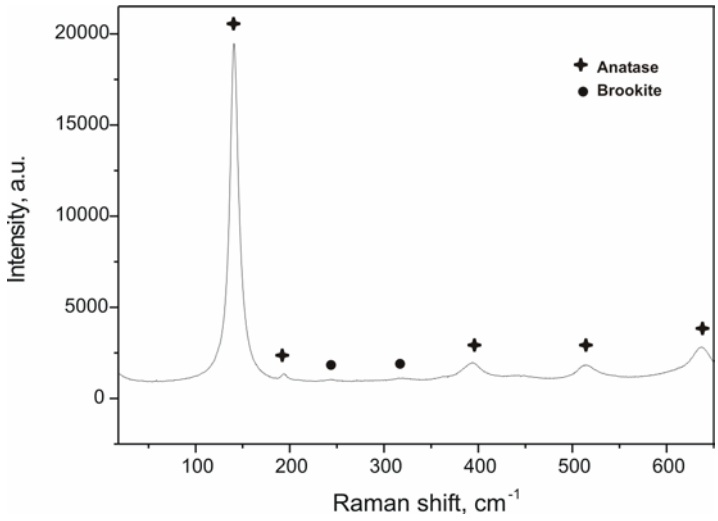

Figure III.47 *Raman spectrum of M6-700 nanopowder*

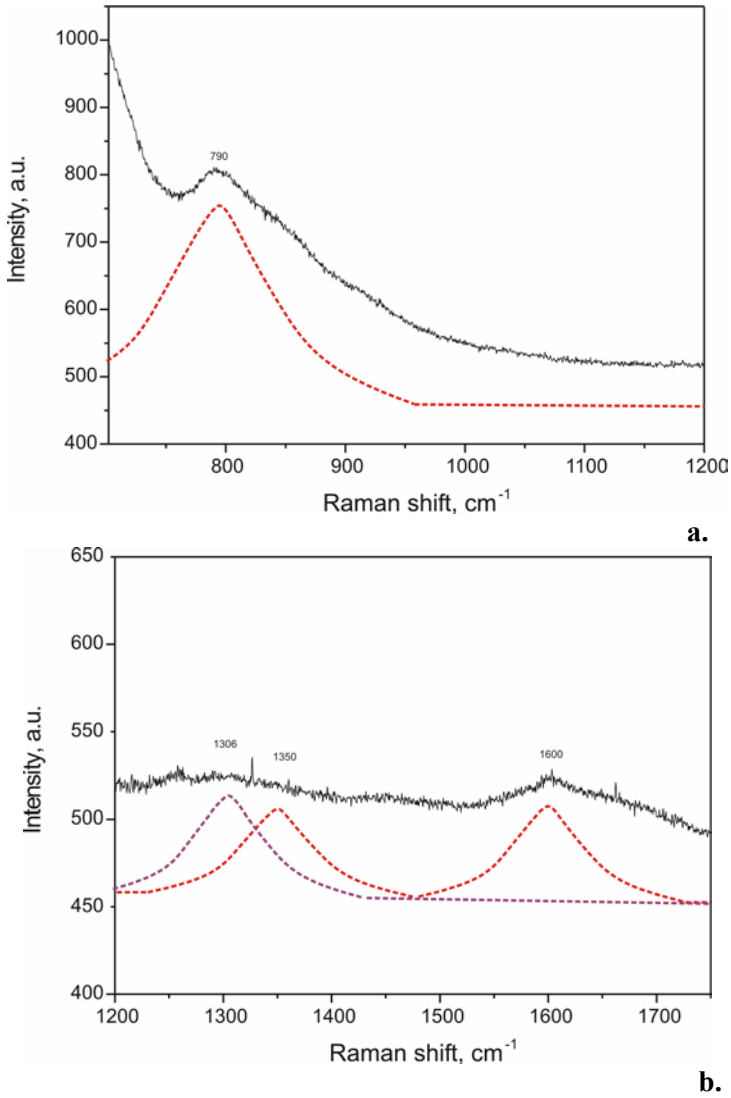

Figure III.48 *Raman spectrum at high frequencies of M6-700 nanopowder at room temperature*

III.6. Conclusions

ICP and EDS techniques were used to corroborate the content of Niobium in the doped materials (M6 and M8). Both results are near to the nominal values, that is 3 %. This confirms that the doping process was carried out correctly.

The XRD results showed that the addition of Niobium ions to the Titania lattice retards the phase transition in the crystalline structure of the material. It was observed that doped materials calcined between 600 ºC and 700 ºC have a mostly content of anatase. In the other materials, the content of rutile phase is most abundant in the crystalline structure. The slower temperature ramp employed for calcination process also produces a slight retard in the phase transition. Nevertheless, this retard is not so strong and can not be compared with that produced by the Nb ions. XRD technique also showed that the crystallites grow proportional to the temperature. This growth is hindered by the addition of Niobium to the Titania, and also by the use of a slower calcination ramp.

BET analyses showed that the surface area decreases when calcination temperature increases. It was observed that the addition of niobium retards the reduction process of the surface area with the temperature and also improves the porosity of the material.

The SEM analysis allowed knowing the grain growth evolution of the layers. It was observed that the grain size in doped materials (M6 and M8) is smaller than in pure Titania at calcination temperatures between 600 ºC and 800 ºC. Then, at 900 ºC, the grain growth in all materials is almost the same. The introduction of the Niobium in the Titania lattice not only hinders the growth of the crystals but also the coalescence between them retarding the grain growth. The slower ramp employed in M7 and M8 also help to retard the grain growth, then the lowest grain sizes were found in M8 based materials.

From the three techniques previously commented (XRD, BET and SEM) it was obtained information about crystallite and grain size. These results are summarized in Table III.31. The crystallites are the minimum structures formed by crystal lattices. These structures may join together forming polycrystalline samples, which at the same time join together to form grains. It may happen that a grain is formed by only one crystallite, in such case it is called a monocrystalline grain. With XRD technique it is possible to know the size of the crystallites; this is why XRD size values are in general the smallest.

From SEM micrographs it can be obtained the size of grains. It is observed that the values from SEM analysis are very similar to those from XRD, which may means that the grains are monocrystallines. Sometimes the SEM values are smaller than XRD values, which is physically impossible since the grains are formed by crystallites. The reason of this flimsiness is that SEM results are based on statistical methods applied to samples obtained manually from images. Some errors may be induced during sampling process. On the other hand, XRD is a completely automatic process.

Table III.31 *Results obtained from XRD, BET and SEM analysis related with crystallite and grain size*

M5			
Calcination Temperature (ºC)	**XRD results – Crystallite size (nm)**	**BET results – Crystallite size (nm)**	**SEM results – Grain size (nm)**
600	50.87	204.00	48.90
700	76.06	1224.00	56.50
800	76.52	2449.00	64.00
900	88.59	2449.00	110.10

M6			
Calcination Temperature (ºC)	**XRD results – Crystallite size (nm)**	**BET results – Crystallite size (nm)**	**SEM results – Grain size (nm)**
600	12.99	23.00	48.90
700	27.52	68.00	56.50
800	52.36	153.00	64.00
900	52.88	1224.00	110.10

M7			
Calcination Temperature (ºC)	**XRD results – Crystallite size (nm)**	**BET results – Crystallite size (nm)**	**SEM results – Grain size (nm)**
600	42.76	204.00	57.90
700	52.36	612.00	54.90
800	53.72	1224.00	67.70
900	65.20	2041.00	93.60

M8			
Calcination Temperature (ºC)	**XRD results – Crystallite size (nm)**	**BET results – Crystallite size (nm)**	**SEM results – Grain size (nm)**
600	13.01	22.00	46.50
700	25.91	51.00	50.00
800	51.23	122.00	46.50
900	59.94	408.00	97.40

The highest size values were obtained from BET analysis. Some authors call crystallite size the value obtained from BET [8, 55], and that is the reason of why it is called that way in this thesis. However, that name is not completely exact. With BET analysis it is obtained the size of the minimum solid structure (without pores) which is totally surrounding by the gas. These structures may be formed by several crystallites or even by several grains that are fused. Then it was expected that the size values obtained from BET analysis are the highest.

Regarding to the oxygen detection measurements, the physical characterization done to materials showed that doped ones calcined at lower temperatures (600 ºC and 700 ºC) were expected to have the best response toward oxygen. The high surface area of such materials benefits the detection mechanism and their crystalline phase, mostly anatase, permits the detection at desire temperatures (300 ºC – 600 ºC). The Niobium species may also contribute to the catalytic process.

The sensors made from the considered materials, showed that only those calcined at 700 ºC have good response toward 20 ppm of oxygen, the best response was obtained at a working temperature of 500 ºC. On the other hand, the doped materials calcined at 600 ºC had a poor response, in spite of they have better physical characteristics than doped materials calcined at 700 ºC. A possible explanation of this low response may be the brookite phase contained in doped materials calcined at 600 ºC; at this temperature the crystallinity of the brookite particles is improved with the consequent diminishing of the surface defects, which can affect the adsorption of oxygen species on the surface. Raman spectroscopy shows other possible reason for the low response of these materials toward oxygen. Some peaks corresponding to carbon with different morphologies were found in their structure. These deposits of carbon are the residual of the synthesis process, which could not be eliminated during the calcination. The problem with these deposits of carbon is that they cover the surface of the active material and hinder its interaction with the oxygen. So, since these carbon structures are also poorly catalytic, the result is a deactivation of the catalysis. This is reflected in the low response of this material toward oxygen.

Calculations of the response and recovery times of the sensors showed that these parameters do not depend on the crystalline phase, but on the calcination temperature. For the recovery time, it was also observed a difference between doped and pure materials. However these behaviours could not be explained with the physical characterization carried out in this project. In all cases the fastest response and recovery times were obtained from materials calcined at 700 ºC.

In this chapter it was also shown that Nb-doped Titania responds to oxygen in CO_2 environments. However the response toward 15 ppm of oxygen presented an inversion from oxidation type to reduction type. This phenomenon was explained as the effect of the CO species, from CO_2 dissociation, which is adsorbed on the active material surface, on the low concentration of oxygen species. On the other hand, the responses toward other pollutant gases such H_2S, SO_2 and CH_4 were of reduction type, as they were expected. Moreover, very high responses, compared with other authors, were obtained for SO_2 and CH_4. No response was obtained for C_2H_4.

The responses obtained for H_2S, SO_2 and CH_4 give rise to a problem of cross sensitivity when the developed sensor is employed for oxygen detection in a flux of CO_2. This problem may be solved by the use of other sensors sensible to such gases working in parallel, forming a gas sensor matrix [56-60]. That way there will be a responses pattern for each gas combination arrangement. The gas detection may be done by analysing this pattern [61-63].

III.7. References

[1] H. Tang, K. Prasad, R. Sanjinés and F. Lévy, "*TiO_2 Anatase Thin Films as Gas Sensors*", Sensors and Actuators B: Chemical, Vol. 26 1-3 (1995) 71-75

[2] Y. Xu, X. Zhou and O.T. Sorensen, "*Oxygen Sensors Based on Semiconducting Metal Oxides: an Overview*", Sensors and Actuators B: Chemical, Vol. 65 (2000) 2-4

[3] K. Zakrzewska, "*Gas Sensing Mechanism of TiO_2-Based Thin Films*", Vacuum, Vol. 74 (2004) 335-338

[4] R. Diaz, J. Arbiol, F. Sanz, A. Cornet and J.R. Morante, "*Electroless Addition of Platinum to SnO_2 Nanopowders*", Chemistry of Materials Vol. 14 8 (2002) 3277-3283

[5] S.C.-U.d. Barcelona, "*ICP-MS i ICP-OES*", Available from: http://www.sct.ub.es/v2/wcat/s15/s15_0000.htm

[6] J. Cabré, "*Obtenció I Caracterització de Grans Monodominis D'Ybco per Solidificació Direccional*", Doctoral thesis, Universitat de Barcelona, Departament de Física Aplicada, 1996

[7] B.A.X.-R. Solutions, "*Difract Plus Topas 2.1, Tehnical Reference*", Edited by 2003

[8] G. Cappelletti, C. Ricci, S. Ardizzone, C. Parola and A. Anedda, "*Aged Titania Nanoparticles: The Simultaneous Control of Local and Long Range Properties*", Journal of Physical Chemistry B, Vol. 109 (2005) 4448-4454

[9] L.E. Depero, L. Sangaletti, B. Allieri, E. Bontempi, A. Marino and M. Zocchi, "*Correlation between Crystallite Sizes and Microstrains in TiO_2 Nanopowders,*" Journal of Crystal Growth, Vol. 198 (1999) 516-520

[10] R.K. Sharma and M.C. Bhatnagar, "*Improvement of the Oxygen Gas Sensitivity in Doped TiO_2 Thick Films*", Sensors and Actuators B: Chemical, Vol. 56 (1999) 215-219

[11] J. Arbiol, "*Metal Additive Distribution in TiO_2 and SnO_2 Semiconductor Gas Sensor Nanostructured Materials*", Doctoral thesis, Universitat de Barcelona, Departament d'Electrónica, 2001

[12] P.H. Zimmermann, "*Temperature Dependence of the EPR Spectra of Niobium-doped TiO_2*", Physical Review B, Vol. 8 (1973) 3917–3927

[13] A. Bernasik, M. Radeeka, M. Rekes and M. Sloma, "*Electrical Properties of Cr and Nb Doped TiO_2 Thin Films*", Applied Surface Science, Vol. 65-66 (1993) 240-245

[14] R.K. Sharma, M.C. Bhatnagar and G.L. Sharma, "*Mechanism in Nb Doped TiO_2 Oxygen Gas Sensor*", Sensors and Actuators B: Chemical, Vol. 46 (1998) 194-201

[15] M.C. Carotta, M. Ferroni, D. Gnani, V. Guidi, M. Merli, G. Martinelli, M.C. Casale and N. Norato, "*Nanostructured Pure and Nb-doped TiO_2 as Thick Film Gas Sensors for Environmental Monitoring*", Sensors and Actuators B: Chemical, Vol. 58 (1999) 310-317

[16] M. Ferroni, M.C. Carotta, V. Guidi, G.Martinelli, F. Ronconi, O. Richard, D.V. Dyck and J.V. Landuyt, "*Structural Characterization of Nb-TiO_2 Nanosized Thick-Films for Gas Sensing Application*", Sensors and Actuators B: Chemical, Vol. 68 (2000) 140-145

[17] R.D. Shannon and J.A. Pask, "*Kinetics of the Anatase-Rutile Transformation*", Journal of the American Ceramic Society, Vol. 48 (1965) 391-398

[18] S. Hishita, I. Mutoh, K. Koumoto and H. Yanagida, "*Inhibition Mechanism of the Anatase-Rutile Phase Transformation by Rare Earth Oxides*", Ceramics International, Vol. 9 2 (1983) 61-67

[19] M.K. Akhtar, S.E. Pratsinis and S.V.R. Mastrangelo, "*Dopants in Vapor-Phase Synthesis of Titania Powders*", Journal of the American Ceramic Society, Vol. 75 1 (1992) 3408-3416

[20] Y. Djaoued, R. Brüning, D. Bersani, P.P. Lottici and S. Badilescu, "*Sol–Gel Nanocrystalline Brookite-Rich Titania Films*", Materials Letters, Vol. 58 (2004) 2618– 2622

[21] M. Koelsch, S. Cassaignon, C. Ta, T. Minh, J.F. Guillemoles and J.P. Jolivet, "*Electrochemical Comparative Study of Titania (Anatase, Brookite and Rutile) Nanoparticles Synthesized in Aqueous Medium*", Thin Solid Films, Vol. 451-452 (2004) 86-92

[22] I.C. Cosentino and R. Oliveira, "*Physical characterization of materials (BET, Hg porosimetry and thermal analysis)*", Materials Science and Technology Center (2001)

[23] G.H. Findenegg, "*Fundamentals of Adsorption*", Edited by Engineering Foundation, New York, 1984

[24] J.T. Nolan, T.W. McKeehan and R.P. Danner, "*Equilibrium Adsorption of Oxygen, Nitrogen, Carbon Monoxide, and their Binary Mixtures on Molecular Sieve Type 10X*", Journal of Chemical & Engineering Data Vol. 26 2 (1981) 112 - 115

[25] S. Brunauer, L.S. Deming, W.E. Deming and E. Teller, "*On a Theory of the Van Der Waals Adsorption of Gases*", Journal of the American Chemical Society Vol. 62 7 (1940) 1723 - 1732

[26] J. Rouquerol, D. Avnir, C.W. Fairbridge, D.H. Everett, J.M. Haynes, N. Pernicone, J.D.F. Ramsay, K.S.W. Sing and K.K. Unger, "*Recommendations for the Characterization of Porous Solids (Technical Report)*", Pure & Applied Chemistry, Vol. 66 8 (1994) 1739-1758

[27] K.S.W. Sing, D.H. Everett, R.A.W. Haul, L. Moscou, R.A. Pierotti, J. Rouquerol and T.Siemieniwska, "*Reporting Physisorption Data for Gas/Solid Systems*", Pure & Applied Chemistry, Vol. 57 (1985) 603

[28] P. Somasundaran, "*Adsorption at the Gas—Solid and Liquid—Solid Interface* ", Colloids and Surfaces, Vol. 9 1 (1984) 96-97

[29] M. Stankova, "*Gas Sensing Properties of RF Sputtered WO_3 Thin Films*", Doctoral thesis, Universitat Politècnica de Catalunya, Departament d'Electrónica, 2004

[30] J. Marien, T. Wagner, G. Duscher, A. Koch and M. Rühle, "*Nb on (110) TiO_2 (Rutile): Growth, Structure and Chemical Composition of the Interface*", Surface Science, Vol. 446 (2000) 219-228

[31] J.I. Goldstein, D.E. Newbury, P. Echlin, D.C. Joy, A.D.R. Jr., C.E. Lyman, C. Fiori and E. Lifshin, "*Scanning Electron Microscopy and X-ray Microanalysis. A Text for Biologists, Material Scientists, and Geologists*", Edited by Plenum, New York, 1992

[32] J.M. Catalyst, "*Impurities in CO_2 – Sources and Specifications*", Available from: http://www.jmcatalysts.com/pct

[33] J. Arbiol, J. Cerdà, G. Dezanneau, A. Cirera, F. Peiró, A. Cornet and J.R. Morante, "*Effects of Nb doping on the TiO2 anatase-to-rutile phase transition*", Journal of Applied Physics, Vol. 92 2 (2002) 853-861

[34] R.K. Sharma, "*Development and Characterization Solid State Materials for Oxygen Gas Sensors*", Doctoral thesis, Indian Institute of Technology, Department of Physics, 1996

[35] M.Z. Atashbara, H.T. Sunb, B. Gongc, W. Wlodarskia and R. Lambc, "*XPS Study of Nb-Doped Oxygen Sensing TiO_2 Thin Films Prepared by Sol-Gel Method*", Thin Solid Films, Vol. 326 (1998) 238–244

[36] L. Hong-Ming, H. Teh-Yu, T. Chin-Yea and H. Cl-Ming, "*Hydrogen Sulfide Detection By Nanocrystal Pt Doped TiO_2-Based Gas Sensors*", Nanastrured Materials, Vol. 6 (1995) 1001-1004

[37] D. Morris and R.G. Egdell, "*Application of V-Doped TiO_2 as a Sensor for Detection of SO_2*", Journal of Materials Chemistry, Vol. 11 (2001) 3207–3210

[38] N. Savage, B. Chwieroth, A. Ginwalla, B.R. Patton, S.A. Akbar and P.K. Dutta, "*Composite n–p Semiconducting Titanium Oxides as Gas Sensors* ", Sensors and Actuators B: Chemical, Vol. 79 1 (2001) 17-27

[39] K. Nakamoto, "*Infrared and Raman Spectra of Inorganic and Coordination Compounds*", Edited by John Wiley, New York, 1986

[40] J.G. Grasselli and B.J. Bulkin, "*Analytical Raman Spectroscopy*", Edited by John Wiley, New York, 1991

[41] H.C. Choi, Y.M. Jung and S.B. Kim, "*Characterization of Raman Spectra of Size-Selected TiO2 Nanoparticles by Two-Dimensional Correlation Spectroscopy*", Bulletin of Korean Chemical Society, Vol. 25 3 (2004) 426-428

[42] H. Kominami, Y. Ishii, M. Kohno, S. Konishi, Y. Kera and B. Ohtani, "*Nanocrystalline Brookite-Type Titanium (IV) Oxide Photocatalysts Prepared by a Solvothermal Method: Correlation between Their Physical Properties and Photocatalytic Activities*", Catalysis Letters, Vol. 91 1-2 (2003) 41-47

[43] Schoolsience, "*Catalysis: Carbon Formation*", Available from: http://www.schoolscience.co.uk/content/5/chemistry/catalysis/catsch4pg3.html

[44] Z. Paál, A. Wootsch, R. Schlögl and U. Wild, "*Carbon Accumulation, Deactivation and Reactivation of Pt Catalysts upon Exposure to Hydrocarbons*", Applied Catalysis A: General, Vol. 282 (2005) 135-145

[45] N.M. Rodriguez, P.E. Anderson, A. Wootsch, U. Wild, R. Schlögl and Z. Paál, "*XPS, EM, and Catalytic Studies of the Accumulation of Carbon on Pt Black*", Journal of Catalysis, Vol. 197 (2001) 365–377

[46] J. Schwan, S. Ulrich, V. Batori and H. Ehrhardt, "*Raman Spectroscopy on Amorphous Carbon Films*", Journal of Applied Physics, Vol. 80 1 (1996) 440-447

[47] M.A. Tamor and W.C. Vassel, "*Raman "Fingerprinting" of Amorphous Carbon Films*", Journal of Applied Physics, Vol. 76 6 (1994) 3823-3829

[48] W. Yarbrough and R. Rey, "*In Diamond and Related Materials*", Edited by M. Geis A. Badzian, and G. Johnson (Materials Resource Society), EA-15, Pittsburgh, 1988

[49] J. Filik, "*Raman Spectroscopy: A Simple, Non-Destructive Way to Characterise Diamond-Like Materials*", Spectroscopy Europe, Vol. 17 5 (2005) 10-17

[50] J. Kohanoff, "*Phonon Spectra from Short Non-Thermally Equilibrated Molecular Dynamics Simulations*", Computational Materials Science, Vol. 2 (1994) 221-232

[51] D. Knight and W. White, "*Characterization of Diamond Films by Raman Spectroscopy*", Journal of Materials Research, Vol. 4 (1989) 385-393

[52] R.O. Dillon and J.A. Woollam, "*Use of Raman Scattering to Investigate Disorder and Crystalline Formation in As-Deposited an Annealed Carbon Films*", Physical Review B, Vol. 29 6 (1984) 3482-3489

[53] R.J. Nemanich and S.A. Solin, "*First- and Second-Order Raman Scattering from Finite-Size Crystals of Graphite*", Physical Review B, Vol. 20 2 (1979) 392-401

[54] J.C. Parker and R.W. Siegel, "*Calibration of the Raman Spectrum to the Oxygen Stoichiometry of Nanophase TiO2*", Applied Physics Letters, Vol. 57 9 (1990) 943-945

[55] I.H. Campbell and P.M. Fauchet, "*The Effects of Microcrystal Size and Shape on the One Phonon Raman Spectra of Crystalline Semiconductors* ", Solid State Communications, Vol. 58 10 (1986) 739-741

[56] M. Stankova, X. Vilanova, J. Calderer, E. Llobet, P. Ivanov, I. Gràcia, C. Cané and X. Correig, "*Detection of SO_2 and H_2S in CO_2 Stream by Means of WO_3-Based Micro-Hotplate Sensors*", Sensors and Actuators, Vol. 102 (2004) 219–225

[57] M. Stankova, X. Vilanova, E. Llobet, J. Calderer, M. Vinaixa, I. Gràcia, C. Cané and X. Correig, "*On-line Monitoring of CO2 Quality Using Doped WO3 Thin Film Sensors*", Thin Solid Films, Vol. In press (2006)

[58] X. Vilanova, X. Correig, E. Llobet, J. Brezmes, R. Calavia and X. Sánchez, "*Sistema Analizador para la Detección de Gases Reductores y Oxidantes en un Gas Portador y Sensor de Gases Basado en Óxidos Metálicos de Tipo Semiconductor*", Spain, Patent No. ES2212739, (2003)

[59] X. Vilanova, E. Llobet, J. Brezmes, R. Calavia, X. Sánchez and X. Correig, "*A Multisensor System for Monitoring the Quality of Carbon Dioxide in the Beverage Industry*", Proceeding of IEEE Transducers 2003, Boston, USA, Vol. 2, 1347-1350

[60] M. Stankova, P. Ivanov, E. Llobet, J. Brezmes, X. Vilanova, I. Gràcia, C. Cané, J. Hubalek, K. Malysz and X. Correig, "*Sputtered and Screen-Printed Metal Oxide-Based Integrated Microsensor Arrays for the Quantitative Analysis of Gas Mixtures*", Sensors and Actuators B, Vol. 103 (2004) 23-30

[61] M. Penza, G. Cassano and F. Tortorella, "*Gas Recognition by Activated WO_3 Thin-Film Sensors Array*", Sensors and Actuators B, Vol. 81 (2001) 115-121

[62] J. Brezmes, P. Cabré, S. Rojo, E. Llobet, X. Vilanova and X. Correig, "*Discrimination Between Different Samples of Olive Oil Using Variable Selection Techniques and Modified Fuzzy Artmap Neural Networks*", IEEE Sensors Journal, Vol. 5 3 (2005) 463 - 470

[63] M. Stankova, X. Vilanova, J. Calderer, E. Llobet, J. Brezmes, I. Gràcia, C. Cané and X. Correig, "*Sensitivity and Selectivity Improvement of RF Sputtered WO_3 Microhotplate Gas Sensors*", Sensors and Actuators B, Vol. 113 (2006) 241–248

IV. MESOPOROUS Nb-DOPED TiO_2

IV.1. Introduction

One of the objectives of this work is the improvement of the material physical characteristics that may help the oxygen detection processes. As it was observed in the results obtained in last session, materials with high surface area and porosity tend to have the best sensing capabilities. Surface area of active material plays an important role in gas sensing process in semiconductor gas sensors, since catalysis occurs on the surface of material in direct contact with the gas. Therefore increasing the surface area gives rise to an improvement in sensor sensitivity toward gases. Thus, nano-sized mesoporous TiO_2 with large surface area offers a prospect to provide a highly active catalytic material.

Since the discovery of mesoporous aluminosilcate materials at Mobil corporation in 1992 [1, 2], much research has been reported on the synthesis of mesoporous molecular sieves. The mesoporous materials, with large surface area, were derived with supramolecular assemblies of surfactants, which acted as templates of the organic components during synthesis [3]. Soon afterwards, this technique of using surfactants as supramolecular templates to produce materials was considered very promising for preparation of mesoestructured/mesoporous metal oxide.

IV.1.1. Surfactants

Surfactants (short for surface-active-agent) are substances whose molecule exhibits both polar and apolar groups. The polar group contains heteroatoms such as O, S, N, P as part of some functional group such as carboxylate, sulfonate, sulphate, ammonium, phosphate, etc. Nonionic polar groups such as -OH or -O- are not very polar, and thus must occur several times to form a proper polar group, i.e., as polyalcohol or polyether. The nonpolar group is a hydrocarbon radical of the alkyl or alkyl-aryl kind, with typically 12 to 20 carbons atoms. Figure IV.1 shows the molecular structure of some common surfactants.

IV.1.2. Properties of Surfactant Solutions

Surfactants molecules possess two fundamental properties. On the one hand they tend to be located preferentially at the interface between a polar and an apolar phase, which

is called adsorption. On the other hand, surfactants molecules in solution exhibit a tendency to self associate to produce aggregation polymer called micelles, as well as other structures. All the properties of surfactant solutions come from one of these fundamental properties.

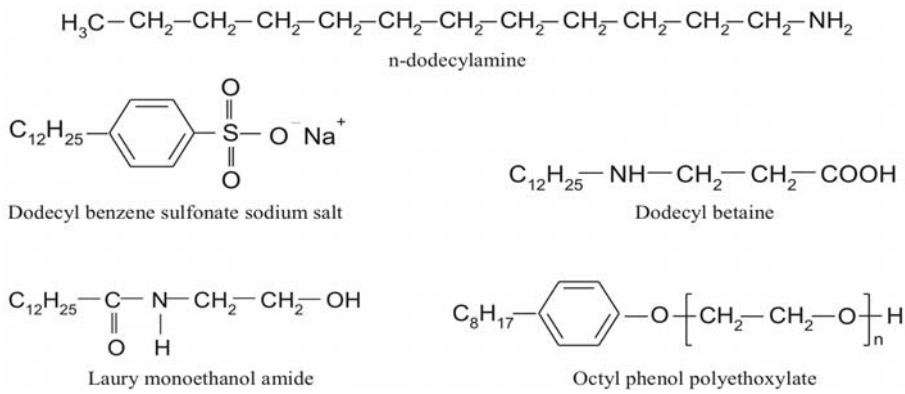

Figure IV.1 *Some common surfactants*

IV.1.2.1. Adsorption

Due polar-apolar duality of surfactants, they have been called amphiphiles [4] (from Greek *amphi*: double, and *philos*: affinity). An amphiphile molecule does not match in any solvent, be it polar or non polar, since there is always one of the groups which repeal solvent environment. Because of this fact, amphiphilic molecules exhibit a very strong tendency to migrate to interfaces or surfaces.

When a surfactant molecule goes to the interface and locates itself there with some preferential orientation, it is said that the molecule is adsorbed. The adsorption is a spontaneous phenomenon which is driven by a reduction of the energy when the surfactant lyophobic (which repel the solvent) group is removed from the solvent, and when one or both affinities are satisfy respectively at the liquid-solid interface. Here, the relative polarity of the solid with respect to the liquid would decide whether the surfactant adsorbs by the head or by the tail (Figure IV.2).

Adsorption is a dynamic phenomenon which is opposed by desorption, i.e., the transfer of a surfactant molecule to a bulk phase. The adsorption and desorption steps are often very rapid; as a consequence an adsorption-desorption equilibrium is reached after some time, which depends upon the surfactant concentration in the bulk phase.

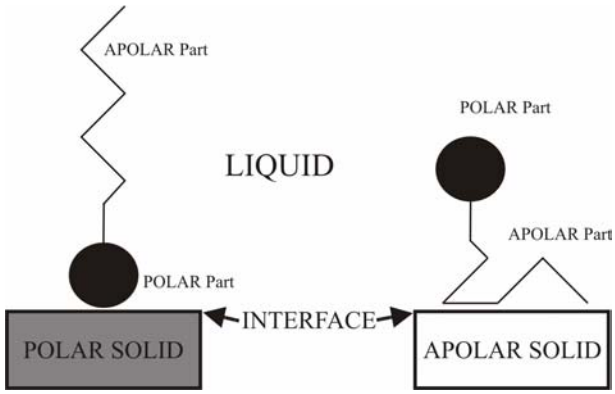

Figure IV.2 *Adsorption at a solid-liquid interface [5]*

Since the surfactant molecule has a lower free energy when it is adsorbed at interface than in the solvent bulk phase, the equilibrium is very much displaced toward the adsorbed state. In fact, the interface is very rapidly covered by a monolayer of surfactant molecules. In such monolayer the molecules are arranged in some specific pattern which depends upon structural and geometrical characteristics. When a monolayer is formed, everything happens as if the interface were coated with a thin layer of a new material.

IV.1.2.2. Self-Association

The second fundamental property of surfactant molecules is their capability of self-association in aqueous solutions.

When the surfactant concentration increases in the aqueous phase, the surfactant molecules first saturate the interface, and then accumulate in the solution. Each time a new surfactant molecule is added to the solution, the unfavourable interaction between the surfactant hydrophobic tail and the water molecules is increased. At some point the surfactant molecules start aggregating into the so-called micelles, a self-association structure in which the hydrophobe tail is removed from the aqueous environment. The concentration at which the first micelles are formed is called the Critical Micelle Concentration, which is abbreviated as CMC. The CMC is the concentration at which the factors that favour the formation of the micelle (for instance the hydrophobic effect) start dominating the effects which oppose it. Calculation of the CMC value is not easy due it highly depends on the acidity of the substance, temperature and other physical properties of the surfactant. These

micelles are no longer spherical, but cigar shaped or hexagonal packed or even degraded into lamellar liquid crystals (Figure IV.3).

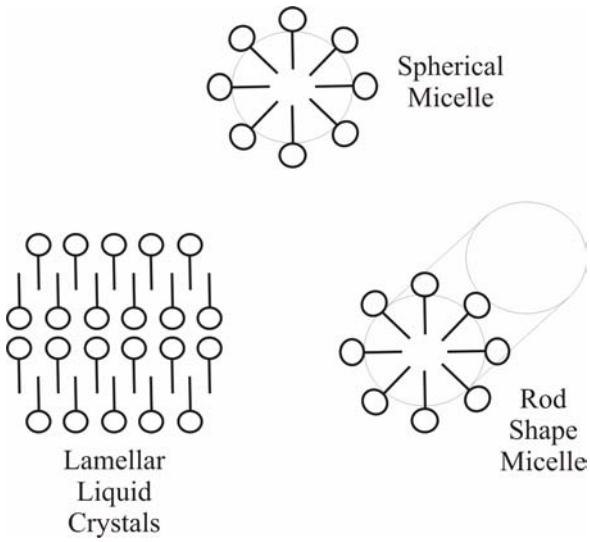

Figure IV.3 *Examples of surfactant micelles [5]*

IV.1.3. Interfacial Phenomena

The cohesion between the molecules of a piece of matter is due to the so-called Van der Waals intermolecular forces. These forces are the glue that keeps the material under a solid or liquid state. They have a very short range of action, and typically change as the inverse of the 6th power of the distance.

There are three kinds of Van der Waals forces: (1) Keesom forces, which are produced by the interaction of a permanent dipole with another permanent dipole. (2) Debye forces, which result from the interaction of a permanent dipole with an induced dipole. (3) London or dispersion forces, which have no specific direction of action and are said to be nonpolar interactions, though they result from the interaction of fluctuating dipoles.

The two first forces involve polar molecules and binding energies in the few Kcal/mol range, whereas the third one occurs in all kind of molecules, specially apolar ones, with a much lower interaction energy, typically ten times lower.

The cohesion forces are the ones that determine the attractive forces between solid particles dispersed in a continuous liquid phase. These forces tend to produce the aggregation of the dispersed phase fragments, and thus they are driving forces behind the dispersion instability mechanisms.

It is worth remarking that a (mono) layer of adsorbed surfactant can substantially modify the cohesion forces, since these forces action range is extremely short, as a matter of fact of the same order of magnitude than the surfactant layer thickness. Figure IV.4 illustrates the action of dispersing agents as substances that coat the solid particles and drastically change the cohesion situation [5].

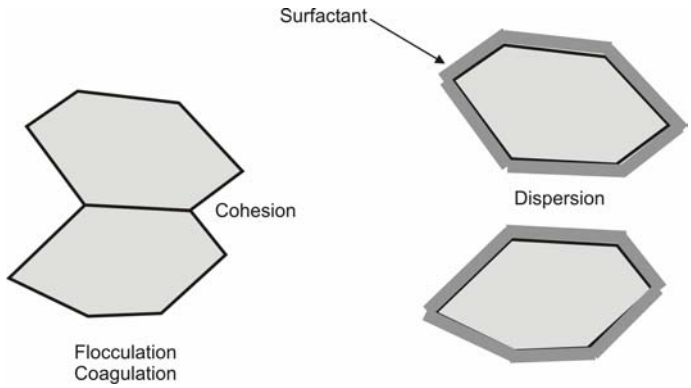

Figure IV.4 *Surfactants acting as dispersing agent [5]*

IV.1.4. Synthesis of Mesostructured Titanium Dioxide

The properties of the surfactants described in section IV.1.2 are used to obtain mesostructured materials. The general self-assembly pathway for mesostructured metal oxides is illustrated in Figure IV.5. The micelle structures or micelle arrays act as a mould for the metal oxide species, producing an ordered hybrid array composed of the metal oxide and the surfactant. Finally, the surfactant is removed by either calcination or solvent extraction, to form the metal oxide mesoporous structure.

The surfactant can be also used at later stages of the synthesis process as a dispersing agent, as it was described in section IV.1.3. In this way, the surfactant retards the coalescence of the material particles reducing the size of the final grains.

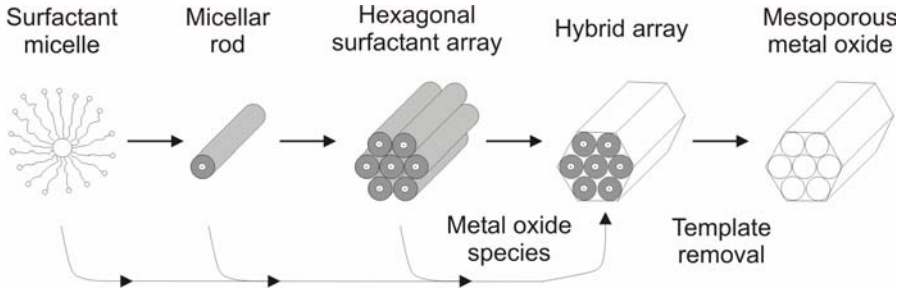

Figure IV.5 *Self-assembly of mesoporous metal oxides possessing a 2D hexagonal pore structure [6]*

To date, several preparative approaches utilizing a supramolecular templating mechanism had been reported for the preparation of mesoporous titanium dioxide. Mesoporous TiO_2 was first prepared using phosphate surfactant through a modified sol-gel process[7]. However, they were not pure titanium oxides, because a significant amount of phosphorous still remained in these materials, and underwent partial collapse of the mesostructure during template removal by calcination. The preparation of non-phosphated mesoporous TiO_2 using dodecylamine as directing agent, titanium isopropoxide as inorganic precursor, and emptying the pore by extraction has been reported by Antonelli [8]. Since then, many works had used dodecylamine as template in mesoporous Titania synthesis [9-13].

In this chapter, it is reported the synthesis of mesoporous Nb-doped Titania using dododecylamine as template and dispersing agent. Three approaches were done, adding the surfactant in different stages of the synthesis process. Three different concentration of surfactant were also employed for synthesis. Based on the results of the last chapter, the temperature ramp employed for calcination was 10 ºC/min.

The materials were characterized to obtain information about the material structure, which could be related with its detection properties. X-ray Diffraction (XRD) was used to establish the phases present in the crystalline structure of the material and determine the size of the crystallites in each material. Area Bet analysis was carried out for those materials with good results to establish their total surface area.

The layers, once deposited over the sensors were also characterized. Scanning Electron Microscopy (SEM) was used to obtain details on the film structure and the grain size. The sensing capabilities of the best materials were also tested. The target gas was oxygen (20 ppm) and the carrier gas nitrogen. To understand some behaviour of the sensors, Raman spectroscopy was employed again.

IV.2. Material Preparation

The properties of the surfactants were employed to attempt the synthesis of mesoporous Nb-doped Titania. It was expected the dodecylamine to form micelles that act as supramolecular template, given rise to a mesoporous structure. The process is described as follows. The material preparation process has been based on the process described in section II.3.1.

IV.2.1. Mesoporous Nb-Doped Titania: First Approach (M9)

In the first approach, 1 ml of the template (dodecylamine) was added to the solution of the precursors in the first part of the process, before the nucleation phase (see section II.3.1.1). The decision of introducing the surfactant in this stage of the process is based on the supposition that the surfactant micelles will interact easily with the hydrated metal oxide network, moulding the material during the nucleation.

IV.2.1.1. Material Synthesis

The material M9 was synthesized in the same way than materials M6 and M8 (doped materials) with the same quantities of the compounds. The sol-gel route followed in the preparation of this material is represented in Figure IV.6. Dodecylamine (1 ml), as template, and the two alkoxide precursos, Titanium isopropoxide (25 ml) and Niobium ethoxide (636 µl) were dissolved in isopropanol (143.9 ml). This solution was added drop wise to water (151.3 ml) and acid nitric (5.5 ml) under stirring, giving rise to a transparent sol. The pH of the sol was increased carefully by adding, drop wise, an aqueous solution (1 M) of Ammonium Hydrogen Carbonate (pH = 9), to achieve a consistent gel. The quantity of Ammonium Hydrogen Carbonated employed in this process was approximately 30 ml.

The gel was dried in an oven UNE 300 of Memmert Co. First, the temperature was set to 100 ºC for 20 hours to evaporate water. Then, temperature was increased to 300 ºC for 20 hours to eliminate dodecylamine and some residual compounds generated during synthesis. At the end, the gel was turned into powder.

The firing process of the powder was carried out in a programmable muffle Carbilite RWF 1200. The synthesised material was separated in four parts to be fired in air at 600 ºC, 700 ºC, 800 ºC and 900 ºC respectively. To avoid a fast growing of nanoparticles size, it was applied a ramp of temperature of 10 ºC/min to reach each firing temperature as described in section II.3.1.3.

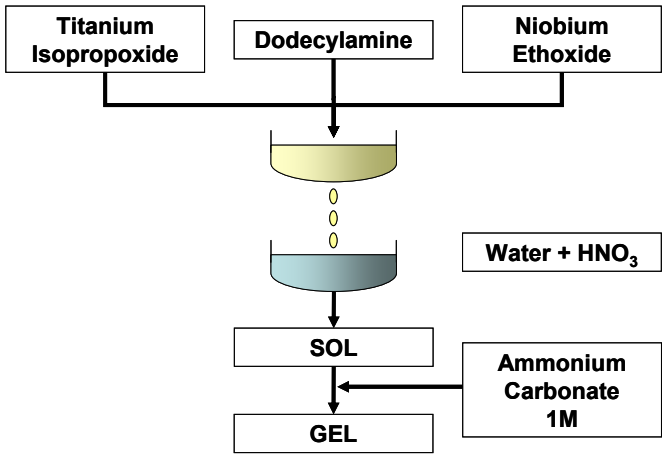

Figure IV.6 *Chemical route followed to obtain material M9*

XRD and SEM analyses were carried out to see the effects of the addition of dodecylamine during synthesis on the Titania. These analyses and the results obtained are described as follows.

IV.2.1.2. XRD Results

The XRD measurements were done with the same parameters described in section III.2.2. The XRD pattern of material M9 is shown in Figure IV.7. In this figure it is possible to appreciate the fast evolution of phase in this material. The results of the quantitative analysis are represented in Figure IV.8. As it was showed in the last chapter, the addition of Niobium ions to Titania lattice induces a retard in the phase transition; however in M9 it is observed a faster phase transition in comparison with the doped material already analyzed (M6 and M8). While in M6 and M8 calcined at 700 ºC the quantity of anatase phase is about 70 % of the material, in M9 calcined at this same temperature, the quantity of anatase phase does not exceed the 40 % of the material. The change of phase from anatase to rutile is almost complete at 800 ºC, and only a 3.7 % of anatase is remaining, while in M6-800 and M8-800 the quantity of anatase was more than 10 %.

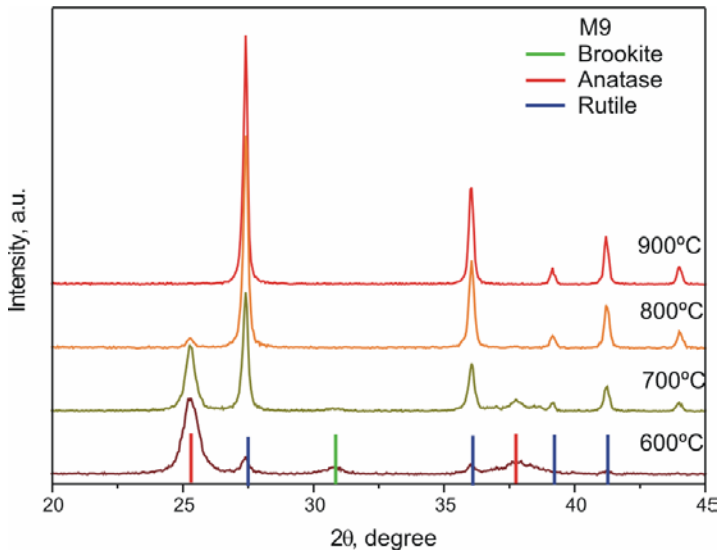

Figure IV.7 *XRD patterns of material M9 calcined at different temperatures*

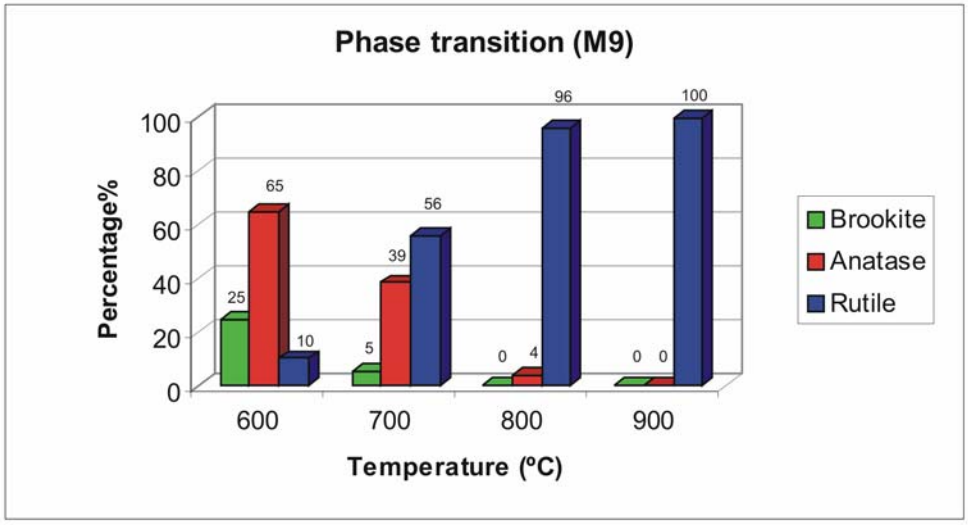

Figure IV.8 *Representation of the quantitative analysis of XRD pattern of material M9*

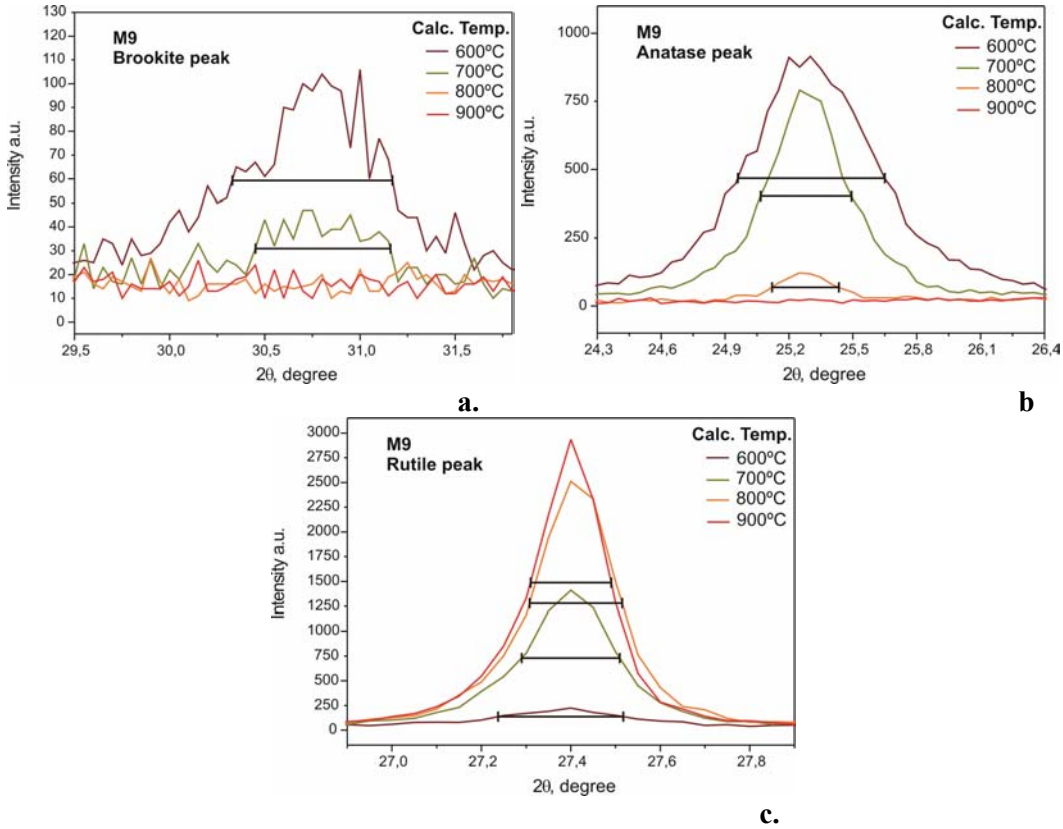

Figure IV.9 *Measurement of the FWHM in* ***a.*** *main brookite peak,* ***b.*** *main anatase peak and* ***c.*** *main rutile peak, in M9*

In the case of brookite phase, its quantity is also slightly reduced in comparison with the other doped materials; however this reduction is not comparable with that of the anatase phase.

It can be seen that the addition of the surfactant in the first part of the synthesis process may favour the phase transition. A possible explanation is that the surfactant molecules avoid the insertion of the Niobium ions in the Titania lattice. Thus the effects of the Niobium ions in the material, regarding to the crystalline phase transition, are inhibited.

Nevertheless, the behavior of the crystallites growth is in accordance with doped materials. In Figure IV.9 it is shown the FWHM of all the main peaks in XRD patterns of M9. The changes of crystallite size with the increment of the calcination temperature of brookite, anatase and rutile phase are summarized in Table IV.1, Table IV.2 and Table IV.3

respectively. Even that the addition of dodecylamine produced an acceleration of the phase transition in material M9, the size of the crystallites is similar to M6 and M8 in all calcination temperatures. This hindering in the crystallites growth could be attributed to the presence of the surfactant, which wraps the crystallites impeding the nucleation instead of the effect of Niobium doping. Then, the two behaviours, the one of the phase transition opposite to other doped materials and that of the crystallite growth, similar to other doped materials, have not to be contradictory at all. The surfactant could hinder the introduction of the Niobium ions in the Titania lattice, helping the acceleration of the phase transition. At the same time, the dodecylamine wraps the crystallites impeding the nucleation and thus, its growth.

Table IV.1 *Size of brookite crystallites in M9 and the values employed for its calculation*

Temperature (ºC)	FWHM (rad)	θ (rad)	Crystallite size (nm)
600	1.47E-02	5.36E-01	12.22
700	1.24E-02	5.37E-01	14.50

Table IV.2 *Size of anatase crystallites in M9 and the values employed for its calculation*

Temperature (ºC)	FWHM (rad)	θ (rad)	Crystallite size (nm)
600	1.20E-02	4.41E-01	14.15
700	7.44E-03	4.41E-01	22.89
800	5.48E-03	4.41E-01	31.10

Table IV.3 *Size of rutile crystallites in M9 and the values employed for its calculation*

Temperature (ºC)	FWHM (rad)	θ (rad)	Crystallite size (nm)
600	4.88E-03	4.78E-01	35.54
700	3.83E-03	4.78E-01	45.36
800	3.61E-03	4.78E-01	48.06
900	3.14E-03	4.78E-01	55.18

It was made a weighting average of the crystallite size of each material using the values of crystallite sizes of the phases, shown in Table IV.1, Table IV.2 and Table IV.3, and the quantity of each phase in the materials. The result of this average is shown in Table IV.4. The average of the crystallites size is slightly higher than in other doped materials, in some calcination temperatures. This is due to the higher percentage of rutile phase in M9 based materials than in the other doped materials.

Table IV.4 *Weighting average crystallite size of M9 in function of the calcination temperature*

Temperature (ºC)	Average crystallite size (nm)
600	15.85
700	35.02
800	47.44
900	55.18

The crystalline features of material M9 are not very attractive for our purpose. As it was already explained, the anatase phase has better sensing capabilities than rutile phase at the working temperatures we are using in this project (300 ºC to 600 ºC). The only M9 based material with mostly anatase phase is M9-600. However, Raman results of materials calcined at 600 ºC showed in the last chapter, reveal the presence of carbon deposits on the surface of these materials. Then, M9 appears not to be useful for oxygen sensor application in our case.

IV.2.1.3. SEM

The SEM analysis was done with the same parameters described in section III.3.1. The SEM pictures of the material M9 calcined at 600 ºC, 700 ºC, 800 ºC and 900 ºC is shown in Figure IV.10. The histograms of the grain sizes are showed in Figure IV.11 and the evolution of the grain diameter of this material is summarized in Table IV.5.

It is possible to appreciate that there is not a great change in the grain size when calcination temperature is increased. This is the contrary effect that in other doped materials (M6 and M8). In M9 the increment of the grain diameter from material calcined at 600 ºC (30.34 nm) to the one calcined at 900 ºC (41.42 nm) is approximately 35 %. In M6 and M8 this increment exceeds the 100%. The grain size is also smaller than in the mentioned doped materials for all the calcination temperatures. In M9, the dodecylamine appears to obstruct the coalescence of the crystals and thus the growth of the grains. The effect of the surfactant in the grain size is observed even at 900 ºC.

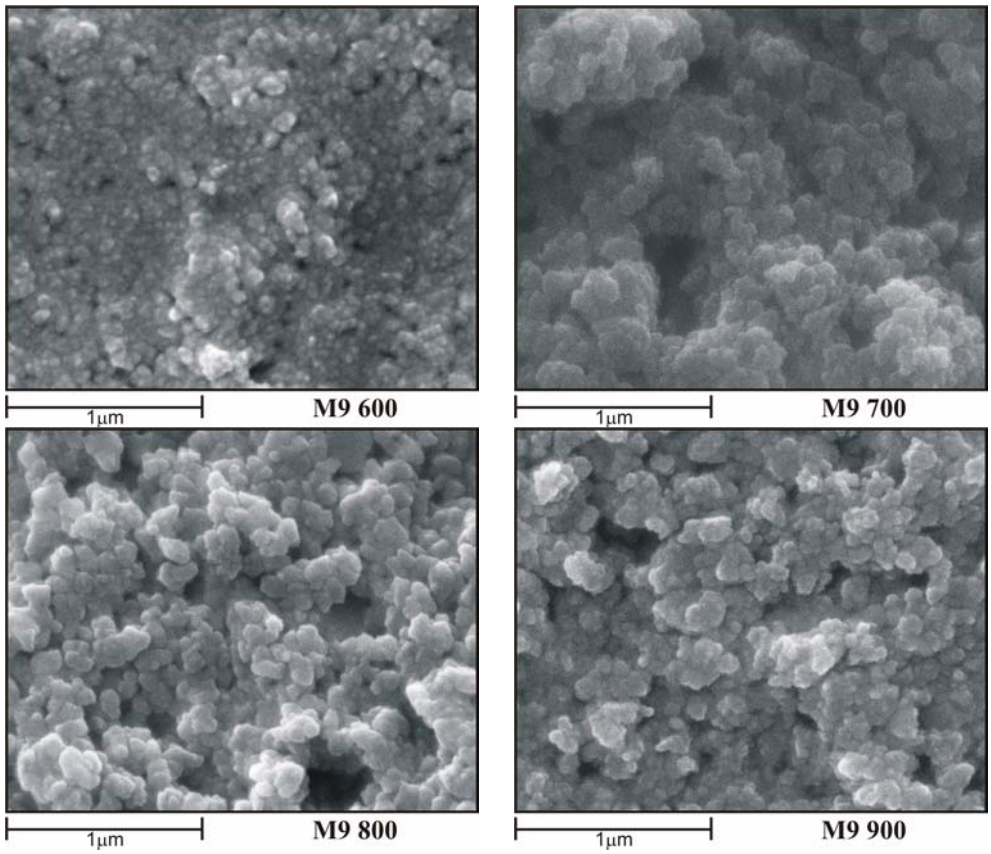

Figure IV.10 *SEM images of M9 calcined at different temperatures*

Comparing the crystallite sizes from XRD results with grain sizes from SEM, it is observed that these values are similar for M9 based materials calcined above 700 ºC, which indicates that grains may be monocrystallines. In material M9 calcined at 600 ºC, the grain size from SEM is higher than crystallite size from XRD. This may be an indication of polycrystalline grains; however it could be also a product of an increase of crystallites after temperature treatment of the layer.

In conclusion, the small grains of M9 are proper for sensor application; however, as it was commented, the crystalline characteristic of this material make it useless for our work.

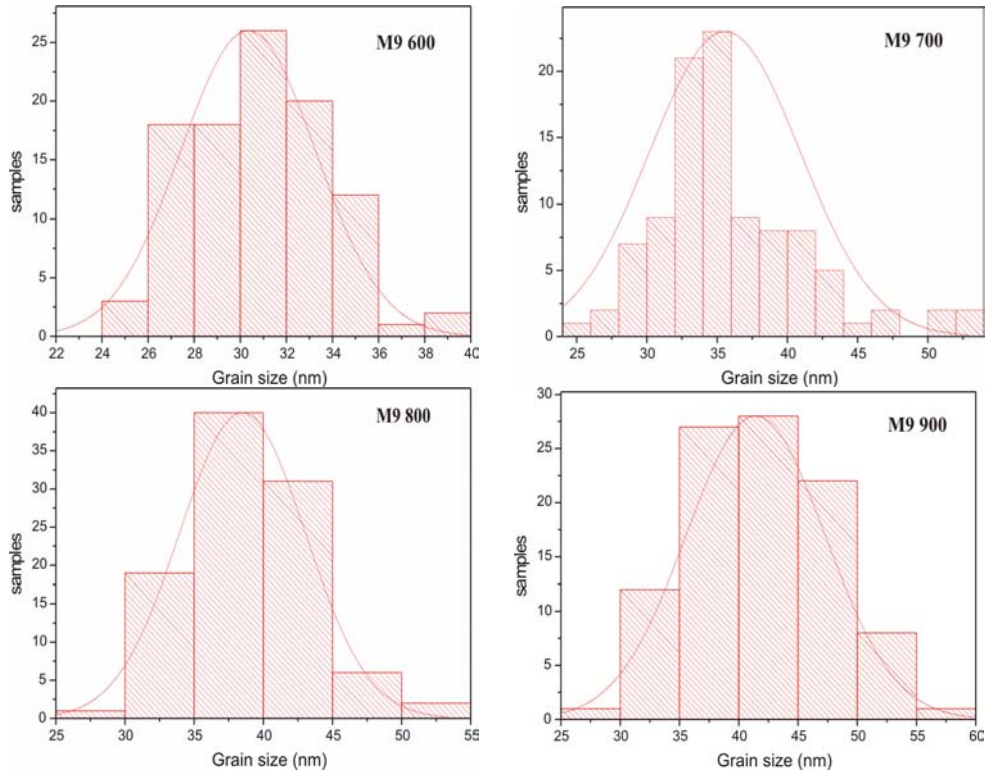

Figure IV.11 *Grain size histograms of M9 calcined at different temperature*

Table IV.5 *Grain size evolution of the grains belong to material M9*

Material	*d* (nm)	SD	SE
M9-600	30.34	2.9	0.29
M9-700	35.55	5.3	0.53
M9-800	38.49	4.5	0.45
M9-900	41.42	5.8	0.59

To improve the material it is necessary to avoid the effect of the dodecylamine in the doping process. Because of this it was thought, for next attempts, to add the surfactant after

the hydrolysis of the metal alkoxides. After the hydrolysis process it is expected that the Nb ions are inserted in the Titania crystalline network and thus the only effect of the surfactant will do is the hindering of the nucleation process. The quantity of dodecylamine will be also slightly increased to assure the formation of micelles, since in M9 synthesis process they were not evidence of their formation. This new attempt of material synthesis gives rise to the material M10 which is explained as follows.

IV.2.2. Mesoporous Nb-Doped Titania: Second Approach (M10)

In the second approach, 2 ml of dodecylamine were added to the sol in the sol-gel route, just before the addition of the ammonia carbonate for the gellification. At this stage, it was expected that the Niobium ions are already inserted in the Titania network and that the micelles formed will only hinder the coalescence of the crystals and then the growth of these particles.

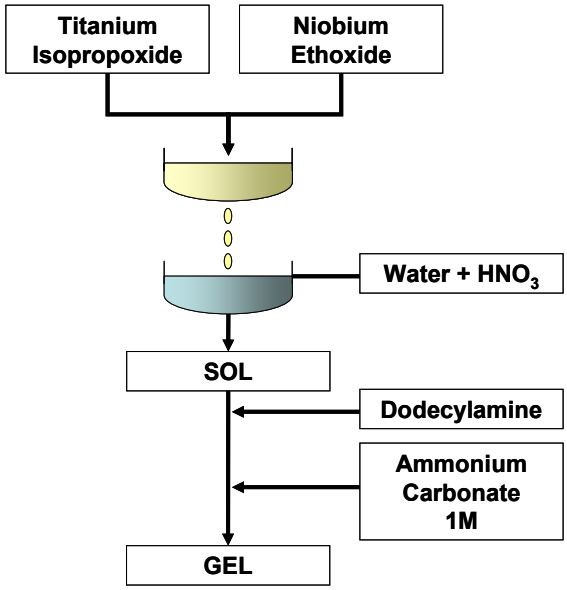

Figure IV.12 *Chemical route followed to obtain material M10*

IV.2.2.1. Material Synthesis

The sol-gel route followed in the preparation of the material M10 is represented in Figure IV.12. The process is very similar to that described in section IV.2.1.1, with the difference that for M10 the dodecylamine was not added at the same time with the organic precursors, but at the end of the process, during gellification. The other difference is that, as it was commented, the quantity of surfactant employed for M10 synthesis was 2 ml instead 1 ml used for M9. Because the cationic character of dodecylmine, the pH of the solution is slightly increased and thus the quantity of Ammonium Hydrogen Carbonated used for gellification was reduced to approximately 20 ml. The drying and the firing process were carried out in the same way that for M9.

IV.2.2.2. XRD Results

The XRD measurements were done with the same parameters described in section III.2.2. Figure IV.13 shows the XRD pattern of material M10. The results of the quantitative analysis are represented in Figure IV.14. As it happened in material M9, the evolution of the crystalline phase transition in material M10 appears to be faster than in the dedecylamine-free doped materials. However, this acceleration of the phase transition is more moderate in M10 than in M9, even when the quantity of dodecylamine employed in the synthesis is the double. It appears that the addition of the dodecylamine in the final step of the sol-gel process does not affect so much the doping process. It also appears that the surfactant hinders the doping process only when it is at low concentration, at higher concentration the surfactant molecules stop the interaction with the crystallites and start to join to form micelles. These micelles form structures that could assemble the material but it looks like they do not affect so much the crystallites and then the hinder of the doping process is less than in M9.

The quantity of rutile phase in the material M10 is high compared to doped materials synthesized without surfactants at the same calcination temperatures. Thus material M10 seems not to be as suitable as M6 and M8 for oxygen detection at working temperatures around 500 ºC. However, there is more anatase phase in M10 than in M9. For example, in M10-700 the quantity of anatase phase is 23 % higher than in M9-700. And in M10-700, the quantity of anatase surpasses the rutile's in 5 %.

To analyse again the crystallite sizes evolution, the results of XRD were studied. In Figure IV.15 it is shown the FWHM of all the main peaks in XRD patterns for M10. The changes of crystallites size with the increment of the calcination temperature of brookite, anatase and rutile phase are summarized in Table IV.6, Table IV.7 and Table IV.8 respectively. It is observed that the crystallites are slightly bigger in M10 than in M9. This supports the idea that the higher concentration of dodecylamine drives the formation of groups of surfactant molecules (micelles) which appear to affect the crystallites in less

proportion than the surfactant molecules that are not grouped. Then, the crystallites in M10 tend to grow easier than in M9.

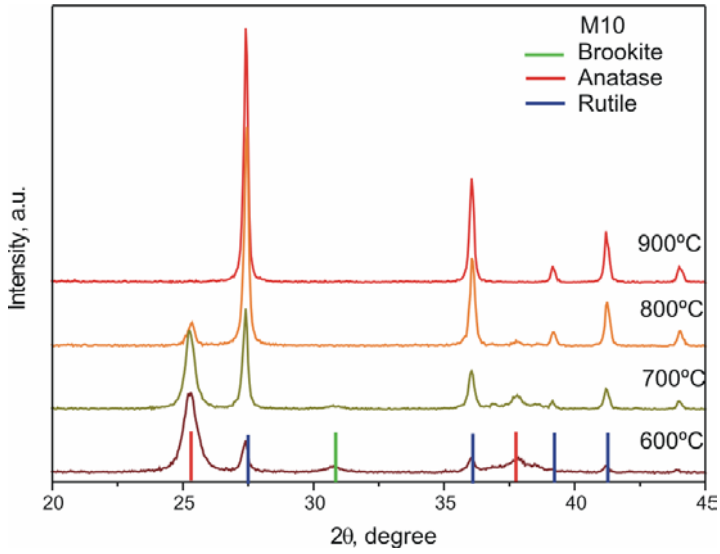

Figure IV.13 *XRD patterns of material M10 calcined at different temperatures*

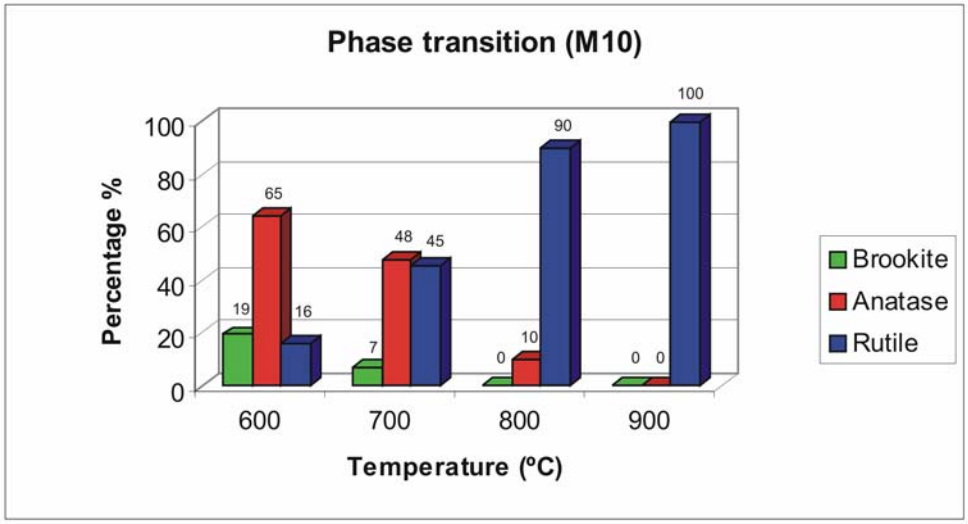

Figure IV.14 *Representation of the quantitative analysis of XRD pattern of material M10*

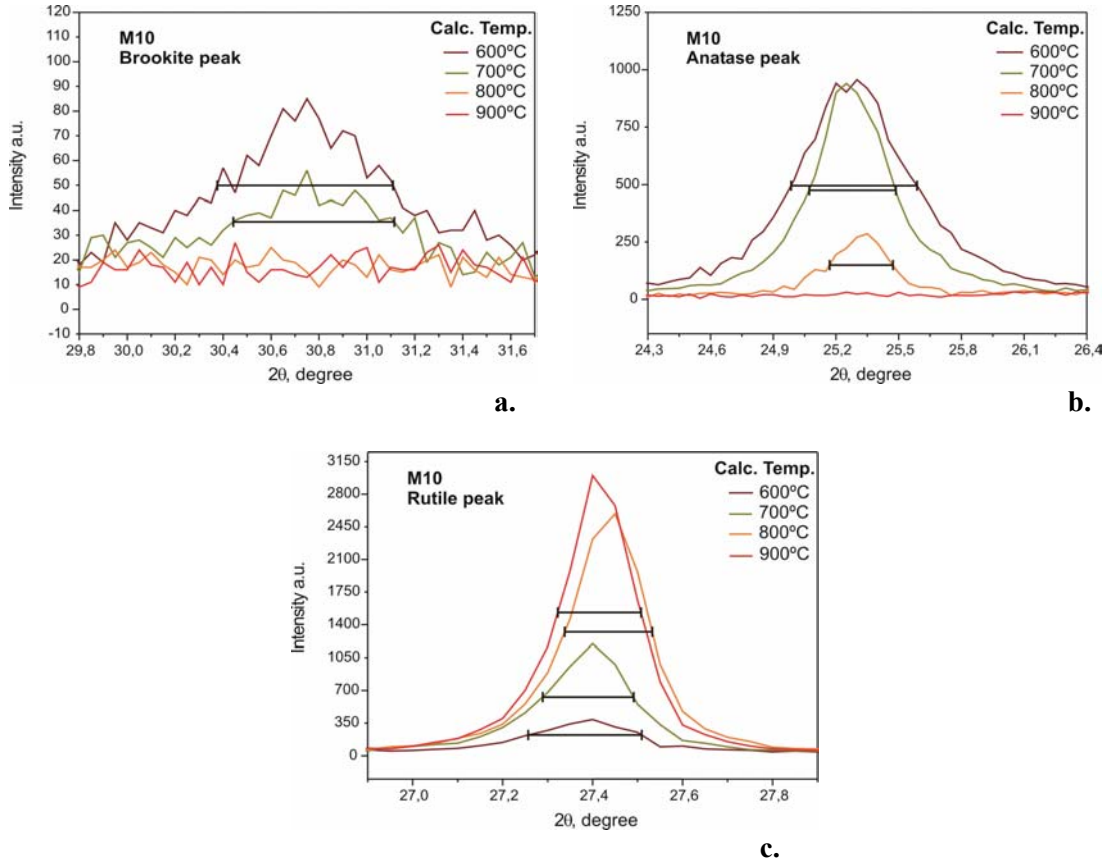

Figure IV.15 *Measurement of the FWHM in* ***a.*** *main brookite peak,* ***b.*** *main anatase peak and* ***c.*** *main rutile peak, in M10*

Table IV.6 *Size of brookite crystallites in M10 and the values employed for its calculation*

Temperature (ºC)	FWHM (rad)	θ (rad)	Crystallite size (nm)
600	1.28E-02	5.37E-01	13.96
700	1.18E-02	5.37E-01	15.23

Table IV.7 *Size of anatase crystallites in M10 and the values employed for its calculation*

Temperature (ºC)	FWHM (rad)	θ (rad)	Crystallite size (nm)
600	1.05E-02	4.41E-01	16.21
700	7.22E-03	4.41E-01	23.58
800	5.29E-03	4.42E-01	32.21

Table IV.8 *Size of rutile crystallites in M10 and the values employed for its calculation*

Temperature (ºC)	FWHM (rad)	θ (rad)	Crystallite size (nm)
600	4.41E-03	4.78E-01	39.38
700	3.53E-03	4.78E-01	49.18
800	3.40E-03	4.79E-01	51.09
900	3.23E-03	4.78E-01	53.74

Once more, a weighting mean of the crystallite size of each material was made using the values of crystallite sizes of the phases and the quantity of each phase in the materials. The result of this average is shown in Table IV.9. The average of the crystallites size is similar to that of M9.This is because the compensation between crystallite size and the quantity of each phase in both materials.

Table IV.9 *Weighting average crystallite size of M10 in function of the calcination temperature*

Temperature (ºC)	Average crystallite size (nm)
600	19.48
700	34.57
800	49.22
900	53.74

Although the crystalline properties of material M10 are better than in material M9, the quantities of rutile phase remaining in M10 (45 % in material calcined at 700 ºC) is still very high. In the last chapter, it was observed that materials with high quantity of rutile,

(over ~40 %) are useless for oxygen detection at the working temperatures employed in this work. Then, crystalline properties of material M10 does not look appropriate to help the oxygen detection.

IV.2.2.3. SEM

The SEM analysis was done with the same parameters described in section III.3.1. The SEM pictures of the material M10 calcined at 600 ºC, 700 ºC, 800 ºC and 900 ºC are shown in Figure IV.16. The evolution of the grain diameter of this material is summarized in Table IV.10. The histograms of the grain size are showed in Figure IV.17.

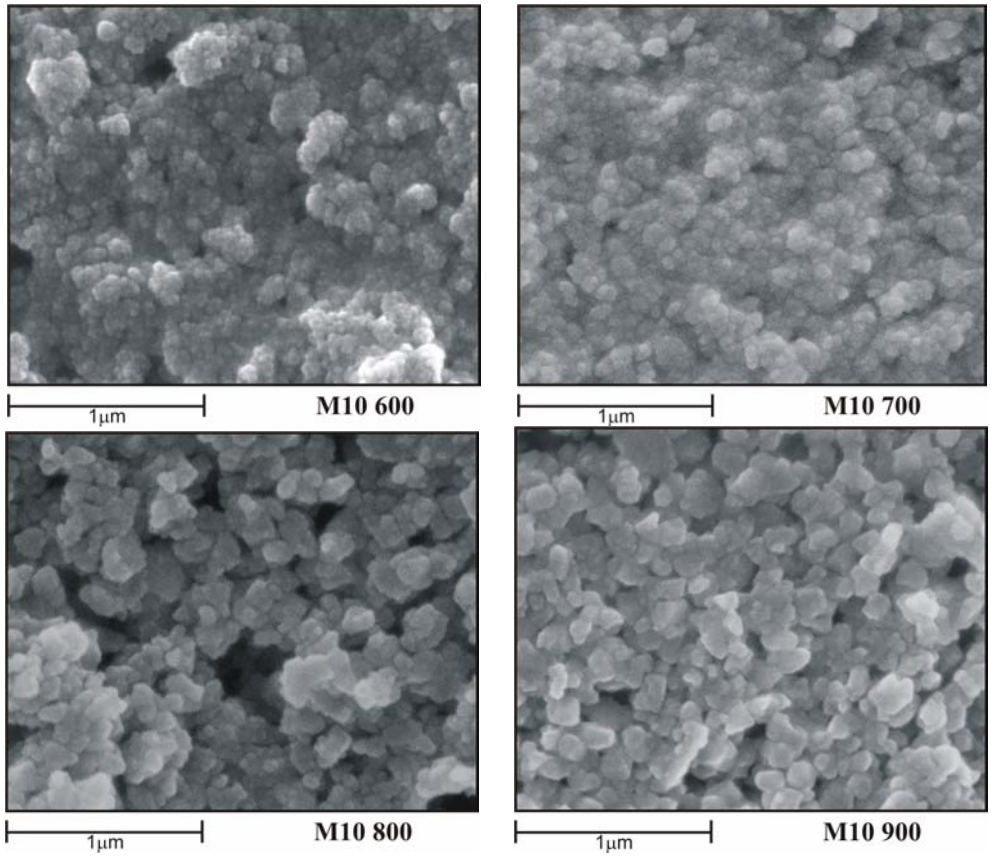

Figure IV.16 *SEM images of M10 calcined at different temperatures*

The grain sizes in material M10 are smaller than in the doped materials synthesized without a template. The change of phase is also slower. This improvement in the material features is probably due to the addition of the surfactant during the synthesis process. As it happened in the case of material M9, the dodecylamine appears to surround the particles hindering their fusion and growth.

If material M10 is compared with material M9, the other material synthesized with a template, it is observed that the increment of the grain size in material M10 is faster than in M9. The grains are also smaller in M9 than in M10. Even when the quantity of surfactant used for the synthesis of material M10 was the double than the used for material M9, the effects in the retarding of the grain growth are more evident in M9 than in M10. It is necessary to remember that when the surfactant is added in the first part of the process, as it was done with material M9, it retards the growth of the crystallites. This happened in less proportion in the material M10 where the surfactant affects the crystal fusion and grain growth but not the crystallites. The grains formed by small crystallites are smaller. This explains the bigger size of the grains in material M10 compared with those in material M9.

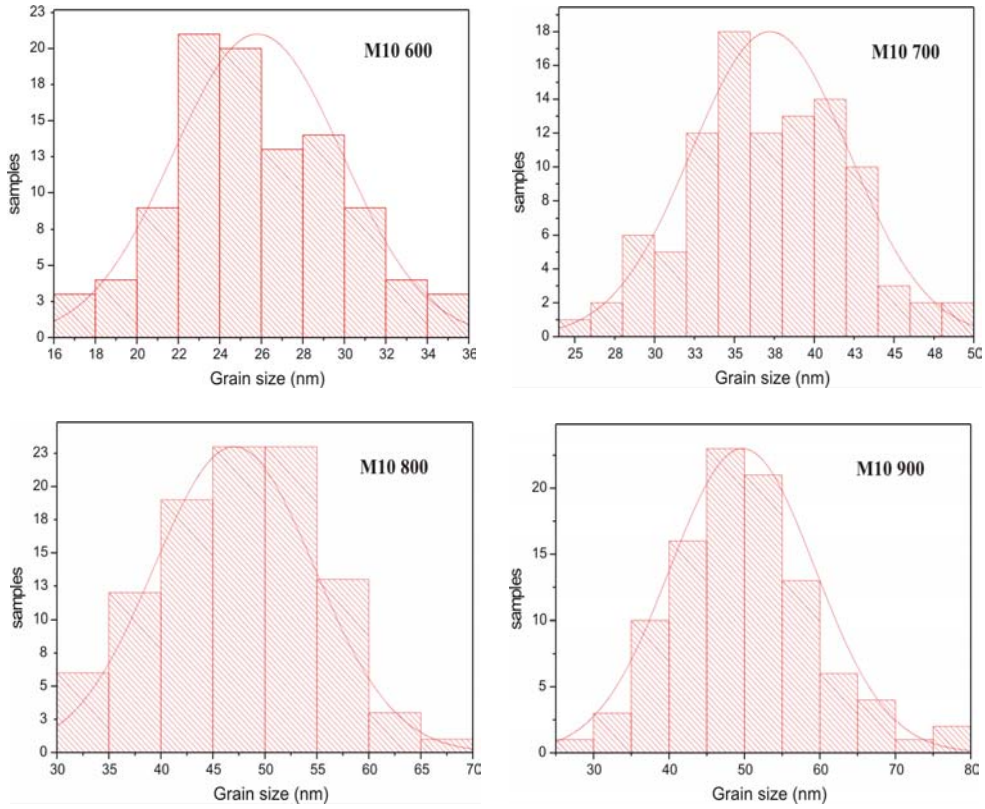

Figure IV.17 *SEM histograms of M10 calcined at different temperatures*

Table IV.10 *Grain size evolution of the grains belong to material M10*

Material	*d* (nm)	SD	SE
M10-600	25.82	4	0.4
M10-700	37.23	4.9	0.49
M10-800	47.04	7.7	0.77
M10-900	49.74	9.6	0.96

The results of Table IV.10 show that the crystallite size obtained by this method for this material are similat to those obtained for M9, as in XRD Analysis. Once more, comparing the crystallite size evaluated from XRD and SEM, the higher differences are for those mayerials calcined at 600 º C. This can be produced by the firing process of the active layer that may produce agglomerations of the material crystals.

In conclusion, the addition of the dodecylamine in the last part of the synthesis process does not affect the doping process as much as when it is added together with the organic precursors. However, the quantity of surfactant used for M10 was still too low to form a considerable quantity of micelles that can mould the material morphology without affect its crystalline structure.

IV.2.3. Mesoporous Nb-Ddoped Titania: Third Approach (M11)

For the third approach of the template assembly materials, 8 ml of dodecylamine were added to the sol in the sol-gel route in the same way than in M10. Due the cationic characteristic of dodecylamine, the addition of the surfactant increases the pH of the sol, helping the gellification. Then, the ammonia carbonate was added to finish the gellification. As in M10, it was expected that the micelles formed will difficult the coalescence of the crystals and then the growth of the particles.

IV.2.3.1. Material Synthesis

The sol-gel route followed in the preparation of the material M11 was similar to that used for M10 and is represented in Figure IV.12. After the hydrolysis, the dodecylamine (8 ml) was slowly added to the sol, a partial gellification was observed at this moment. The

complete gellification was achieved by adding, drop by drop, an aqueous solution (1 M) of Ammonium Hydrogen Carbonate (pH = 9). The quantity of Ammonium Hydrogen Carbonate added to the solution for its complete gellification was approximately 5 ml. The drying and the firing process were carried out in the same way that for M9 and M10.

IV.2.3.2. XRD Results

The XRD measurements were done with the same parameters described in section III.2.2.The XRD patterns of M10 based materials are shown in Figure IV.18. The results of the quantitative analysis are represented in Figure IV.19. On the contrary of other materials synthesized with template, the change of phase in M10 is slow. This behaviour can be explained considering the formation of micelles. So, the amount of surfactant introduced this time has been sufficient to achieve the Critical Micelle Concentration. . These micelles form structures that could assemble the material but do not affect so much the crystallites. Besides, it is observed that the change of phase in M11 is even slower than in M6 and in M8. The quantity of anatase phase in M11-700 (74.69 %) is slightly higher than in M6-700 (69.61 %) and M8-700 (70.83 %). When the materials are calcined at 800 ºC the differences are more notorious. In M11-800 the quantity of anatase phase is more than the 50 % of the whole material, which is 95 % more than in M6 and 300 % more than in M8. The characterizations of the material do not explain this retard of phase produced for the addition of the surfactant. Nevertheless, it may be attributed to mesoporous structure of M11, which difficults the reorientation of the crystallites in anatase phase and thus, the crystallization of the rutile phase. In any case, this higher quantity of anatase phase in M11 benefits the mechanism of oxygen detection at temperatures about 500 ºC.

It was also found considerable quantities of brookite phase in material M11 calcined at 600 ºC (25.74 %) and 700 ºC (14.85 %), similar to brookite values in M8. At 800 ºC there is not evidence of brookite phase in the material. As it was commented before, the brookite phase has less free carriers than anatase and its electrochemical behaviour is very alike to rutile's [18]. Its presence could hinder the response of a material towards oxygen at working temperatures around 500 ºC

Regarding the crystallite sizes, in Figure IV.20 it is shown the FWHM of all the main peaks in XRD patterns of M11. The changes of crystallites size with the increment of the calcination temperature of brookite, anatase and rutile phase are summarized in Table IV.11, Table IV.12 and Table IV.13 respectively. It can be seen that the size of the M11 crystallites in all phases are similar to those in M10, M8 and M6. This evidence that at higher concentrations of surfactant, the micelles formed do not affect the doping process and the growth of the crystallites.

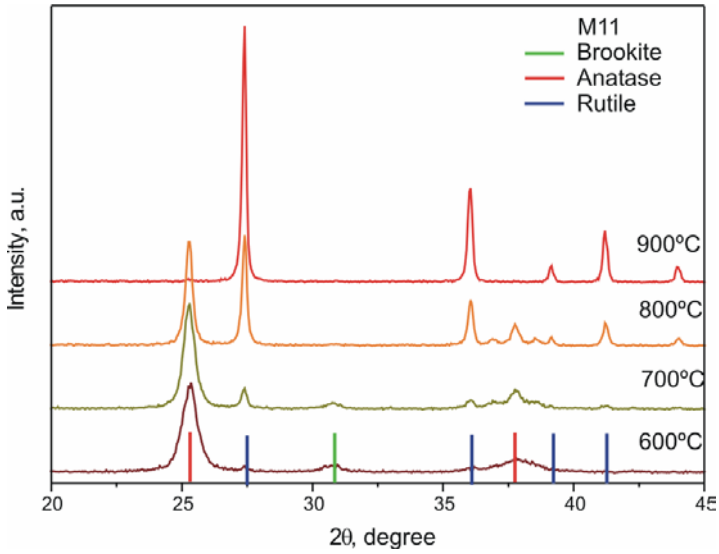

Figure IV.18 *Percentage of each crystalline phase contained in the materials. These values were obtained from the quantitative analysis of XRD patterns of sample M11*

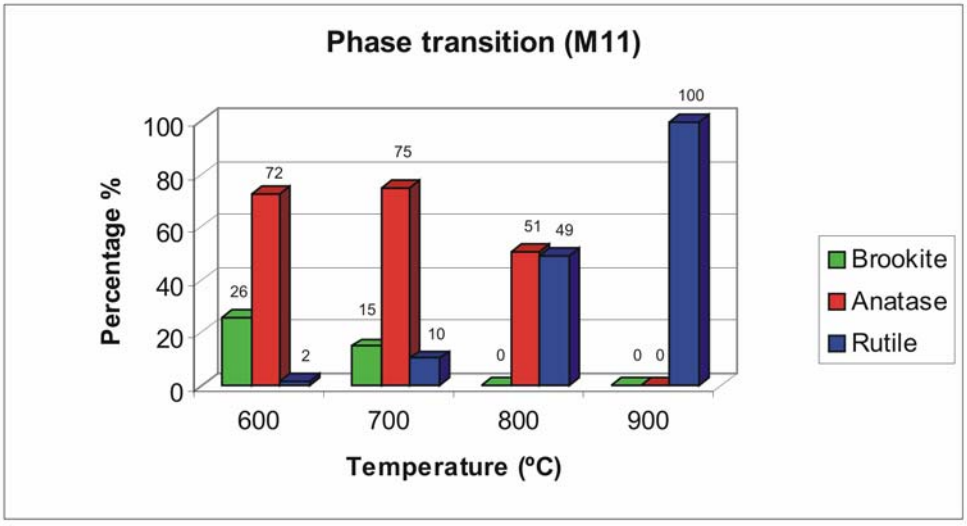

Figure IV.19 *Representation of the quantitative analysis of XRD pattern of material M6*

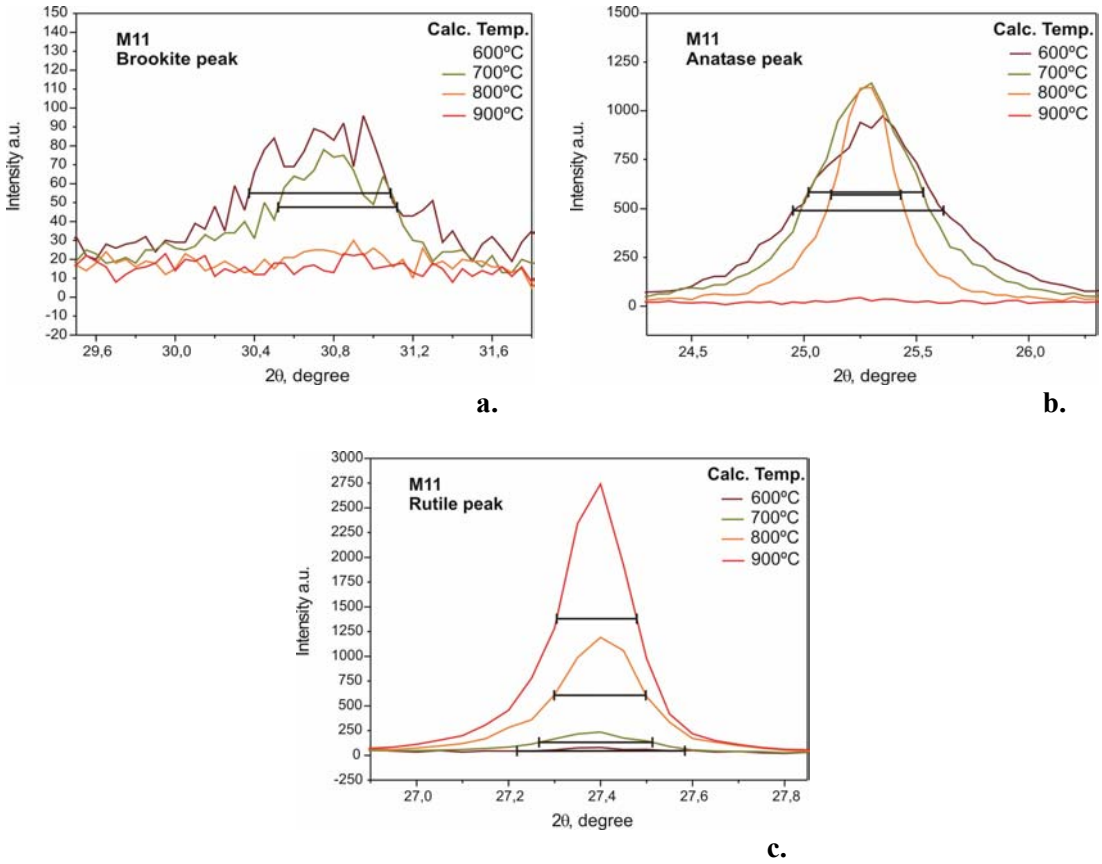

Figure IV.20 *Measurement of the FWHM in* ***a.*** *main brookite peak,* ***b.*** *main anatase peak and* ***c.*** *main rutile peak, in M11*

Table IV.11 *Size of brookite crystallites in M11 and the values employed for its calculation*

Temperature (ºC)	FWHM (rad)	θ (rad)	Crystallite size (nm)
600	1.25E-02	5.37E-01	14.37
700	1.05E-02	5.37E-01	17.11

Table IV.12 *Size of anatase crystallites in M11 and the values employed for its calculation*

Temperature (ºC)	FWHM (rad)	θ (rad)	Crystallite size (nm)
600	1.17E-02	4.42E-01	14.59
700	8.91E-03	4.41E-01	19.12
800	5.41E-03	4.42E-01	31.49

Table IV.13 *Size of rutile crystallites in M11 and the values employed for its calculation*

Temperature (ºC)	FWHM (rad)	θ (rad)	Crystallite size (nm)
600	6.38E-03	4.78E-01	27.20
700	4.31E-03	4.78E-01	40.25
800	3.48E-03	4.78E-01	49.83
900	3.04E-03	4.78E-01	57.05

Finally, in Table IV.14 it is shown the weighting average of the crystallite size in each material. This average was carried out in the same way than in previous cases. The higher content of anatase phase in the calcination temperatures below 800 ºC makes the average of the crystalline size in M11 lower than in M10.

Table IV.14 *Weighting average crystallite size of M9 in function of the calcination temperature*

Temperature (ºC)	Average crystallite size (nm)
600	14.76
700	21.03
800	40.51
900	57.05

IV.2.3.3. Area BET

Since the results of XRD were promising, area BET analyses were carried out in the same way described in section III.2.3. Figure IV.21 show the isotherms of adsorption and

desorption of M11 based materials. The isotherms are of IV type in the IUPAC classification, which means that all of them are mesoporous materials, as expected. The values of surface area (Table IV.15) are the highest among all materials. The higher the surface that interacts with the gas, better will be the response toward it. Then, it is expected that this characteristic of the surface added to the crystalline properties makes M11 based sensors very useful for oxygen detection

It is also observed that the grain diameter, calculated from surface area values, of M11 based material calcined at 600 ºC, 700 ºC and 800 ºC, are close to that obtained from XRD and SEM analyses. However, the values of the BET grain size of M11 calcined at 900 ºC are not equivalent to any other result of the commented techniques. This may be attributed to the acceleration of the adhesion of grains among them when all the residual dodecylamine that surround the grains is completely eliminated.

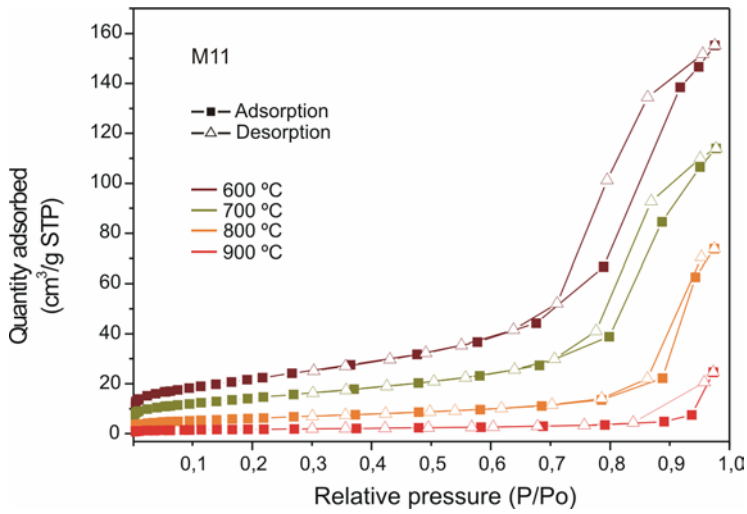

Figure IV.21 *Adsorption and desorption isotherms of N_2 at 77K of M11 calcined at different temperatures*

It is also observed that the grain diameter, calculated from surface area values, of M11 based material calcined at 600 ºC, 700 ºC and 800 ºC, are close to that obtained from XRD. However, the values of the BET grain size of M11 calcined at 900 ºC are not equivalent. This may be attributed to the acceleration of the adhesion of grains among them when all the residual dodecylamine that surround the grains is completely removed.

Table IV.15 *BET surface of M11 in function of the calcination temperature*

Temperature (ºC)	S_{BET} (m^2/g)	Grain size (nm)
600	77	16
700	50	25
800	21	57
900	6	202

IV.2.3.4. SEM

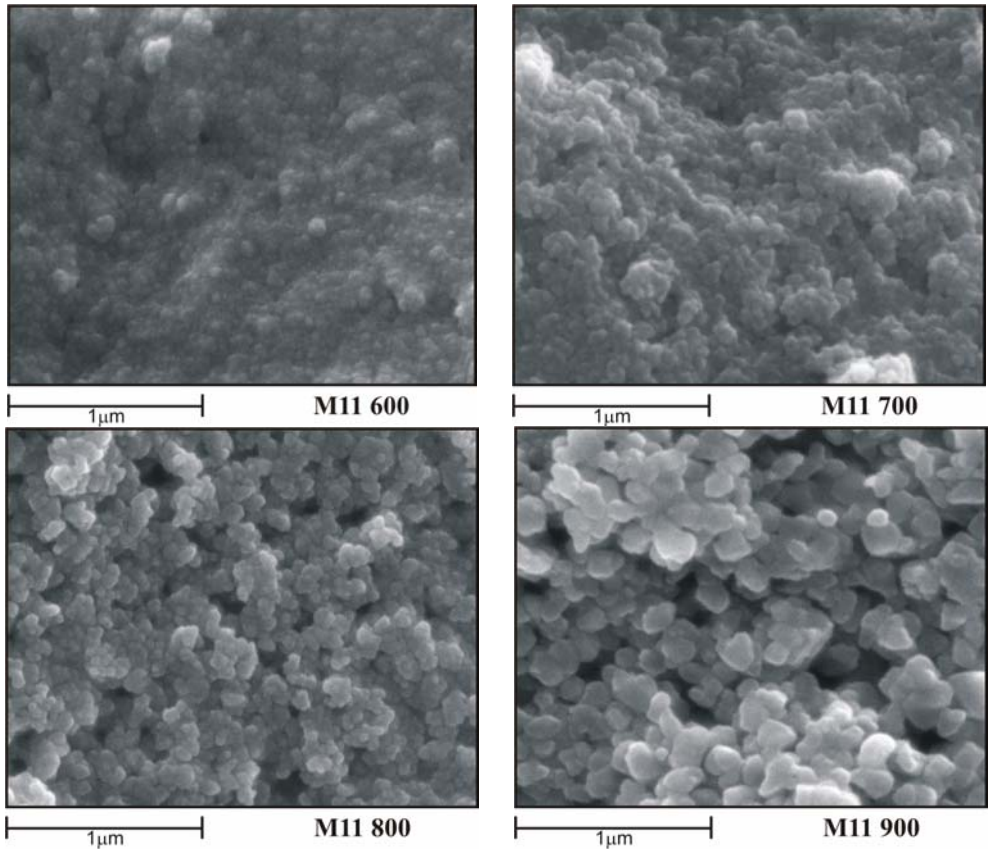

Figure IV.22 *SEM images of M11 calcined at different temperatures*

Finally, SEM analysis of the active layer was performed. The parameters for SEM analysis were the described in section III.3.1. The SEM pictures of the material M11 calcined at 600 ºC, 700 ºC, 800 ºC and 900 ºC are shown in Figure IV.22. The evolution of the grain diameter of this material is summarized in Table IV.16. The histograms of the grain size are showed in Figure IV.23.

The grain sizes in material M11 are similar to those in M10 and M9. So, they are smaller than in the doped materials synthesized without a template. As it happened in M10 and M9, it appears that the dodecylamine surrounds the particles hindering their fusion and growth. These results show that amouny of dodecylamine added do not affect the crystallite and grain sizes.

Materials M11-800 and M11-900 have a content of rutile higher than 50 %, so, as explained before, their best performance in the oxygen detection will be for working temperatures higher than those considered in our approach. On the other hand, material M11-600, probably will have residual carbonic deposits, as M6-600. So, probably the best material to sense oxygen in the desired working temperature range will be M11-700.

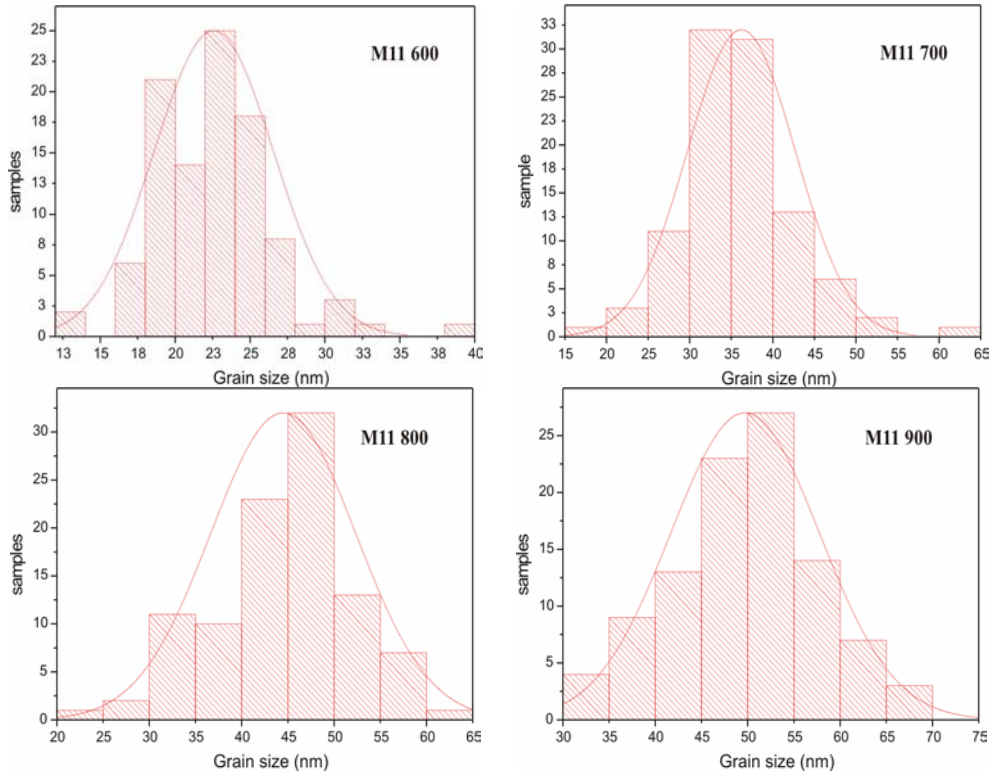

Figure IV.23 *SEM histograms of M11 calcined at different temperatures*

Table IV.16 *Grain size evolution of the grains belong to material M11*

Material	*d* (nm)	SD	SE
M11-600	22.57	3.9	0.39
M11-700	36.22	6.4	0.64
M11-800	44.49	7.8	0.78
M11-900	49.71	8.07	0.80

IV.2.3.5. Oxygen Sensing Characterization

As it was previously commented, material M11-700 was chosen as the best option among the M11 based materials to be tested in a sensor toward 20 ppm of oxygen. The sensor was prepared in the same way as it is described in section II.3.2. The measurements were done as it was showed in section III.4.1.

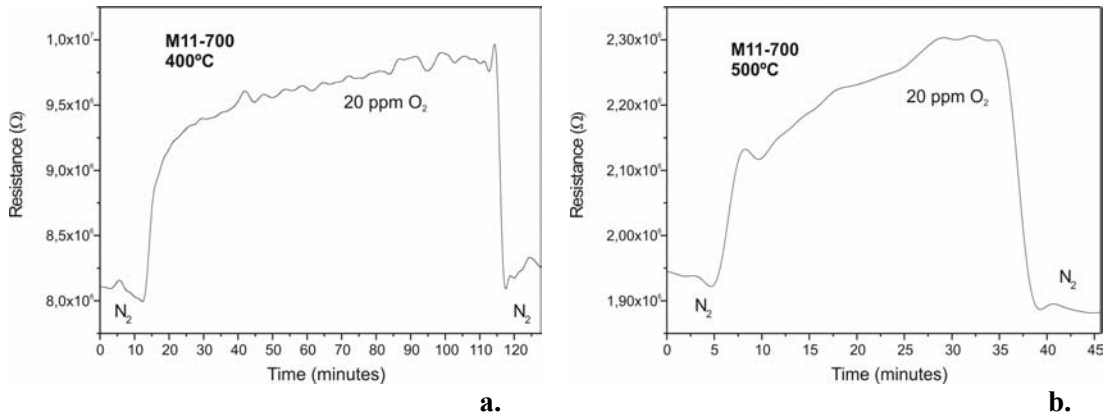

Figure IV.24 *Typical response of the sensor made from M11-700 toward 20 ppm of oxygen, working at* ***a.*** *400 ºC and* ***b.*** *500 ºC. The carrier gas employed was pure nitrogen*

Table IV.17 *Responses of the sensor made from M11-700 toward 20 ppm of oxygen working at different temperatures. The carrier gas was pure nitrogen*

Working Temperature (ºC)	Sensor response ($\Delta R / R_{N_2}$)	Error
500	0.18	4.8 %
400	0.21	7.0 %

The response of the M11-700 based sensor working at 400 ºC and 500 ºC are shown in Figure IV.24, and the values are summarized in Table IV.17.The responses at both temperatures of M11-700 sensor are very low compared with the responses obtained for M6-700 and M8-700 based sensors.

Parameters as grain size, active area and crystalline structure of M11-700 are better than in the other doped materials. However, there is something that is retarding the interaction between the material and the gas. This could be deposits of carbon compounds, located on the material surface that difficult the contact between the material and the gas, and thus the response of the sensor. To clarify this problem Raman measurements were done to M11-700. The results are the following.

IV.2.3.6. RAMAN

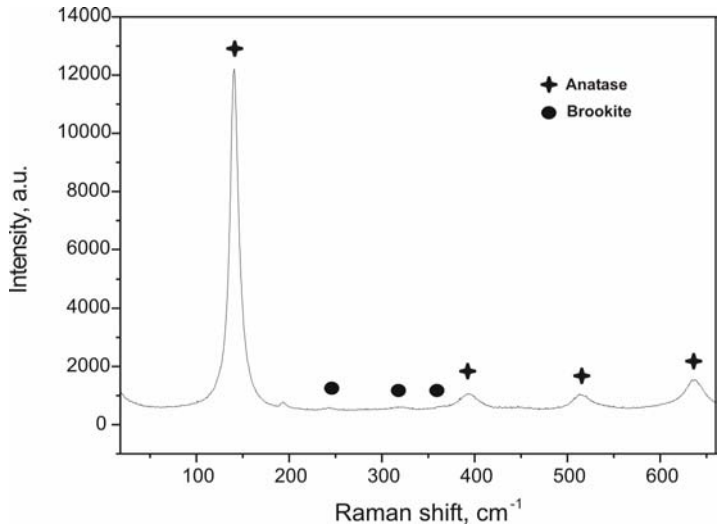

Figure IV.25 *Raman spectrum of M11-700 nanopowder at room temperature*

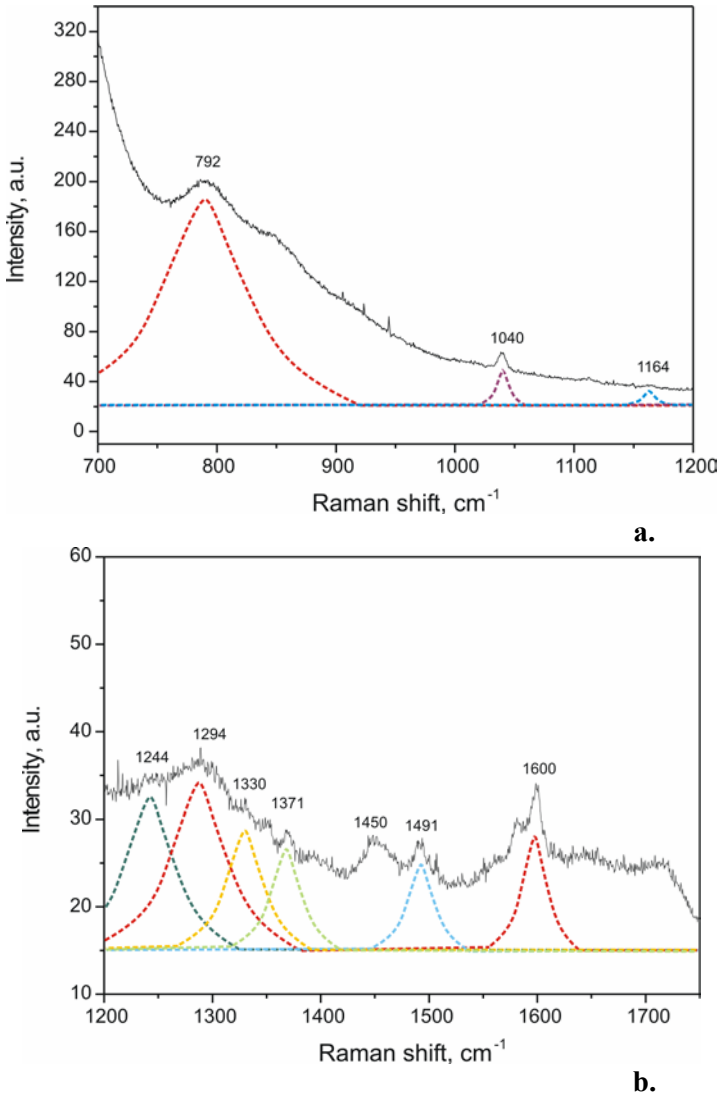

Figure IV.26 *Raman spectrum at high frequencies of M11-700 nanopowder at room temperature*

The Raman analysis was carried out as it is described in section III.5. The Raman spectrum between 18 and 650 cm^{-1} of M11-700 nanopowder is shown in Figure IV.25. The peaks that correspond to anatase phase are located at 141, 393, 515 and 636 cm^{-1}. The small peaks situated at 243, 322 and 363 cm^{-1} indicates the presence of brookite phase, but in lower proportion to anatase[14, 15].

Figure IV.26 shows the Raman spectrum of M11-700 at high frequencies. It is clearly observed the presence of carbon compounds in the material. Some peaks were identified: These peaks are summarized in Table IV.18. The source of these carbonic compounds could be found in the synthesis process. Then it is clear that, even that material M11-700 has the best features in all synthesized materials in order to be used for oxygen detection, the residual carbon compounds in its surface difficult the interaction of the oxygen species with the material and diminishes the response of the M11-700 based sensor.

Table IV.18 *Some Raman features in the range between 700 and 1750 cm^{-1}, present in the spectrum of M11-700*

Raman peak (cm^{-1})	**Possible correspondence**
792	Hydrogen free carbon structure [16, 17]
1040	Ammonium Carbonate
1164	Nanosized diamond crystals [18, 19]
1244	Contributions from the photon density of states in Crystalline Diamond [20]
1294	Hexagonal diamond [21, 22]
1330	Cubic diamond [16]
1371	*D* peak of microcrystalline graphite [17, 23]
1491	Contributions from the photon density of states in finite-size crystals of graphite [16, 24]
1600	*G* peak of graphite [17, 23]

IV.3. Conclusion

Three different attempts for mesoporous Titania synthesis were carried out using dodecylamine surfactant as template. For the first material, M9, 1 ml of the surfactant was added together with the alkoxide precursors. XRD analyses showed high contents of rutile phase in this material. It appears that in the stage of the process where the dodecylamine was added, inhibits the insertion of the Niobiums ions in the Titania network.

To avoid the effect of the dodecylamine in the doping process, in the second attempt (M10) the surfactant was added after the hydrolysis of the metal alkoxides. At this stage it is expected that the Nb ions are already inserted in the Titania crystalline network and thus, the only effect of the surfactant will do is the hindering of the nucleation process. The quantity of dodecylamine was also slightly increased up to 2 ml to assure the formation of micelles. XRD analysis showed that the phase transition is slower than in M9, but it is still faster than in other doped materials, M6 and M8. It looks that the addition of the dodecylamine in the final step of the sol-gel process does not affect so much the doping process. However, the quantities of rutile phase remaining in M10 based materials is still very high, which is useless for oxygen detection at the working temperatures considered in this work.

Finally, the process followed to obtain M10 was repeated increasing the amount of surfactant up to 8 ml (M11). From XRD results, it was observed that in M11, the phase transition was even slower than in M6 and M8. At a calcination temperature of 800 ºC, M11 was the unique material with a quantity of anatase phase over the 50 %. What probably happened is that at higher concentration of surfactant, its molecules join together forming micelles. On the contrary of the surfactant molecules, it appears that these structures do not affect the doping process. They even contribute to retard the crystallinization and thus the change of phase.

On the other hand, SEM analysis, as well as the calculations derived from XRD, show that the grain sizes of M9, M10 and M11 are smaller than in other doped materials (M6 and M8) without surfactant. It appears that the surfactant may act as a dispersing agent that surrounds the grains and inhibits their adhesion. The grains start to adhere when the dodecylamine is eliminated from the surface of the particles. Then, the effects of the dodecylamine in the grain size do not depend so much on the stage where the surfactant is added, as well as on its concentration.

The area BET analyses carried out to materials M11 show that the addition of the surfactant contributes to increase the porosity of the materials. Wang et al [25] obtained a mesoporous TiO_2 with wormhole-like framework structure following a similar synthesis process. However, the surface area that they got with Titania calcined at 450 ºC was only 48 m^2/g. In our work, we obtained a surface area of 77 m^2/g in M11 calcined at 600 ºC.

For the oxygen detection measurement only the material M11-700 were taking in account. This material was chosen for the high content of the anatase phase and high surface area.

The results of the oxygen measurement reveal a poor response of the considered material. The Raman spectroscopy of this material shows some peaks that correspond to

carbon with different morphologies, as it happened in the previous materials (without surfactant) calcined at 600 ºC. As it was explained before, these deposits of carbon cover the surface of the active material and hinder its interaction with the oxygen. And, because these carbon structures are also poorly catalytic, the result is a deactivation of the catalysis. This is reflected in the low response of this material toward oxygen. The fact that the residual carbon compounds remain in the material could be attributed to the dodecylamine. It is possible that the electrostatic forces in the inorganic-inorganic interface are strong and need very high temperatures to be eliminated. The improvement in the material when a template is used for the synthesis is evident, but probably the dodecylamine is not the adequate surfactant to be used. It is recommended for future approaches the use of a non-ionic oligomeric surfactant with lower bonding forces [26, 27].

IV.4. References

[1] C.T. Kresge, M.E. Leonowicz, W.J. Roth, J.C. Vartuli and J.S. Beck, "*Ordered Mesoporous Molecular Sieves Synthesized by a Liquid-Crystal Template Mechanism*", Nature, Vol. 359 6397 (1992) 657-758

[2] J.S. Beck, J.C. Vartuli, W.J. Roth, M.E. Leonowicz, C.T. Kresge, K.D. Schmitt, C.T.-W. Chu, D.H. Olson, E.W. Sheppard, S.B. McCullen, J.B. Higgins and J.L. Schlenkert, "*A New Family of Mesoporous Molecular Sieves Prepared with Liquid Crystal Templates*", Journal of American Chemical Society, Vol. 114 27 (1992) 10834 - 10843

[3] J.Y. Ying, C.P. Mehnert and M.S. Wong, "*Synthesis and Applications of Supramolecular-Templated Mesoporous Materials*", Angewandte Chemie International Edition, Vol. 38 1 (1999) 56-77

[4] P.A. Winsor, "*Binary and Multicomponent Solutions of Amphiphilic Compounds. Solubilization and the Formation, Structure, and Theoretical Significance of Liquid Crystalline Solutions*", Chemical Reviews, Vol. 68 1 (1968) 1-40

[5] J.-L. Salager, "*Interfacial Phenomena in Dispersed Systems*", Universidad de los Andes, Edited by E120-N, Mérida, 1994

[6] M.A. Carreon and V.V. Guliants, "*Ordered Meso- and Macroporous Binary and Mixed Metal Oxides*", European Journal of Inorganic Chemistry, Vol. 2005 1 (2005) 27-43

[7] D.M. Antonelli and J.Y. Ying, "*Synthesis of Hexagonally Packed Mesoporous TiO2 by a Modified Sol Gel Method*", Angewandte Chemie International Edition, Vol. 34 (1995) 2014-2017

[8] D.M. Antonelli, "*Synthesis of Phosphorus-Free Mesoporous Titania Via Templating with Amine Surfactants*", Microporous and Mesoporous Materials, Vol. 30 (1999) 315–319

[9] S.H. Jang, M.J. Kim, J.R. Ko and W.S. Ahn, "*Catalytic Properties of Ti-HMS with High Titanium Loadings*", Bulletin of the Korean Chemical Society Vol. 26 8 (2005) 1214-1218

[10] Z.H. Liu, X.H. Tang, C.X. Zhang and Q. Zhou, "*A Novel TiO_2-Pillared Microporous Manganese Oxide* ", Chemistry Letters, Vol. 34 10 (2005) 1312-1313

[11] Y. Wang, S. Zhang and X.H. Wu, "*Synthesis and Optical Properties of Mesostructured Titania-Surfactant Inorganic-Organic Nanocomposites* ", Nanotechnology, Vol. 15 9 (2004) 1162-1165

[12] V.I. Pârvulescu, S. Boghosian, V. Pârvulescu, S.M. Jung and P. Grange, "*Selective Catalytic Reduction of NO with NH_3 over Mesoporous V_2O_5–TiO_2–SiO_2 Catalysts*", Journal of Catalysis, Vol. 217 (2003) 172–185

[13] T.V. Anuradha and S. Ranganathan, "*Synthesis of Mesoporous Materials Based on Titanium(IV)Oxide and Titanium Nitride*", NanoStructured Materials, Vol. 12 (1999) 1063-1069

[14] G. Cappelletti, C. Ricci, S. Ardizzone, C. Parola and A. Anedda, "*Aged Titania Nanoparticles: The Simultaneous Control of Local and Long Range Properties*", Journal of Physical Chemistry B, Vol. 109 (2005) 4448-4454

[15] H.C. Choi, Y.M. Jung and S.B. Kim, "*Characterization of Raman Spectra of Size-Selected TiO2 Nanoparticles by Two-Dimensional Correlation Spectroscopy*", Bulletin of Korean Chemical Society, Vol. 25 3 (2004) 426-428

[16] J. Schwan, S. Ulrich, V. Batori and H. Ehrhardt, "*Raman Spectroscopy on Amorphous Carbon Films*", Journal of Applied Physics, Vol. 80 1 (1996) 440-447

[17] M.A. Tamor and W.C. Vassel, "*Raman "Fingerprinting" of Amorphous Carbon Films*", Journal of Applied Physics, Vol. 76 6 (1994) 3823-3829

[18] W. Yarbrough and R. Rey, "*In Diamond and Related Materials*", Edited by M. Geis A. Badzian, and G. Johnson (Materials Resource Society), EA-15, Pittsburgh, 1988

[19] J. Filik, "*Raman Spectroscopy: A Simple, Non-Destructive Way to Characterise Diamond-Like Materials*", Spectroscopy Europe, Vol. 17 5 (2005) 10-17

[20] T. López-Ríos and E. Sandre, "*Application of to Study Chemical Vapour SERS Deposition Processes : The Example of Diamond Films*", Journal of Raman Spectroscopy, Vol. 29 (1998) 733-737

[21] J. Kohanoff, "*Phonon Spectra from Short Non-Thermally Equilibrated Molecular Dynamics Simulations*", Computational Materials Science, Vol. 2 (1994) 221-232

[22] D. Knight and W. White, "*Characterization of Diamond Films by Raman Spectroscopy*", Journal of Materials Research, Vol. 4 (1989) 385-393

[23] R.O. Dillon and J.A. Woollam, "*Use of Raman Scattering to Investigate Disorder and Crystalline Formation in As-Deposited an Annealed Carbon Films*", Physical Review B, Vol. 29 6 (1984) 3482-3489

[24] R.J. Nemanich and S.A. Solin, "*First- and Second-Order Raman Scattering from Finite-Size Crystals of Graphite*", Physical Review B, Vol. 20 2 (1979) 392-401

[25] Y.-d. Wang, C.-l. Ma, X.-d. Sun and H.-d. Li, "*Synthesis and Characterization of Amorphous TiO_2 with Wormhole-Like Framework Mesostructure*", Journal of Non-Crystalline Solids, Vol. 319 (2003) 109–116

[26] P. Yang, D. Zhao, D. Margolese, B. Chmelka and G. Stucky, "*Generalized Syntheses of Large-Pore Mesoporous Metal Oxides with Semicrystalline Frameworks*", Nature, Vol. 396 (1998) 152-155

[27] P. Yang, D. Zhao, D. Margolese, B. Chmelka and G. Stucky, "*Block Copolymer Templating Syntheses of Mesoporous Metal Oxides with Large Ordering Lengths and Semicrystalline Framework*", Chemistry of Materials, Vol. 11 (1999) 2813-2826

V. CONCLUSIONS

In this work an alumina substrate for gas sensor application has been developed. This substrate can support four active layers working at the same temperature forming a sensor array. The working temperature can reach 800 ºC, with a power consumption of approximately 5 W. This substrate is being used for gas sensor application with good results. However, due some problems related with the substrate package at working temperatures above 450 ºC, the use of this substrate for oxygen sensor application was delayed and the results obtained whit it were not complete enough to be presented in this work. In order to resolve the necessity of a substrate that can resist high working temperatures for oxygen sensing applications, a new substrate acquired from the Kurchatov Institute (Moscow-Russia) was introduced. This new substrate can reach working temperatures of 700 ºC with a power consumption of approximately 300 mW for a single sensor. The results exposed in this work were obtained by using this last substrate.

For the active layer, pure Titania and Niobium doped Titania nanopowders were synthesized by a simplified sol-gel route. Based on the literature, the doping concentration in doped materials was set to Nb/Ti = 3 at%. ICP (Inductively Coupled Plasma) and EDS (Energy-Dispersive X-ray Spectroscopy) techniques confirmed that the content of Niobium in the doped materials was near to the nominal value (3 at%), which indicate that the doping process was carried out correctly.

In order to find the best the crystalline structure of the active materials, the powders were calcined at four different temperatures: 600 ºC, 700 ºC, 800 ºC and 900 ºC. Two different calcination ramps were employed to reach the calcination temperature: 10 ºC/min and 2.5 ºC/min.

XRD (X-Rays Diffraction) analysis confirmed that addition of Niobium ions to Titania lattice helps to retard the crystalline phase transition from anatase to rutile when calcination temperature is increased. The complete change of phase in such materials took place over 800 ºC. It was found that the doped materials calcined at 600 ºC and 700 ºC had a content of anatase around 70 %. On the other hand, in undoped materials the complete change of crystalline phase took place at 700 ºC. In such materials calcined at 600 ºC the content of rutile was over 50 %. The slower temperature ramp employed for calcination process also produces a slight retard in the phase transition. Nevertheless, this retard is not so remarkable and can not be compared with that produced by the Nb ions. XRD technique also showed that the crystallites grow proportional to the temperature. This growth is hindered by the addition of Niobium to the Titania, and also by the use of a slower calcination ramp.

BET analyses showed that the surface area decreases when calcination temperature increases. It was observed that the addition of niobium retards the reduction process of the

surface area with the temperature and also improves the porosity of the material. So, the results of this analysis, combined with the XRD results suggests that the more promising materials for best sensitivity to oxygen are de doped ones calcined at the lowest temperatures.

The SEM analysis allowed to know the grain growth evolution of the layers. It was observed that the grain size in doped materials is smaller than in pure Titania at calcination temperatures between 600 ºC and 800 ºC. Then, at 900 ºC, the grain growth in all materials is almost the same. The introduction of the Niobium in the Titania lattice not only hinders the growth of the crystals but also the coalescence between them retarding the grain growth. The slower ramp used to reach calcination temperature also help to retard the grain growth, and then, the lowest grain sizes were found in doped materials calcined by using the slowest temperature ramp. So these results reaffirm the hypothesis that doped materials calcined at the lower temperatures are the more promising one to achieve the objectives of this work.

Regarding the oxygen detection measurements, the best responses toward oxygen traces in N2 were achieved for sensors based on doped materials calcined at 700 ºC. This is probably due to the high surface area of such materials, which clearly benefits the detection mechanism and their crystalline phase, mostly anatase, which permits the detection at desire temperatures (300 ºC – 600 ºC). The Niobium species may also contribute to the catalytic process. The optimum working temperature for oxygen sensing with these materials was found at 500 ºC. The calcination ramp did not have any effect on the sensing capabilities of materials. So, these results confirm that doped materials has better performance than undoped ones or doped ones calcined at the higher calcination temperatures. Nevertheless, the results obtained for doped materials calcined at 600 ºC (the lowest one) do not agree with the previous hypotheses.

It was observed that the doped materials calcined at 600 ºC had a poor response, in spite of they have better physical characteristics than doped materials calcined at 700 ºC. The retard in oxygen sensing capabilities of these materials may be caused by the brookite phase they contain. At 600 ºC the crystallinity of the brookite particles is improved, with the consequent diminishing of the surface defects that can affect the adsorption of oxygen species on the surface. However, deeper analysis with Raman spectroscopy shows some peaks corresponding to carbon with different morphologies in the surface of these materials. These deposits of carbon are the residual of the synthesis process, which could not be eliminated during the calcination. The problem with these deposits of carbon is that they cover the surface of the active material and hinder its interaction with the oxygen. So, since these carbon structures are also poorly catalytic, the result is a deactivation of the catalysis. This is reflected in the low response of this material toward oxygen.

It was also shown that Nb-doped Titania calcined at 700 ºC has a good response to traces of oxygen in CO_2, which indicates that a sensor based on this material may be used in applications such food packaging and beverage carbonation. However, the response toward

15 ppm of oxygen presented an inversion from oxidation type to reduction type. This phenomenon was explained as the effect of the CO species, from CO_2 dissociation, which is adsorbed on the active material surface on the low concentration of oxygen species. This sensor was also tested toward other pollutant gases of CO_2 such as H_2S, SO_2 C_2H_4 and CH_4. Very high responses, compared with other authors, were obtained for SO_2 and CH_4. No response was obtained for C_2H_4. These last responses toward other pollutant gases give rise to a problem of cross sensitivity that may be solved by the use of a gas sensor array. In that way, the gas detection may be done by analyzing the response patterns of the sensor array toward each gas combination.

Following the goals outlined in the beginning of this work, it was attempted to modify the materials properties in order to improve the oxygen sensing capabilities of doped materials. This was done by using surfactants (dodecylamine) as template during the material synthesis process. It was expected that the use of a template leads to an increment of the surface area and porosity of the materials. Among three different attempts, the best results were obtained when 8 ml of surfactant were added to the solution after the hydrolysis of the metal alkoxides during the sol-gel process. This material was labelled M11.

XRD results showed that in M11, the phase transition was even slower than in other doped materials synthesized without template. At a calcination temperature of 800 ºC, M11 was the unique material with a quantity of anatase phase over the 50 %. SEM analysis, as well as the calculations derived from XRD, showed that the grain sizes of M11 based materials are smaller than in other doped materials without surfactant. The area BET analyses carried out to material M11 showed that the addition of the surfactant also contributes to increase the porosity of the materials. The surface area obtained from material M11 was even better than other synthesized materials recently published. However, the results of the oxygen measurement reveal a poor response of the considered material. The Raman spectroscopy of this material showed some peaks corresponding to carbon with different morphologies, as it happened in the previous materials (without surfactant) calcined at 600 ºC. As it was explained before, these deposits of carbon cover the surface of the active material and hinder its interaction with the oxygen. Since these carbon structures are also poorly catalytic, the result is a deactivation of the catalysis. This is reflected in the low response of this material toward oxygen. The fact that the residual carbon compounds remain in the material could be attributed to the dodecylamine. It is possible that the electrostatic forces in the inorganic-inorganic interface are too strong and need very high temperatures to be eliminated. The improvement in the material when a template is used for the synthesis is evident, but probably the dodecylamine is not the adequate surfactant to be used. It is recommended for future approaches the use of a non-ionic oligomeric surfactant with lower bonding forces.

PUBLICATIONS

Communications

E. Sotter, J. Prásek, R. Kuchka. "*Drop-Coating Deposition Procedure in Micro-Hotplate Gas Sensor Fabrication*". Elektrotechnika a informatika 2003 Proceedings. Plzen (Czech Rep.) 2003

E. Sotter, J. Prásek, M. Adámek, X. Vilanova. "*Fabrication of Nb-doped Titania Nanopawders by Sol-Gel Route*". Workshop on electron devices and microelectronics. Tarragona (Spain) 2004

E. Sotter, J. Prásek, X. Vilanova, E. Llobet, X. Correig. "*Fabrication of a TiO_2 Based Oxygen Sensor*". 11th Electronic devices and systems conference. Brno (Czech Rep.) 2004

E. Sotter, X. Vilanova, A. Vasiliev, X. Correig. "*Thick Film Titania Based Sensors for Detection of Oxygen at ppm Levels*". 5th Conference on Electron Devices, Tarragona, Spain, 2005

E. Sotter, X. Vilanova, A. Vasiliev, X. Correig. "*Thick Film Titania Based Sensors for Detection of Oxygen at ppm Levels*". Eurosensors XIX. Barcelona (Spain) 2005

E. Sotter, X. Vilanova, E. Llobet, M. Stankova, X. Correig. "*Niobium-Doped Titania Nanopowders for Gas Sensor Applications*". 3rd International Symposium on Irradiation Induced Phenomena in Chalcogenide, Oxide and Organic Thin Films, Tryavna, Bulgaria (2005)

Journal Articles

E. Sotter, X. Vilanova, E. Llobet, M. Stankova, X. Correig. "*Niobium-Doped Titania Nanopowders for Gas Sensor Applications*". Journal of Optoelectronics and Advanced Materials 7 (3) 2005, p. 1395-1398

Other Publications

J. Prásek, E. Sotter. "*A New Way in Thick Film Sensors Response Measurements*". Elektrotechnika a informatika 2003 Proceedings. Plzen (Czech Rep.) 2003

E.H. Espinosa, R. Ionescu, E. Sotter, E. Llobet, A. Felten, C. Bittencourt, J.J. Pireaux. "*Micro-Hotplate Gas Sensors Based on Functionalized Carbon Nanotube Films*". Workshop on electron devices and microelectronics. Tarragona (Spain) 2004

M. Adámek, J. Prásek, E. Sotter. "*The Dependence of Output Current Response on Materials of Chemical Sensors Working Electrodes*". Workshop on electron devices and microelectronics. Tarragona (Spain) 2004

J. Prásek, M. Adámek, E. Sotter. "*Thick Film Graphite Pastes for Working Electrodes of Amperometric Sensors*". Workshop on electron devices and microelectronics. Tarragona (Spain) 2004

E.H. Espinosa, R.Ionescu, E. Sotter, E. Llobet, A. Felten, C. Bittencourt, J.J. Pireaux. "*Micro-Hotplate Gas Sensors Based on Functionalised Carbon Nanotube Films*". IX European Conference on Organised Films, ECOF. Valladolid (Spain) 2004

P. Ivanov, J. Laconte, J.-P. Raskin, D. Flandre, M. Stankova, E. Sotter, E. Llobet, X. Vilanova, X. Correig. "*SOI-CMOS Compatible Low-Power Gas Sensor Using Sputtered and Drop-Coated Metal-Oxide Active Layers*". Symposium on Design, Test, Integration and Packaging of MEMS/MOEMS. Montreux (Switzerland) 2004

J. Prásek, M. Adamek, J. Hubalek, I. Szendiuch, E. Sotter. "*New Thick Film Sensor Design and Its Material Optimization for Heavy Metal Detection*". 11th Electronic devices and systems conference. Brno (Czech Rep.) 2004

R. Ionescu, E. Sotter, E.H. Espinosa, E. Llobet, X. Vilanova, X. Correig, A. Felten, C. Bittencourt and J.J. Pireaux. "*Detection of NO2 and NH3 with Oxygen Functionalysed MWNT Based Microhotplate Gas Sensors*". Eurosensors XVIII. Roma (Italy) 2004

Felten, R. Ionescu, E. Sotter, E. Llobet, X. Vilanova, X. Correig, C. Bittencourt, J.J. Pireaux. "*Oxygen Functionalized MWNT as Active Layer for Gas Sensing: Detection of NO2 and NH3*". American Vacum Society - AVS 51st International Symposium & Exhibition. Anaheim (USA) 2005

P. Ivanov, J. Laconte, J. P. Raskin, M. Stankova, E. Sotter, E. Llobet, X. Vilanova, D. Flandre, X. Correig. "*SOI-CMOS Compatible Low-Power Gas Sensor using Sputtered and Drop-Coated Metal-Oxide Active Layers*". Microsystem Technologies-Micro-And Nanosystems-Information Storage And Processing Systems 12 (1-2), 2005, p.160-168

R. Ionescu, E.H. Espinosa, E. Sotter, E. Llobet, X. Vilanova, X. Correig, A. Felten, C. Bittencourt, G. Van Lier, J.-C. Charlier and J.J. Pireaux. "*Oxygen Functionalisation of MWNT and Their Use as Gas Sensitive Thick-Film Layers*". Sensors and Actuators B: Chemical, Volume 113 (1), 2006, p.36-46